NOTICE

The quality of this microform is heavily dependent upon the quality of the original thesis submitted for microfilming. Every effort has been made to ensure the highest quality of reproduction possible.

If pages are missing, contact the university which granted the degree.

Some pages may have indistinct print especially if the original pages were typed with a poor typewriter ribbon or if the university sent us an inferior photocopy.

Reproduction in full or in part of this microform is governed by the Canadian Copyright Act, R.S.C. 1970, c. C-30, and subsequent amendments.

AVIS

La qualité de cette microforme dépend grandement de la qualité de la thèse soumise au microfilmage. Nous avons tout fait pour assurer une qualité supérieure de reproduction.

S'il manque des pages, veuillez communiquer avec l'université qui a conféré le grade.

La qualité d'impression de certaines pages peut laisser à désirer, surtout si les pages originales ont été dactylographiées à l'aide d'un ruban usé ou si l'université nous a fait parvenir une photocopie de qualité inférieure.

La reproduction, même partielle, de cette microforme est soumise à la Loi canadienne sur le droit d'auteur, SRC 1970, c. C-30, et ses amendements subséquents.

Canada

PHOTOPHYSICAL STUDIES ON ULTRA-SMALL SEMICONDUCTOR PARTICLES:

CdS Quantum Dots, Doped and Undoped TiO_2, and Silver Halides

Darren LAWLESS

A Thesis
in
the Department
of
Chemistry & Biochemistry

Presented in Partial Fulfilment of the Requirements for the
Degree of Doctor of Philosophy
at
Concordia University,
Montréal, Québec, Canada

January 1993

ISBN 0-315-84678-X

ABSTRACT

PHOTOPHYSICAL STUDIES ON ULTRA-SMALL SEMICONDUCTOR PARTICLES: CdS Quantum Dots, Doped and Undoped TiO_2, and Silver Halides

Darren Lawless, Ph.D.
Concordia University, 1993

The photophysical and photocatalytic properties of TiO_2, doped in the bulk with a number of transition metal ions, were investigated using UV/Vis and fluorescence spectroscopy, pulse radiolysis, and transient absorption and emission spectroscopy. The dopants added at various concentrations included: Cr^{+3}, Fe^{+3}, V^{+5} and V^{+3}, Ru^{+3}, Pt^{+4}, Rh^{+1}, Pd^{+2}, Cu^{+2}, Mn^{+2}, Ni^{+2}, W^{+6}, Mo^{+6}, Ce^{+3}, Co^{+2}, Nd^{+3}, Re^{+3} and Re^{+7}, Y^{+3}, Ti^{+3}. The size, morphology, crystal structure and surface area of both doped and undoped TiO_2 specimens were determined using dynamic light scattering, electron microscopy, x-ray diffraction and surface area measurements. The effect of different anatase/rutile ratios, particle size and nature of the dopant on the photocatalytic activity was examined. The relative photooxidative and photoreductive ability of the TiO_2 samples were examined. The effect of particle size on the photophysics of e^-/h^+ separation/recombination events was examined in TiO_2 colloids of various size. in AgI colloids and in CdS microcrystallites in aqueous media; the latter was also examined in a silicate matrix.

The reaction of •OH radicals with 133-Å TiO_2 particles was studied using pulse radiolysis; it occurs at a nearly-diffusion-controlled rate. The product was identified as a trapped hole at the surface of TiO_2, namely as $\{Ti^{IV}\text{-}O^{\bullet-}\text{-}Ti^{IV}\}\text{-}OH^- \leftrightarrow \{Ti^{IV}\text{-}O^{\bullet-}\text{-}Ti^{IV}\}\text{-}\bullet OH$; it exhibited a broad absorption band centred at about 350 nm.

No differences were noted in the absorption properties between 23, 133 and 281 Å diameter TiO_2 particles; significant variations in the dynamics of charge carrier recombination

were observed. These TiO_2 particles do not display typical quantum-size properties such as blue shifts in the UV-vis spectrum.

Some transition metal dopants added to the lattice of TiO_2 extended the absorption characteristics of TiO_2 into the visible spectral region, while others do not appear to affect the band-edge-absorption of TiO_2; rather they seem to sensitize the material through the formation of a broad band in the visible region. The concentration and the oxidation state of the dopant have a marked effect on the absorption properties. The effect of the dopant concentration on the band-edge-emission intensity of TiO_2 is non-linear. Transient emission studies indicate that the different dopants have only small effects on the band-edge-emission decay times. Transient absorption studies reveal that the different dopants used may act as either electron or hole traps.

The particle size of TiO_2 appears to have a slight effect on the photooxidative activity of TiO_2. Addition of transition metal dopants to the bulk of TiO_2 does not enhance the photooxidative activity of TiO_2; in some cases it does improve the reductive properties of the materials. Increasing the dopant concentration, in general, leads to decreased photooxidative catalytic activity.

The reduction of Ag^+ ions and formation of silver atoms and/or dimeric Ag_2 molecules on three different size AgI particles were examined by picosecond laser spectroscopy. The rates of formation of these silver species and/or higher nuclearity clusters followed simple exponential growth kinetics and correlated linearly with (size) ^{1}.

CdS glasses prepared with different surface-active materials displayed different charge carrier dynamics, demonstrating the importance of the CdS particle/silicate glass interface. Excitation of the glasses at high laser power generated several excitons in the same particle to give multiexcitonic states. Upon relaxation, these excited states led to the formation of Cd^0 and/or Cd_n^0 clusters, and $S^{\bullet-}$ radicals.

To

Rita

Acknowledgements

I would like to express my sincerest gratitude and thanks to Professor Nick Serpone for not only taking an active interest in my work and encouraging me in my research but also in putting up with my little quirks. I am particularly grateful for his willingness to send me to conferences in warm climates in the dead of winter and for his sending me to spend a fruitful 3-month period at Argonne National Laboratory in Chicago.

I am thankful to Dr. Dani Meisel, Argonne National Laboratory, for his kind hospitality during the time I spent at Argonne and for truly making me feel like a member of his research group. My thanks to his group for their hospitality in their lab. I would also like to thank Dr. Meisel for agreeing to serve on my research committee. My thanks also extend to Mr. Liao Youxin of the Material Science Division of Argonne National Laboratory for his assistance with the electron microscopy and EDAX measurements.

My thanks to Mr. Robert Patterson of Science Industrial Research Unit at Concordia, Dr. Dev Sharma and Mr. Reza Danesh of the Canadian Centre for Picosecond Laser Spectroscopy (Concordia University), Miss Anne Marie Pelletier (COOP student from the Université de Sherbrooke), and Mr. Pierre Kennepohl (Concordia University) for their technical assistance in some of the measurements. I would like to thank Dr. Le Van Mao and Mr. B. Sjiariel (Concordia University) for help with the surface area measurements, and Prof. J. Fendler and his group at the university of Syracuse, particularly Ms. Youxin Yuan, for access and assistance with the light scattering measurements. I am grateful to Dr. O.I. Micic and her coworkers of the Boris Kidric Institute of Nuclear Sciences, Belgrade for pulse radiolysis work on the AgI clusters, and for providing some of the CdS glasses (courtesy of Dr. T. Rajh).

Not least,I would like to thank Mr. Pierre Kennepohl for proofreading some of the chapters, Mr. Chris Kutyla of E.A.C.H New Design for his invaluable assistance in the preparation of the coloured images and a number of other figures in the text, and Professor R.T. Rye for serving on my Research Committee.

Finally, I am grateful to my parents for encouraging me to pursue my studies and for always stressing the importance of a good education. Lastly, but surely not least, my sincerest gratitude goes to my best friend, my colleague and the best chemist I know, my wife, Rita Terzian, for not only her help, support, and understanding but also for not divorcing me during this odyssey! I could not have made it without her.

TABLE OF CONTENTS

CHAPTER 3

PHYSICOCHEMICAL PROPERTIES OF TiO_2 AND TRANSITION METAL DOPED TiO_2

CHAPTER 4

A PULSE RADIOLYSIS STUDY OF •OH RADICALS AT THE SURFACE OF COLLOIDAL TiO_2

CHAPTER 5

PHOTOPHYSICAL STUDIES OF NAKED COLLOIDAL TiO_2

CHAPTER 6

PHOTOPHYSICAL STUDIES OF TRANSITION METAL DOPED COLLOIDAL TiO_2

CHAPTER 7

PHOTOCATALYTIC STUDIES OF NAKED AND TRANSITION METAL DOPED TiO_2

CHAPTER 8

CHARGE CARRIER TRAPPING IN ULTRASMALLSILVER IODIDE PARTICLES AND KINETICS OF SILVER ATOM CLUSTERS

CHAPTER 9

PHOTOLUMINESCENCE AND PICOSECOND CHARGE CARRIER DYNAMICS IN CdS QUANTUM DOTS CONFINED IN A SILICATE GLASS

LIST OF FIGURES

LIST OF TABLES

CHAPTER 1

INTRODUCTION

1.1 GENERAL INTRODUCTION

Considerable interest and research activity have been directed towards solar energy conversion and storage.[1] Of particular interest has been the prospect of photocleavage of water into dihydrogen and dioxygen as an alternative fuel energy source.[2] Particularly attractive about this energy production route is the fact that the process is both thermally and chemically non-polluting. Research has also focused on using solar energy in attempts to resolve many environmental problems: for example, the pollution of streams, rivers and ground water tables with toxic organic and inorganic contaminants from industrial and agricultural activities. Given the current worldwide concern about the present state of the environment, together with the depletion of limited fossil fuel resources, research in this area has become of increased importance and urgency; it continues unabated.

An important component of the many research efforts has been the utilization of semiconductor materials as light harvesters, as light converters and as photocatalysts in a variety of redox reactions. Semiconductor particulate systems have shown promise in the conversion of light energy[3-13] and numerous studies[14-22] have demonstrated that semiconductors can be used to initiate and control various photocatalytic processes. For

example, recent reports[23] in which TiO_2 has been used have detailed the complete mineralization of a number of organic pollutants such as cresols,[24] chlorophenols,[25] and surfactants,[26] as well as the removal of several toxic metals such as lead,[27] chromium,[28] and mercury,[29] from waste waters. The results have shown that titanium dioxide, particulary Degussa TiO_2 P25, to be the preferred catalyst for environmental applications. It has aroused a considerable amount of interest in examining the mechanistic details of the TiO_2 photoactivity in order to improve its photocatalytic efficiency.

The high commercial potential of semiconductor technology has stimulated interest in understanding and elucidating the primary photochemical and photophysical properties of semiconductors and the dynamics of the interfacial processes at the semiconductor/electrolyte interface.[30-35] In achieving a greater understanding of these processes, it is hoped that the photocatalytic properties of a particular semiconductor may be modified to meet a specific need.[36]

Research into the photophysical properties of a number of semiconductors have been made possible by recent advances in the preparation of colloids of uniform size and shape.[37] The synthesis of these materials typically involves precipitation of the semiconductor by controlled release of anions or forced hydrolysis.[16] For example, colloidal CdS may be prepared by mixing Cd^{+2} with sulphide ions.[38-44] Similarly, TiO_2,[45-49] ZnO,[50-52] WO_3,[53] CdO and In_2O_3[54] have been prepared through forced hydrolysis. Other techniques in preparing colloidal semiconductors include phase transformations,[55-59] reaction in the vapour phase,[60,61] and radiolytic generation of the material.[62-65] In addition to being prepared in homogenous environments, colloidal

semiconductors have also been synthesized in polymer films,[66-69] microemulsions,[70-72] zeolites[73] and glasses.[74-77]

The reproducible synthesis of transparent colloidal solutions in different environments has permitted the use of a number of state-of-the-art optical techniques to characterize the electronic properties of the conduction and valence bands, as well as the events taking place at the particle surface traps, preexisting or formed upon bandgap excitation. The development of picosecond and, more recently, femtosecond laser flash photolysis techniques has permitted characterization of the ultrafast electronic processes that follow bandgap excitation by directly monitoring the absorbance changes in the subnanosecond time domain. As noted by Kamat,[36] the characterization of these fast photochemical processes is important in our understanding the kinetics and mechanistic details of the corrosion and interfacial charge transfer reactions. For example, charge trapping and recombination processes in TiO_2 and CdS sols have been examined.[78-81] In the case of TiO_2, several reports[33,41,46,82-84] detailing the optical characteristics of the photogenerated electron have appeared and it is now fairly well accepted that within a few picoseconds, following bandgap excitation, the electron is trapped near or at the surface, resulting in the formation of a Ti^{+3} centre.[84]

A number of electronic and photochemical processes can occur following bandgap excitation of a semiconductor. Figure 1.1 illustrates the possible sequence of photochemical and photophysical events and the possible redox reactions which could occur at the surface of a semiconductor particle in solution. Absorption of light energy greater than or equal to the bandgap (E_{bg}) of the semiconductor results in the migration

of electrons (e^-) from the valence band to the conduction band and the creation of holes (h^+) in the valence band. These charge carriers can then recombine (radiatively and/or nonradiatively) in competition with rapid diffusion to the surface where the resulting non-equilibrium distribution of electrons and holes gives rise to reduction or oxidation processes with adsorbed species, surface groups and with the semiconductor components.

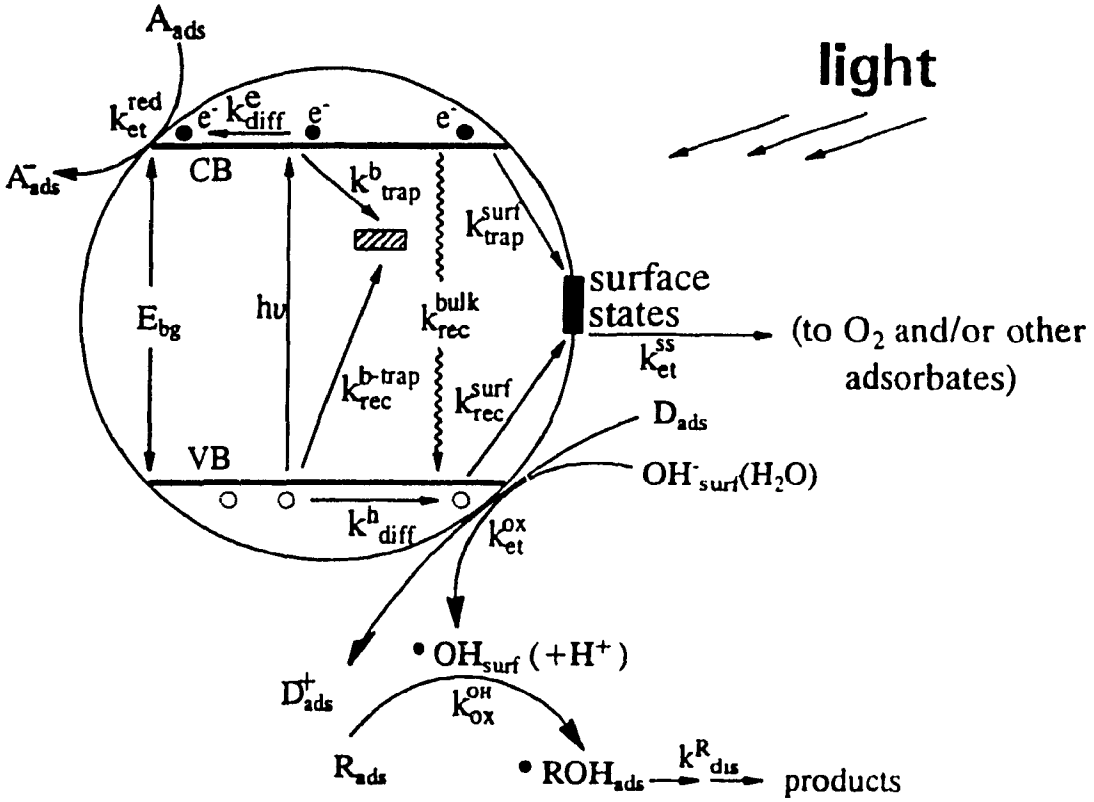

Figure 1.1 Photophysical and photochemical processes in a semiconductor cluster.

Thus when illuminated with light of sufficient energy ($\geq$ bandgap energy), the semiconductor particle becomes part of a particulate system capable of mimicking a microphotoelectrochemical cell at which efficient reduction and oxidation chemistries may

take place.[85] The efficiency of the reduction and oxidation processes will largely be determined by five factors:[86]

1) Fast charge separation after light absorption;

2) Separation of products in order to prevent reverse reactions;

3) Efficient absorption of solar light with minimal entropy production;

4) Adjustment of the redox potentials of the excited states to the redox reactions which store the energy;

5) Long term stability (or continuous reproduction).

The dominant competitive process to charge separation is electron/hole recombination, which for semiconductor clusters primarily occurs via non-radiative processes.[4c] This occurs as a result of a strong coupling of the wavefunctions of the trapped electrons and holes to lattice vibrations (so-called phonons). The lifetime of the electron, and the hole, as well as carrier reactivity may also be affected by the addition of traps or dopants into the lattice, as well as by the existence of surface states, either pre-existing or formed upon illumination.

Semiconductors which have been intentionally doped can be said to be extrinsic semiconductors. Dopants can have profound effects on their optoelectronic properties; they may occupy either a lattice site (i.e., a position of one of the components of the semiconductor), an interstitial site or a vacancy (a defect location in the lattice). Semiconductor materials that are doped with electron donors are known as n-type; in this case, electrons are the majority carriers and the holes are the minority carriers. The

opposite holds for p-type semiconductors: they are doped with electron acceptors, and holes are the majority carriers while electrons are the minority carriers.[87]

The lifetime of the charge carriers may also be affected by the existence of surface states. These states are energy levels located in the forbidden gap (see Figure 1.2) and may originate in one or two different ways.[87] Intrinsic surface states (referred to as Tamm states) form due to a lack of periodic structure of the lattice or result from reconstruction of the surface. Shockley states (so-called extrinsic states) result from the bonding between surface atoms and atoms of a new phase, or alternatively originate from adsorption of impurity ions (eg. Cl^- on TiO_2 from the hydrolysis of $TiCl_4$) or from chemical attachment of molecular systems to semiconductor surfaces.

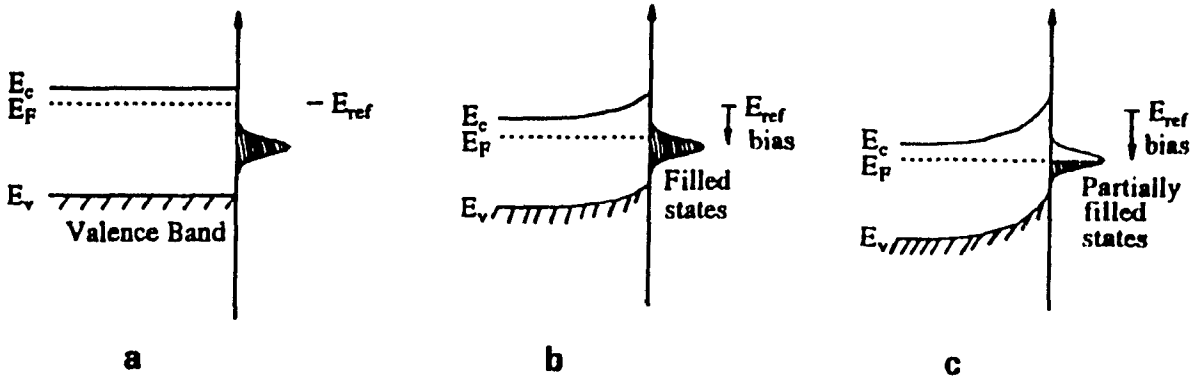

Figure 1.2 Fermi level at an n-type semiconductor with surface states. (a) Flat band potential, (b) depletion of charge until the energy level of the surface state, (c) discharging of surface states.

Surface states can act as either electron or hole traps and may affect the electrochemical equilibrium between the Fermi level (free energy of the electrons) of the semiconductor and the Fermi level of the redox species in solution. In the presence of surface states of lower energy than the Fermi level of the semiconductor, depletion of charge from the conduction band will continue until the Fermi level reaches the energy level of the surface states. It will remain pinned at this level until all surface states have been discharged. This effect, known as Fermi-level pinning,[87] is expected to be more pronounced in colloidal systems than in bulk crystalline semiconductor samples. This is because the large surface-to-volume ratio of the colloids and the irreversible precipitation processes, used to prepare the materials, are likely to create more surface states. Charge transfer is therefore more likely to occur at the colloid particle/solution interface; the band positions of the colloids will shift to equilibrate the Fermi level of the solid with that of the liquid.

1.2 OBJECTIVES

Much of the research into the photophysical and photocatalytic properties of semiconductor materials has focused on cadmium sulphide and titanium dioxide. The success of TiO_2 in photocatalytic applications can be attributed to its stability in aqueous environments and to the rapid charge separation following bandgap excitation. The stability of TiO_2 in solution is related to the fact that the surface of TiO_2 is highly hydroxylated. If a surface hydroxyl group is oxidized (by holes) and is removed from the particle, the exposed Ti(IV) will immediately hydrolyse and thereby reconstruct the

surface.

Despite the positive attributes of titanium dioxide, there are some drawbacks associated with the use of TiO_2. First, charge carrier recombination occurs within nanoseconds.[78] Second, the band edge absorption of TiO_2 is approximately 400 nm and as such only a small fraction ($\approx$ 3%) of the solar irradiance is used.

A number of strategies have been proposed to improve the light absorption and carrier lifetime characteristics of TiO_2. Surface derivatization of TiO_2 with a number of organic dyes has shown promise in extending the sensitivity of TiO_2 into the visible region.[88-91] Direct excitation of the dye results in the injection of electrons from the dye into the conduction band. Grätzel and co-workers have also shown that substitutionally doping the TiO_2 lattice with Fe^{+3} can extend the lifetime of the charge carrier to minutes or hours.[92] Vanadium doping has, in addition to increasing carrier lifetime,[93] shown promise in extending the absorptive range of TiO_2.[4d] A number of other dopants have also been added to TiO_2 both in the bulk and at the surface for solar energy applications.[94-96] However, the majority of these studies have examined the photocatalytic properties of the solid material and only a few photophysical investigations have been carried out.[4d,92,93]

Despite the large number of reports concerning TiO_2 in the literature, a number of questions remain unanswered. For example, ***the chemical nature of the photoformed hole and the role this species plays in heterogenous reactions at the TiO_2/electrolyte interface need to be examined. The effect of different anatase/rutile ratios, particle size and the nature of the dopant on the photocatalytic activity of TiO_2 are also***

unknown. This thesis will examine these aspects. The question as to ***whether doping TiO_2 with various transition metal ions will improve the efficiency of charge separation and/or the absorptive properties of TiO_2*** is another consideration that this thesis addresses. Recent advances in the preparation of colloidal semiconductors makes it possible to study these materials using fast optical techniques. Dopants may act as either electron or hole traps and thus either prolong the lifetime of these charge carriers, or alternatively act as recombination centres and thereby reduce electron/hole lifetimes. ***The effect of varying the dopant (e.g., Cr, V, Fe, Rh) and the dopant concentration on the photophysical properties (e.g. recombination of electrons and holes) of TiO_2 has been assessed using picosecond laser flash photolysis as well as conventional spectrophotometric techniques (UV/VIS absorption, fluorescence). The photocatalytic activity of these materials has also been examined and correlated to the photophysical properties.***

An equally intriguing problem in the study of the photophysical properties of semiconductor particles has been the optical effects associated with decreasing the size of the particle. For a large atomic array, many closely spaced electron states form bands of allowed electron energies. The energy difference between these levels is so small that a continuous band structure is formed (Figure 1.3). However, as the particle size of a finite crystal is diminished, the lattice may no longer be considered as an infinite array of atoms and a transformation from a continuous spectrum of states to discrete quantum levels then occurs . Ostwald[97] has suggested that this transition should be a gradual one; Brus,[98] however, suggests a crossover point between 80-1000 atoms per particle and 10^3-

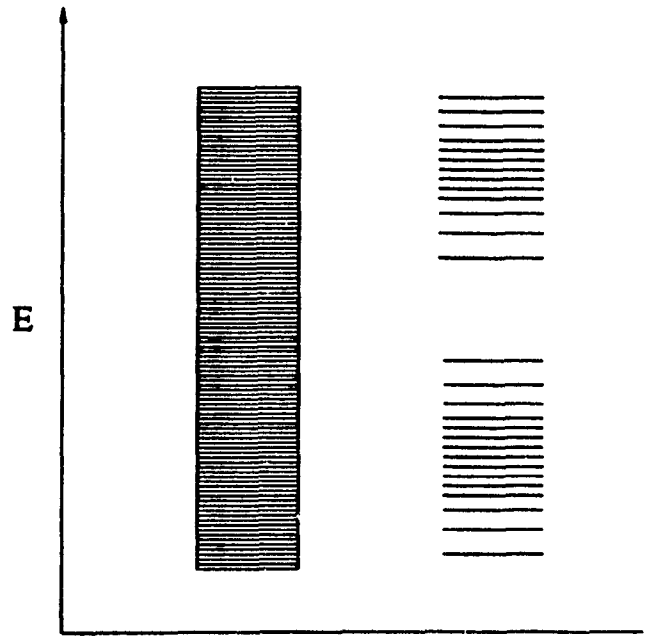

Figure 1.3 Band structure of a bulk (left) and quantized particle.

10^5 atoms per particle.

Size quantization effects in ultrasmall semiconductor particles ($\leq$ 50 Å for CdS) dramatically alter their light absorption and emission characteristics, along with other such electronic properties as standard electrochemical potentials, effective bandgaps and effective masses of electrons and holes.[51,99-102] In recent investigations of nanometre-scale semiconductor clusters (so called quantum dots), much attention has focused on their optical properties owing to their potential use in fast optoelectronics.[103-123] To understand the origin of the nonlinear behaviour in these materials, the question of their recovery time following light excitation continues to be of interest.[33,34,73,108,112-116,118] The final objective of this thesis is ***to explore size quantization effects on the photophysics of electron/hole separation/recombination events***. To achieve this, AgI colloids of various

sizes (25, 35, 100 Å) were synthesized and the initial photochemical events were probed using picosecond laser flash photolysis and pulse radiolysis techniques. As well, ***the CdS microcrystalites in aqueous media and in a silicate matrix have been examined by photoluminescence and picosecond laser spectroscopies.***

References

1. For some recent reviews see:
(a) *"Photochemical Energy Conversion"*; Norris, J.R. & Meisel, D. (Eds.), Elsevier, New York, 1989;
(b) Harriman, A., *Photochemistry*, **1986**, 17, 601;
(c) *"Homogenous and Heterogenous Photocatalysis"*, Pelizzetti, E. & Serpone, N. (Eds.), Reidel, Dordrecht, The Netherlands, **1986.**

2. Nahor, G.S., Hapicot P., Neta, P. and Harriman, A., *J. Phys. Chem.*, **1991**, 95, 616.

3. Serpone, N., Lawless, D., Terzian, R., Minero, C. and Pelizzetti, E., *"Photochemical Conversion and Storage of Solar Energy"*, Pelizzetti, E. and Schiavello, M. (Eds.), Kluwer Academic Publ., Netherlands, **1991**, 451.

4. See for examples:
(a) *"Photocatalysis, Fundamentals and Applications"*, Serpone, N. & Pelizzetti, E. (Eds.), John Wiley & Sons, New York, **1989**;
(b) *"Semiconductor Electrodes"*, Finklea, H.O. (Ed.), Studies in Physical and Theoretical Chemistry 55, Elsevier, Amsterdam, **1988**;
(c) *"Heterogenous Photochemical Electron Transfer"*, Grätzel, M., CRC Press, **1987**;
(d) Moser J., dissertation, Thesis no. 616, Ecole Polytechnique Fédérale de Lausanne, Switzerland, **1986.**

5. Bard, A.J., *J. Phys. Chem.*, **1982**, 86, 172.

6. Bockris, J. O'M. and Uosaki, K., *Adv. Chem. Ser.*, **1977**, 163, 33.

7. Gerisher, H., in *"Photochemical Conversions"*, Braun, A.M. (Ed.), Presses Polytechnique Romandes, Lausanne, **1983**, 211.

8. Memming, R., *Top. Curr. Chem.*, **1988**, 143, 79.

9. Burevich, Yu. Ya. and Pleskov, Yu. V., *Russ. Chem. Rev.*, **1983**, 318.

10. Heller, A., *Science*, **1984**, 233, 1141.

11. Nozik, A.J., *Ann. Rev. Phys. Chem.*, **1978**, 29, 189.

12. Wrighton, M.S., *Pure & Appl. Chem.*, **1985**, 57, 57.

13. Rajeshwar, K., Singh, P. and Bubow, J., *Electrochim. Acta*, **1978**, 23, 1117.

14. (a) Fox, M.A., *Acc. Chem. Res.*, **1983**, 16, 314;
(b) Fox, M.A. in *"Topics in Organic Electrochemistry"*, Fry, A.J. and Britton, W.E. (Eds.), Plenum Press, New York, **1986**, 177;
(c) Fox, M.A., *Top. Curr. Chem. 142 (Electrochem. I)*, **1987**, 71;
(d) Fox, M.A. and Channon, M. (Eds.), *"Photoinduced Electron Transfer"*, Part D-6, Elsevier, Amsterdam, **1988**.

15. Grätzel, M. (Ed.), *"Energy Resources Through Photochemistry and Catalysis"*, Academic Press, New York, **1983**.

16. Childs, L. and Ollis, D.F., *J. Catal.*, **1980**, 66, 383.

17. Pichat, P. in *"Organic Phototransformations in Nonhomogenous Media"*, Fox, M.A. (Ed.), ACS Symp. Ser. 278, American Chemical Society, Washington, D.C., **1985**, 21.

18. Anpo, N. and Kubokawa, Y., *Rev. Chem. Intermed.*, **1987**, 8, 105.

19. (a) Fendler, J.H., *Chem. Rev.*, **1987**, 87, 877;
(b) Fendler, J.H., *J. Phys. Chem.*, **1985**, 89, 2730.

20. Borgarello, E., Serpone, N., Grätzel, M. and Pelizzetti, E., *Int. J. Hydrogen Energy*, **1985**, 10, 737.

21. (a) Baird, N.C., Draper, A.M. and De-Mayo, P., *Can. J. Chem.*, **1988**, 66, 1579;
(b) Al-Ekabi, H. and De-Mayo, P., *J. Org. Chem.*, **1987**, 52, 4756.

22. Willner, I. and Willner, B.S., *Int. J. Hydrogen Energy*, **1988**, 13, 593.

23. see as an example, *"Photocatalysis and Environment-Trends and Applications"*, Schiavello, M. (Ed.), NATO ASI Series C237, Kluwer Academic, Dordrecht, The Netherlands, **1988**.

24. Terzian, R., Serpone, N., Minero, C. and Pelizzetti, E., *J.Catal.*, **1991**, 128, 352.

25. Al-Ekabi, H., Serpone, N., Pelizzetti, E., Minero, C., Fox, M.A. and Draper, R.B., *Langmuir*, **1989**, 2, 250.

26. Hidaka, H., Ihara, K., Fujita, Y., Yamada, S., Pelizzetti, E. and Serpone, N., *J. Photochem. Photobiol. A*, **1988**, 375.

27. Lawless, D., Res, A., Harris, R., Serpone, N., Minero,C., Pelizzetti, E. and Hidaka, H., *Chem. Ind. (Milano)*, **1990**, 72, 139.

28. Domenech, J. and Munoz, J., *J. Electrochim. Acta*, **1987**, 32, 1383.

29. Serpone, N., Ah-You, Y.K., Tran, T.P., Harris, R., Pelizzetti, E. and Hidaka, H., *Sol. Energy*, **1987**, 39, 491.

30. Grätzel, M., *Acc. Chem. Res.*, **1981**, 41, 376.

31. Grätzel, M., *"Heterogeneous Photochemical Electron Transfer"*, CRC Press, Boca Raton, **1989**.

32. Kalyansundaram, K., Grätzel, M. and Pelizzetti, E., *Coord. Chem. Rev.*, **1986**, 69, 57.

33. (a) Henglein, A., *Top. Curr. Chem.*, **1988**, 143, 113.
(b) Henglein, A., *Chem. Rev.*, **1989**, 89, 1861.

34. Kamat, P.V. and Dimitrijevic, N.M., *Solar Energy*, **1990**, 44, 83.

35. Brus, L., *J. Phys. Chem.*, **1986**, 90, 2555.

36. Kamat, P.V. in *"Kinetics and Catalysis in Microheterogenous Systems"*, Grätzel, M. and Kalyansundaram, K. (Eds.), Marcel Dekker Inc., New York, **1991**.

37. Matijevic, E., *Langmuir*, **1986**, 2, 12.

38. Kuczynski, J. and Thomas, J.K., *Chem. Phys. Lett.*, **1982**, 86, 301.

39. Kalyansundaram, K., Borgarello, E., Duonghong, D. and Grätzel, M., *Angew. Chem.*, **1982**, 104, 2977.

40. Henglein, A., *Ber. Bunsenges. Phys. Chem.*, **1982**, 86, 301.

41. Duonghong, D., Ramsden J. and Grätzel, M., *J. Am. Chem. Soc.*, **1982**, 104, 2977.

42. Kamat, P.V., Dimitrijevic, N.M. and Fessenden, R.W., *J. Phys. Chem.*, **1987**, 91, 396.

43. Becker, W.G. and Bard, A.J., *J. Phys. Chem.*, **1983**, 87, 4888.

44. Wilhemy, D.M. and Matejevic, E., *J. Chem. Soc. Faraday Trans. 1*, **1984**, 80, 563.

45. Kiwi, J., Borgarello, E., Duonghong, D. and Grätzel, M. in *"Preparation of Catalysts III"*, Poncelet, G., Grange, P. and Jacobs, P.A. (Eds.), Elsevier, Amsterdam, **1983**, 135.

46. Bahnemann, D., Henglein, A., Lilie, J. and Spanhel, L., *J. Phys. Chem.*, **1984**, 88, 709.

47. Fox, M.A., Chen, C.C. and Lindig, B., *J. Am. Chem. Soc.*, **1982**, 104, 5828.

48. Kormann, C., Bahnemann, D. and Hoffmann, M.R., *J. Phys. Chem.*, **1988**, 92, 5196.

49. Nishimoto, S., Ohtani, B., Kajiwara, H. and Kagiya, T., *J. Chem. Soc. Faraday Trans. 1*, **1985**, 81, 61.

50. Bahnemann, D., Kormann, C., and Hoffmann, M.R., *J. Phys. Chem.*, **1987**, 91, 3789.

51. Koch, U., Fojtik, A., Weller, H. and Henglein, A., *Chem. Phys. Lett.*, **1985**, 122, 507.

52. Darwent, J.R. and Mills, A., *J. Chem. Soc. Faraday Trans. 2*, **1982**, 78, 359.

53. Nenadovic, M.T., Rajh, T., Micic, O.I. and Nozik, A.J., *J. Phys. Chem.*, **1984**, 88, 5827.

54. Fojtik, Henglein, A., Katsikas, L. and Weller, H., *Chem. Phys. Lett.*, **1987**, 138, 535.

55. Sorum, C.H., *J. Am. Chem. Soc.*, **1982**, 50, 1263.

56. Matijevic, E., *Ann. Rev. Mater. Sci.*, **1985**, 15, 483.

57. Stramel, R.D. and Thomas, J.K., *J. Colloid Interf. Sci.*, **1986**, 110, 121.

58. Kiwi, J. and Grätzel, M., *J. Chem. Soc. Faraday Trans. 1*, **1987**, 83, 1101.

59. Mulvaney, P., Swayambunathan, V., Grieser, F and Meisel, D., *J. Phys. Chem.*, **1988**, 92, 1988.

60. Visca, M. and Matijevic, E., *J. Colloid Interf. Sci.*, **1979**, 68, 308.

61. Fojtik, A., Weller, H., Fiechler, S. and Henglein, A., *Chem. Phys. Lett.*, **1987**, 134, 477.

62. Baral, S., Lume-Periera, C., Janata, E. and Henglein, A., *J. Phys. Chem.*, **1986**, 90, 6025.

63. Hayes, D., Micic, O.I., Nenadovic, M.T., Swayambunathan, V., and Meisel, D., *J. Phys. Chem.*, **1989**, 93, 4603.

64. Schmidt, K.H., Patel, R. and Meisel, D., *J. Am. Chem. Soc.*, **1988**, 110, 4882.

65. Hayes, D., Schmidt, K.H., and Meisel, D., *J. Phys. Chem.*, **1989**, 93, 6100.

66. Krishman, M., White, J.R., Fox, M.A. and Bard, A.J., *J. Am. Chem. Soc.*, **1983**, 105, 7002.

67. Finayson, M.F., Park, K.H., Kakuta, N., Bard, A.J., Campion, A., Fox, M.A., Webber, S.E. and White, J.M., *J. Lumines.*, **1988**, 39, 205.

68. Wang, Y. and Mahler, W., *Opt. Commun.*, **1987**, 61, 233.

69. Honda, K., Kuwana, A., Chiba, K., Ishikawa, A. and Miyama, H., *Chem. Lett.*, **1988**, 195.

70. Meyer, M., Wallberg, C., Kurihara, K. and Fendler, J.H., *J. Chem. Soc., Chem. Commun.*, **1984**, 90.

71. (a) Tricot, Y.M. and Fendler, J.H., *J. Am. Chem. Soc.*, **1984**, 106, 7359; (b) Tricot, Y.M., Emerson, A. and Fendler, J.H., *J. Phys. Chem.*, **1985**, 89, 4721.

72. Lianos, P. and Thomas, J.K., *Chem. Phys. Lett.*, **1986**, 125, 299.

73. (a) Wang, Y. and Herron, N., *J. Phys. Chem.*, **1987**, 91, 257; (b) Herron, N., Wang, Y., Eddy, M.M., Stucky, G.D., Cox, D.E., Moller, K. and Bein, T., *J. Am. Chem. Soc.*, **1989** ,111, 530.

74. Ekimov, A.J. and Onushchenko, A., *JETP Lett.*, **1984**, 40, 1136.

75. Rajh, T., Vucemilovic, M.I., Dimitrijevic, N.M., Micic, O.I. and Nozik, A.J., *Chem. Phys. Lett.*, **1988**, 143, 305.

76. Kuczynski, J. and Thomas, J.K., *J. Phys. Chem.*, **1985**, 89, 2720.

77. Rajh, T., Micic, O.I., Lawless, D. and Serpone, N., *J. Phys. Chem.*, **1992**, 96, 4633.

78. Rothenberger, G., Moser, J., Grätzel, M., Serpone, N. and Sharma, D.K., *J. Am. Chem. Soc.*, **1985**, 107, 8054.

79. Kamat, P.V., Ebbesen, T.W., Dimitijevic and Nozik, A.J., *Chem. Phys. Lett.*, **1989**, 157, 384.

80. Kamat, P.V., Dimitijevic, N.M and Nozik, A.J., *J. Phys. Chem.*, **1989**, 93, 2873.

81. Hilenski, E.F., Lucas, P.A. and Wang, Y., *J. Phys. Chem.*, **1988**, 89, 3435.

82. Henglein, A., *Ber. Bunsenges Phys. Chem.*, **1982**, 86, 241.

83. Bahnemann, D., Henglein, A. and Spanhel, L., *Faraday Discuss. Chem. Soc.*, **1984**, 78, 151.

84. Howe, R.F. and Grätzel, M., *J. Phys. Chem.*, **1985**, 89, 4495.

85. Serpone, N., Borgarello, E. and Pelizzetti, E., *J. Electrochem. Soc.*, **1988**, 135(11), 2760.

86. Gerischer, H., *Pure & Appl. Chem.*, **1980**, 52, 2649.

87. Lewis, N.S and Rosenbluth, M.L. in "*Photocatalysis, Fundamentals and Applications*", Serpone, N. & Pelizzetti, E. (Eds.), John Wiley & Sons, New York, **1989**.

88. Moser, J. and Grätzel, M., *J. Am. Chem. Soc.*, **1984**, 106, 6557.

89. Fessenden, R.W. and Kamat, P.V., *Chem. Phys. Lett.*, **1984**, 123, 233.

90. Kamat, P.V. and Ford, W.E., *Chem. Phys. Lett.*, **1987**, 135, 421.

91. Kamat, P.V., Chauvet, J.-P. and Fessenden, R.W., *J. Phys. Chem.*, **1986**, 90, 1389.

92. Moser, J., Grätzel, M. and Galloy, R., *Helv. Chim. Acta.*, **1987**, 70, 1596.

93. Grätzel, M. and Howe, R.F., *J. Phys. Chem.*, **1990**, 94, 2566.

94. Wong, W.K. and Malati, M.A., *Solar Energy*, **1986**, 2, 163.

95. Goodenough, J.B., *Studies in Inorganic Chem., vol. 3.; Proceedings of the Second European Conference, Velhoven, The Netherlands, 7-9 June, 1982*, **1983**.

96. Finklea, H.O. in *"Semiconductor Electrodes"*, Studies in physical and theoretical chemistry 55, Elsevier, Amsterdam, **1980**, p. 43 and references therein.

97. Ostwald, Wo., *"Die Welt der Vernachlassigter Dimensionen 4, Auf. Th. Steinkopff"*, **1920**, p. 115.

98. Rossetti, R., Nakahara, S. and Brus, L.E., *J. Chem. Phys.*, **1983**, 79, 1086.

99. Brus, L.E., *J. Chem. Phys.*, **1983**, 79, 5566.

100. Fojtik, A., Weller, H., Koch, U. and Henglein, A., *J. Phys. Chem.*, **1984**, 88, 969.

101. Nozik, A.J., Williams,F., Nenadovic, M.T., Rajh, T. and Micic, O.I., *J. Phys. Chem.*, **1985**, 89, 397.

102. Schmidt, K.H., Patel, R. and Meisel, D., *J. Am. Chem. Soc.*, **1988**, 110, 4882.

103. Takagahara, T., *Phys. Rev. B*, **1987**, 36, 9293, and references therein.

104. Kull, M. and Coutaz, J.-L. *J. Opt. Soc. Am. B*, **1990**, 7, 1463.

105. Schmitt-Rink, S., Miller, D.A.B., Chemla, D.S., *Phys. Rev. B*, **1987**, 35, 8113.

106. Morgan, J.R. and Natarajan, L.V., *J. Phys. Chem.*, **1989**, 93, 5.

107. Chestnoy, N., Harris, T.D., Hull, R. and Brus, L.E., *J. Phys. Chem.*, **1986,** 90, 3393.

108. Liu, C.-Y and Bard, A.J., *J. Phys. Chem.*, **1989,** 93, 3232.

109. Wang, Y., Herron, N., Mahler, W. and Suna, A., *J. Opt. Soc. Am. B,* **1989**, 6, 808.

110. Bawendi, M.G., Wilson, W.L., Rothnerg, L., Carroll, T.M., Jedjiu, T.M., Steigerwald, M.L. and Brus, L.E., *Phys. Rev. Lett.*, **1990,** 65, 1623.

111. (a) Hilinski, E.F., Lucas, P.A. and Wang, Y., *J. Chem. Phys.*, **1988,** 89, 3435.
(b) Wang, Y., *Acc. Chem. Res.*, **1991**, 24, 133.

112. (a) O'Neil, M., Marohn, J. and McLendon, G., *Chem. Phys.Lett.*, **1990,** 168, 208;
(b) O'Neil, M., Marohn, J. and McLendon, G., *J. Phys. Chem.*, **1990,** 94, 4356.

113. Ernsting, N.P., Kaschke, M., Weller, H. and Katsikas, L., *J. Opt. Soc. Am. B,* **1990,** 7, 1630.

114. Kaschke, M., Ernsting, N.P., Muller, U. and Weller, H., *Chem. Phys. Lett.*, **1990,** 168, 543.

115. Eychmuller, A., Hasselbarth, A., Katsikas, L. and Weller, H. *Ber. Bunsenges. Phys. Chem.*, in press (1991).

116. Wang, Y., Suna, A., McHugh, J., Hilinski, E.F., Lucas, P.A., Johnson, R.D., *J. Chem. Phys.*, **1990,** 92, 6927.

117. Morgan, R.A., Park, S.-H., Koch, S.W., Peyghambrain, N., *Semicond. Sci. Technol.*, **1990,** 5, 544.

118. Haase, M., Weller, H. and Henglein, A., *J. Phys. Chem.*, **1988,** 92, 4706.

119. (a) Roussignol, P., Kull, M., Ricard, D., Rougemont, F.; Frey, R. and Flytzanis, C., *Appl. Phys. Lett.*, **1987**, 51, 1882.
(b) Rougemont, P., Frey, F., Roussignol, P., Ricard, D., Flytzanis, C., *Appl.Phys.Lett.*, **1987,** 50, 1619.
(c) Roussignol, P., Ricard, D., Lukasik, J. and Flytzanis, C. *J. Opt. Soc. Am., B,* **1987,** 4, 5.

120. Horan, P. and Blau, W., *J. Opt. Soc. Am. B*, **1990**, 7, 304.

121. Ekimov, A.I. and Efros, A.L., *Phys. Stat. Sol.(b)*, **1988**, *150*, 627.

122. Henglein, A., Kumar, A., Janata, E. and Weller, H., *Chem. Phys. Lett.*, **1986**, 132, 133.

123. Warnock, J. and Awschalom, D.D., *Phys. Rev. B*, **1985**, 32, 5529.

CHAPTER 2

EXPERIMENTAL

2.1 CHEMICALS

All chemicals employed in this work were of reagent grade quality and were used as received unless otherwise stated. The water used throughout was doubly distilled and deionized. The following transition metal salts were purchased from the sources noted and used for doping purposes: ammonium *meta*vanadate (NH_4VO_3; Anachemia), ammonium *para*molybdate ($(NH_4)_6Mo_7O_{24}\bullet 4H_2O$; Anachemia), cerium nitrate ($Ce(NO_3)_3\bullet 6H_2O$; Alfa), copper dichloride ($CuCl_2\bullet 6H_2O$; Fisher-Purified), cobalt dichloride hexahydrate ($CoCl_2\bullet 6H_2O$; Fisher-Purified), iron trichloride ($FeCl_3$, Fisher-Purified, anhydrous, sublimed), manganese dichloride tetrahydrate ($MnCl_2\bullet 4H_2O$; Matheson), neodymium trichloride hexahydrate ($NdCl_3\bullet 6H_2O$; Aldrich 99.9%), nickel nitrate hexahydrate ($Ni(NO_3)_2\bullet 6H_2O$; Fisher certified), palladium chloride ($PdCl_2$; Sigma), potassium hexachloroplatinate (K_2PtCl_6; Fisher-Purified), potassium hexachlororuthenate (K_3RuCl_6; Strem Chemicals), rhenium heptoxide (Re_2O_7; Aldrich), rhenium trichloride ($ReCl_3$; Aldrich), rhodium trichloride trihydrate ($RhCl_3\bullet 3H_2O$; Alfa), sodium tungstate dihydrate ($Na_2WO_4\bullet 2H_2O$; Fluka purissa), titanium trichloride (20%-Fisher), vanadium dioxide (V_2O_4; Aldrich), vanadium pentoxide (V_2O_5; Baker analyzed), vanadium trichloride (VCl_3; Aldrich) and yttrium trichloride hexahydrate ($YCl_3\bullet 6H_2O$;

Aldrich 99.9%). Chromium metal powder (Fisher, dissolved with gentle heating in concentrated HCl) was used in the doping of TiO_2 with chromium. Titanium tetrachloride, $TiCl_4$ (Fisher purified), was doubly distilled *in vacuo* prior to use. The final distillate was clear and colourless; it was stored under an argon atmosphere in the dark. Under these conditions, no discoloration was noticed even after 2 months. Titanium isopropoxide, $Ti[OCH(CH_3)_2]_4$ (Aldrich), was used as received.

2.2 PREPARATION OF MATERIALS

2.2.1 Synthesis of TiO_2 Colloids

2.2.1.1 General Synthesis

Clear and optically transparent colloidal sols of TiO_2 were prepared via the controlled hydrolysis of $TiCl_4$ at low temperature[1] or via the hydrolysis of $Ti\text{-}[OCH(CH_3)_2]_4$.[2] In the former case, a narrow distribution of particle sizes, mean diameter approximately 120 Å, was obtained, whereas the use of titanium isopropoxide gave much larger particles (diameter approximately 400 Å). Further, the use of titanium tetrachloride permitted the synthesis of stable, unprotected (no stabilizers) TiO_2 colloids up to a concentration of 50 g/L, distinct from the maximum concentration of TiO_2 possible, 1.2 to 2 g/L, obtained when titanium tetraisopropoxide was used. During the course of this work, TiO_2 sols were successfully made using both synthetic routes. Both sols were stable with time when stored in the dark.[3] Because the controlled hydrolysis of $TiCl_4$ yields a more concentrated, narrower size distribution of particles, this method was chosen to dope the TiO_2 particles in the bulk with various transition metals.

2.2.1.2 HYDROLYSIS OF $TiCl_4$

In a typical preparation, 5.2 mL of fresh, doubly distilled $TiCl_4$ was slowly added dropwise to 200 mL of doubly distilled, deionized water rigorously maintained at 0 (± 0.2) °C under vigorous stirring. The solution was subsequently dialysed (Viscase membrane, presoaked 24 hours in distilled water and then thoroughly rinsed prior to use) against about 4 litres of distilled water (replaced several times) for about 8 hours. Approximately 20% titanium was lost during the dialysis procedure.[14] The concentration of TiO_2 was 15 g/L and the resulting pH of the solution was between 2.5 and 3 (dependent upon time of dialysis and concentration of TiO_2 prepared).

Although the synthesis was relatively straightforward and highly reproducible,[4] a high quality (i.e. stable, narrow size distribution) TiO_2 product made using $TiCl_4$ could only be obtained if careful attention was paid to the following details. First, the $TiCl_4$ must be spectroscopically colourless. This was best accomplished by doubly distilling the material under vacuum. Alternatively, the material may be repetitively distilled in air. When the colourless $TiCl_4$ was stored under an argon or nitrogen atmosphere in a desiccator, the material showed no discoloration for at least 6-8 weeks. Sols made with undistilled or slightly coloured (pale yellow) $TiCl_4$ were not stable and precipitated out of solution within 24 hours. Second, the rate of addition of $TiCl_4$ and the temperature of the water to which it is added was critical. Typically, to synthesize 15 g/L of TiO_2 required between 45 to 60 minutes to add the $TiCl_4$ (followed by dialysis) and a water temperature of 0 ± 0.2 °C. The exothermicity of $TiCl_4$ addition necessitated the use of a $CaCl_2$ ice bath. This was prepared by alternating thin layers of crushed ice and $CaCl_2$

kept at 0 °C. To prevent water from freezing and as a necessary step in the synthesis, efficient and vigorous stirring was essential. Third, the dialysis membrane (tubing) must be presoaked in distilled water for a minimum of 24 hours and then must be rinsed thoroughly prior to use. This was necessary to remove any organic residues, such as formaldehyde, which may be present when the tubing is shipped from the manufacturer and which may adversely affect the synthetic process. During hydrolysis, the pH of the solution increased from about 0 to between 2.5 and 3 and the ionic strength of the TiO_2 sol decreased. The importance of pretreating the dialysis tubing cannot be overstressed and has been confirmed in various communications with different researchers, also interested in preparing TiO_2 sols.[5] The choice of manufacturer of dialysis membrane tubing does not appear to be as critical. During the course of this work, regenerated cellulose visking dialysis tubing {33 mm flap width (dry), size 27} made by Viscase Canada was used. In other instances, the dialysis of several successfully prepared sols also used Spectra/POR (Spectrum Medical Industries) molecular porous membrane dialysis tubing {MW cutoff ~ 3500, 28.6 mm flap diameter (dry)}.

Solid samples of the doped TiO_2 materials were obtained by removing the colloid from solution. This was accomplished by roto-evaporating the colloid under vacuum and with the aid of a hot water bath. After further drying the solid in air at 110 °C, the material was ground to a fine powder using a mortar and pestle. Between samples, both the mortar and pestle were effectively and thoroughly cleaned using a specially prepared cleaning solution. The cleaning solution was a concentrated highly alkaline solution prepared by dissolving finely ground sodium hydroxide pellets (Fisher, certified) in a 1N

NaOH solution (Acculute volumetric NaOH solution from Anachemia) in a plastic vessel. The items to be cleaned were then placed in the cleaning container and to this mixture was added a 30% hydrogen peroxide (H_2O_2) solution (Fisher; 1 part H_2O_2 to 4 parts solution (v/v)). This mixture was found effective to remove any traces of adsorbed TiO_2 from the surfaces of ceramics and glass.[6] However, extreme caution must be taken as this mixture will also dissolve glass and ceramic materials; thus materials to be cleaned must not be left in the solution for prolonged periods of time. After repeated rinsing in distilled water, the mortar and pestle showed no visible traces of the TiO_2 material. The solid doped TiO_2 powders obtained by removing the colloid from solution and subsequently grinding could not be redispersed into solution, even with the use of ultrasounds. However, TiO_2 powder which could be redispersed into either water or propanol may also be obtained but required subtle changes in the synthetic procedure and in the way the colloid was removed from solution.[7] First, the rate of addition of $TiCl_4$ must be significantly slower and a much more dilute TiO_2 colloid must be prepared. In a typical synthesis, 3.5 mL of $TiCl_4$ was added to 900 mL of distilled water kept at 1 °C over a period of ~ 8.5 hrs. The resulting solution was then twice dialysed against 4 L of water for 2 hrs until the resulting solution pH was exactly 2.5. After storing the solution in the dark at 5 °C overnight, 200-mL aliquots were dried with the aid of a rotary evaporator coupled with a high pressure vacuum pump. Removal of solvent was done using a water bath kept at 30 °C. The residue was further dried *in vacuo* yielding a shiny white powder which could be redispersed in water. The absorption characteristics of a colloid made using this powder were identical to the original colloidal

solution. No attempts were made to verify that the procedure would also work with the doped material.

2.2.1.3 CONTROL OF PARTICLE SIZE

The size of the TiO_2 particles produced by the controlled hydrolysis of $TiCl_4$ may be controlled by careful manipulation of the temperature of either the $TiCl_4$ or the water to which it is added. Extremely small TiO_2 particles (diameter ~ 20 Å) were produced when the synthetic procedure described in Section **2.2.1.2** was followed but with the $TiCl_4$ maintained at -20 °C. The $TiCl_4$ (5.2 mL) was cooled to -20 °C by placing a pyrex flask containing the $TiCl_4$ into a constant temperature cell filled with pure ethylene glycol (Anachemia) coupled to a model K4R Lauda constant temperature bath filled with a 50/50 mixture of Prestone® antifreeze coolant. Once the -20 °C temperature was achieved, the $TiCl_4$ containing flask was allowed to equilibrate with the ethylene glycol in the constant temperature cell for ~ 30 min prior to synthesis start-up. As noted in Table 2.1, raising the temperature of the $TiCl_4$ to 0, 24 (ambient temperature), 44 and 66 °C, while maintaining the temperature of the water at 0 °C, did not significantly affect the average diameter of the TiO_2 particles. However, adjusting the temperature of the water to which the $TiCl_4$ was added significantly affected the average particle diameter. When $TiCl_4$ addition was carried out at room temperature to a water sample for which the temperature was adjusted and maintained at 10 °C, the average particle diameter of the particles, as determined by dynamic light scattering, was about 280 Å. If the $TiCl_4$ were added to water kept at 24 °C (room temperature), the colloid was

unstable and precipitated within hours of synthesis start-up.

Table 2.1 Effect of Temperature of $TiCl_4$, Water on TiO_2 Particle Diameter [a]

Temperature of $TiCl_4$ (°C)	Temperature of Water (°C)	Average particle diameter (Å)
-20	0	23 ± 1
0	0	159 ± 21
24	0	133 ± 12
44	0	132 ± 9
66	0	111 ± 3
24	10	281 ± 20
24	24	b

[a]Determined from dynamic light scattering measurements.
[b]Colloid precipitated within hours of synthesis start-up.

2.2.1.4 ADDITION OF DOPANTS TO TiO_2

Table 2.2 lists the transition metal ions, the initial oxidation state of the metal (M^{+n}) and the concentration (as wt.% of TiO_2) at which they were added to the TiO_2 during the synthesis. The concentration of the dopant is based on the amount of TiO_2 which would have been present if no metal had been added and assumes that none of the dopant was lost during the dialysis procedure. In all cases, the dopant was added to the solution prior to the addition of the $TiCl_4$. For example, 0.03 g of M was added to get 1.0 wt.% M in 15 g/L TiO_2/M made using 200 mL of water; i.e., to get a 1 wt.% V doping level, 68.89 mg of NH_4VO_3 was dissolved in 200 mL of distilled water and 5.2 mL of $TiCl_4$ was slowly added. In all cases, except for chromium and iron, 200 mL

Table 2.2 Transition Metal Dopants added to TiO_2

Dopant	Initial Oxidation State of Dopant	Concentration (wt/wt% TiO_2)
Cr	+ 3	0.1, 0.5, 1, 3, 5, 10, 20
Fe	+ 3	0.1, 0.5, 1, 5, 10
Cr, Fe (1:1)	+ 3	1
V	+ 5	0.1, 0.5, 1, 3, 5, 10
V	+ 4	1
V	+ 3	1
Ru	+ 3	0.05, 0.1, 0.3, 0.5, 1, 5, 10
Pt	+ 4	0.05, 0.1, 0.5, 1
Ru,Pt (1:1)	+ 3 (Ru), + 4 (Pt)	0.05, 0.1, 0.5, 1
Rh	+ 3	0.1, 0.5, 1, 3, 5, 10
Pd	+ 2	1, 10
Cu	+ 2	1, 10
Mn	+ 2	1, 10
Ni	+ 2	1
W	+ 6	1
Mo	+ 6	1
Ce	+ 6	1
Co	+ 2	1
Nd	+ 3	1
Ti	+ 3	1
Re	+ 3	1
Re	+ 7	1
Re	+ 3, + 7 (1:1)	1 (each oxidation state)
Y	+ 3	1

solutions containing M were made the night before the synthesis and stored in the dark at 5 °C. In the case of chromium, a stock solution was prepared by dissolving, with heat, exactly 2500 mg of chromium metal powder in 1012 mL of concentrated HCl (Fisher). Aliquots of this solution were then added to a sufficient quantity of water to bring the final volume to 200 mL. Similarly, a stock solution of aqueous iron(III) was prepared by dissolving exactly 7272.8 mg of purified anhydrous $FeCl_3$ in 1000 mL of 1N HCl. In both cases, the stock solution was kept no longer than 1 week. The selection of the dopant salt was very important; salts containing divalent (e.g., SO_4^{2-}) and trivalent (e.g., PO_4^{3-}) counter anions can lead to gelation of the colloid during the dialysis procedure. It is interesting to note that in all such cases, the gel was optically clear and in no instance did any of the material ever precipitate out of solution (or gel).

2.2.1.5 Hydrolysis of Titanium Tetraisopropoxide

Colloidal TiO_2 was also prepared via the controlled hydrolysis of titanium tetraisopropoxide.[8] The advantage of this procedure is that no chloride is present. Chloride ions are known to strongly adsorb to TiO_2 and are expected to be occluded in the TiO_2 sols made using the controlled hydrolysis of $TiCl_4$.[9] The presence of chloride ions at the surface (and in the bulk) may affect the catalytic activity and the photophysical and photochemical events of the TiO_2.

Initially, attempts were made to synthesize TiO_2 sols repeating the procedure of Section **2.2.1.2** using 14 mL of titanium tetraisopropoxide rather than 5.2 mL of $TiCl_4$ (projected final concentration of TiO_2 ~ 15 g/L). Unfortunately, precipitation of the sol

occurred immediately. Attempts to prepare the colloid at a lower concentration also proved unsuccessful. However, a stable colloid was obtained by dissolving 0.5 mL of titanium tetraisopropoxide in isopropanol, followed by dropwise addition (30-40 minutes) into 100 mL of a 0.1 M $HClO_4$ solution. The resultant solution was "hazy" but optically clear. Avoiding stirring during the addition resulted in a clearer, more stable product. The mixture was subsequently stirred overnight, after which a virtually clear sol formed. To remove the propanol or isopropanol, the colloid was dialysed against 4 litres of 0.1M $HClO_4$ for 24 hours.

2.2.2 Preparation of Silver Iodide Colloids

The preparation of silver iodide colloids followed a method very similar to that previously reported in the literature.[10] Three different size particles, average diameter ~ 100, 35 and 25 Å, were prepared as follows. The 100 Å AgI particles were prepared by diluting 0.25 mL of 0.04 M aqueous $AgNO_3$ (**solution A**) with 44.75 mL of acetonitrile (Omnisolv, BDH) and immediately adding 5 mL of a fresh aqueous (5 % v/v) acetonitrile solution 2.0 x 10^{-3} M in KI. The resulting silver iodide concentration was 2.0 x 10^{-4} M. It was important that the KI solution be immediately mixed with the silver nitrate solution since I^- oxidizes to I_3^- in acetonitrile. The smaller 25 Å $(AgI)_{coll}$ particles were made by adding to a solution consisting of 0.1 mL of **solution A** in 17.9 mL of acetonitrile, a solution containing of 0.1 mL of 0.04 M aqueous KI, 0.5 mL of Polybrene (Sigma; 0.7 g/L 100 mL in aqueous media) and 1.4 mL of acetonitrile; [AgI] = 2.0 x 10^{-4} M. It is important that the polybrene solution be prepared fresh. A fourfold dilution

of the 25 Å $(AgI)_{coll}$ solution with water gave colloid particles with average diameter of 35 Å; [AgI] = 5.0 x 10^{-5} M.

2.2.3 Preparation of CdS Glasses

The silicate glasses were kindly prepared in the Gamma Laboratory of Solid State Physics and Radiation Chemistry of the Boris Kidric Institute (Belgrade, Yugoslavia) by Drs. T. Rajh and O.I. Micic using a low temperature sol/gel process with alkoxysilane as the starting material.[11] The polymerization was accelerated by addition of hydrochloric acid. The acidic glass samples picked up moisture with time (glasses appeared cloudy) and they were therefore heated at 110 °C overnight prior to spectroscopic examination. Following the heat treatment the glasses were optically clear.

A typical method for preparing the glasses is given here for information only. In some cases, a slightly modified procedure was used in which the concentrations of the starting materials were different. Tetramethoxysilane (TMOS; 1.2 mL) was added to a 2.8 mL solution containing 2.8 x 10^{-4} M $CdSO_4$ and different stabilizers: 2.86 x 10^{-4} M sodium hexametaphosphate or 0.143 vol.% polyvinyl alcohol. The solution was stirred vigorously for 15 min until clear, following which 0.05 mL of 0.1 M HCl was added and stirring continued for a few seconds more. The resulting mixture was poured into the plastic spectroscopic cuvette of the desired shape (rectangular; 1 cm x 1 cm x 4 cm). The glasses were then dried slowly in air. When the size of the gels was ca. 65% of the original volume upon condensation, the gels were exposed to an atmosphere of H_2S until the sulphide diffused through the semirigid gel. The drying of the gel was

continued until condensation terminated (the volume reduced to ~ 10% of the original value: 0.5 cm x 0.5 cm x 1.7 cm).

2.3 MODIFICATION OF P25 DEGUSSA TiO_2

Commercial samples of P25 Degussa TiO_2 were a generous gift of Degussa Canada. The physico-chemical data as provided by Degussa Canada[12] is collected in Table 2.3.

The relative ratio of anatase to rutile in the TiO_2 was changed by placing a sample of commercial P25 TiO_2 in a crucible and heating the material in air in a Type 48000 Thermolyne furnace for 24 hours. The temperatures used and the heat effect on the anatase and rutile content of the sample, as determined from x-ray diffraction measurements, are summarized in Table 2.4.

2.4 CHARACTERIZATION OF MATERIALS

2.4.1 Physical Measurements and Instrumentation

Absorption spectra of the colloids were recorded in either a 0.2 or a 1 cm Suprasil quartz cells using either a Shimadzu UV-265 double beam UV/VIS recording spectrophotometer or a Varian 2300 spectrophotometer. In both cases, distilled water (pH 3, adjusted with HCl) was used as a reference. Absorbance spectra of the CdS glass samples were obtained by mounting the samples on specially designed sample holders such that only the transmitted light reached the R-928-09 PMT detector on the Shimadzu spectrophotometer. Diffuse reflectance measurements were obtained employing the

Table 2.3 Physico-chemical Data for P25 Degussa TiO_2

BET Surface Area (m^2/g)	50 ± 15
Average Particle Diameter (nm)	30
Compacted apparent density (g/L)	~ 150
X-ray Structure	80% anatase, 20% Rutile#
Isoelectronic point at pH value	6.6
Density (g/cm^3)	3.8
% Al_2O_3	< 0.3
% TiO_2	> 99.5
% SiO_2	< 0.2
% Fe_2O_3	< 0.01
% HCl	< 0.3

this work.

Table 2.4 Temperature treatment of P25 Degussa TiO_2

Temperature Treatment °C	% Anatase	% Rutile
-	80	20
575	64	36
600	52	48
625	47	53
650	22	78
750	0	100
900	0	100

Shimadzu UV-265 spectrophotometer fitted with a P/N 204-05857 integrating sphere assembly reflectance unit. A schematic of the integrating sphere reflectance unit is given in Figure 2.1. $BaSO_4$ (Wako Pure Chemicals) was used as the reference.

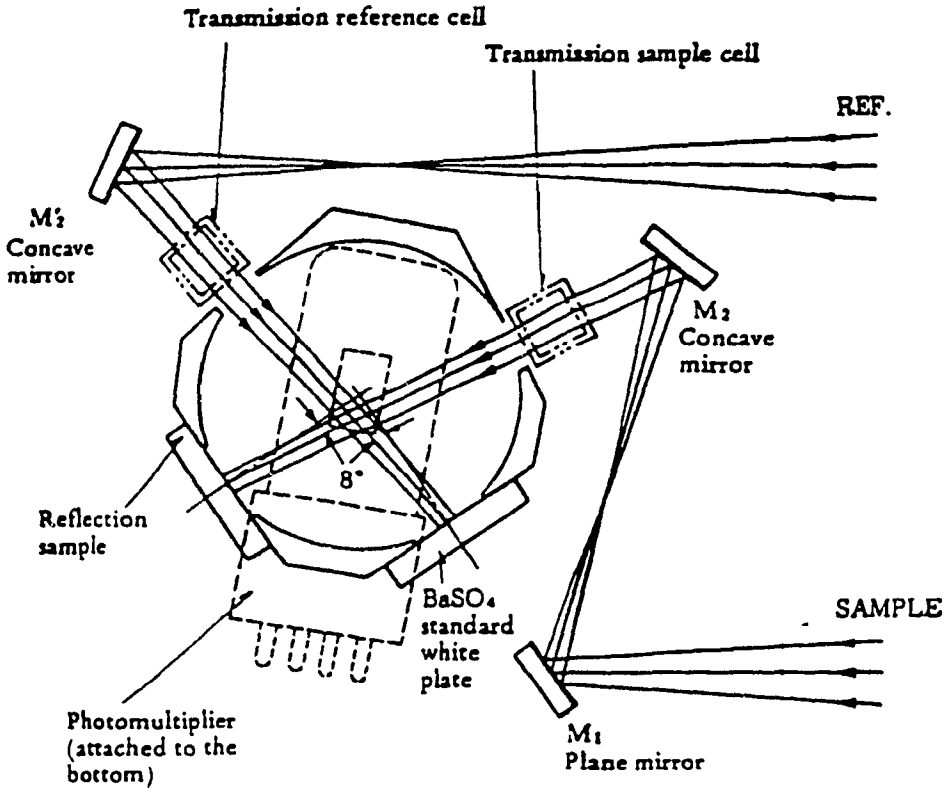

Figure 2.1 Schimadzu double-beam integrating sphere assembly reflectance unit.

Solid samples for reflectance measurement were prepared by filtering a slurry containing the solid TiO_2 material through a 25 mm diameter, 0.22 μm pore size MSI nylon 66 filter. The filter paper was then mounted (by using two small pieces of Scotch tape on the back of the filter paper) on an integrating sphere spacer attachment containing a 1.8 cm diameter circle in such a way that only the solid material was visible through the hole (Figure 2.2a and 2.2b). None of the scotch tape was visible to the analyzing

light. The spacer unit was placed in front of a powder sample dish containing pure $BaSO_4$ (Wako) (Figure 2.2c) and the scan taken.

Reflectance measurements on the CdS glasses were obtained by embedding the samples in a sample dish containing $BaSO_4$ and measuring the reflected light relative to a sample dish containing only the $BaSO_4$ reference (Figure 2.2d).

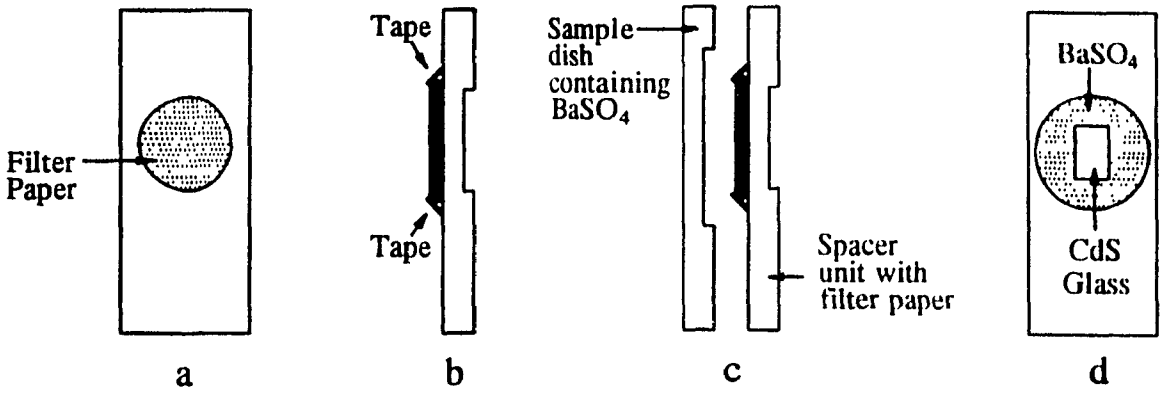

Figure 2.2 Arrangement of samples for reflectance measurements: **(a)** front view of filter paper mounted on integrating sphere spacer attachment; **(b)** side view of filter paper on the integrating sphere attachment; **(c)** final arrangement for measuring reflectance of a solid material on filter paper; **(d)** CdS glass embedded in sample dish containing $BaSO_4$.

Fluorescence spectra of the colloids were obtained using a Perkin-Elmer MPF-44B spectrofluorimeter. A Corning 0-54 filter was placed in front of the analyzing light in order to effectively eliminate scattered 280 nm excitation light. Photo-luminescence spectra of the CdS glasses were recorded using either a 90° geometry or using a solid state sample holder (front surface illumination). The recorded spectra were

identical in both cases, albeit for the latter the spectra were of lower intensity.

Powder x-ray diffraction patterns of the TiO_2 samples were obtained with a Phillips PW 1050-25 diffractometer using the Ni-filtered Kα radiation of copper (λ = 1.5417 Å). The powder was contained in a flat holder made of Plexiglas.

Transmission electron microscopy was carried out on a Philips EM 420 instrument equipped with an accessory for *in situ* elementary analysis by energy dispersive x-ray fluorescence (EDAX) which is a very sensitive technique for detecting the elemental composition of the material.[#] This technique essentially uses a high energy beam of electrons to remove a core electron of the element. An outer shell electron will then replace this electron with a subsequent release of energy in the form of x-ray fluorescence. Since the energy of the valence shell electrons is unique to each element, the technique can unambiguously identify which elements are present in the material.

Surface area (BET) analysis (low temperature N_2 adsorption) of the TiO_2 samples of varying anatase/rutile composition and some of the TiO_2 colloids was obtained from a Micrometrics Instrument Corp. instrument interfaced to a 286 IBM compatible PC.[##]

Solutions in which the metal-doped TiO_2 samples had been employed were analyzed for metal concentration using a Perkin-Elmer 502 atomic absorption

---

[#] The author thanks Dr. Dani Meisel of Argonne National Laboratory for allowing the author to use the electron microscope facilities and Mr. Liao Youxin of the Material Science Division of Argonne National Laboratory for his assistance with the electron microscopy and EDAX measurements.

[##] The author thanks Dr. Le Van Mao of Concordia University for allowing the author to use the BET instrument and Mr. B. Sjiariel for assistance with the operation of the instrument.

spectrophotometer. All atomic absorption lamps were hollow cathode single element type and the wavelengths of analysis were: Au, 242.8 nm; Co, 240.7 nm; Cr, 357.9 nm; Cu, 324.8 nm; Fe, 248.3 nm; Mo, 313.3 nm; Ni, 232.0 nm; Pd, 247.6 nm; Pt, 265.9 nm; Rh, 343.5 nm; Ru, 349.9 nm; Ti, 365.3 nm; V, 318.4 nm; W, 255.1 nm.

2.4.2 Dynamic Light Scattering

The average hydrodynamic particle diameter of the colloidal materials was measured using the dynamic light scattering technique.[#] The system[19] consisted of a 12-Watt Spectra Physics Model 171 Ar^+ ion laser (λ=514.3 nm), which served as the illumination source, and a goniometer interfaced to a Model M2000 digital correlator microprocessor (Brookhaven Instrument). The colloids to be measured were placed in a thoroughly clean[20] quartz cell and the scattering intensity, typically 10^7 accumulated counts, was measured in the microsecond time domain. Small fluctuations in intensity were monitored utilizing an Ortec model 776 counter and timer.

The average particle diameter was calculated from a statistical analysis of the observed intensities assigned to each particle diameter. Based on the Central Limit Theorem of statistics,[21] the weighted mean particle diameter, $\bar{x}$, of a normal or skewed particle distribution was calculated using equation 2.1.

$$\bar{x} = \frac{\Sigma xy}{\Sigma y} \qquad (2.1)$$

[#] The author thanks Prof. J. Fendler for allowing the author to use their facility at the University of Syracuse, Syracuse, New York. The author also thanks Ms. Youxin Yuan for her assistance in using the light scattering apparatus.

where x is the particle diameter and y is the value assigned to each particle diameter (based on the observed intensities). The standard deviation of the mean, $\sigma_{\bar{x}}$, was determined from equations 2.2 and 2.3.

$$\sigma_{\bar{x}} = \frac{\sigma}{\sqrt{n}} \tag{2.2}$$

where **n** is the number of cases in a sample and σ is the population standard deviation, given by:

$$\sigma = \sqrt{\frac{\sum_{i=1}^{N}(x_i - \bar{x})^2}{N}} \tag{2.3}$$

where x_i is the particle diameter and **N** denotes the total number of cases in the population.

2.4.3 Picosecond Laser Flash Photolysis

Excitation of a semiconductor with light energy greater than or equal to the bandgap energy results in the creation of conduction band electrons and valence band holes. The formation of these charge carriers occurs in femtoseconds (10^{-15} s)[13] in TiO_2 and their subsequent decay via recombination, radiationless decay, etc., occurs in nanosecond (10^{-9} s) time. Picosecond laser absorption and emission spectroscopies are

therefore a convenient means to observe some of the fundamental photochemical and photophysical events.[14]

All picosecond laser absorption and emission flash photolysis experiments were carried out at the Canadian Centre for Picosecond Laser Spectroscopy (Concordia University). A schematic of the system is described in Figure 2.3.

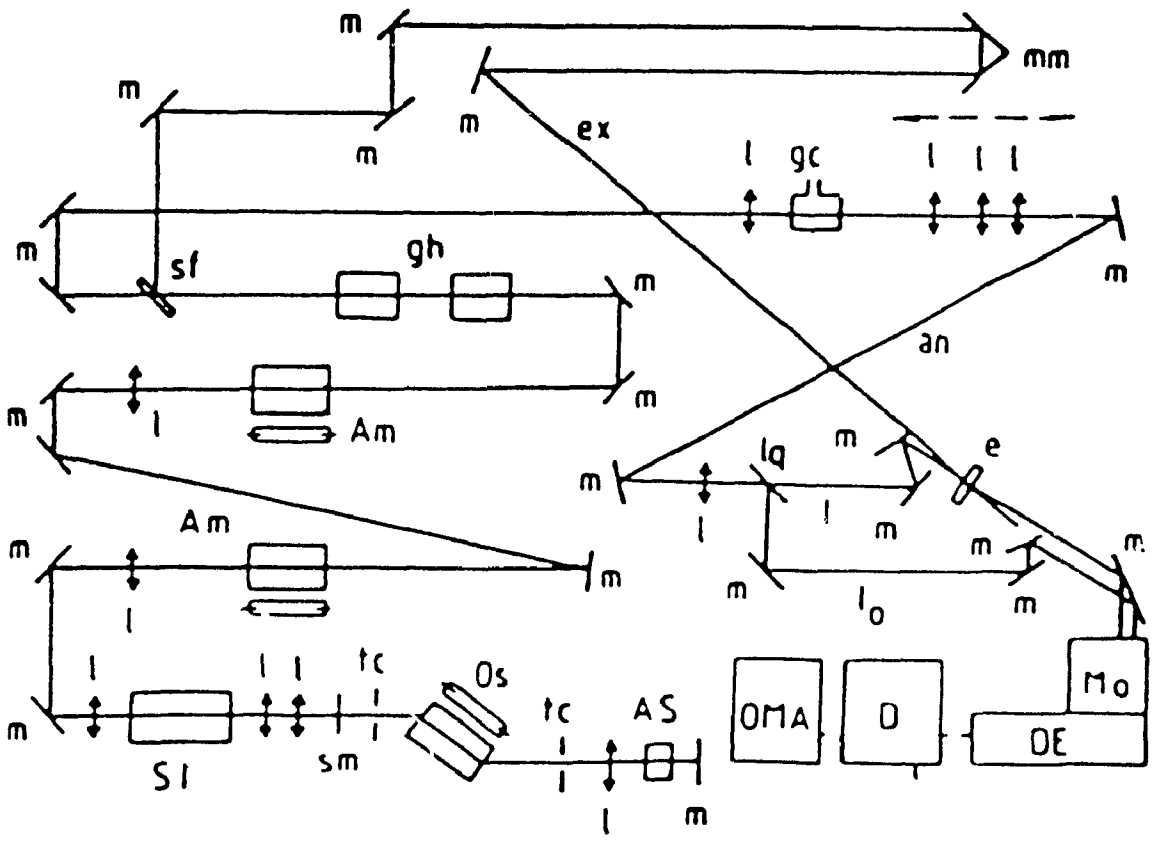

Figure 2.3 Schematic illustration of the passively mode-locked Nd:YAG picosecond laser system. Description: **m**, mirror; **AS**, saturable absorber dye (Eastman Kodak 9740 in chlorobenzene); **l**, lens; **tc** diaphragm; **OS**, laser head (Nd:YAG) placed at the Brewster angle in the oscillator cavity; **SI**, pulse selector (pockels cell); **AM** amplifier (Nd:YAG); **gh**, harmonic generating crystals; **sf**, dichroic mirrors; **mm**, mirrors mounted on an optical delay stage; **gc**, continuum generation (deuterated phosphoric acid); **ex**, excitation beam; **an**, analyzing probe beam; **lq**, 50%/50% double prism; e, sample; Mo, double monochromator; **DE**, monochromator coupled to a SIT-Vidicon; **D**, analog-to-digital converter; **OMA**, optical multichannel analyzer.

Picosecond absorbance measurements were made using a double beam, frequency tripled (355 nm) and passively mode locked Nd:YAG laser system, coupled to a fast detection unit comprising of a Silicon Intensified Target Vidicon and an EG&G optical channel analyzer OMA-2. Pulses (fwhm, $\approx$ 30 ps) of energy $\sim$ 0.5 to 3 mJ were used. The white probe light (spectral window from 425 nm to 675 nm) was generated by focusing the fundamental 1054-nm laser light into a 5 cm cell containing D_2O. Zero time was taken as the maximum overlap of the probe and pump pulses, which in the present case corresponded to the time when approximately half of the integral intensity of the excitation (actinic) pulse had been absorbed. Different time delays were achieved by varying the time when the pump and probe pulses entered the sample. This was made possible by manually changing the position of a series of mirrors positioned on the rails of a calibrated optical delay line capable of yielding delay times from -75 ps to 12 ns. Negative time is taken to indicate that the longest wavelength light of the white light probe arrives before the actinic pulse.

Transient emission decays monitored at wavelengths above 400 nm were obtained by using 355 nm excitation with 385 and 400 nm cutoff filters (to filter out the actinic pulse) in front of a Hamamatsu Streak Camera (10 ps time resolution). Colloidal sols were contained in 2 mm Suprasil quartz cells of high quality (Hellma) CdS glass samples were mounted on a Plexiglass sample holder. Glass samples were checked for signs of permanent bleaching (or darkening) after each laser shot.

2.4.4. Pulse Radiolysis

Pulse radiolysis experiments on colloidal TiO_2 were carried out at Argonne National Laboratory (Argonne, Illinois).[#] A block diagram of the pulse radiolysis set-up is shown in Figure 2.4. The system is made up of a pulsed LINAC electron source and a spectrophotometric detection system which is made up of a pulsed xenon lamp, a monochromator and a photomultiplier tube shielded against electromagnetic fields and radiation. Electron pulses of 2 to 40 ns width, from the Argonne 15 MeV LINAC electron accelerator, were used to produce 1.7×10^{-6} to 2.5×10^{-5} M OH• radicals per pulse. Concentration changes in a 10 cm Suprasil cell were monitored spectrophotometrically; the output signal was digitized on a Biomation 8100 transient recorder and stored in a LSI 11/23 minicomputer. The data were then transferred for analysis to a VAX 11/780 computer.[15] A N_2O-saturated aqueous solution of 10 mM KSCN {$G(OH•) = G(SCN)_2^{-•} = 6.0$ molecules/100 eV; $\epsilon_{480} = 7600\ M^{-1}\ cm^{-1}$) was used as a dosimeter to calculate the absorbed radiation dose.

The advantage of using the pulse radiolysis technique over flash photolysis techniques lies in the ability to explore the chemical and physical properties of a charge carrier (electron or hole produced on irradiation of a semiconductor) without the fast recombination of charge carriers and without the interference from absorption by the other carrier.[17] This work was focused solely on the reaction of the hydroxyl radical with colloidal TiO_2. Solutions for pulse radiolysis study were prepared by diluting

---

[#] The author thanks Dr. Dani Meisel for allowing the author to use the pulse radiolysis facilities at Argonne National Laboratory, Argonne, Illinois and for the several useful discussions about the experiments.

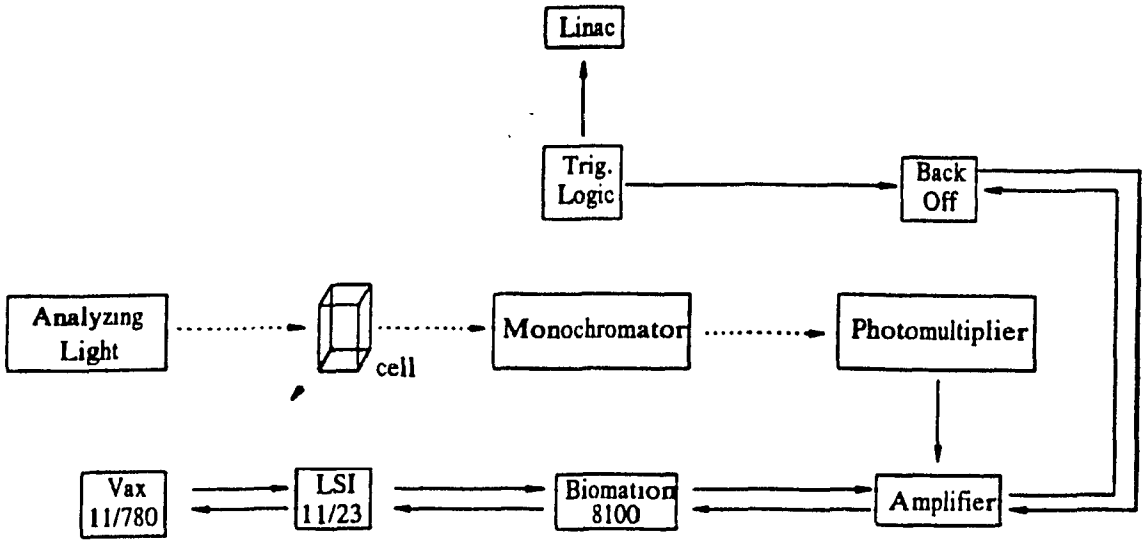

Figure 2.4 Scheme of the pulse radiolysis system at Argonne National Laboratory.

10 mL of a 15 g/L TiO_2 sol to 3 g/L with 40 mL of 0.1 M $HClO_4$, the resulting pH being between 2.5 and 3; solutions were purged with N_2O gas for a minimum of 15 minutes. Irradiation of N_2O-saturated aqueous solutions with high energy electrons generates primarily OH• radicals via equations 2.4 and 2.5:

$$H_2O \rightarrow\rightarrow\rightarrow OH\bullet,\ e^-_{aq},\ H\bullet,\ H_2,\ H_2O_2 \qquad (2.4)$$

$$N_2O + e^-_{aq} + H_2O \rightarrow OH\bullet + N_2 + OH^- \qquad (2.5)$$

$$(k = 8.7 \times 10^9\ M^{-1}s^{-1})^{18}$$

H• atoms are formed either directly (reaction 2.4) or by reaction of H_3O^+ with the e^-_{aq}

(reaction 2.6). At the pH of the sols, approximately 12 % of the solvated electrons are lost via reaction 2.6:

$$H_3O^+ + e^-_{aq} \rightarrow H\bullet + H_2O \qquad (2.6)$$

$$(k = 2.3 \times 10^{10}\ M^{-1}s^{-1})^{18}$$

Radiolytic irradiation of colloidal silver iodide solutions were carried out using the set-up at the Boris Kidric Institute of Nuclear Sciences (Belgrade, Yugoslavia) and employed a Febetron 707 (Field Emission Cap) electron accelerator. These experiments were kindly done by Dr. O.I. Micic and her group. Pulses were 20 ns in duration and the total light path through the cell was 5.1 cm. The absorption doses ranged from 0.5 to 120 Gy# per pulse and were determined by potassium ferrocyanide dosimetry.[16]

2.5 PROCEDURES TO ASSESS PHOTOCATALYTIC ACTIVITY

The various TiO_2 samples prepared were tested for their photocatalytic activity by illuminating the solid materials in water at pH 3 (reductive tests; formation of H_2), in oxalic acid solutions (oxidative tests; degradation of oxalic acid) and in phenol solutions (effect of anatase/rutile ratio) as described below.

In all cases, irradiation was carried out using aqueous dispersions in which the TiO_2 concentration was 2 g/L (for example, 50 mg catalyst in 25 mL solution). The light source used was a 1000 watt Hg/Xe lamp, operated at approximately 900 watts,

1 Gy = 1 Gray = 1 J/Kg, the SI unit for absorbed dose.

which was fitted with a water jacket to filter out infrared radiation. Illumination with near UV light (λ = 300 to 400 nm; Figure 2.5) was achieved by placing a Corning 7-60 filter in front of the reaction flask. Similarly, only visible light illumination was obtained by placing a Corning 4-97 filter in series with a 400 nm Oriel cut-off filter (spectral window: 400 to 650 nm; Figure 2.6).

2.5.1 Photooxidative Tests

The photooxidative activity of the different TiO_2 samples was determined by monitoring the oxidation of oxalic acid in aqueous suspensions of the catalyst illuminated with either UV or visible light for 30 minutes. Unreacted oxalic acid was determined using a permanganate titration procedure.

2.5.1.1 Preparation of Standard Potassium Permanganate Solution

A 0.1 N standard $KMnO_4$ solution was prepared using an official method of analysis of the Association of Official Analytical Chemists (AOAC).[23] Approximately 3.2 g of $KMnO_4$ (Baker analyzed) was dissolved in 1 litre of distilled water. The solution was boiled for approximately 1 hour and left to stand (covered) overnight in the dark. The $KMnO_4$ solution was then filtered, by gravity, through a glass sintered porcelain filter. A large amount of brown MnO_2 product was observed. The filtered $KMnO_4$ solution was subsequently stored in an amber bottle in the dark.

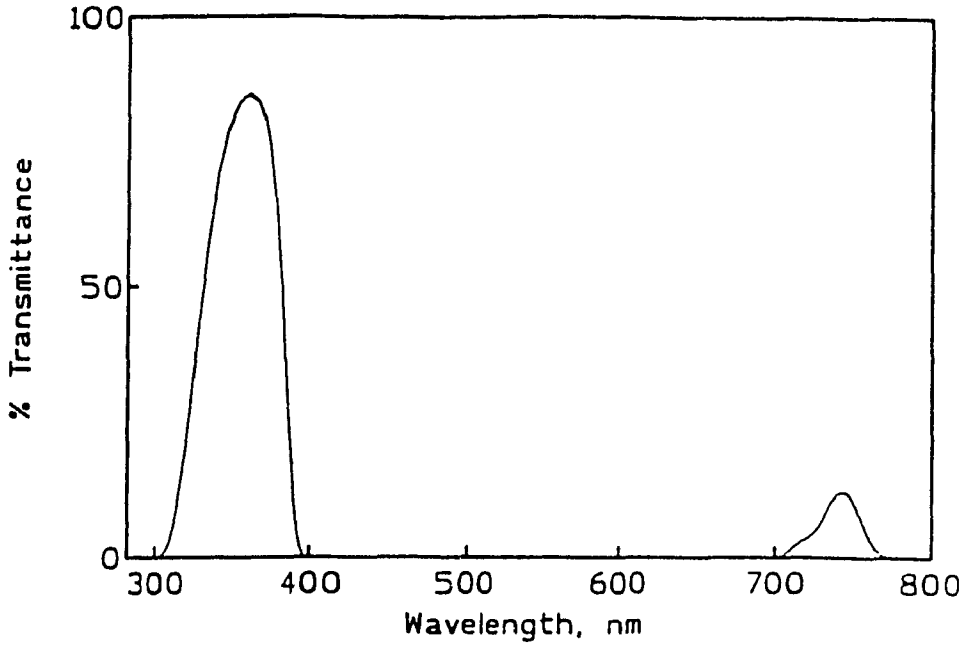

Figure 2.5 Transmittance spectrum of Corning 7-60 filter

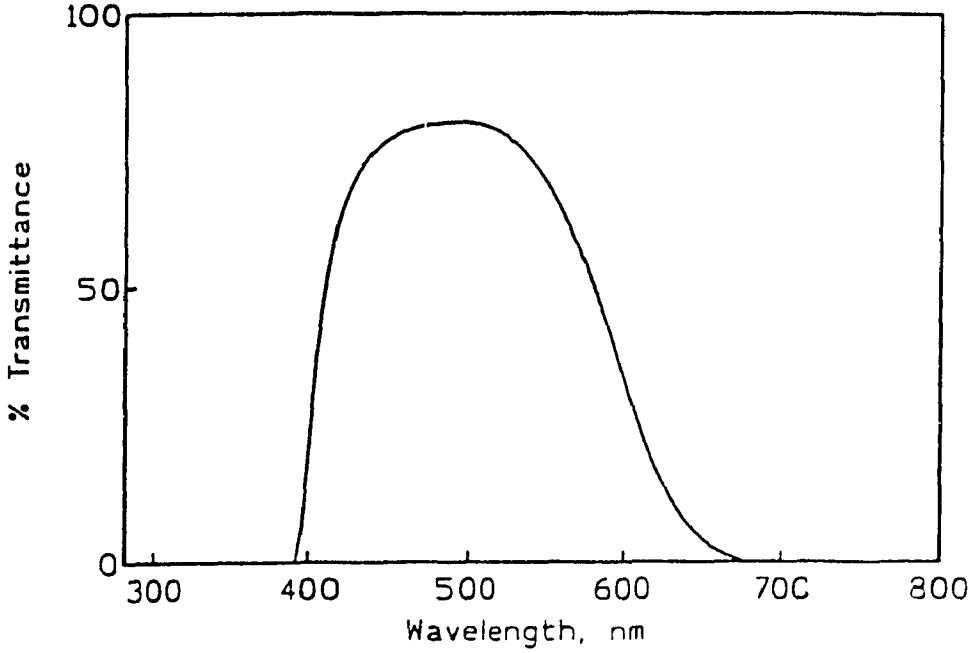

Figure 2.6 Transmittance spectrum of Corning 4-97 + 400 nm cut-off filters

2.5.1.2 STANDARDIZATION OF THE PERMANGANATE SOLUTION

A quantity of oxalic acid was dried at 110 °C for approximately 3 hours; subsequently it was placed in a desiccator for 30 minutes and allowed to cool prior to weighing. Accurately weighed (~ 0.3 g) quantities of oxalic acid were then transferred to 600 mL beakers and dissolved in 250 mL of H_2SO_4 (5% by vol.) previously boiled for 10 to 15 minutes and later cooled to room temperature. Approximately 40 mL of the $KMnO_4$ solution was added to the solution at a rate of 25-35 mL/min with slow stirring. The solution was allowed to stand for 45 to 60 sec until the pink colour disappeared. The solution was subsequently heated to 55-60° and the titration completed by adding $KMnO_4$ solution until a faint pink colour persisted for 30 sec. The last 0.5-1 mL was added dropwise, letting each drop decolorize before adding the next. The endpoint was determined by matching the colour of the solution to the colour obtained by adding $KMnO_4$ to the same volume of boiled and cooled dilute H_2SO_4 at 55-60°. The normality (N) of the standard $KMnO_4$ solution was calculated by equation 2.7.

$$N \text{ of } KMnO_4 = \frac{\text{wt. oxalic acid(g) x 1000 mL/L}}{\text{mL } KMnO_4 \text{ x } \dfrac{133.998 \text{ g/mole}}{2 \text{ equivalents/mole}}} \qquad (2.7)$$

2.5.1.3 OXIDATION OF OXALIC ACID USING TiO_2 MATERIALS

A 5.0×10^{-3} M solution of oxalic acid was prepared by dissolving 0.6304 g of oxalic acid (pre-dried for 2 hrs at 110 °C) in 1 litre of distilled water. The final pH of the solution was 2.25. The exact concentration of the stock solution was determined by

titration with the standardized $KMnO_4$ solution in a manner similar to the way the quantity of unreacted oxalic acid was determined in the TiO_2/oxalic acid slurries. Four millilitres of the solution to be analyzed was placed in a 20 mL beaker to which 1 mL of concentrated H_2SO_4 was added. Addition of the sulphuric acid was critical as it ensured that the hydrogen ion concentration was sufficient to cause complete reaction between the permanganate and the oxalic acid (reaction 2.8).

$$2\ MnO_4^- + 5\ H_2C_2O_4 + 6\ H^+ \rightleftharpoons 2\ Mn^{2+} + 10\ CO_2 + 8\ H_2O \quad (2.8)$$

A suspension consisting of 20 mg of the TiO_2 material in 10 mL of the stock oxalic acid solution was stirred using a magnetic stirrer in a flat, three-sided reaction flask consisting of two round ($\approx$ 3 cm diameter) quartz windows. Pre-purified oxygen was bubbled through the solution at a constant rate of 10 mL/min. Excess oxygen was bubbled into a saturated solution of barium chloride (ACP Chemicals). After 30 min. stirring either in the dark or under illumination (UV and visible), the reaction was stopped and the slurry filtered through a 0.22 μm MSI nylon 66 filter. The filtrate was analyzed for unreacted oxalic acid as described previously. In all samples, the titration was repeated a minimum of two times and the results averaged; agreement between the two values was better than 5%. The amount of unreacted oxalic acid was calculated from equation 2.9:

$$moles\ oxalic\ acid\ unreacted = (vol.\ KMnO_4\ , L)([stand.\ KMnO_4])(2.5) \quad (2.9)$$

2.5.2 Photoreductive Tests

Detection of hydrogen gas was accomplished with a Gow Mac Model 550 gas chromatograph equipped with a 5 Å molecular sieve column and a thermoconductivity detector; it was interfaced to a Hewlett Packard 3396A integrator. A summary of the operating conditions used on the GC is reported in Table 2.5.

Table 2.5 GC Operating conditions.

Carrier gas	Pre-purified Argon
Flow rate	60 mL/min
Column Temperature	110 °C
Detector Temperature	110 °C
Injection Port Temperature	160 °C (setting 45)
Attenuation (on GC)	x 2
Bridge Current	70 mA

The instrument was calibrated for hydrogen by adding exactly 20 mL of distilled water (pH 3, adjusted with HCl) to a 60 mL pyrex flask whose exact volume had been determined exactly by adding known volumes of distilled water until the flask was completely full. The solution was then degassed with pre-purified argon for at least twenty-five minutes following which 500 μL of pre-purified hydrogen was added to the flask; the solution was stirred for 10 minutes prior to sampling the headspace gas and injecting into the GC. The concentration of hydrogen in the injection volume was calculated by equation 2.10 for calibration purposes.

$$[H_2] = \frac{(injection\ vol.\ (\mu L))(500\mu L - vol.\ removed^{*})}{Headspace^{**}} \qquad (2.10)$$

* = 0 for the first injection.

** Headspace is defined as: Vol. of reaction flask (μL) - Vol. of solution (μL).

Gas samples during the reaction were taken by first injecting 500 μL of pre-purified argon into the reaction flask and then sampling 500 μL of the reaction gas volume. The concentration of hydrogen in the flask was calculated using equation 2.11.

$$[H_2]\ \mu l = \frac{Peak\ area}{slope\ of\ calibration\ curve} \times \frac{Headspace}{500} + vol.\ H_2\ previously\ removed \times \frac{500}{Headspace} \qquad (2.11)$$

2.5.3. EFFECT OF ANATASE/RUTILE RATIO ON THE PHOTO-OXIDATIVE ACTIVITY OF P25 DEGUSSA TiO_2

The effect of varying the anatase/rutile ratio in P25 Degussa TiO_2 was examined by comparing the relative activity of the different samples to degrade 20 ppm (212.8 μM) solutions of phenol. The solutions of phenol were prepared by dissolving the appropriate amount of phenol (Aldrich, redistilled 99+%) in 1 litre of doubly distilled deionized water. The pH of the solution was adjusted to 3 using concentrated HCl. The oxidation of phenol to various intermediates[23,24] was monitored by high performance liquid chromatographic (HPLC) techniques using a Waters Associates liquid chromatograph

equipped with a 501 HPLC pump, a 441 absorbance detector and a Hewlett Packard 3396A integrator. The detection wavelength was 214 nm (Zn lamp). The column was a Waters reverse phase μ-Bondapack C-18 column and the mobile phase consisted of a mixture of methanol/water (35/65) filtered through a 0.22 μm pore size nylon 66 filter. The flow rate was 2 mL/min. Aliquots from the reaction slurry (temperature of reaction, ~ 35 °C) were also filtered through a 0.22 μm pore size filter prior to analysis.

References and Notes

1. (a) Shaw, D.J., *Introduction to Colloid & Surface Chemistry*, Butterworths, London, 1970.
(b) Moser, J. and Grätzel, M., *Helv. Chim. Acta.*, **1986**, 65, 1436.
(c) Moser, J. and Grätzel, M., *J. Am. Chem. Soc.*, **1987**, 105, 6547.
(d) Moser, J., Ph.D dissertation, Thesis No. 616, Ecole Polytechnique Fédérale de Lausanne, Lausanne, Switzerland, 1986.

2. (a) Duonghong, D., Borgarello, E., and Grätzel, M., *J. Am. Chem. Soc.*, **1981**, 103, 4685.
(b) Henglein, A. *Ber. Bunsenges. Phys. Chem.*, **1982**, 86, 241.
(c) Bahnemann, D., Henglein, A., Lilie, J., and Spanhel, L., *J. Phys. Chem.*, **1984**, 88, 709.

3. Colloidal solutions (25 g/L) of TiO_2 prepared by Dr. Jacques Moser (Ecole Polytechnique Fédérale de Lausanne) via the controlled hydrolysis of $TiCl_4$ and stored unprotected (no stabilizer) in the dark have remained stable (i.e. no signs of precipitation, extreme haziness or change in the absorption characteristics) since 1984 in our laboratory. Similar preparations done in this laboratory have demonstrated the same stability. Further, a sol made in 1990 using the controlled hydrolysis of titanium isopropoxide shows no signs of precipitation and remains optically transparent after 2 years.

4. During the course of this work over 120 stable doped and undoped TiO_2 sols were prepared.

5. Personal communication with Dr. Jacques Moser of the Ecole Polytechnique Fédérale de Lausanne, and Dr. G. Mills of the University of Auburn (formerly doctorate student of Prof. A. Henglein of the Hahn-Meitner-Institut in Berlin) and Dr. U. Resch (also former doctorate student of Prof. Henglein).

6. The resulting cleaning solution becomes yellow suggesting the formation of titanates or titanium peroxides. Further, several quartz cells in which TiO_2 had become embedded (as shown by the absorption spectra) were successfully cleaned in this way. Following the cleaning the absorption spectra of these cell showed **no** evidence of the presence of TiO_2.

7. Kormann, C., Bahnemann, D.W. and Hoffman, M.R., *J. Phys. Chem.*, **1988**, 92, 5196.

8. (a) Grätzel, M., *J. Am. Chem. Soc.*, **1981**, 103, 4685.
(b) Henglein, A., *Ber. Bunsenges Phys. Chem.*, **1982**, 80, 241.
(c) Henglein, A., *J. Phys. Chem.*, **1984**, 88, 7091.

9. (a) Bérubé, Y.G. and de Bruyn, P.L, *J. Colloid Interface Sci.*, **1968**, 28, 92.
(b) Yates, D.E., and Healy, T.W., *J. Chem. Soc. Faraday Trans. I*, **1980**, 76, 9.

10. Schmidt, K.H., Patel, R., and Meisel, D., *J. Am. Chem. Soc.*, **1988**, 110, 4882.

11. (a) Rajh, T., Vucemilovic, M.I., Dimitrijevic, N.M., Micic, O.I., and Nozik, A.J., *Chem. Phys. Lett.*, **1988**, 143, 305.
(b) Avnir, D., and Kaufman, V.R., *J. Non. Cryst. Solids*, **1987**, 92, 180.

12. *Technical Bulletin Pigments*, **No. 56-3-205-282K**, 3rd edition, 1982, Degussa, Germany.

13. Rothenberger, G., Moser, J., Grätzel, M, Serpone, N., and Sharma, D.K., *J. Am. Chem. Soc.*, **1985**, 107, 8054.

14. Serpone, N., in *Photoelectrochemistry, Photocatalysis and Photoreactors - Fundamentals and Developments*, Schiavello, M. (ed.), Nato ASI Series C., vol. 146, D. Reidel Publishing Co., Dodrecht, 1985.

15. A more detailed description of the experimental set up is given in:
(a) Schmidt, K.H., Gordon, S. *Rev. Sci. Instrument.*, **1979**, 50, 1656.
(b) Schmidt, K.H., Gordon, S., Thompson, M., Sullivan, J.C., Mulac, W.A., *Radiat. Phys Chem.*, **1983**, 21, 321.

16. Rabani, J., and Matheson, M.S., *J. Phys. Chem.*, **1966**, 70, 761.

17. Henglein, A., *Chem. Rev.*, **1989**, 89, 1861.

18. Buxton, G., Greenstock, C.L., Helman, W.P., and Ross, A.B., *J. Phys. Chem. Ref. Data*, **1988**, 17, 573.

19. Reed, W., Guterman, L., Tundo, P., and Fendler, J., *J. Am. Chem. Soc.*, **1984**, 106, 1897.

20. A cell was considered clean if no condensation formed on the cell after the cell was exposed to a steam jet, and if the steam rolled off in a continuous sheet.

21. Mansfield, E., *Statistics for Business & Economics - Methods & Applications*, 2nd ed., W.W. Norton Company, New York, 1983.

22. *Official Methods of Analysis of the Association of Official Analytical Chemists*, 14th ed., Williams, Sidney (ed.), published by the Associates of Official Analytical Chemists Inc., U.S.A.. **1984**, 1005.

23. Okamoto, K., Yamato, Y., Tanaka, H. and Itaya, A., *Bull. Chem. Soc. Jpn.*, **1985**, 58, 2015.

24. Okamoto, K., Yamato, Y., Tanaka, H. and Itaya, A., *Bull. Chem. Soc. Jpn.*, **1985**, 58, 2523.

CHAPTER 3

PHYSICOCHEMICAL PROPERTIES OF TiO_2 AND TRANSITION METAL DOPED TiO_2

3.1 INTRODUCTION

The photocatalytic activity of a semiconductor material can be influenced significantly by its crystal structure and method of preparation.[1-5] For example, anatase TiO_2 has been shown to successfully lead to the total mineralization of a number of organic pollutants,[6] whereas the rutile phase of TiO_2 has shown negligible or minimal activity in these same processes.[7] Sclafani and co-workers have recently[1] shown that the photoactivity of rutile TiO_2 is related to its method of preparation; they concluded that photoactivity is determined not only by the semiconducting properties (e.g. bandgap, electron/hole lifetimes, etc.) but also by physicochemical ones. Correlations between these properties and the order of activity are meaningless without knowing the main structural and surface properties together with the semiconducting features.

A number of techniques have been developed recently to assess the physico-chemical properties of both solid and particulate systems. An illustrative sampling of some of these techniques is given in Table 3.1 with a more in depth discussion of these and other techniques given elsewhere.[8,9] During the course of this work, the size, morphology, crystal structure and surface area of both the doped and undoped TiO_2

specimens were determined using, respectively: dynamic light scattering, electron microscopy, x-ray diffraction and surface area measurements (B.E.T.). This part of the thesis reports on the results of these investigations. The photophysical, pulse radiolytic and photocatalytic results appear in later chapters.

Table 3.1 Physicochemical Methods for Characterization of Particulates*

Property	Method or Technique
Surface charge	Acid-base charge titration
Potential	Microelectrophoresis Electroacoustics
Point of Zero Charge (pzc)	sedimentation or coagualtion studies Microelectrophoresis Electroacoustics
Surface area, particle size, polydispersity	B.E.T. Light scattering Electron microscopy Chemical reactions
Surface Concentration	XPS, UPS, EDAX, EXAFS
Band gap	Absorption spectroscopy Diffuse reflectance spectroscopy
Intermediates in reaction	Flash photolysis and pulse radiolysis coupled with optical absorption, conductivity or ESR
Doping density	Transient microwave conductivity Static conductivity measurements

* adapted from reference 8

3.2 PHYSICAL AND VISUAL DESCRIPTION OF MATERIALS

A visual representation of the homemade TiO_2 as well as of the transition metal doped TiO_2 systems is shown in Figures 3.1 to 3.6. Samples were obtained by filtering a dispersion of the material in water and computer scanning (HP Scanjet IIc colour flatbed scanner) the resulting residual on the filter paper. The scanned image was manipulated using the Photostyler® and CorelDRAW!® software packages such that the final printed image (Seiko Colour Point colour Post Script laser printer) was a true colour match to the actual colour of the TiO_2/x wt.% M particulates.

Several of the TiO_2/M powders are highly coloured with the degree of coloration increasing, in most cases, with increasing dopant concentration. For example, Figure 3.1 illustrates that increasing the concentration of chromium in the bulk of TiO_2 results in a change of the TiO_2 colour from off-white (opal white) to a light pale yellowish green (oyster green; 0.1 wt.% Cr) to a darker spruce green colour (20 wt.% Cr). By contrast, chromium metal powder is metallic grey. A close examination of the chromium doped TiO_2 samples failed to reveal any evidence of metallic grey particles, as would have been the case had chromium metal been present with the chromium doped TiO_2; this would have been particularly evident in the case of the 20 wt.% chromium doped sample.

Inspection of the other doped TiO_2 samples also indicated that the TiO_2/M powders were homogenous in nature. Further, there was no evidence (e.g. discolouration) of the metal being deposited at the surface of the particle. A summary of the effect of the different dopants on the colour of the TiO_2 is given in Table 3.2.

Figure 3.1 Scanned images of TiO_2 particle filtrates (on MSI Nylon filters); upper section: TiO_2; middle section: TiO_2 doped with chromium(III); lower section: TiO_2 doped with palladium(II).

TiO_2

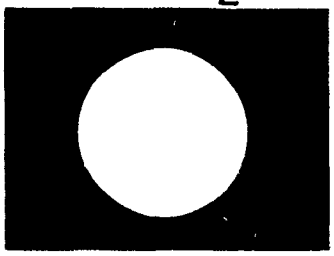

TiO_2 / x % Cr^{+3}

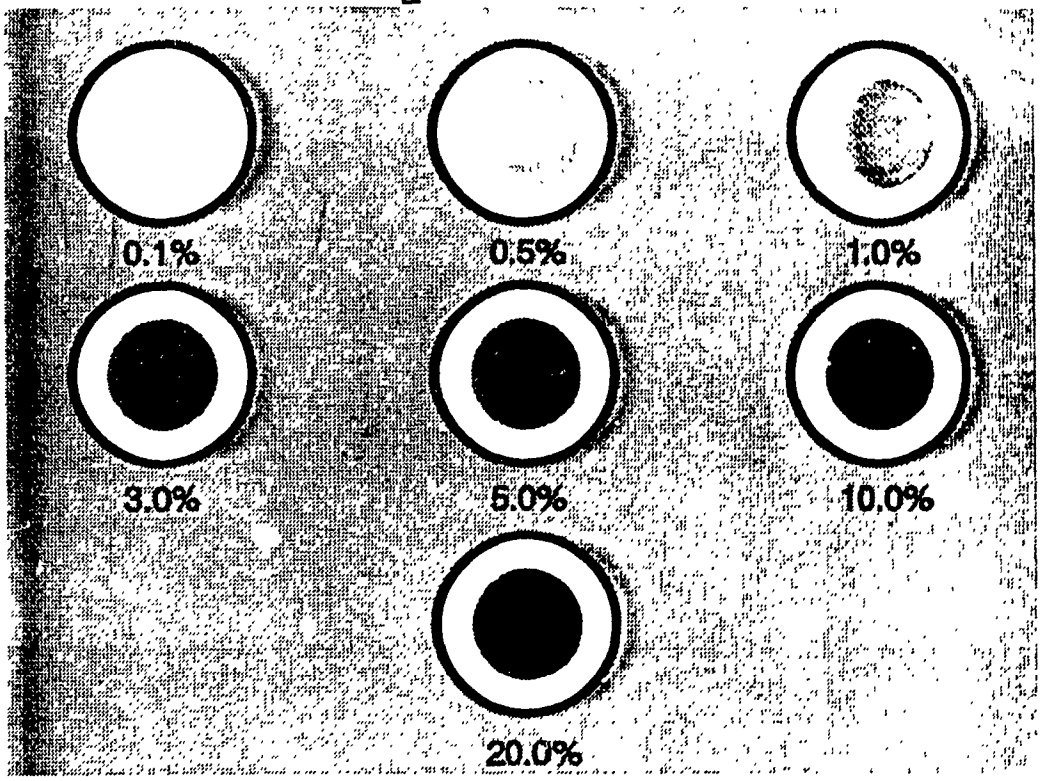

TiO_2 / x % Pd^{+2}

Figure 3.2 Scanned images of TiO_2 particle filtrates (on MSI Nylon filters); upper section: TiO_2 doped with vanadium(V and III); lower section: TiO_2 doped with copper (II).

TiO_2 / x % V

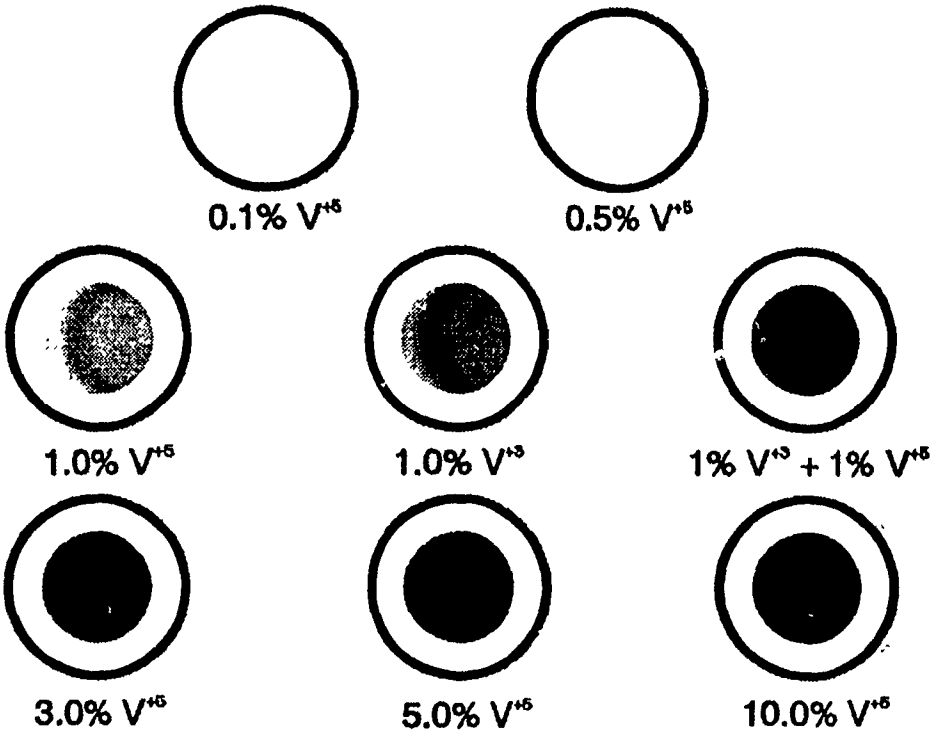

TiO_2 / x % Cu^{+2}

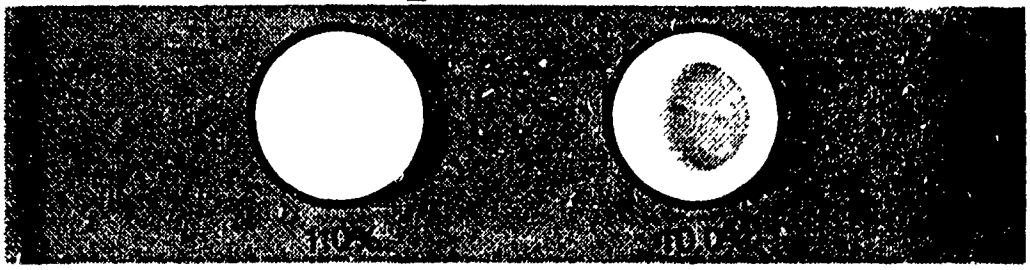

Figure 3.3 Scanned images of TiO_2 particle filtrates (on MSI Nylon filters); upper section: TiO_2 doped with ruthenium(III); lower section: TiO_2 doped with manganese(II).

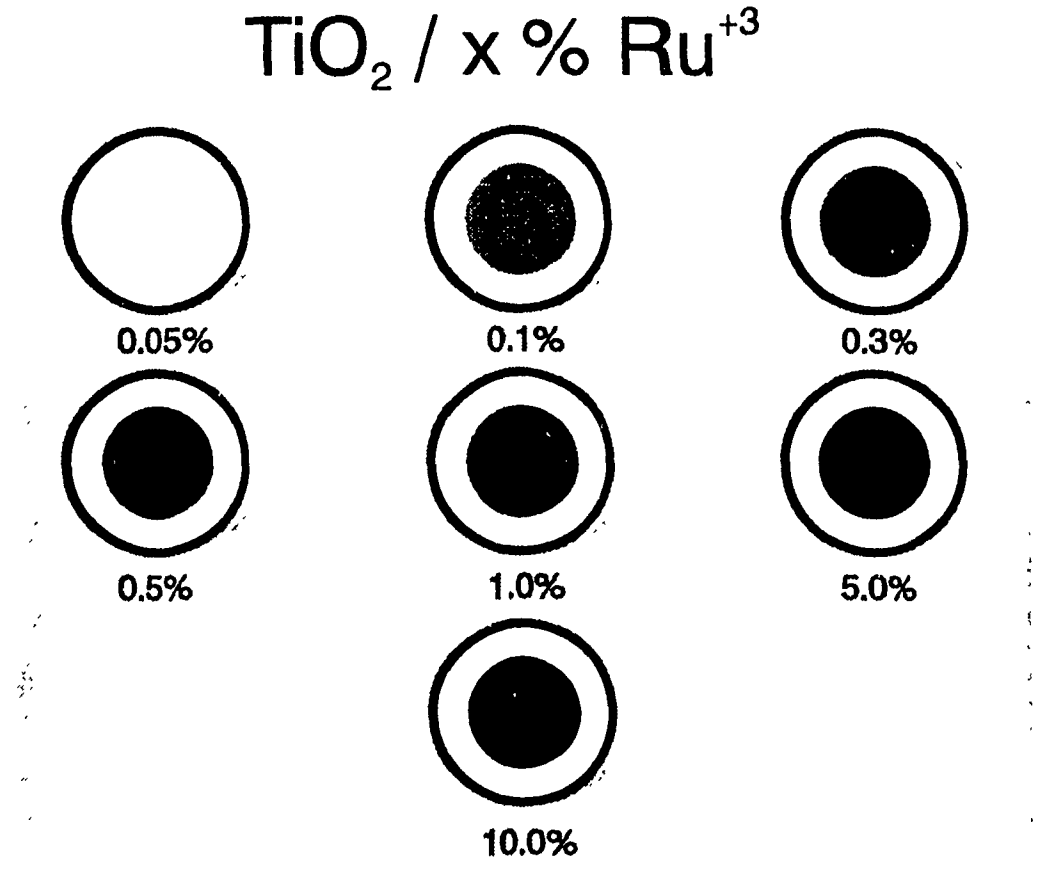
TiO_2 / x % Ru^{+3}
0.05%
0.1%
0.3%
0.5%
1.0%
5.0%
10.0%

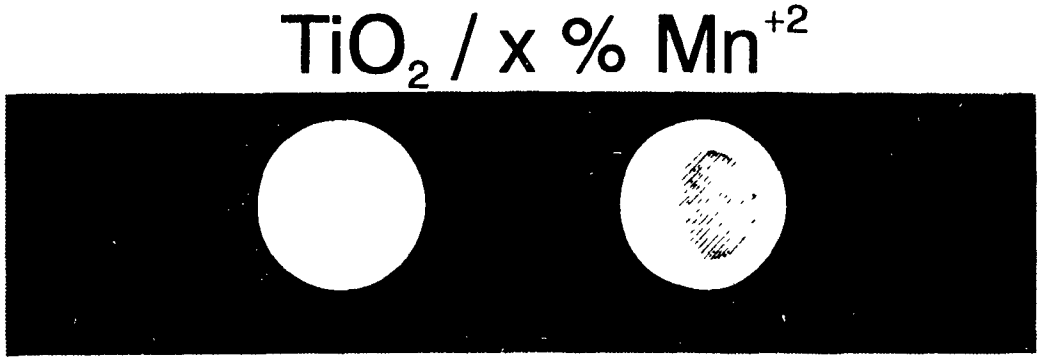
TiO_2 / x % Mn^{+2}

Figure 3.4 Scanned images of TiO_2 particle filtrates (on MSI Nylon filters); upper section: TiO_2 doped with rhodium(III) and lower section: TiO_2 doped with platinum(IV).

TiO_2 / x % Rh^{+3}

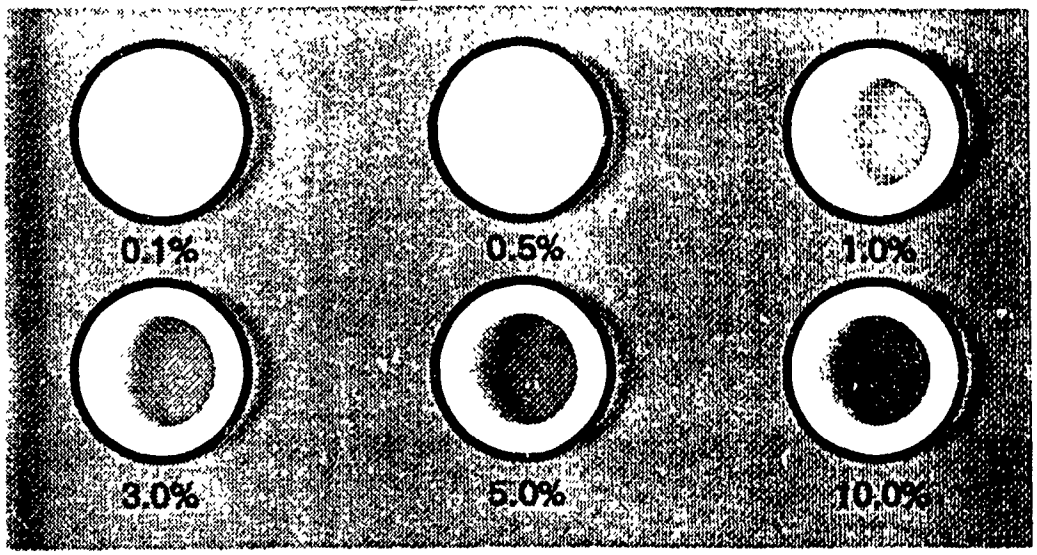

TiO_2 / x % Pt^{+4}

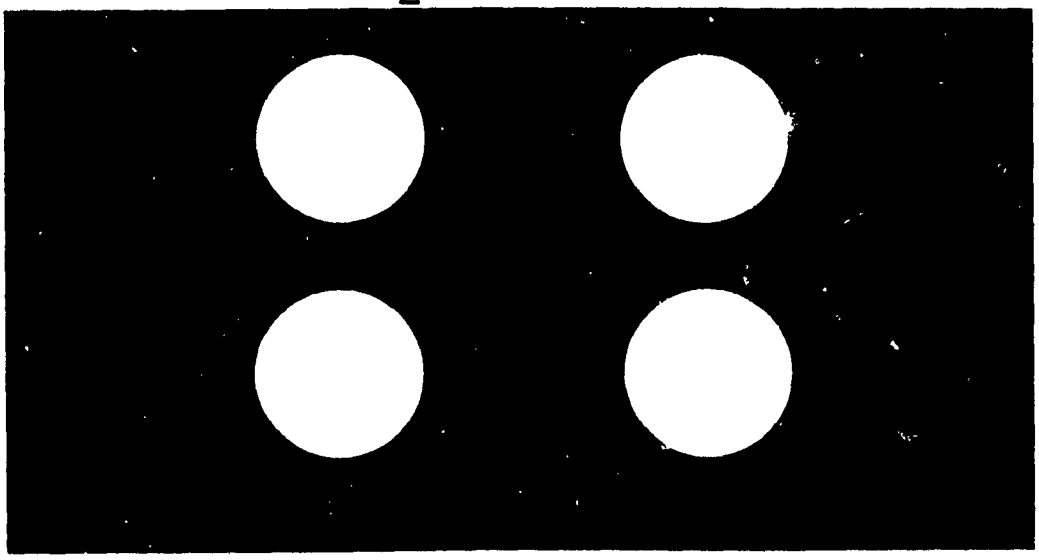

Figure 3.5 Scanned images of TiO_2 particle filtrates (on MSI Nylon filters); upper section: TiO_2 doped with iron(III); lower section: TiO_2 doped with a 1:1 mixture of platinum(IV) and ruthenium(III).

TiO_2 / x % Fe^{+3}

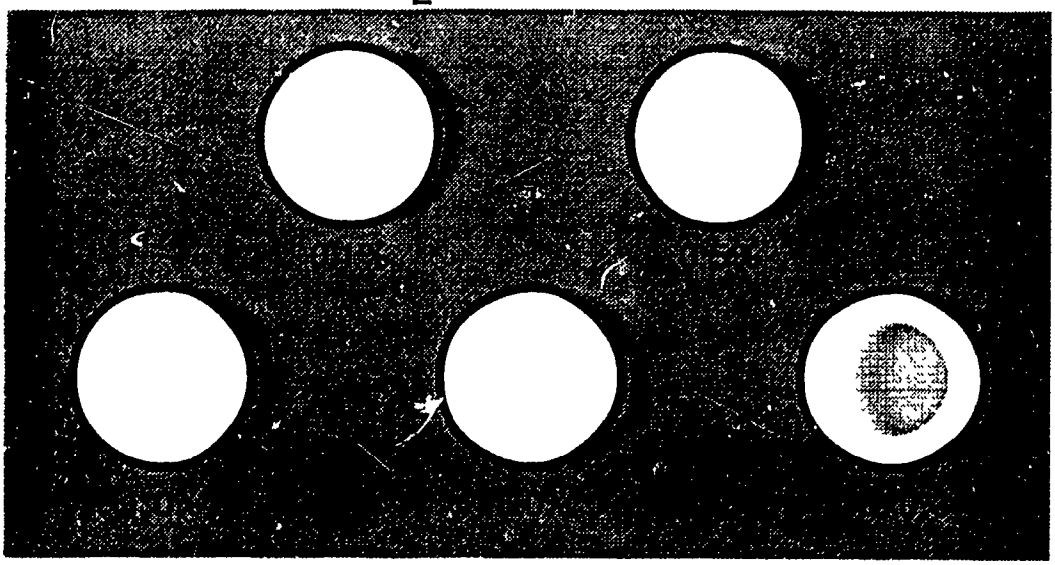

TiO_2 / x % (Ru^{+3}, Pt^{+4} (1:1))

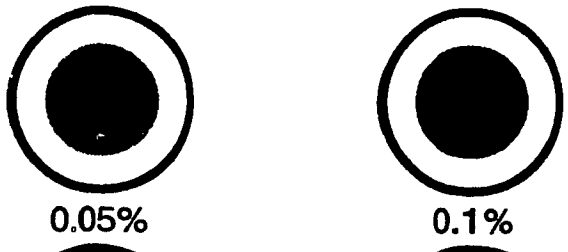

Figure 3.6 Scanned images of TiO_2 particle filtrates (on MSI Nylon filters); upper section: TiO_2 doped with rhenium(III, VII and 1:1 mix of III, VII); lower section: TiO_2 doped with: a 1:1 mixture of chromium(III) and iron(III), nickel(II), tungsten(VI), molybdenum(VI), cerium(III), cobalt(II), neodynium(III), yttrium(III) and titanium(III).

TiO_2 / 1% Re

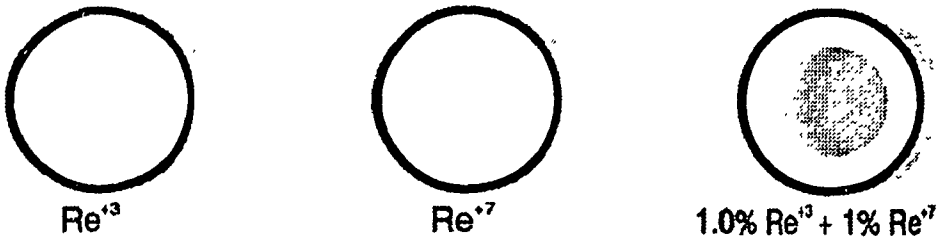

TiO_2 / 1% M

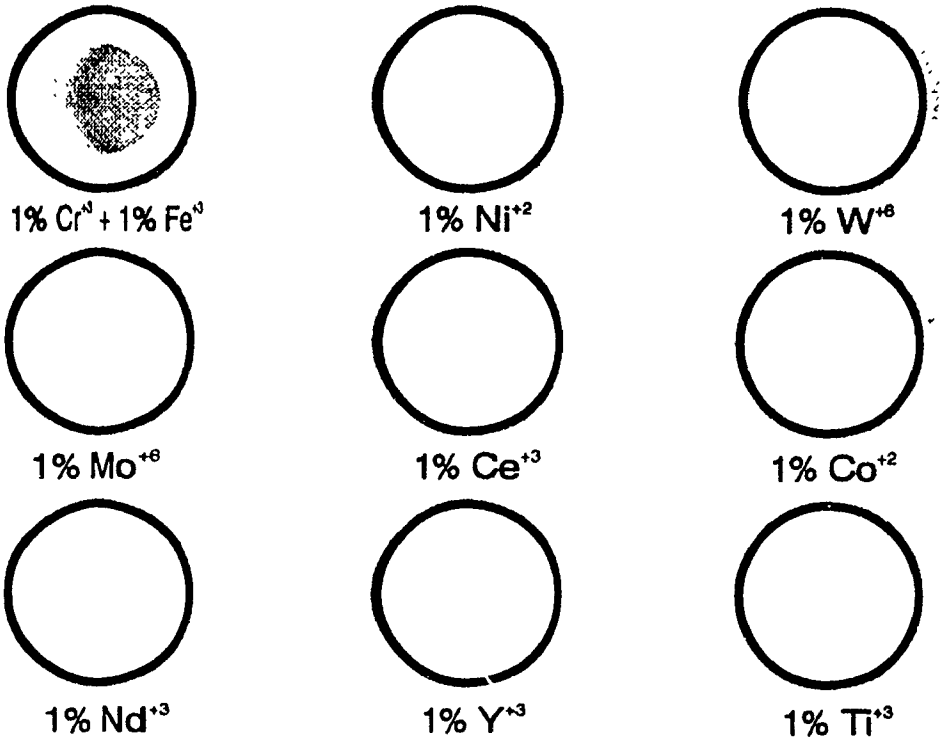

Table 3.2 Colour of Doped and Undoped TiO_2 Particles*

Dopant	Dopant Concentration (wt. % TiO_2)	Colour of Material
-	-	opal white
Cr	0.1	oyster green
	0.5	arizona sand green
	1.0	arizona sand green
	3.0	absinthe green
	5.0	absinthe green
	10.0	spruce green
	20.0	spruce green
V^{+5}	0.1	honey cream beige
	0.5	chamoline
	1.0	colonial gold
	3.0	spice gold
	5.0	bronze brown
	10.0	bronze brown
V^{+3}	1.0	beige
$V^{+5} + V^{+3}$ (1:1)	1.0	cinnamon sand
Fe	0.1	celery heart
	0.5	celery heart
	1.0	yellow reed
	5.0	jonquil yellow
	10.0	jasmine yellow
Rh	0.1	custard
	0.5	corn husk orange
	1.0	mellow orange
	3.0	hearthside
	5.0	nishi orange
	10.0	sunset brick
Ru	0.05	beige

Ru	0.1	cinnamon sand
	0.3	creamy coffee
	0.5	bronze brown
	1.0	durango tan
	5.0	chocolate brown
	10.0	moka java
Pt	0.05	yellow reed
	0.1	sunlight
	0.5	spring yellow
	1.0	yellow
Ru + Pt (1:1)	0.05	beige
	0.1	cinnamon sand
	0.5	durango tan
	1.0	chocolate
Pd	1.0	light sphinx brown
	10.0	brass button
Cu	1.0	arizona sand
	10.0	tropic turquoise
Mn	1.0	dirty white
	10.0	canary yellow
Cr + Fe (1:1)	1.0	willow gold
Ni	1.0	dirty white
W	1.0	dirty white
Mo	1.0	light pale grey
Ce	1.0	yellow reed
Co	1.0	beige
Nd	1.0	dirty white
Y	1.0	dirty white
Ti[a]	1.0	white

[a] colour names as matched to *Color Your World* paint cards.

3.3 PARTICLE SIZE OF TiO_2 AND TRANSITION METAL DOPED TiO_2 COLLOIDAL SOLS

3.3.1 Particle Size

The average particle diameter of the colloids was determined by the dynamic light scattering technique. This method, which is based on the theories of Rayleigh-Gans and Mie[1], measures the statistical fluctuation of laser light intensity at a particular angle in a small volume of the colloidal sol. The slope of the autocorrelation function gives an estimate of the average displacement velocity resulting from the Brownian motion of the spherical particles that diffuse the light. The Einstein and Stokes-Einstein relationships are used to calculate average diffusion coefficients (D_p) and hydrodynamic radii of the colloidal particles (see equation 3.1):

$$D_p = \frac{kT}{6\pi\eta r} \tag{3.1}$$

where, **k** is the Boltzmann constant, **T** is the temperature in degrees Kelvin, **r** is the radius of the moving sphere, and η the viscosity of the medium. A statistical distribution of the particle size of the polydispersed sol can also be obtained using a multichannel autocorrelator and the appropriate algorithms.

Table 3.3 lists the mean particle diameter as determined from a statistical analysis (see chapter 2) of the light scattering data for the various colloids. A fit a normal Gaussian distribution to the data gave identical results. Figures 3.7 and 3.8 are

representative particle size distribution plots for the undoped (various sizes) and doped TiO_2 samples. Figures 3.7a and 3.7b are in good agreement with size distributions previously presented in the literature.[10,11] Both Figures 3.7 and 3.8 indicate that the particles are monodisperse, with a narrow size distribution which is Gaussian in nature. The choice of dopant does not appear to greatly affect the size distributions obtained as shown by the histograms obtained for TiO_2 doped with 10 wt.% iron (Figure 3.8a), 1 wt.% rhodium (Figure 3.8b) and 0.1 wt.% platinum (Figure 3.8c). Particle size distributions for other doped TiO_2 systems showed the same type of behaviour and are presented in Appendix A.

3.3.2 Effect of Dopant on Particle Size

The size of a colloid may be controlled effectively by judicious selection of such reaction conditions as reaction temperature, reaction time, reagent concentration, media, etc.[12,13] The stability, i.e the ability of the colloid to remain suspended in an energetically metastable state for an arbitrary length of time,[14] will be dependent on the surface charge of the colloid, the concentration of the colloid, the ionic strength of the medium and the pH.[15] However, a question which remains a mystery is why a particle grows to a given size and then its growth is arrested. In this sense, the synthesis of colloids has remained somewhat of an art; procedures are followed and modified to meet specific needs.

Table 3.3 Particle Diameter of Doped and Undoped TiO_2 Particles as Determined from Light Scattering Measurements.

Dopant	Dopant Concentration (wt % TiO_2)	Particle Size (nm)
-	-	13.3 ± 1.2
Cr	0.1	5.3 ±0.5
	0.5	6.0 ± 0.5
	1.0	6.0 ± 0.6
	3.0	6.0 ± 0.6
	5.0	8.5 ± 0.3
	10.0	22.1 ± 2.3
	20.0	47.0 ± 2.7
V	0.1	7.8 ± 0.2
	0.5	5.8 ± 0.4
	1.0	2.1 ± 0.2
	3.0	6.6 ± 0.2
	5.0	14.0 ± 0.4
	10.0	10.1 ± 0.7
Fe	0.1	9.1 ± 0.5
	0.5	4.4 ± 0.2
	1.0	4.1 ± 0.1
	5.0	5.3 ± 0.1
	10.0	5.8 ± 0.2
Rh	0.1	8.4 ± 0.4
	0.5	7.0 ± 0.3
	1.0	4.2 ± 0.1
	3.0	8.8 ± 0.4
	5.0	5.0 ± 0.5

Rh	10.0	5.0 ± 0.5
Ru	0.05	3.2 ± 0.2
	0.1	4.5 ± 0.1
	0.3	3.4 ± 0.1
	0.5	6.4 ± 0.4
	1.0	8.3 ± 0.8
	5.0	11.5 ± 0.8
Pt	0.05	6.5 ± 0.5
	0.1	5.7 ± 0.4
	.5	6.5 ± 0.5
	1.0	6.9 ± 0.5
Ru + Pt (1:1)	0.05	3.8 ± 0.2
	0.1	4.0 ± 0.4
	0.5	6.1 ± 0.2
	1.0	5.5 ± 0.4
Pd	1.0	4.7 ± 0.3
	10.0	10.3 ± 0.5
Cu	1.0	5.5 ± 0.4
Mn	1.0	21.9 ± 2.8
Cr + Fe (1:1)	1.0	15.9 ± 2.1
Ni	1.0	12.0 ± 0.5
W	1.0	15.9 ± 2.1
Mo	1.0	21.0 ± 1.5
Ce	1.0	12.1 ± 0.6
Co	1.0	11.8 ± 0.5
Ti^{+3}	1.0	16.8 ± 1.2

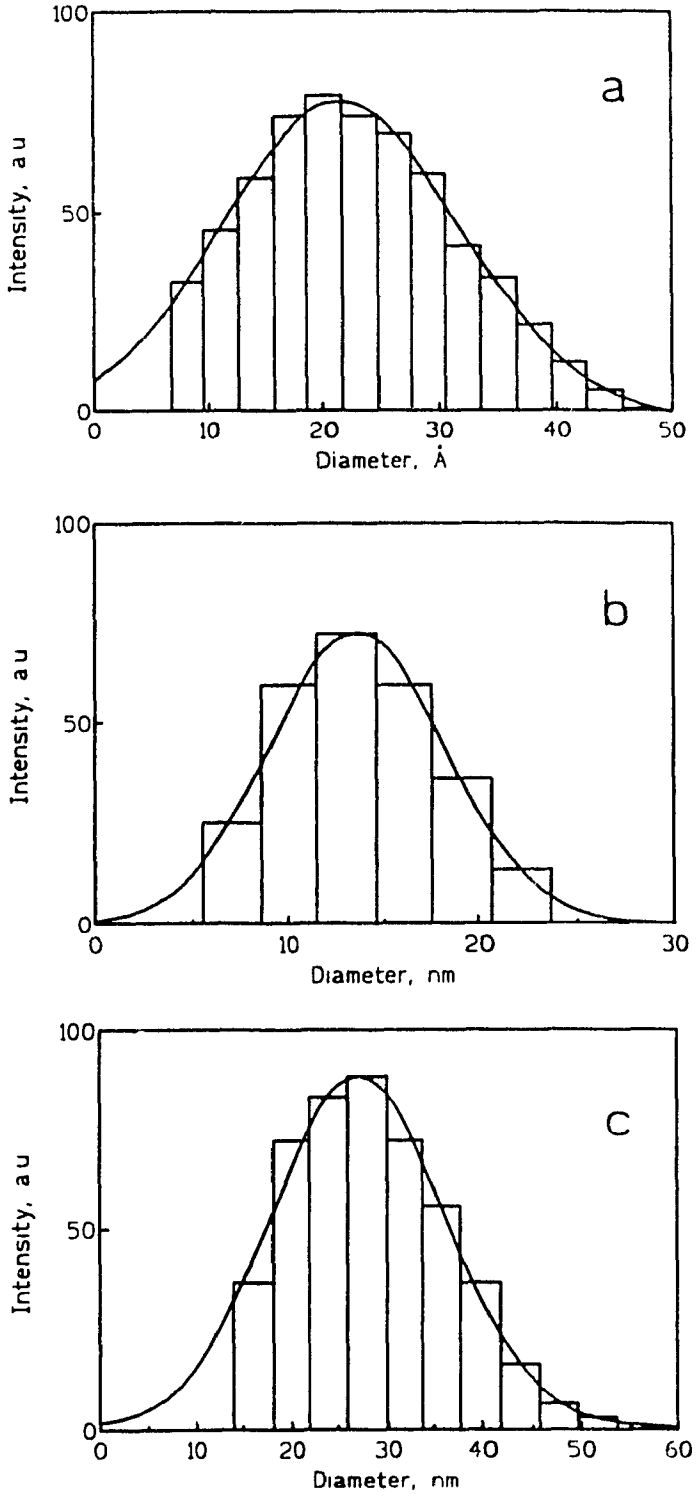

Figure 3.7 Particle size distribution of 0.3 g/L (a) small (23 Å) TiO_2, (b) regular (133 Å) TiO_2 and (c) large (281 Å) TiO_2.

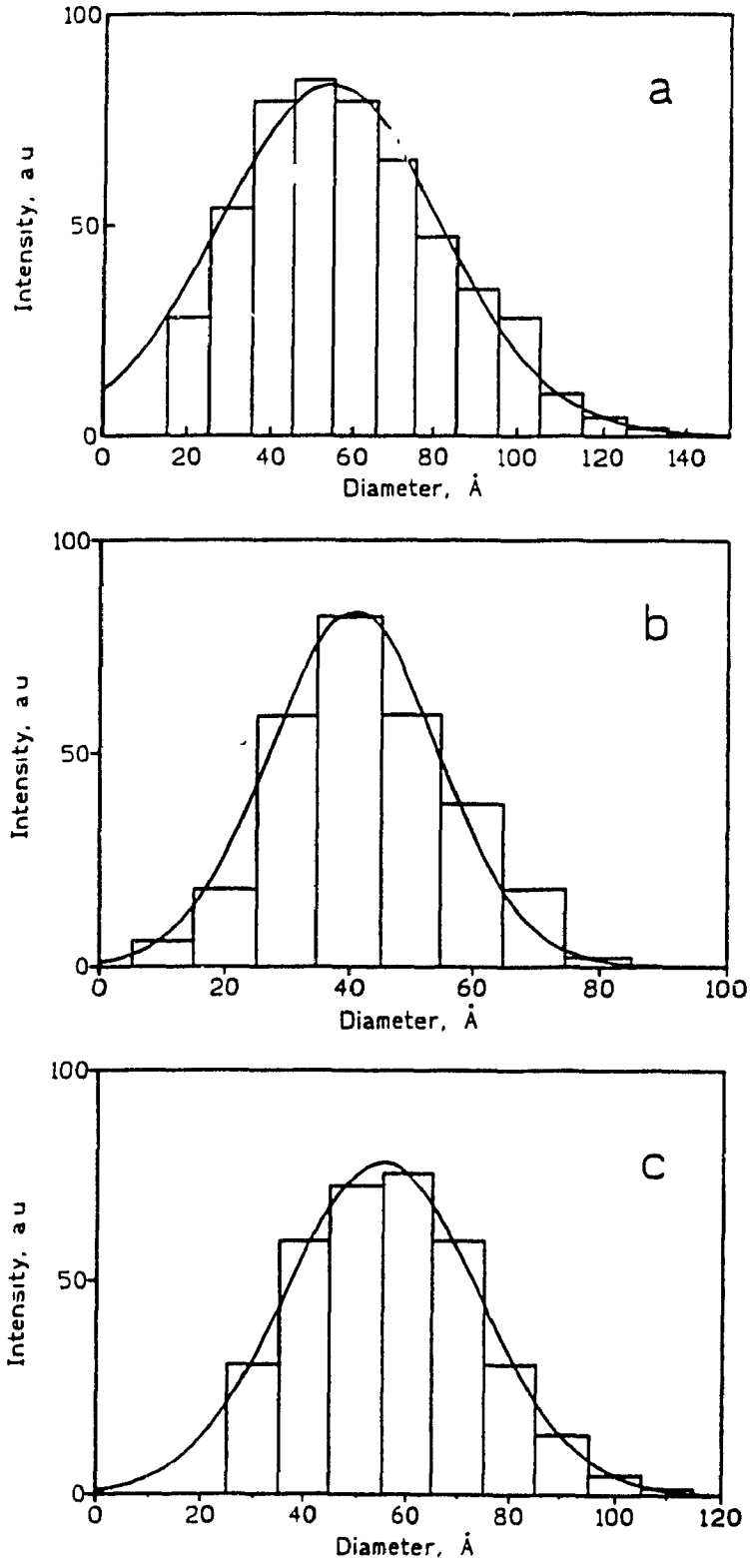

Figure 3.8 Particle size distribution of 0.3 g/L TiO_2 doped with (a) 10 wt.% Fe, (b) 1 wt.% Rh and (c) 0.1 wt.% Pt.

The effect of addition of the various dopants on the particle size of the TiO_2 colloids is illustrated in Figures 3.9 and 3.10. In general, addition of the dopants tends to reduce the size of the TiO_2 colloids. The effect of the dopant may be rationalized in the following manner. Titanium dioxide colloids form as the result of the forced hydrolysis of $TiCl_4$, as shown in equation 3.2:

$$TiCl_4 + 2H_2O \rightarrow TiO_2 + 4H^+ + 4Cl^- \qquad (3.2)$$

The size of the colloid will depend on the effective rate of diffusion of smaller $(TiO_2)_n$ clusters to form a larger particle $(TiO_2)_N$ (equation 3.3) and on factors affecting Ostwald ripening.

$$(TiO_2)_N + (TiO_2)_n \rightarrow (TiO_2)_{N+n} \qquad (3.3)$$

The diffusion through the medium may be controlled by changing the viscosity of the medium, which is best realized by controlling the reaction temperature. Thus, smaller crystallites form in reactions carried out at lower temperatures.[13,16] Most likely the lower temperature reduces the rate of Ostwald ripening processes. Hence, if the titanium is added at a low enough temperatures smaller particles should result. Similarly, if the temperature of the water medium to which the $TiCl_4$ is added is raised, the rate of Ostwald ripening processes should increase with the result that larger particles should form. This is exactly what is observed and is shown in Table 2.1 (chapter 2). The same argument can be extended to systems in which the transition metal ion dopant is present. To incorporate a dopant into the lattice of TiO_2 will also be expected to affect Ostwald

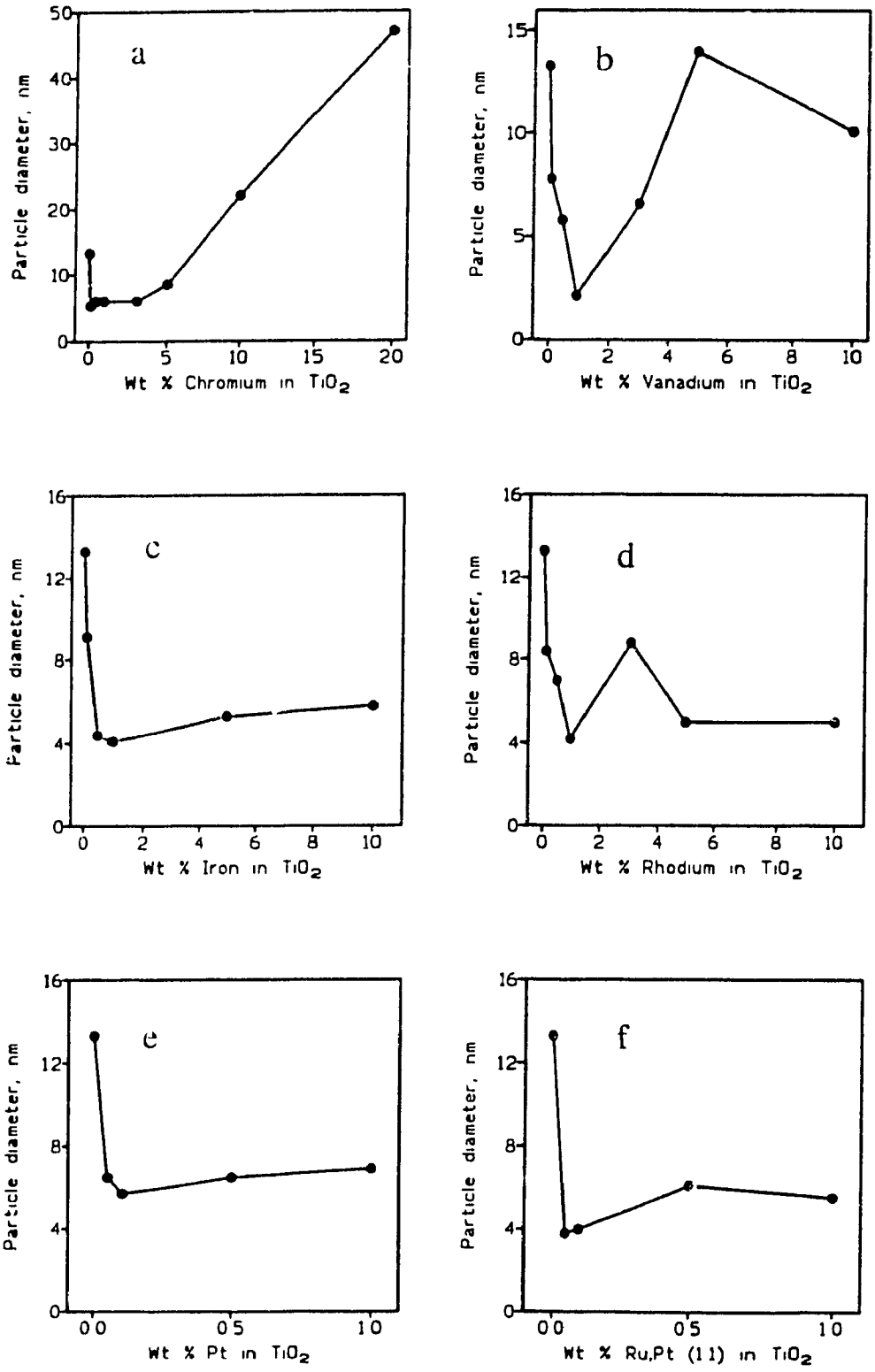

Figure 3.9 Effect of dopant concentration on particle size as determined by dynamic light scattering; TiO_2 doped with (a) chromium, (b) vanadium, (c) iron, (d) rhodium, (e) platinum, (f) ruthenium and platinum (1:1)

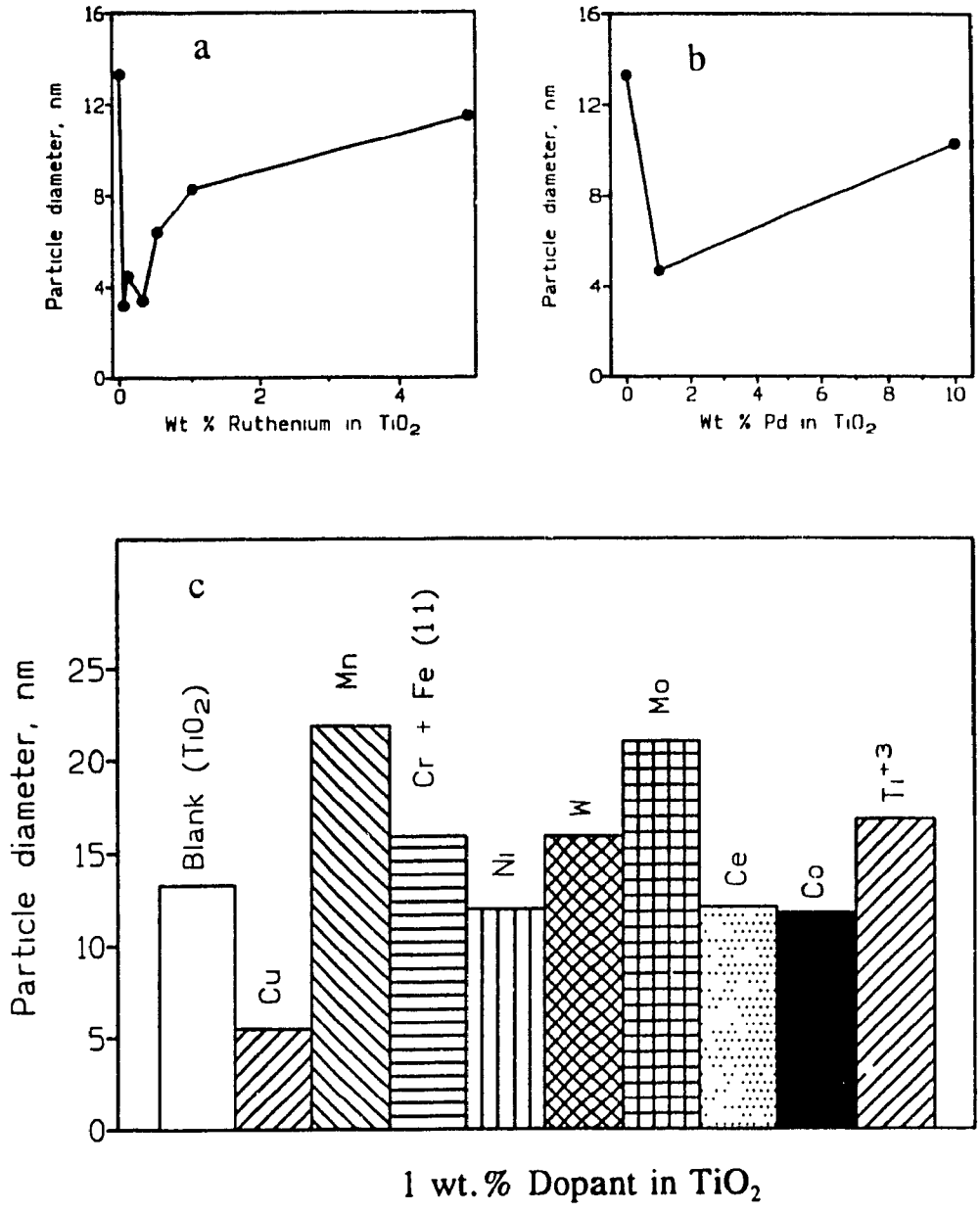

Figure 3.10 Effect of dopant concentration on particle size as determined by dynamic light scattering; TiO_2 doped with (a) ruthenium, (b) palladium, (c) 1 wt.% of: copper, manganese, chromium and iron (1:1), nickel, tungsten, molybdenum, cerium, cobalt, titanium (III). TiO_2 blank included for comparison.

ripening processes. Addition of the dopant in solution must slow the rate of growth; the particles formed will therefore be smaller. In the case of chromium (Figure 3.9a), addition of more than 5 wt.% chromium to the lattice caused a sharp linear increase in the size of the particles. This probably arises from the increased ionic strength of the medium (from the increase in the number of chromium ions in solution) which screens electrostatic repulsion and thereby allows the particles to grow to a larger size. A similar trend is observed in the cases where TiO_2 is doped with vanadium (Figure 3.9b), ruthenium (Figure 3.10a), palladium (Figure 3.10b) and, to a lesser extent, iron (Figure 3.9c). Several of the transition metal dopants, such as nickel, tungsten, cobalt and cerium (Figure 3.10c) do not appear to affect significantly the size of the TiO_2 colloid, which suggests that these transition metals are easier to incorporate into the lattice of TiO_2 than may be other metals such as chromium and vanadium.

3.4 TRANSMISSION ELECTRON MICROSCOPY

The morphology and particle size of the materials was also examined using transmission electron microscopy (T.E.M.). Figure 3.11 is a representative T.E.M. photograph of undoped TiO_2; the inset displays an enlargement of one section of the photograph. The particles were nearly spherical and polydispersed. An analysis of the particle size distributions from several T.E.M. photographs indicated that the average static particle diameter was 84 $\pm$ 28 Å, in reasonably good agreement with the hydrodynamic radius determined from light scattering experiments (133 $\pm$ 12 Å). Figure 3.12 illustrates typical T.E.M. photographs obtained for the metal doped TiO_2 systems.

Figure 3.12a is a representative photograph of TiO_2 doped with 0.5% percent iron (wt.% TiO_2) in the bulk, whereas Figure 3.12b is TiO_2 doped in the bulk with 5 wt.% iron. A tenfold increase in the concentration of iron added to the TiO_2 showed no changes in the morphology of the particles. In both cases, the particles remained spherical in nature and polydispersed having a narrow particle size distribution. An analysis of several T.E.M. photographs of TiO_2/0.5 wt% Fe indicated an average static particle diameter of 53 $\pm$ 21 Å, in excellent agreement with the average hydrodynamic particle diameter of 44 $\pm$ 2 Å obtained from dynamic light scattering. Of particular interest and importance is that the photographs (additional representative T.E.M. photographs of a number of different TiO_2 systems are presented in Appendix B) of the doped material show no evidence (i.e. ridges, shadows, etc.) that the material is anything other than TiO_2; i.e., there is no indication, even at high doping levels, of any metal deposition on the surface of the particles nor is there any evidence to suggest that the metal co-exists with the TiO_2 (in such a case, two distinct types of particles would have been observed). This suggests that the metal dopant is either at some interstitial location or has substituted at a lattice position for Ti^{+3}.

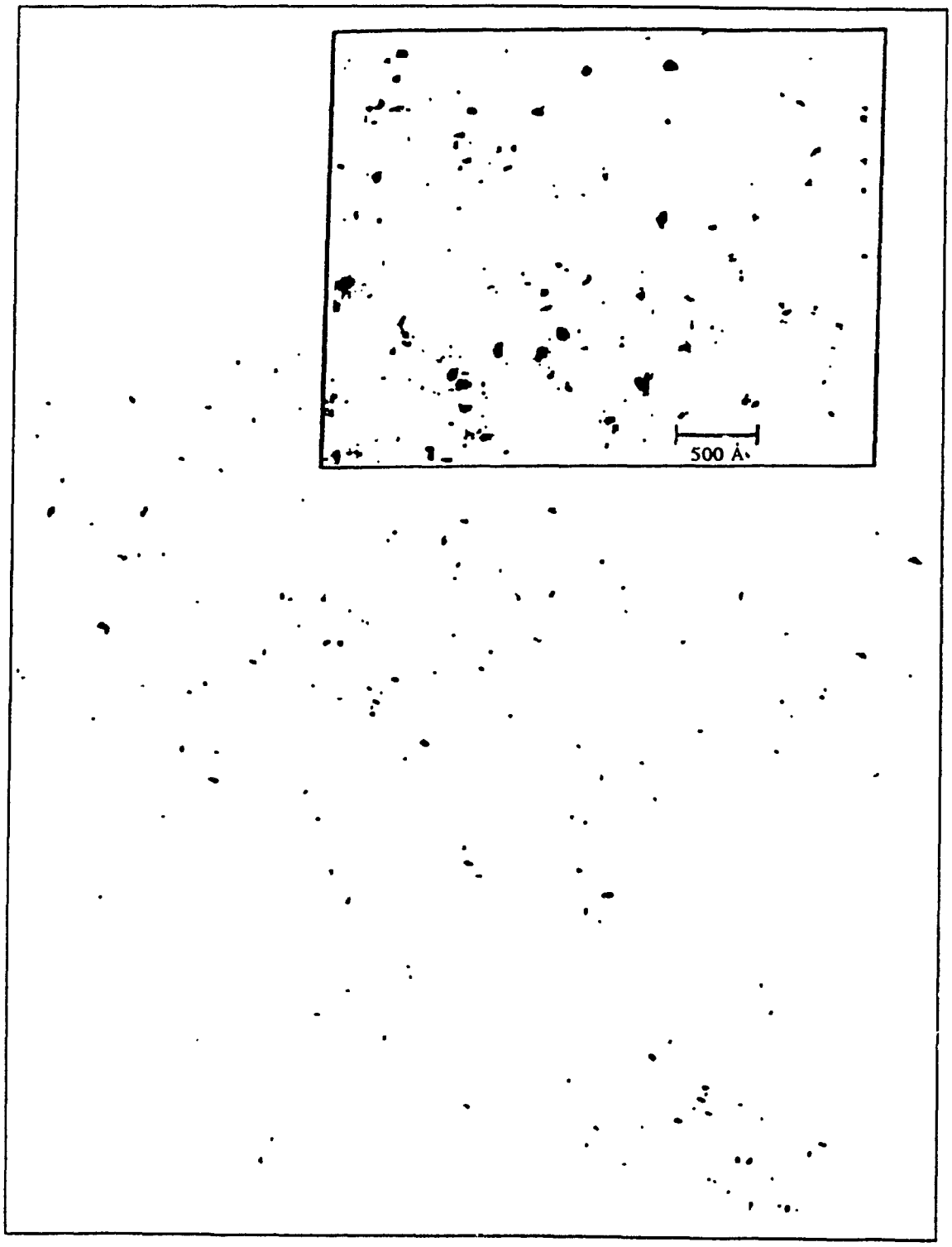

Figure 3.11 T.E.M. photograph of a representative sample of TiO_2 determined using a Philips EM 420 at a magnification of 120 000. Inset is an enlargement of a small portion of the photograph.

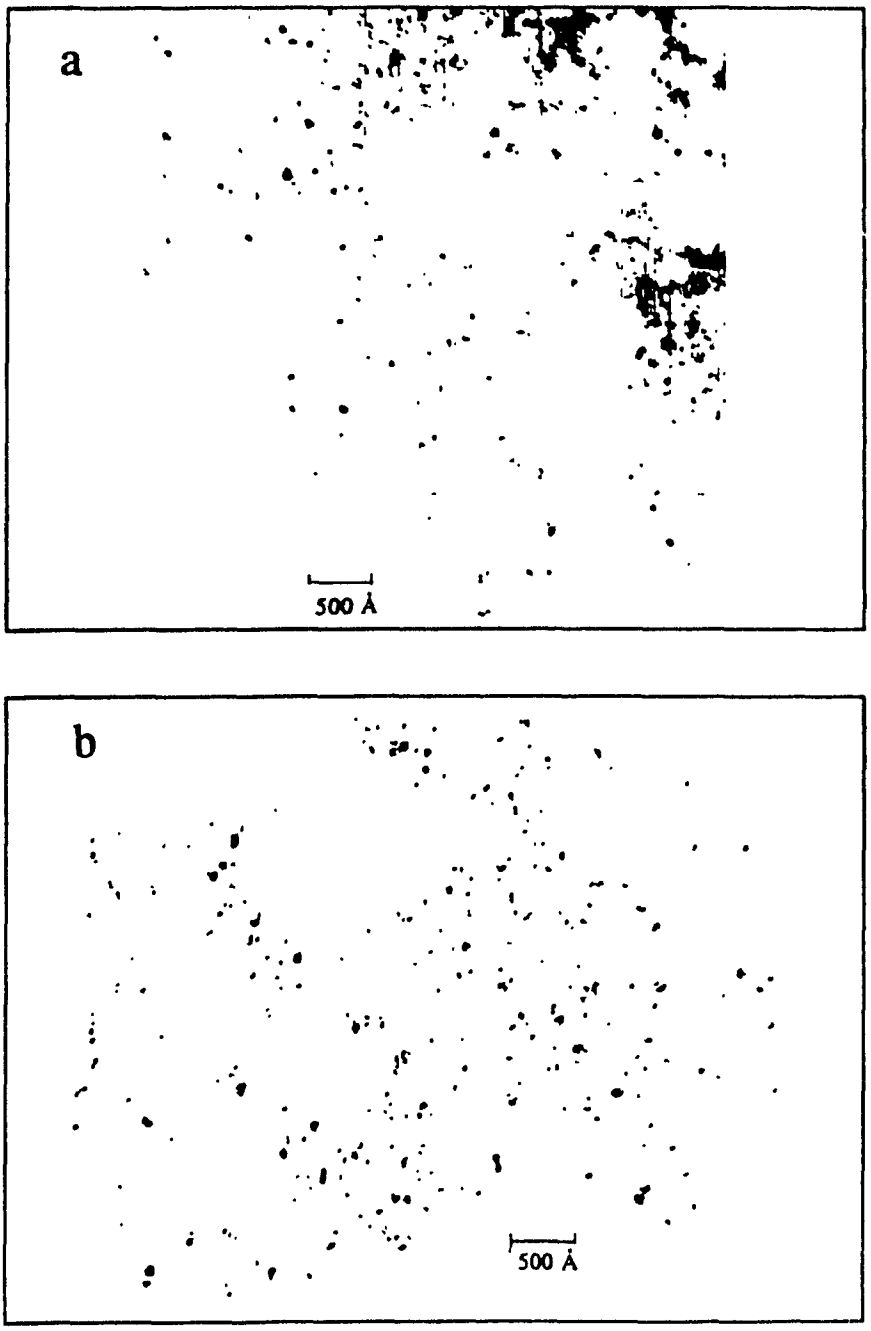

Figure 3.12 T.E.M. photographs of representative samples of TiO_2 doped with iron (III) determined using a Philips EM 420 at a magnification of 105 000; (a) 0.5% Fe (wt/wt% TiO_2), (b) 5% Fe (wt/wt% TiO_2).

3.5 ELECTRON AND X-RAY DIFFRACTION STUDIES

3.5.1 Electron Diffraction Studies

Electron diffraction patterns of both the doped and undoped TiO_2 samples were taken in order to elucidate the crystal structure of the material. Tables 3.4 and 3.5 are tabulations of the d values calculated from the electron diffraction patterns (values for pure TiO_2 anatase are shown in brackets in Table 3.4) for both naked TiO_2 and TiO_2 doped with 20 wt.% chromium. For the undoped TiO_2, both the x-ray and electron diffraction patterns unambiguously indicate that the only crystalline phase present is anatase. The electron diffraction data for the chromium-doped TiO_2 show several characteristic peaks of anatase TiO_2, yet also show several peaks not attributable to this structure. These extraneous peaks could arise from the presence of another phase present within the TiO_2 matrix. Other data indicate that only the anatase phase is present. The strongest support for this assertion comes from the x-ray diffraction pattern (see below) which shows some hints of amorphicity. The absorption and reflectance spectra (see chapter 5) of the colloid are also indicative of an anatase structure (comparison of the band edge absorption of this material to that of naked TiO_2). The photograph used to resolve the structure may not have been representative of the material or perhaps it was too poorly resolved to determine accurately the distance between the points used to calculate the d values. The possible formation of an entirely new material is not precluded by the above discussion.

Table 3.4 Electron Diffraction Values for TiO_2

R measured (mm)	d, Å
7.550	3.550 (3.520)
9.250	2.900 (missing in TiO_2 anatase)
11.200	2.390 (2.378)
13.990	1.890 (1.890)
15.700	1.690 (1.700)
18.100	1.480 (1.481)
19.100	1.370 (1.364)
20.900	1.260 (1.265)

N.B. numbers in brackets are the d values for pure TiO_2 anatase.[17]

Table 3.5 Electron Diffraction Values for TiO_2/20 wt.% Cr

R measured (mm)	d, Å
6.71	3.554
8.2	2.908
9.2	2.592
10.11	2.359
12.21	1.953
14.32	1.665
15.00	1.590

3.5.2 X-Ray Diffraction Studies of TiO_2 and Metal Doped TiO_2

3.5.2.1 X-Ray Diffraction Patterns

The powder x-ray diffraction patterns of TiO_2 and a number of the transition metal doped materials were taken to elucidate the structure of the solid and to determine whether any other phases or surface deposited metals were present in the material. This was determined by comparing the d spaces, calculated from the observed diffraction peaks and using Bragg's law as shown in equation 3.4, to known literature values.

$$d = \frac{\lambda}{2 \sin\theta} \qquad (3.4)$$

The three strongest observed d spaces for anatase TiO_2 are (relative intensity in brackets) 3.51 (100), 1.89 (33) and 2.38 (22).[17] Similarly, the three most intense diffraction lines observed for rutile TiO_2 are 3.25 (100), 1.69 (50) and 2.49 (41).[17]

The x-ray diffraction pattern obtained for Degussa P25 TiO_2 is shown in Figure 3.13. A number of diffraction peaks are observable and are in excellent agreement with those peaks expected for a mixture of anatase and rutile TiO_2. The peaks are sharp and intense which suggest that the material is predominantly crystalline. From the ratio of the two strongest peaks for anatase (d=3.51) and rutile (d=3.24) TiO_2, the sample is calculated to be made up of ~ 80% anatase and ~ 20% rutile, in agreement with previously reported values.[1]

The x-ray diffraction obtained for the homemade TiO_2 sample is given in Figure 3.14. The peaks are weak and very broad. This suggests that the material has a large

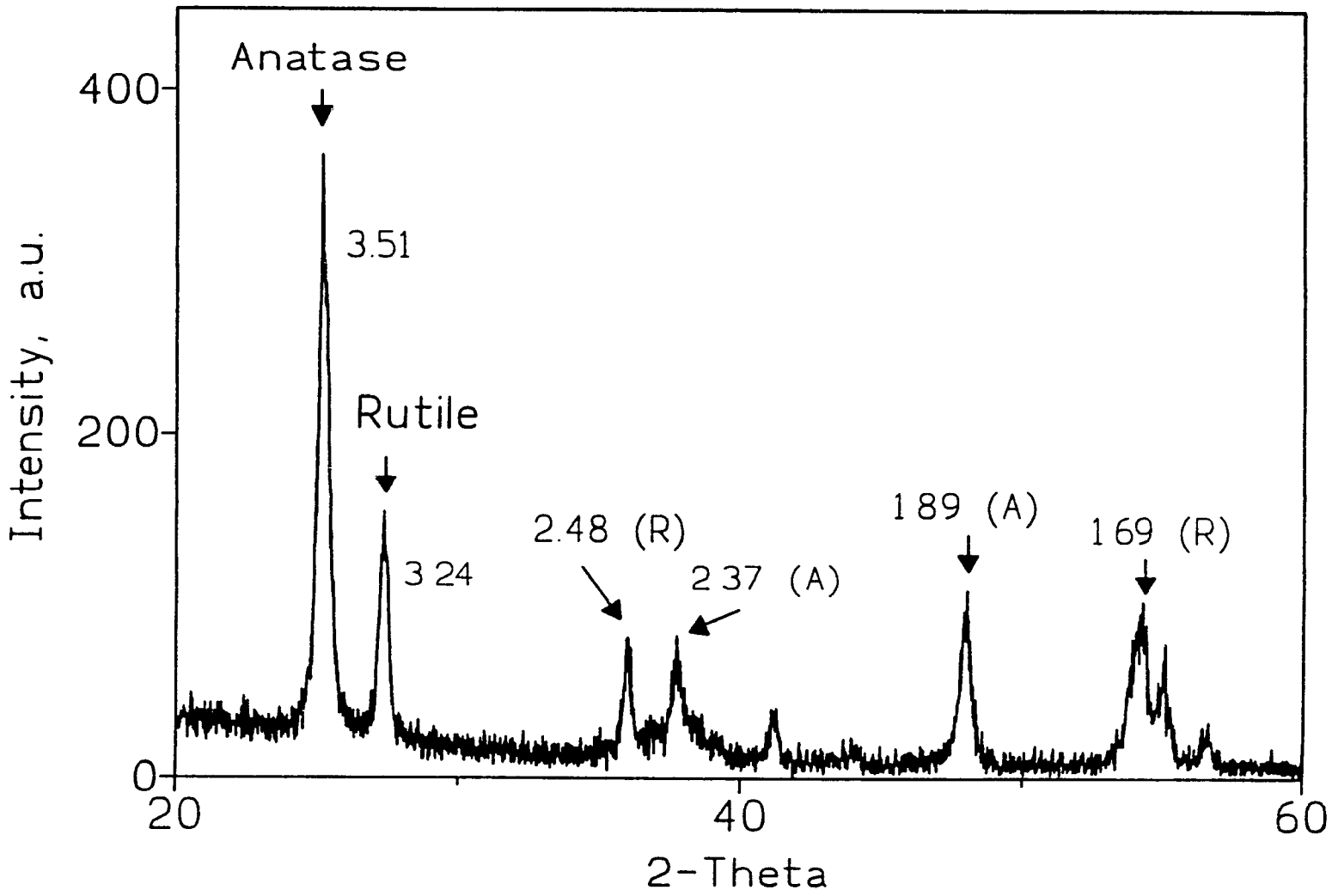

Figure 3.13 X-ray diffraction pattern of Degussa P25 TiO_2. Numbers correspond to calculated d spaces (see text) and assignment to either anatase (A) or rutile (R) phase.

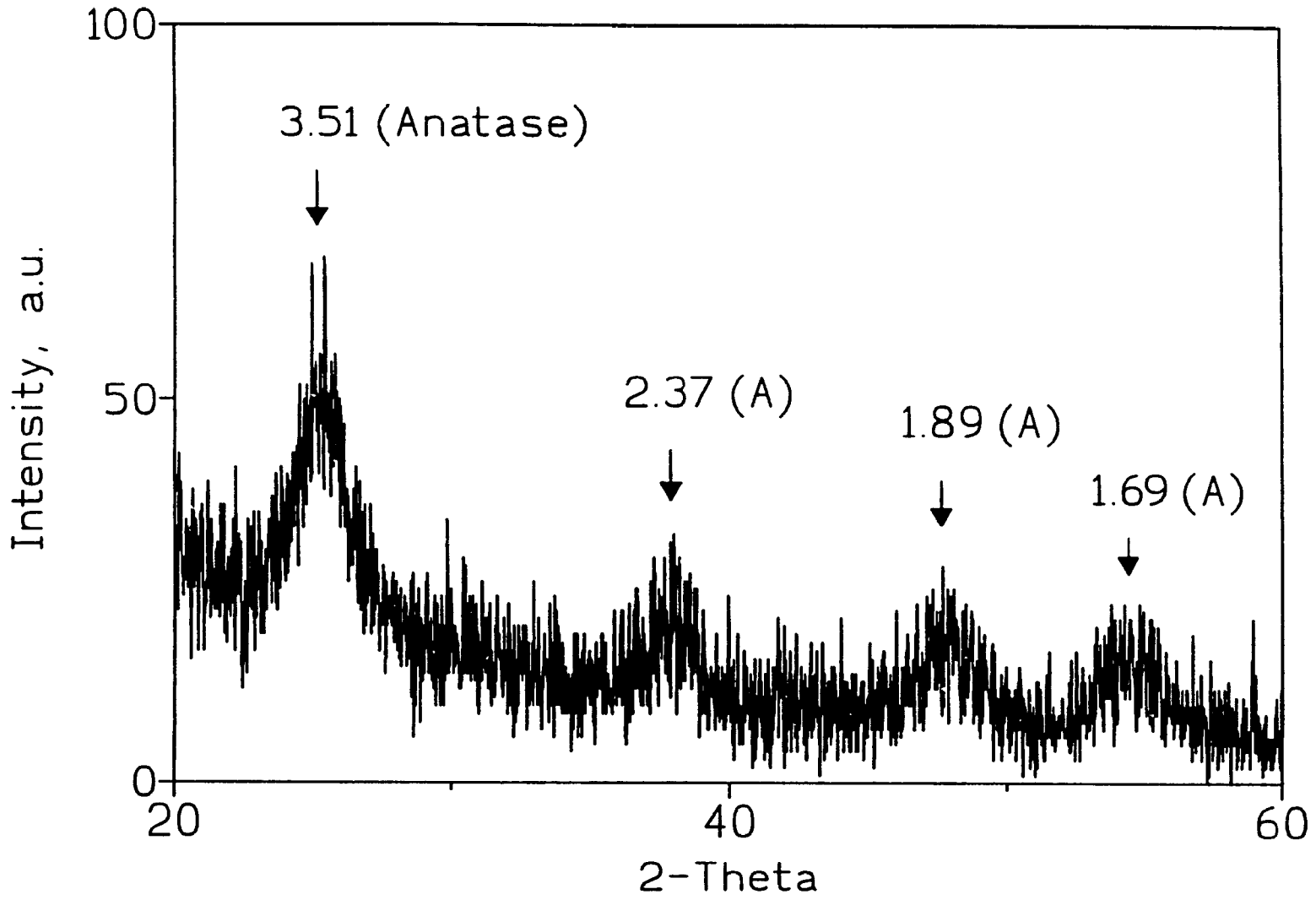

Figure 3.14 X-ray diffraction pattern of homemade TiO_2. Numbers correspond to calculated d spaces (see text). The peaks are those of anatase (A) TiO_2.

amorphous component. However, the peaks which are observable are those of anatase TiO_2. The broadness of the peaks can be attributed, in some part, to a small particle size (see below).

Although it is tempting to compare the relative intensities and broadness of the diffracted peaks to a known sample such as Degussa TiO_2 P-25 and from such a comparison estimate the amount of anatase in the sample, the attempt would be erroneous. The relative intensity of the diffracted peak is related to six factors:[18]

1. polarization factor;
2. structure factor;
3. multiplicity factor;
4. Lorentz factor;
5. absorption factor;
6. temperature factor.

In addition, the intensity of the diffracted peaks will be dependent on the packing of the material, which will vary from sample to sample. A means of quantifying the amount of anatase was to add a standard (e.g. pure NaCl) with no diffraction peaks in the area of interest to each sample. However, this was not done in order to allow the maximum possibility of detecting additional phases and/or metallic islands at the surface of the material to be detected without interference from the standard. From the observed intensities, and given that (as a rule of thumb) for a pattern to be detectable the sample must constitute at least 5% crystalline material,[19] it is concluded that the sample probably consists of between 5% to 20-25% anatase, with the remainder being amorphous.

The x-ray diffraction pattern of the highest doped TiO_2 specimen (TiO_2/20 wt.%

Cr) is shown in Figure 3.15. The pattern is very similar to that obtained for naked TiO_2 and is indicative that the only crystalline phase present is that of anatase TiO_2. The sample is also highly amorphous. The inset of the figure shows a diffraction pattern run on chromium(III) oxide, Cr_2O_3. The three strongest d spaces for Cr_2O_3 (relative intensities in brackets) are 2.67 (100), 2.48 (96) and 1.67 (90).[17] As can be seen from Figure 3.15, these lines are absent in TiO_2/20% Cr. The d spaces for chromium metal {2.04 (100), 1.18(29) and 0.91 (21)} were also absent. This suggests that the chromium is not at the surface nor does it form a detectable Cr_2O_3 phase in the bulk of the material unless the crystal size of this phase is so small as to be undetected by x-ray diffraction (XRD). It is tentatively suggested that the chromium is interstitially located or occupies a titanium location in the lattice.

A close inspection of a number of other metal-doped TiO_2 systems (see Appendix C) also indicated that the only detectable crystalline phase is that of anatase. There were no indications that metal particles formed at the surface of the material.

3.5.2.2 Particle Size Determination from X-ray Patterns

An estimate of the average particle diameter of a crystallite may be made from the line broadening of an x-ray diffraction peak. Assuming that the broadening is attributable solely to crystallite size, the particle diameter can be estimated by Scherrer's equation[20,21] (equation 3.5):

$$L = \frac{K \lambda}{\beta \cos\theta} \qquad (3.5)$$

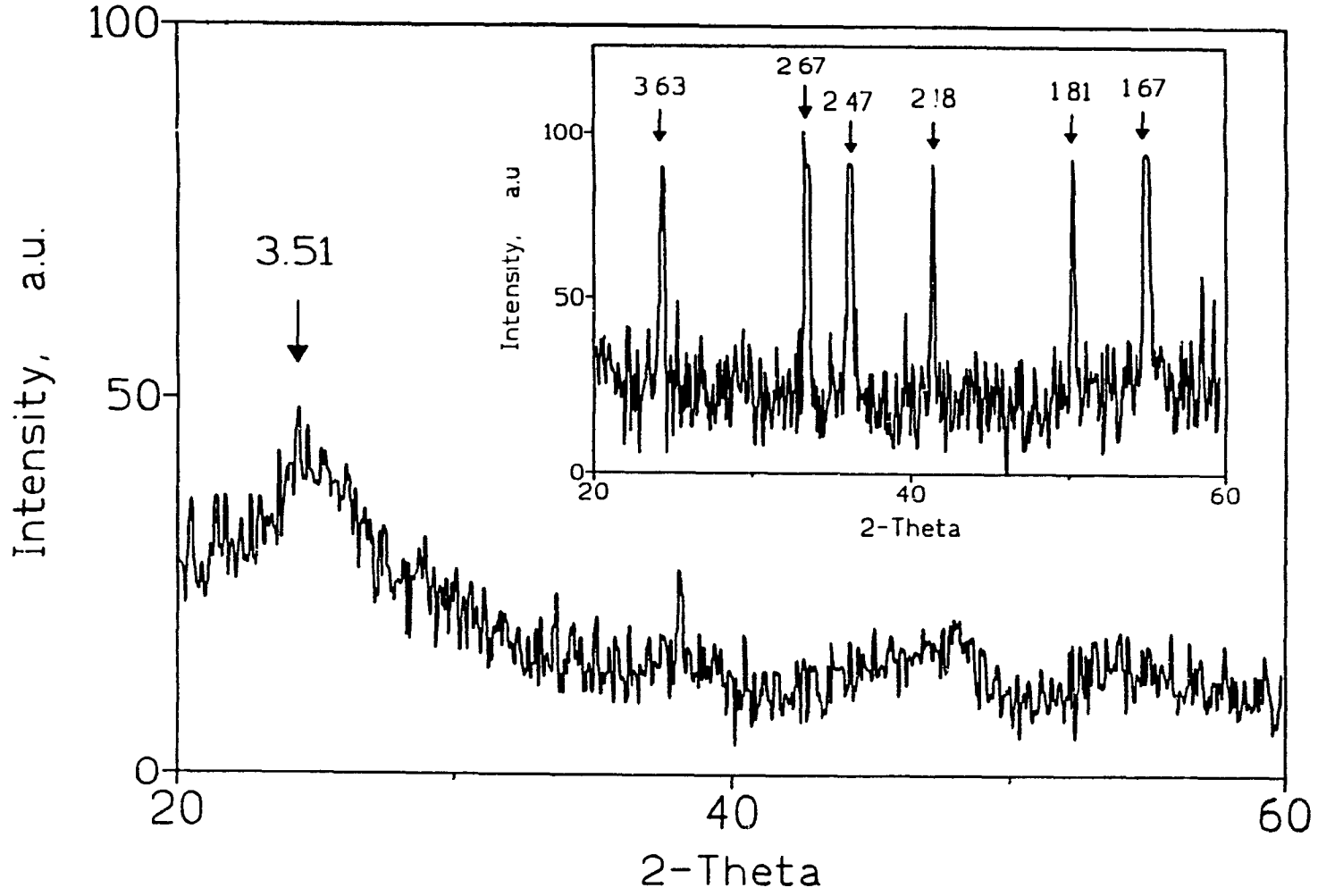

Figure 3.15 X-ray diffraction pattern of TiO_2 doped with 20 wt. % chromium. The pattern is that of anatase TiO_2. The inset shows an x-ray diffraction pattern of Cr_2O_3 with the major d spaces identified. Note that none of these peaks are observable in the pattern obtained for TiO_2/20 wt. % Cr.

where **L** is the particle diameter in the same units as the wavelength λ, **K** is a constant (system dependent), **Θ** is the Bragg angle and β is the breadth of the peak, which is the width at half of the peak intensity and is in 2Θ units (in radians). For semiconductor diffraction patterns, the K value is usually taken to be 1.[22]

Table 3.6 lists the average particle diameter calculated, using Scherrer's equation, from the broad anatase peak (d=3.51) observable in the various TiO_2 systems examined. The values obtained from dynamic light scattering are included for comparison. The values obtained for several of the metal-doped systems are in reasonably good agreement with the particle diameters obtained using dynamic light scattering. It must be noted here that while light scattering aspects of aggregates, the XRD technique reflects crystalline size. As well, the weak broad diffraction peaks and the poor signal-to-noise ratio can easily cause a 10-20% error in the measurement of β. Scherrer's equation also makes the assumption[18,19,21] that the crystals are ideal, i.e. free of imperfections, distortions and lattice strains. This is probably not the case; in fact, the colloidal materials prepared would be expected to have a large number of lattice defects.[23] The effect of strain on the lattice by the rutile phase is readily apparent from the diameter (177 Å) calculated for P25 Degussa TiO_2 which compares to the reported particle diameter of 300 Å.[24] However, despite the uncertainties, the particle diameters calculated from the diffraction patterns are within the same order of magnitude as those obtained from dynamic light scattering and from transmission electron microscopy.

Table 3.6 Particle Diameters calculated from X-ray Diffraction Patterns

Sample [a]	d calculated from x-ray diffraction pattern, Å	d calculated from dynamic light scattering, Å
P25 Degussa TiO_2	177	-
Homemade TiO_2	36	133
TiO_2/1% Cr	40	60
TiO_2/5% Cr	36	85
TiO_2/10% Cr	36	221
TiO_2/20% Cr	36	470
TiO_2/1% V	36	21
TiO_2/10% V	36	101
TiO_2/1% Cu	36	55
TiO_2/10% Cu	36	-
TiO_2/1% Rh	36	42
TiO_2/10% Rh	36	50
TiO_2/1% Ru	33	83
TiO_2/1% Fe	36	41
TiO_2/1% Pd	36	47
TiO_2/1% Mn	45	219
TiO_2/1% Co	39	118
TiO_2/1% Mo	40	210
TiO_2/1% Ni	45	120
TiO_2/1% Ce	43	121
TiO_2/1% Pt	45	69
TiO_2/(1% Pt, 1% Ru)	36	55
TiO_2/1% W	36	159
TiO_2/1% Ti^{+3}	36	168

[a] Percentages are given in wt.%.

3.5.2.3 Effect of Heat on the Crystal Structure of P25 Degussa TiO_2

The rutile form of TiO_2 is thermodynamically more stable than its anatase form.[25] At room temperature, conversion does not occur. Upon heating to temperatures above 500 °C,[25] anatase is converted to rutile (free energy change for anatase to rutile is ~ 5.4 kJ mol^{-1} [26]), although the rate of conversion depends on such factors as morphology, impurities present,[27] atmosphere,[28] and temperature.

Figure 3.16 illustrates the changes which occur in the x-ray diffraction pattern of P25 Degussa TiO_2 when the sample is heated from ambient temperature to 750 °C in air. As the temperature is increased, the anatase phase is converted to rutile and the peaks corresponding to $\underline{d}$ spaces for anatase decrease and concomitant with this decrease the $\underline{d}$ spaces corresponding to rutile increase. After heating at 750 °C for 24 hours, all the anatase is converted to rutile. Figure 3.17 illustrates that, under the conditions employed (24 hours heating, air atmosphere), the conversion of anatase to rutile in P25 Degussa TiO_2 is gradual and proceeds linearly with temperature. Extrapolation (dashed line) of the linear regression from the experimentally determined values to the 80% anatase concentration of P25 Degussa indicates that no conversion of anatase to rutile is expected to occur until a temperature of approximately 525 °C is reached, in good agreement with the predicted behaviour of anatase TiO_2.[25]

3.6 BET SURFACE MEASUREMENTS

The surface area of the heat-treated P25 Degussa TiO_2 specimens as well as homemade TiO_2 was determined using Brunauer, Emmett and Teller (BET) surface area

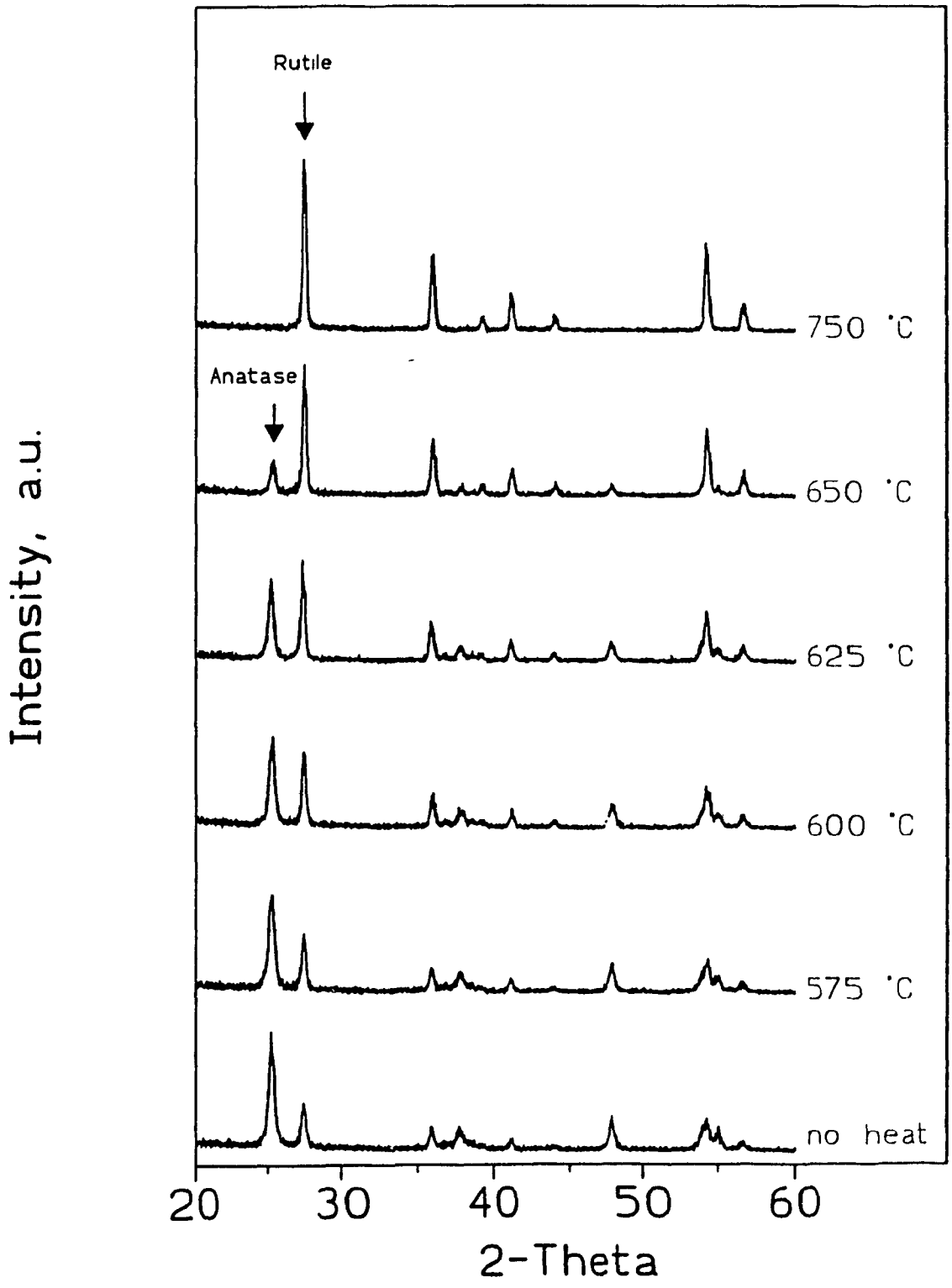

Figure 3.16 Changes in the x-ray diffraction pattern of P25 Degussa TiO_2 as a function of temperature. Samples were heated in air for 24 hrs at the temperature noted.

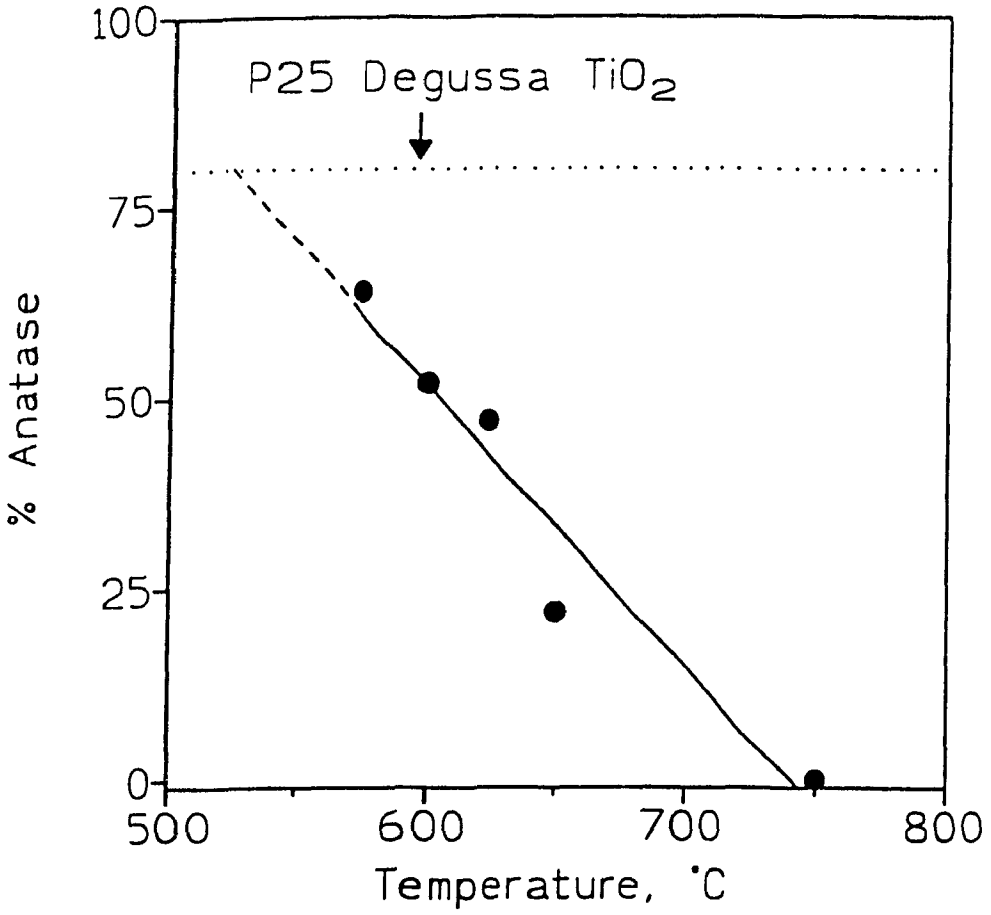

Figure 3.17 Change of anatase composition in P25 Degussa TiO_2 as a function of temperature.

measurements. This technique measures the surface area of powders by using the BET equation (equation 3.6)[29] to fit the adsorption density of, in this case, nitrogen, an inert gas, as a function of the partial pressure of nitrogen. The main limitations of the technique, as critiqued in a recent review,[8] is the failure of the method to provide information on the polydispersity of the material and on a poor correlation between BET area and catalytic activity. The technique does, however, give reproducible results on similarly prepared samples.

$$\frac{P/P_S}{V(1-P/P_S)} = \frac{1}{V_M\,C} + \left[\frac{(C-1)}{V_M\,C}\right]\frac{P}{P_S} \qquad (3.6)$$

where **V** is the volume (at standard temperature and pressure) of gas adsorbed at pressure **P**, $\mathbf{P_S}$ is the saturation pressure (the vapour pressure of liquified gas at the adsorbing temperature), $\mathbf{V_M}$ is the volume of gas required to form an adsorbed monomolecular layer, and **C** is a constant related to the energy of adsorption. Since **C** is a relatively large number **C-1** $\approx$ **C**.

Table 3.7 lists the surface areas determined for the various TiO_2 samples. The homemade and 20 wt.% chromium doped TiO_2 samples have much higher surface areas than does P25 Degussa TiO_2. This is consistent with these materials having a smaller diameter than that of P25 Degussa TiO_2 and is congruous with the particle size determined from dynamic light scattering, T.E.M. and x-ray diffraction measurements. Following BET analysis, the homemade TiO_2 was a light brown colour. An x-ray diffraction pattern of the material was taken following BET analysis; the pattern was identical to one recorded prior to BET analysis (see Figure 3.14). Heating the sample to 300 °C for 1 hr lightened the colour of the material but did not restore it to its initial colour. Similar observations were noticed for the TiO_2/20 wt.% Cr sample. No colour changes were observed for any of the P25 Degussa TiO_2 samples.

The surface area of P25 Degussa decreased linearly when specimens were exposed for 24 hrs in air to temperatures above 575 °C. Figure 3.18 illustrates that this decrease paralleled the decrease in anatase content; in both cases, extrapolation of the linear fits indicated that changes were only expected once the heat treatment exceeded 525 °C.

Table 3.7 Surface area of TiO_2 samples

Sample	Treatment	B.E.T. Surface area, m^2/g
P25 Degussa TiO_2	-	56.0
Homemade TiO_2	-	160.0
TiO_2/20% Cr	-	200.9
P25 Degussa TiO_2	575 °C, 24 hrs	47.4
P25 Degussa TiO_2	600 °C, 24 hrs	42.2
P25 Degussa TiO_2	625 °C, 24 hrs	36.1
P25 Degussa TiO_2	650 °C, 24 hrs	25.2
P25 Degussa TiO_2	750 °C, 24 hrs	11.5
P25 Degussa TiO_2	900 °C, 24 hrs	3.2

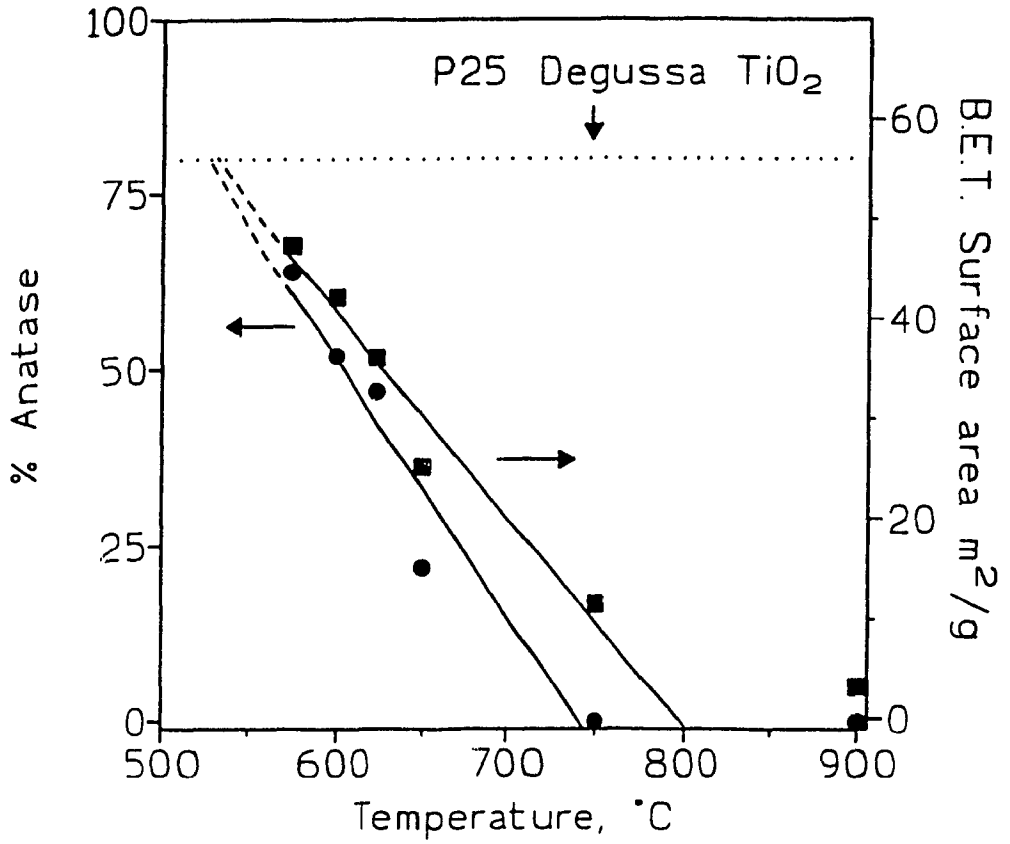

Figure 3.18 Effect of temperature on the percent of anatase and on the BET surface area of P25 Degussa TiO_2.

References

1. Sclafani, A., Palmisano, L. and Schiavello, M., *J. Phys. Chem.*, **1990**, 94, 829.

2. Sclafani, A., Palmisano, L. and Davi, E., *New J. Chem.*, **1990**, 14, 265.

3. *"Photoelectrochemistry, Photocatalyis and Photoreactors. Fundamentals and Developments."*, Schiavello, M., Ed., Reidel, Dordrecht, 1985.

4. Abrahams, J., Davidson, R.S. and Morrison, C.J., *J. Photochem.*, **1985**, 29, 353.

5. Ohtani, B, Handa, J., Nishimoto, S. and Kagiya, T., *Chem. Phys. Lett.*, **1985**, 120, 292.

6. (a) Terzian, R., PhD dissertation, Concordia University, Montreal, Quebec, **1993**.
(b) *"Photocatalysis and Environment-Trends and Applications"*, Schiavello, M. (Ed.), NATO ASI Series C237, Kluwer Academic, Dordrecht, The Netherlands, **1988**.
(c) Terzian, R., Serpone, N., Minero, C. and Pelizzetti, E., *J.Catal.*, **1991**, 128, 352.
(d) Al-Ekabi, H., Serpone, N., Pelizzetti, E., Minero, C., Fox, M.A. and Draper, R.B., *Langmuir*, **1989**, 2, 250.
(e) Hidaka, H., Ihara, K., Fujita, Y., Yamada, S., Pelizzetti, E. and Serpone, N., *J. Photochem. Photobiol. A, Chem.*, **1988**, 42, 375.

7. (a) Augugliaro, V., Palmisano, L., Scalfani,A., Minero, C. and Pelizzetti, E., *Toxicol. Environ. Chem.*, **1988**, 16, 89.
(b) Al-Sayyed, G.H. and Pichat P., *Proceedings XII IUPAC Symposium on Photochemistry, Bologna*, **1988**, 126.
(c) Borgarello, E., Serpone, N., Barbeni, M, Minero, C., Pramauro, E and Pelizzetti, E. in *"Homogenous and Heterogenous Photocatalysis"*, Pelizzetti, E. & Serpone, N. (Eds.), Reidel, Dordrecht, The Netherlands, **1986.**
(d) Matthews, R.W., *Water Res.*, **1986**, 20, 569.
(e) Matthews, R.W., *J. Catal.*, **1986**, 97, 565.
(f) Okamoto, K.J., Yamamoto, Y., Tanaka, H., Tanaka, M. and Itaya, A., *Bull. Chem. Soc. Jpn*, **1985**, 58, 2015.

8. Mulvaney, P., Greiser, F. and Meisel, D. in *"Kinetics and Catalysis in Microheterogenous Systems"*, Grätzel, M and Kalyanasundaram, K. (Eds.), Marcel Dekker, New York, **1991**, 303.

9. Adamson, A.W. *"Physical Chemistry of Surfaces"*, 4th ed, John Wiley and Sons, New York, **1982**.

10. Kormann, C., Bahnemann, D.W and Hoffmann, M.R., *J. Phys. Chem.*, **1988**, 92, 5196.

11. Moser J., dissertation, Thesis no. 616, Ecole Polytechnique Fédérale de Lausanne, Switzerland, **1986**.

12. Kamat, P.V. in *"Kinetics and Catalysis in Microheterogenous Systems"*, Grätzel, M. and Kalyansundaram, K. (Eds.), Marcel Dekker Inc., New York, **1991**.

13. Steigerwald, M.L and Brus, L.E., *Annu. Rev. Mater. Sci.*, **1989**, 19, 471.

14. Myers, D., *"Surfaces, Interfaces, and Colloids. Principles and Applications"*, VCH Publishers, New York, **1991**.

15. Matijevic, E., *Langmuir*, **1986**, 2, 12.

16. Rossetti, R., Hull, R., Gibson, J.M and Brus, L.E., *J. Chem. Phys.*, **1984**, 82, 552.

17. *"Index to the X-ray* Powder Data File", Smith, J.V. (Ed.), ASTM Special Technical Publication 48-L, Philadelphia, **1962**.

18. Cullity, B.D., *"Elements of X-ray Diffraction"*, Addison-Wesley Publishers, London, **1956**.

19. Sproull, W.T. *"X-rays in Practice"*, McGraw-Hill, New York, **1946**, 430.

20. Scherrer, P., *Gött. Nachr*, **1918**, 2, 98.

21. Klug, H.P and Alexander, L.E. *"X-ray Diffraction Procedures"*, 2nd ed., John Wiley & Sons, New York, **1974**.

22. Gallardo, S., Gutiérrez, Henglein, A. and Janata, E., *Ber. Bunsenges. Phys. Chem.*, **1989**, 93, 1080.

23. Lewis, N.S and Rosenbluth, M.L. in "*Photocatalysis, Fundamentals and Applications*", Serpone, N. & Pelizzetti, E. (Eds.), John Wiley & Sons, New York, **1989**.

24. *Technical Bulletin Pigments*, **No. 56-3-205-282K**, 3rd edition, 1982, Degussa, Germany.

25. Finklea, H.O. in *"Semiconductor Electrodes"*, Studies in Physical and Theoretical Chemistry 55", Finklea, H.O. (Ed.), Elsevier, Amsterdam, **1988**, 43.

26. Samsonov, G.V. (Ed.), *"The Oxide Handbook"*, IFI/Plenum, New York, **1982**, 23.

27. Parfitt, G.D., *Progr. in Surf. Membrane*, **1976**, 11, 181.

28. Shannon, R.D., *J. Appl. Phys.*, **1964**, 35, 3414.

29. Hendrix, W.P and Orr, C., *"Rapid Surface Area Analysis Using Low-Temperature Nitrogen Adsorption"*, U.S.A.-Japan Particulate Technology Conference, 6-11 October, 1969, Kyoto, Japan.

CHAPTER 4

A PULSE RADIOLYSIS STUDY OF •OH RADICALS AT THE SURFACE OF COLLOIDAL TiO_2

4.1 INTRODUCTION

Titanium dioxide is a stable, highly photoactive semiconductor material often used in photocatalylic applications. The successful application of TiO_2 towards the complete mineralization of a number of environmentally damaging aqueous organic contaminants[1-7] has led to a considerable amount of interest in examining the mechanistic details of the TiO_2 photoreactivity in an effort to improve its photocatalytic activity. Before the potential of TiO_2 in photocatalytic processes can be maximized, a better understanding of the chemical nature of the photo-formed electrons and holes and the role these species play in heterogenous reactions at the TiO_2/solute interface is required.[8]

Recent advances in reproducible synthesis of transparent colloidal semiconductor solutions[9] has permitted the use of a number of state-of-the-art optical techniques to characterize the electronic properties of the conduction and valence bands as well as the events taking place at the particle surface traps preexisting or formed upon band gap excitation of TiO_2. Several reports[10-16] detailing the optical characteristics of the

photogenerated electron have appeared; it now appears to be fairly well accepted that within several picoseconds, following bandgap excitation, the electron is trapped by titanium(IV) ions near or at the TiO_2 particle surface resulting in the formation of a Ti^{+3} centre.[16] Far less clear, however, are the observations concerning the optical characteristics of the photogenerated hole species. A recent report[17] has proposed that the trapped hole in 120 Å TiO_2 particles is characterized by an absorption maximum at about 630 nm, a feature more in line with surface trapped electrons $\{Ti^{IV}---e^-\}$.[15,18-20] This is intriguing since the "hole" in TiO_2 is essentially Ti^{IV}-$O^{-\bullet}$[10] and such a surface radical is not expected to have an absorption peak in the visible region. As well, this contrasts sharply with the observations of Henglein and co-workers[13,14] who assigned a band at ~ 430 nm to the trapped hole in 250 Å platinized TiO_2 particles.

The present chapter reports results in which the pulse radiolysis technique was used to study the reaction of •OH radicals with small TiO_2 (~ 13 nm) particles in aqueous solution. The advantage of generating radicals this way, over flash photolysis techniques, lies in the ability to explore the chemical and physical properties of a charge carrier (hole in this case) without the fast recombination of charge carriers and without interference from absorption by the other carrier.[21] Hole injection into CdS particles[22] has been reported to lead to formation of surface trapped holes identified as the $S^{-\bullet}$ radicals. This chapter examines the properties of the resulting $\{TiO_2$ + •OH$\}$ product and discusses its implications to the ongoing controversy surrounding the role of •OH radicals in the semiconductor mediated photo-oxidative degradation of organic pollutants.

4.2 REACTION OF •OH WITH TiO_2

Figure 4.1 illustrates a typical trace obtained at 370 nm following the reaction of •OH radicals with the TiO_2 particles. The observed growth rate was linearly dependent on $[TiO_2]$ yielding $k = 6.0 \times 10^{11}$ M^{-1} s^{-1} (concentration in terms of particles), close to the diffusion-controlled limit. The rate also increased with the concentration of •OH radicals suggesting a competing radical-radical reaction. This situation is not unexpected as the concentration of •OH species (1.4×10^{-5} M) was typically higher than that of TiO_2 particles (1.1×10^{-6} M). Addition of 0.1 M *tert*-butyl alcohol as •OH scavenger completely eliminated this signal.

Figure 4.1b illustrates the decay of the absorption at 370 nm of the product species. The decay rate obeys a first-order rate law, indicating a recombination reaction at the surface of a single particle. The decay rate, however, increases linearly with [•OH]; a plot of k_{1d}^{obs} versus [•OH] at constant $[TiO_2]_p = 1.05 \times 10^{-6}$ M yields a rate constant of 1.52 ($\pm$ 0.15) x 10^9 M^{-1} s^{-1} (inset Fig. 4.1b). This rate constant is based on the total concentration of •OH radicals. However, since the reaction is a two-dimensional surface reaction, the actual rate constant within the confined space is different. Such a process is expected to follow a dose dependent first-order rate law. The rate of decay was nearly independent of TiO_2 particle concentration (at [•OH] = 1.50×10^{-5} M). This is attributed to two opposing effects: increasing $[TiO_2]$ leads on the one hand to more efficient scavenging of •OH radicals (in competition with •OH recombination) while, on the other hand, to dilution of the product among a large number of TiO_2 particles. Both the growth and decay rates were wavelength independent thereby

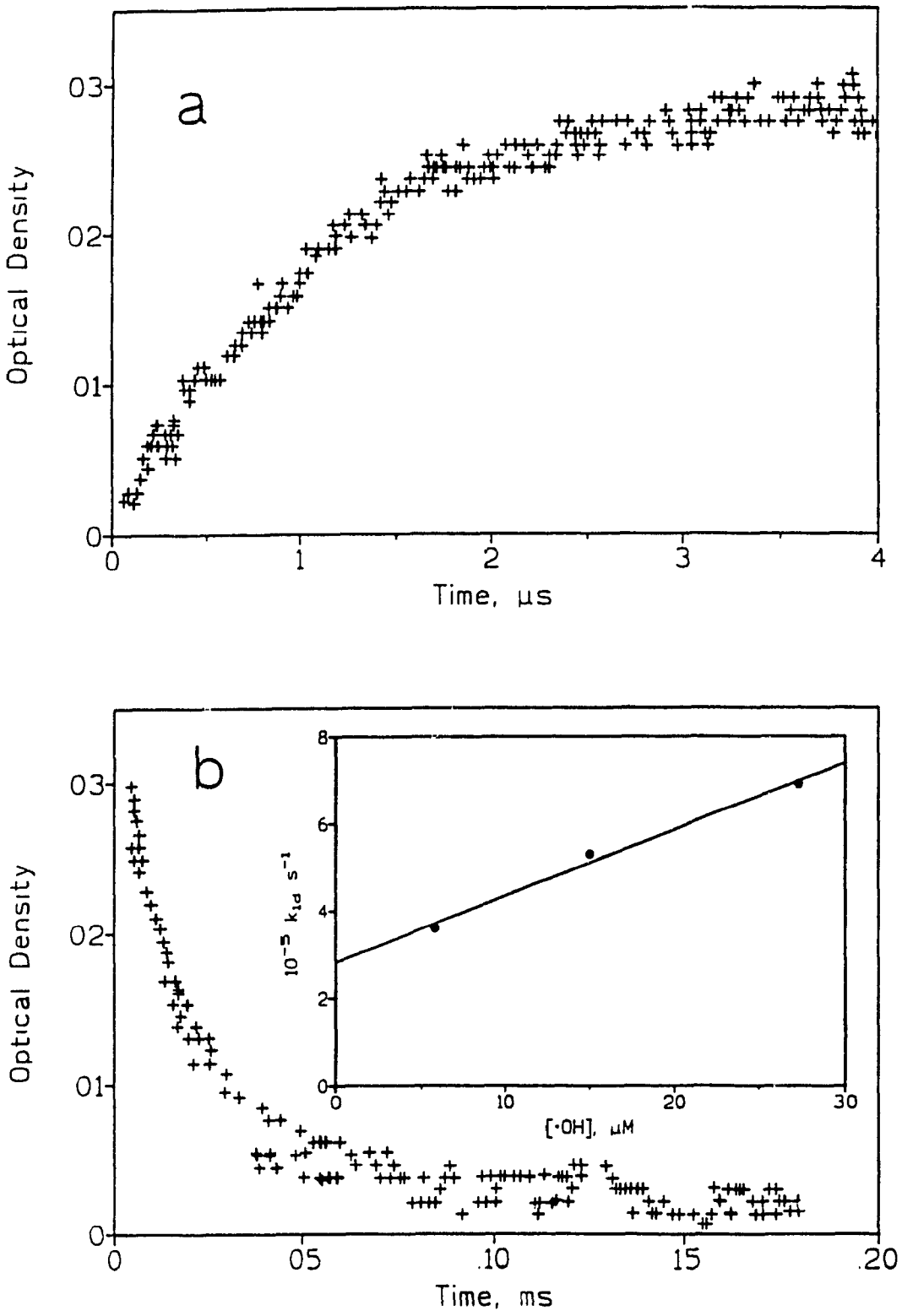

Figure 4.1 Formation (a) and decay (b) of transient species formed from the reaction of •OH radicals with TiO_2 particles followed at 370 nm; $[TiO_2]_p$ = 1.0 x 10^{-6} M, [•OH] = 1.5 x 10^{-5} M. Inset: dependence of pseudo-first-order rate constant on [•OH].

implicating only one species responsible for the spectral feature monitored at 370 nm.

The absorption spectrum of the transient taken 4 μs after the pulse is illustrated in Figure 4.2. The spectrum shows an onset of absorption at ~ 470 nm rising toward the UV and reaching a maximum at ~ 350 nm. At lower wavelengths, the sample absorbed too much of the probe light leading to an unacceptable signal-to-noise ratio.

4.3 pH DEPENDENCE

The dependence of the optical density of the species (discussed above) on pH in the limited accessible range (pH 2 to 3.5) is shown in Figure 4.3. This dependence suggests an acid-base equilibrium with $pK_a \approx 2.8$. Indeed the pK_a measured in Figure 4.3 is similar to the pK_a of TiO_2-OH_2^+. [23] In the pH range examined, the TiO_2 colloidal dispersion was stable and no protective agents were needed.

4.4 PROPERTIES OF THE SPECIES FORMED

Addition of oxygen (5×10^{-4} M O_2; 8×10^{-3} M N_2O) to the solution had no effect on the growth or decay of the transient absorbance. Since oxygen is a good electron scavenger, the species formed on the TiO_2 particle surface is not an efficient reductant. Oxidizing characteristics of the {TiO_2 + •OH} transient were examined by addition of KSCN to the solution. The thiocyanate ion can be oxidized to the radical SCN• (equations 4.1) which in the presence of excess SCN ion yields the radical dimer $(SCN)_2^{-\bullet}$ (equation 4.2):[24]

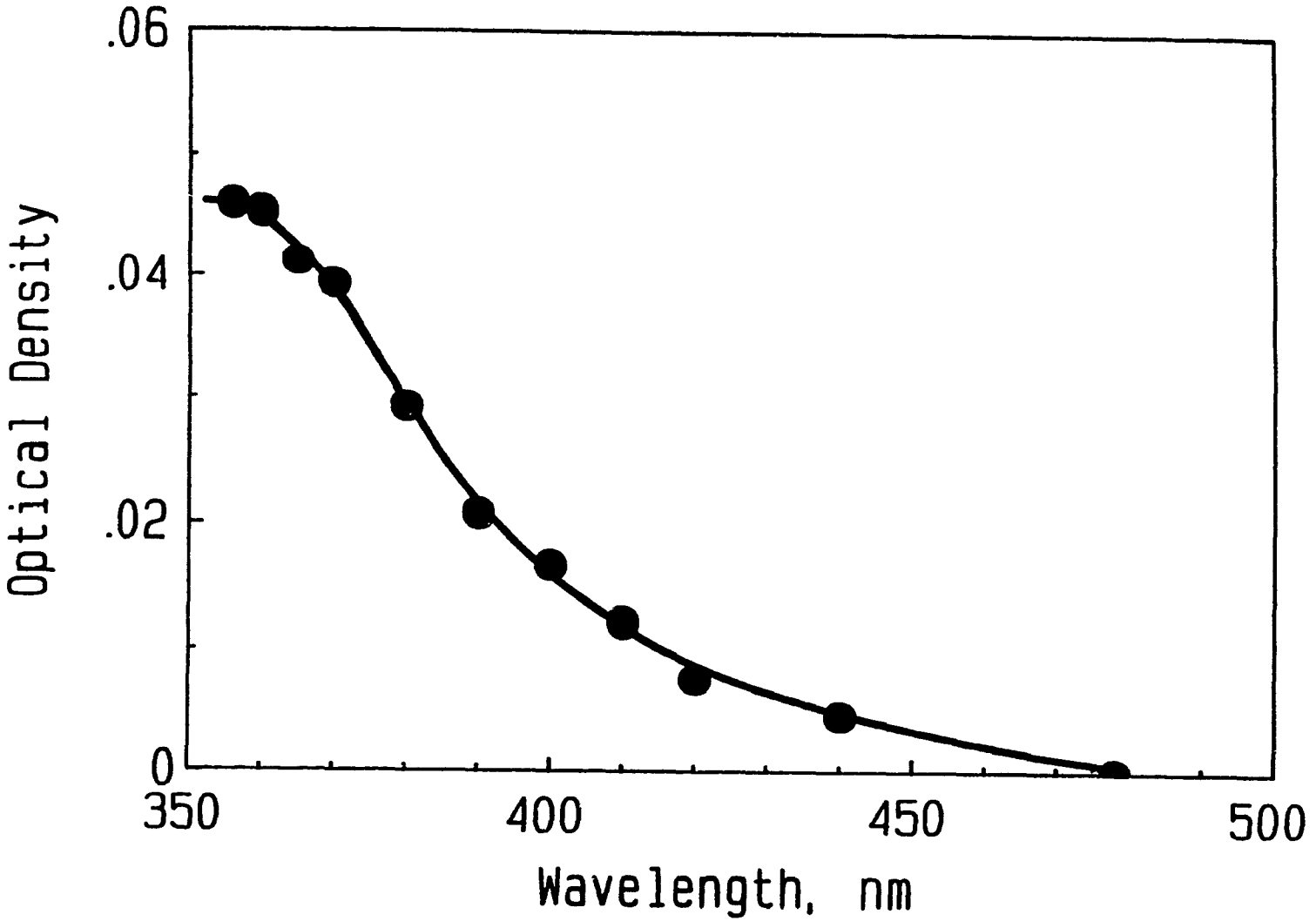

Figure 4.2 Absorption spectrum obtained following reaction of TiO_2 with •OH. Experimental conditions as in Figure 4.1.

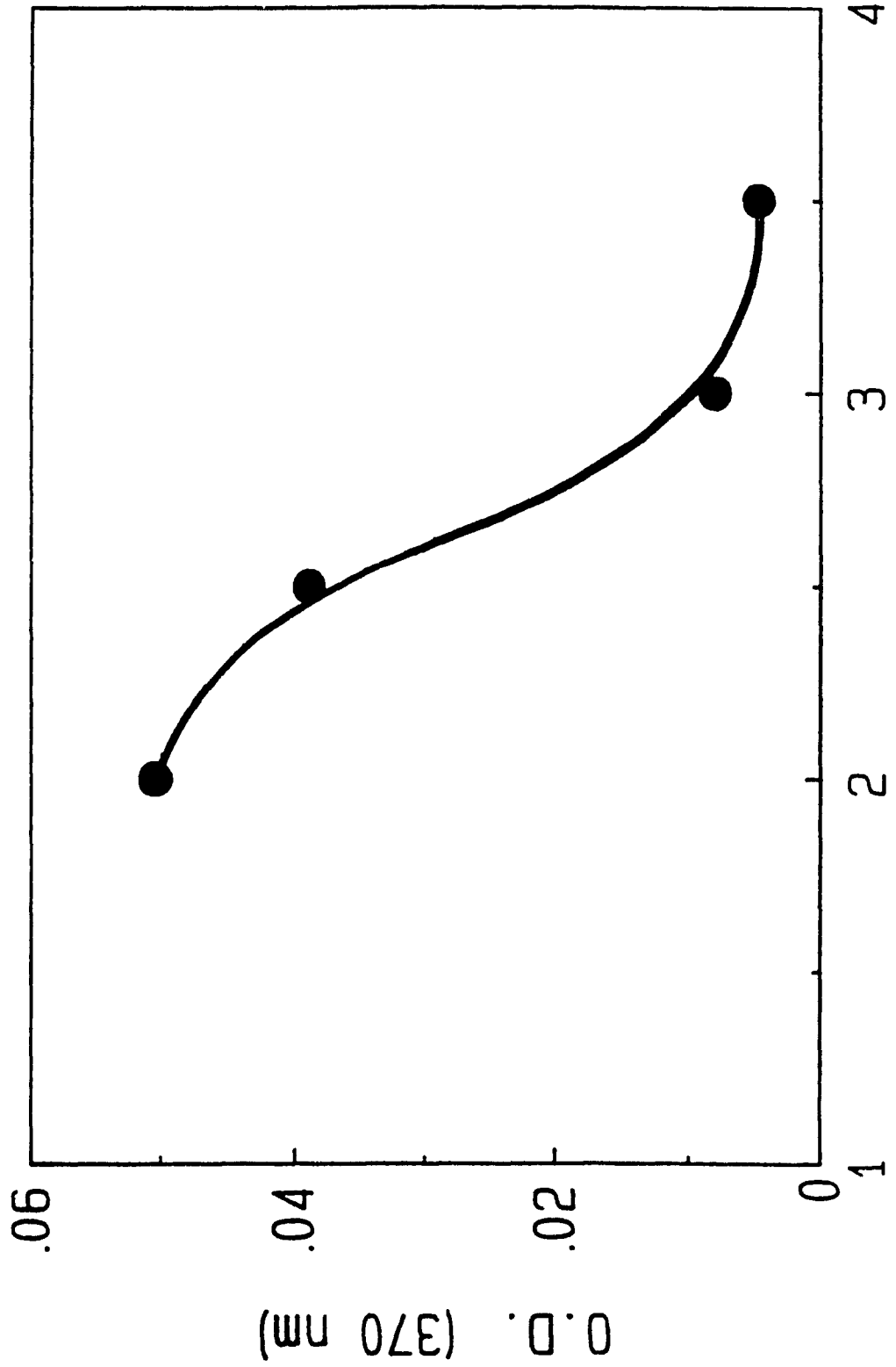

Figure 4.3 pH dependence of the absorbance formed upon reaction of TiO_2 with •OH. Conditions as in Figure 4.1.

$$SCN^- + OX \rightarrow SCN\cdot + OX^{-1} \quad (4.1)$$

$$SCN\cdot + SCN^- \rightarrow (SCN)_2^{-\bullet} \quad (4.2)$$

This radical dimer has a maximum absorption at ~ 478 nm,[24a] a region in which the $\{TiO_2 + \bullet OH\}$ product absorbs negligibly. Similarly, $(SCN)_2^{-\bullet}$ absorbs weakly at 370 nm where the $\{TiO_2 + \bullet OH\}$ species shows optimal signal-to-noise ratio. As can be seen in Figure 4.4, the rate of decay of the absorption at 370 nm increases on increasing $[SCN^-]$. Concomitant with the decay at 370 nm, the absorbance at 478 nm increases owing to the formation of $(SCN)_2^{-\bullet}$ implicating a reaction between $\{TiO_2 + \bullet OH\}$ and SCN^-. At the end of the reaction, the yield of $(SCN)_2^{-\bullet}$ corresponds to ca. 50% of the initial concentration of •OH radicals ($[SCN^-] = 10^{-4}$ M) while the absorbance at 370 nm decayed to ca. half of its maximum height. This observation implies equilibration between the $\{TiO_2 + \bullet OH\}$ product and the $SCN^-/(SCN)_2^{-\bullet}$ couple. From the known redox potential of the latter (+ 1.33 V vs NHE [24b]), the redox level of the $\{TiO_2 + \bullet OH\}$ product is estimated to be at ca. + 1.5 V, a strong oxidizing species, yet a rather deep hole trap, approximately 1.3 eV above (less positive) the valence band.

4.5 IDENTITY OF THE $\{TiO_2 + \bullet OH\}$ PRODUCT

It is generally accepted that bandgap excitation of TiO_2 leads to the photogeneration of electrons and holes. Both species rapidly migrate to the surface and are responsible for chemical reactions occurring at the TiO_2/water interface.[25]

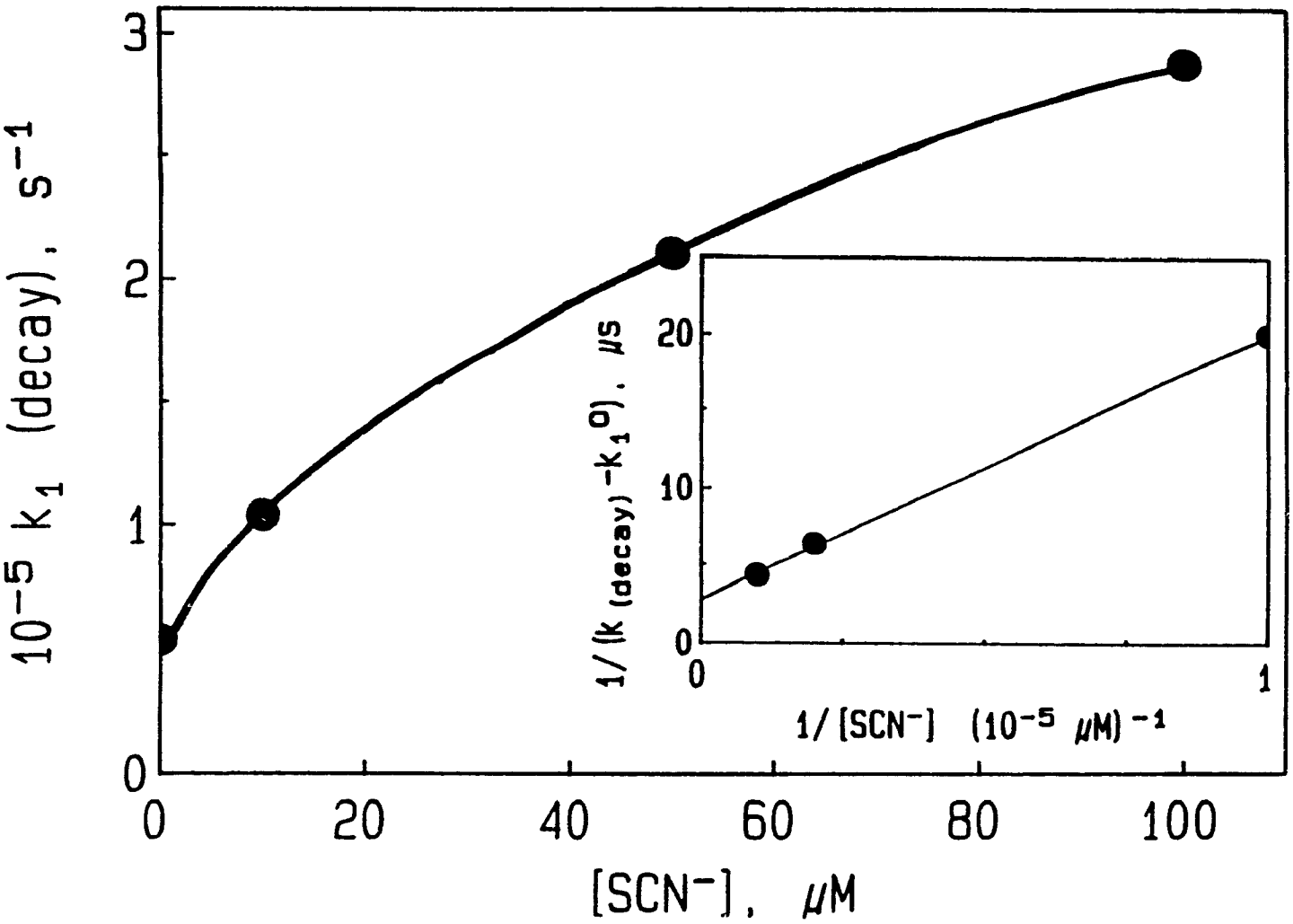

Figure 4.4 Dependence of the pseudo-first-order rate constant for the decay at 370 nm on [SCN^-]. Other conditions as in Figure 4.1. Inset: reciprocal plot analysis of the same results.

Chemically, a trapped electron at or near the particle surface can be described as Ti^{IV}---e^- or a Ti^{+3} centre;[16] the trapped hole can be viewed as the radical Ti^{IV}-$O^{-\bullet}$ radical ion.[13,14] The optical absorption of $O^{-\bullet}$ radicals maximizes at 240 nm;[27] nevertheless, a substantial redshift could result from the interaction with Ti(IV) at the surface.

Henglein and co-workers[13,14] reported that the photogenerated trapped hole in platinized TiO_2 particles displays a broad spectral feature centred at ~ 430 nm. However, using colloidal platinum deposits on TiO_2 to scavenge photogenerated electrons presents some problems. These platinized samples are coloured and could lead to a redshift in the absorption band maximum. Indeed, picosecond laser flash photolysis of colloidal platinum alone display spectral features similar to those for TiO_2/0.5 wt.% Pt under identical conditions.[26] A recent examination of the optical properties of the hole by depositing a presumed electron scavenging dye ($CuPcTS^{4-}$) onto TiO_2[17] has deduced that the trapped hole absorbs at ~ 630 nm. A difficulty in this assertion lies in the close resemblance of the reported difference spectrum for the hole to that of reduced TiO_2.[18-20] Furthermore, it is difficult to rationalize a 400-nm shift in the absorption band of the hole ($O^{-\bullet}$) trapped on TiO_2 particles. This intrigue could be best resolved if injecting a hole into TiO_2 via reaction with the •OH radical proved feasible, since the drawbacks of adding substances foreign to the particle surface could then be avoided. Furthermore, if the •OH radical adsorbed at the particle surface it will be easily assimilated by the highly hydroxylated TiO_2 in aqueous solution and will be indistinguishable from a surface trapped hole. A major issue that needs to be addressed is, therefore, the nature of the product(s) formed from the reaction of TiO_2 with the hydroxyl radical.

Of major concern in the analysis of the results described above is the possibility that Cl^- ions, left over following the controlled hydrolysis of $TiCl_4$, might remain either free in solution or adsorbed on the surface of TiO_2. The hydroxyl radical can oxidize Cl^- according to equations 4.3 and 4.4.

$$OH\cdot + Cl^- \rightarrow Cl\cdot + OH^- \qquad (4.3)$$

$$Cl\cdot + Cl^- \rightarrow Cl_2^-\cdot \qquad (4.4)$$

However, several observations preclude this potentiality. First, TiO_2 sols prepared from titanium isopropoxide[11] instead of $TiCl_4$ (dialysed 24 hours, pH 3 with $HClO_4$ to remove any isopropoxide) displayed similar transient absorbance features, albeit with lower intensity. The smaller absorbance intensity is likely due to the smaller concentration ($\leq$ 3.5×10^{-7} M) of the larger TiO_2 particles (radius $\sim$ 200 Å) achievable in this preparation in the absence of stabilizers.[27] Second, the absorption spectrum in Figure 4.2 is redshifted relative to that for the $Cl_2^{-\bullet}$ radical (λ = 340 nm). Finally, blank experiments under identical conditions, but without TiO_2, indicate that at least 10 mM Cl^- will be required to generate the same absorbance as in the TiO_2 containing solution. Such high concentration of chloride ions could not remain in our solutions after the extensive dialysis utilized; as well, Cl^- ions were not detected by the silver nitrate analytical procedure. Moreover, addition of 1 mM chloride to the TiO_2 solution had no effect on the transient. Taken together, all these observations are convincing arguments that the transient observed is not due to the reaction of •OH with chloride.

It has already been noted that the product of the •OH reaction with TiO_2 is a

strong oxidant. The dependence of the decay rate of this product on [SCN^-] (Figure 4.4) indicates that the production of $SCN^{-\bullet}$ is not due to a direct reaction between •OH and SCN^- in the bulk of the solution (equations 4.5, 4.2).

$$SCN^- + \cdot OH \rightarrow SCN\cdot + OH^- \qquad (4.5)$$

$$SCN\cdot + SCN^- \rightarrow (SCN)_2^{-\cdot} \qquad (4.2)$$

The dependence of the decay rate on SCN^- concentration is reminiscent of a Langmuir-type adsorption/desorption quasi-equilibrium for SCN^-. The data presented in Figure 4.4 suggest that the rate of decay of the {TiO_2 + •OH} product in the presence of SCN^- may be expressed as:

$$Rate = k_{(decay)}\,[TiO_2 + \bullet OH] = \left(k_1^{\,o} + \frac{k_1 K[SCN^-]}{1 + K[SCN^-]}\right)[TiO_2 + \bullet OH] \qquad (4.6a)$$

where $k_1^{\,o}$ is the intrinsic decay of the {TiO_2 + •OH} species (5.4 x 10^4 s^{-1}) and k_1 is the SCN^--dependent first order decay of {TiO_2 + •OH}, identified in equation 4.8. The mechanism for the oxidation of SCN^- is given by the sequence of reactions 4.7 to 4.9. The equilibrium coefficient, K, defined by equation 4.7 is taken to represent an adsorption/desorption coefficient, reminiscent of Langmuir-type kinetics.

$$TiO_2 + SCN^- \overset{K}{\leftrightarrows} (SCN^-)_{ads} \qquad (4.7)$$

The electron-transfer reaction (equation 4.8) is understood to occur between two species,

$$\{ TiO_2 + \bullet OH \} + (SCN^-)_{ads} \xrightarrow{k_1} \{ TiO_2 + OH^- \}\text{-}SCN^{\bullet} \qquad (4.8)$$

$$\{ TiO_2 + OH^- \}\text{-}SCN^{\bullet} \xrightarrow{SCN^-} \{ TiO_2 \} + SCN_2^{\bullet -} \qquad (4.9)$$

SCN^- and •OH radical, both adsorbed at the surface of the same particle. While it is assumed that this step is rate-determining, it is possible that some other reaction (e.g., dimerization or dimer desorption reaction) might be rate limiting. The inset in Figure 4.4 presents the linear transform of equation 4.6a, consistent with the above mechanism (equation 4.6b).

$$\frac{1}{k_{decay} - k_1^0} = \frac{1}{k_1} + \frac{1}{k_1 K[SCN^-]} \qquad (4.6\ b)$$

The intercept and the slope of the curve yield $k_1 = 3.7 \times 10^5\ s^{-1}$ and $K = 1.5 \times 10^4\ M^{-1}$. The coefficient, K, is consistent with previous observations that SCN^- strongly adsorbs to the surface of TiO_2.[12-14] Further, the rate of formation of $(SCN)_2^{\bullet}$ is in good agreement with the rate recently reported by Draper and Fox[28] using diffuse reflectance flash photolysis techniques. The intrinsic decay, represented by k_1^0, is likely a recombination reaction of two adsorbed hydroxyl radicals (trapped holes) at the surface of a single particle yielding H_2O_2. Such a process is expected to follow a dose dependent first-order rate law.

The identity of the species produced by the reaction of •OH radicals with TiO_2

can now be addressed. The hydroxyl radical is a strong oxidizing agent and previous studies have shown that it can be used to inject a hole into other semiconductor colloid materials such as CdS,[22] ZnS,[22a] Cd_3P_2 [22a] and In_2Se_3.[29] The hole in the case of CdS was identified as an $S^{-\bullet}$ species.[22] Similarly, for a hole to be injected into TiO_2 an electron would have to be removed from the valence band with a resulting radical lattice oxygen species formed.[28,30] It is commonly accepted that a valence band hole will react with a water molecule upon arrival at the TiO_2 surface to create an adsorbed •OH radical, a process which will occur on a small particle within a few picoseconds. It will therefore not be possible to distinguish between a trapped hole and an adsorbed •OH radical. Thus, the product of the •OH reaction as the trapped hole (adsorbed hydroxyl radical) may be identified as:

$$\{Ti(IV)-O^{2-}-Ti(IV)\} + \bullet OH \rightarrow \{Ti(IV)-O^{2-}-Ti(IV)\}-OH^{\bullet} \quad (4.10)$$
$$\updownarrow$$
$$\{Ti(IV)-O^{\bullet-}-Ti(IV)\}-OH^{-}$$

Given that the surface of TiO_2 is covered with between 5-15 OH^- groups/nm^2, [31] the additional hydroxyl group is unlikely to assert any influence on the properties of the surface. The pH dependence of the absorbance of Figure 4.3 is attributed to the acid-base equilibrium:

$$\{Ti(IV)-O^{2-}-Ti(IV)\}-OH_2^{+} \rightleftharpoons \{Ti(IV)-O^{2-}-Ti(IV)\}-OH^{\bullet} + H^{+} \quad (4.11)$$

The higher extinction coefficient of the protonated form, relative to the base form, is in

line with similar observations for free •OH radicals. The ~ 9 pH units shift to acidic solutions in the pKa (= 2.8) relative to the pK_a of •OH (= 11.8) is to be expected from the shift of charge density to the lattice oxygen, as shown in the hybrid structures of equation 4.10. On the other hand, the pK_a of the {TiO_2 + •OH} species is essentially identical with the first pK_{a1} of TiO_2 [34] (where pzc = $(pK_{a1} + pK_2)/2$ = 4.8 [21]), indicating that the additional OH^- group is indistinguishable from the original pre-existing ones.

4.6 IMPLICATIONS ON PHOTO-OXIDATION REACTIONS OF TIO_2

Recently, much discussion has centred on mechanistic details of the photo-oxidation of organic substrates mediated by irradiated TiO_2, and on the role and importance of degradation by free *versus* surface-bound •OH radicals on the one hand, and *versus* direct hole oxidation on the other. Several researchers[32-35] have proposed that the hydroxyl radical, produced by oxidation of water or of OH^- groups by holes at the surface, may diffuse away from the surface to oxidize the organic compound in solution. This contention is based mainly on the fact that H_2O_2 and hydroxylated degradation products are formed during this reaction.[36-43] EPR spin-trapping studies[12,44] have shown that the •OH radical is the only radical observable on photoexcitation of TiO_2. Consistent with this, a kinetic deuterium isotope experiment[45] showed that in the photooxidation of isopropanol, the rate-limiting step is formation of active oxygen species through a reaction involving the solvent water. In addition, a number of researchers [46-49] have concluded that hydroxylation of the TiO_2 surface is a prerequisite for the complete

photodegradation of organic compounds. In summary, the prevailing view[46] seems to be that the hydroxyl radical is the primary oxidizing agent.

Evidence in support of direct hole oxidation as the main step in the photooxidation process has been presented. An early study by Boostra and Mutsaers[50] concluded that the hydroxyl radical was **unlikely** to participate in photo-oxidation with TiO_2. Modification of the TiO_2 surface with chlorosilicon compounds led to a decrease in the activity for several photocatalytic reactions, yet the effect was smaller than the extent of the eliminated hydroxyl groups. Stronger evidence for direct hole oxidation comes from a recent study[51] which failed to detect any of the expected hydroxylated intermediate $OH^{\cdot}$ adducts following diffuse reflectance flash photolysis of several TiO_2/substrate combinations. It must be pointed out, however, that experimental difficulties, and the fact that $OH^{\cdot}$ adducts often possess absorption bands in the UV region, inaccessible because of TiO_2 interference below 390 nm, preclude observations of such expected hydroxylated species.

The results provided here are consistent with the interpretation that adsorbed •OH (surface trapped holes is the major oxidant, while free hydroxyl radicals probably play only a minor role, if any. Since the •OH radical reacts with the TiO_2 at a diffusion-controlled rate (see above), the reverse reaction, that is desorption of •OH to the solution, would seem unlikely. The surface-trapped hole, as defined in equation 4.10, could then account for most of the observations which have previously led to the suggestion of •OH radical oxidation. The formation of H_2O_2 and the observation of hydroxylated intermediates can all occur via surface reaction with these •OH species.

While the remote possibility that a small number of •OH radicals may leak out from the "surface" and mediate the photooxidation process in the diffuse Gouy-Chapman layer cannot be excluded, this contribution to the total photo-oxidative process must be considered minimal.

4.7 CONCLUSIONS

Oxidation of 13 nm TiO_2 particles by pulse radiolytically generated •OH radicals yields trapped holes ($\{TiO_2 + \bullet OH\}$) on the particle surface. The product shows a spectral maximum at ~350 nm. The high oxidation potential of the trapped hole is inferred from its observed decay behaviour when thiocyanate is added to a TiO_2 sol. The present observations are in close agreement with the spectral features for a hole trapped on TiO_2 reported by Henglein and co-workers,[13,14] but are in clear contrast with the more recent assertions.[17] The decay of the $\{TiO_2 + \bullet OH\}$ product follows a first-order intrinsic path (forming H_2O_2) by collapse of 2 trapped holes on the same particle surface. In the presence of adsorbed SCN^- ions, the same trapped hole may oxidize the adsorbate to yield the oxidized dimer radical anion $(SCN)_2^{-\bullet}$. From the present work, together with earlier evidence, it can be argued that photo-oxidation reactions occur primarily on the semiconductor particle surface via this trapped hole.

REFERENCES

1. For some recent accounts see:
(a) *"Photocatalysis - Fundamentals and Applications"* Serpone, N. & Pelizzetti, E., Eds. John Wiley & Sons, New York, **1989**;
(b) *"Photocatalysis and Environment - Trends and Applications"* Schiavello, M., Ed. NATO ASI Series C237, Kluver Academic Publ., Dordrecht, The Netherlands, **1988**.

2. Terzian, R., Serpone, N., Minero, C. and Pelizzetti, E., *J. Catal.*, **1991**, 128, 352.

3. Al-Ekabi, H., Serpone, N., Pelizzetti, E., Minero, C., Fox, M.A. and Draper, R.B., *Langmuir*, **1989**, 2, 250.

4. Hidaka, H., Ihara, K., Fujita, Y., Yamada, S., Pelizzetti, E. and Serpone, N., *J. Photochem. Photobiol. A, Chem.*, **1988**, 42, 375.

5. Lawless, D., Res, A., Harris, R., Serpone, N., Minero, C., Pelizzetti, E., and Hidaka, H., *Chem. Ind. (Milano)*, **1990**, 72, 139.

6. Domenech, J. and Monoz, J. *Electrochim. Acta*, **1987**, 32, 1383.

7. Serpone, N., Ah-You, Y.K., Tran, T.P., Harris, R., Pelizzetti, E. and Hidaka, H., *Sol. Energy*, **1987**, 39, 491.

8. Anpo, M. in *"Research on Chemical Intermediates - 11"*, Elsevier Science Publications, Amsterdam p.67, **1989**.

9. Matijević, E., *Langmuir*, **1986**, 2, 12.

10. Henglein, A., *Topics Curr. Chem.*, **1988**, 143, 113.

11. Henglein, A., *Ber. Bunsenges Phys. Chem.*, **1982**, 86, 241.

12. Duonghong, D., Ramsden, J. and Grätzel, M., *J. Am. Chem. Soc.*, **1982**, 104, 2977.

13. Bahnemann, D., Henglein, A., Lillie, J. and Spanhel, L., *J. Phys. Chem.*, **1984**, 88, 709.

14. Bahnemann, D., Henglein, A. and Spanhel, L., *Faraday Disc. Chem. Soc.*, **1984**, 78, 151.

15. Rothenberger, G., Moser, J., Grätzel, M., Serpone, N. and Sharma, D.K., *J. Am. Chem. Soc.*, **1985**, 107, 8054.

16. Howe R.F. and Grätzel, M., *J. Phys. Chem.*, **1985**, 89, 4495.

17. Arbour, C., Sharma, D.K. and Langford, C.H., *J. Phys. Chem.* , **1990**, **94**, 331.

18. Dimitijevic, N.M., Savic, D., Micic, O.I. and Nozik, A.J., *J. Phys. Chem.*, **1984**, 88, 4278.

19. Henglein, A., *Pure & Appl. Chem.*, **1984**, 56, 1215.

20. Grätzel, M. in *"Photoinduced Electron Transfer"*, M.A. Fox & M. Channon Eds., Vol. D, p.422, Elsevier, Amsterdam, **1988**.

21. Henglein, A., *Chem. Rev.*, **1989**, 89, 1861.

22. (a) Baral, S., Fotjic, Weller, A.H. and Henglein, A., *J. Am. Chem. Soc.*, **1986**, 108, 375.
(b) Kumar, A., Janata, E. and Henglein, A., *J. Phys. Chem.*, **1988**, 92, 2587.

23. Moser, J., PhD dissertation, Thesis No. 616, Ecole Polytechnique Fédérale de Lausanne, Lausanne, Switzerland, **1986**.

24. (a) Hug, G.L., *"Optical Spectra of Nonmetallic Inorganic Transient Species in Aqueous Solution"*, NSRDS-NBS 69, **1981**.
(b) Wardman, P.J., *Phys.Chem. Ref. Data*, **1989**, 18, 1637.

25. Howe, R.F. and Grätzel, M., *J. Phys. Chem.*, **1987**, 91, 3906.

26. Serpone, N. and Moser, J., unpublished results (1985).

27. Using titanium isopropoxide the largest concentration which could be made was approximately 1.2 g/L.

28. Draper, R.B. and Fox, M.A., *J. Phys. Chem.*, **1990**, 94, 4628.

29. Dimitrijević, N.M and Kamat, P.V., *Langmuir*, **1987**, 3, 1004.

30. Augustinski, J. *Structure and Bonding*, **1988**, 69, 1.

31. Boehm, H.P., *Discuss. Faraday Soc.*, **1971**, 52, 264.

32. Ceresa, E.M., Burlamacchi, L. and Visca, M., *J. Mater. Sci.*, **1983**, 18, 289.

33. Gonzalez-Elipe, A.R., Munera, G. and Soria, J., *J. Chem. Soc. Faraday Trans. 1*, **1979**, 75, 748.

34. Völz, H.G., Kämpf, G. and Klaeren, A., *Farbe + Lack*, **1976**, 82, 805.

35. Völz, H.G., Kämpf, G., Fitsky, H.G. and Klaeren, A., *ACS Symp. Ser.*, **1981**, 151, 163.

36. Augugliaro, V., Palmisano, L., Sclafani, A., Minero, C. and Pelizzetti, E., *Toxicol. Environ. Chem.*, **1988**, 16, 89.

37. Al-Ekabi, H., Serpone, N., Pelizzetti, E., Minero, C.,Fox, M.A. and Draper, R.B., *Langmuir*, **1989**, 5, 250.

38. Ollis, D.F., Hisao, C., Budiman, L. and Lee, C., *J. Catal.*, **1984**, 88, 89.

39. Barbeni, M., Morello, M., Pramauro, E., Pelizetti, E., Vincent, M., Borgarello, E. and Serpone, N., *Chemosphere*, **1987**, 16, 1165.

40. Turchi, C.S. and Ollis, D.F., *J. Catal.*, **1989**, 119, 480.

41. Metelitsa, D.I., *Russ. Chem. Rev. Engl. Trans.*, **1989**, 119, 480.

42. Cox, R.A., Derwent, R.G. and Williams, M.R., *Environ. Sci. Technol.*, **1980**, 14, 57.

43. Barbeni, M., Minero, C., Pelizzetti, E., Borgarello, E. and Serpone, N., *Chemosphere*, **1987**, 16, 2225.

44. Jaegar, C.D. and Bard, A., *J. Phys. Chem.*, **1979**, 83, 3146.

45. Cunningham, J. and Srijaranai, S., *J. Photochem. Photobiol. A Chem.*, **1988**, 43, 329.

46. Turchi, C.S. and Ollis, D.F., *J. Catal.*, **1990**, 122, 178.

47. Navio, J.A. and Rives-Arneau, V., *Langmuir*, **1990**, 6, 1525.

48. Bickley, R.I., Jayanty, R.K.M., Navio, J.A. and Vishwanatham, V. in *"Homogenous and Heterogenous Photocatalysis"*, Nato-ASI Series C, E. Pelizzetti and N. Serpone Eds., D. Reidel, Dodrecht, 174, 555, **1986**.

49. Munuera, G., Gonzalez-Elipe, A.R., Rives-Arneau, V., Navio, J.A., Malet, P., Soria, J., Conesa, J.C. and Sanz, J. in *"Adsorption and Catalysis on Oxide Surfaces"*, M. Che and G.C. Bonds Eds., Elsevier, Amsterdam, 113, **1985**.

50. Boonstra, H. and Mutsaers, C., *J. Phys. Chem.*, **1975**, 79, 1940.

51. Draper, R.B. and Fox, M.A., *Langmuir*, **1990**, 6, 1396.

CHAPTER 5

PHOTOPHYSICAL STUDIES OF NAKED COLLOIDAL TiO_2

5.1 INTRODUCTION

The application of semiconducting systems in initiating and controlling various photocatalytic processes[1] has stimulated interest in elucidating the photophysical properties of semiconductor colloids and the dynamics of the interfacial processes at the semiconductor-electrolyte interface.[2-7] The photophysical properties of semiconductor materials are of particular interest in the field of heterogenous photocatalysis. Recent advances in the preparation of ultrasmall colloidal particles has permitted the use of time-resolved spectroscopy to elucidate the dynamics of charge carrier reactions within the semiconductor particle. It has also permitted a convenient method for analysis of the elementary steps involved in the catalytic process.

Intense interest has developed in understanding the photophysical behaviour of TiO_2 in the aqueous environment due to its potential commercial application in environmental efforts to clean polluted ecosystems. In addition, TiO_2 is used as a whitening agent in paints and photoinduced charge carrier processes in TiO_2 are believed to play a role in the degradation of paints.[8]

A number of reports concerning the photophysical properties of colloidal TiO_2

have appeared in the literature.[9-15] However, with the exception of one report in which extremely small (20 Å) TiO_2 particles were synthesized,[16] the effect of particle size on the observed photophysical properties of TiO_2 has not been reported. Particle size can have pronounced effects on the spectral properties of semiconductor materials and a number of materials such as CdS,[17] ZnS,[18] AgI[19] have shown so-called size quantization effects in the absorption spectra (i.e. spectral blue shifts) with decreasing particle size. Particle size may also have a pronounced effect on the dynamics of charge carrier reactions within the semiconductor particle.[19] This chapter reports on the absorption, fluorescence, and picosecond transient absorption and emission of 23, 133 and 281 Å (diameter) TiO_2 colloidal particles.

5.2 SPECTRAL PROPERTIES OF COLLOIDAL TiO_2

5.2.1 Absorption Spectra of 23, 133 and 281 Å Colloidal TiO_2 Particles

The absorption spectra of 15 g/L colloidal sols of 23, 133 and 281 Å diameter TiO_2 particles are shown in Figure 5.1. The three spectra are identical, correspond to the expected absorption spectrum of anatase TiO_2 and are in good agreement with previously reported spectra of colloidal TiO_2 (120 Å diameter).[16,20]

The fact that the three spectra are identical and do not display typical quantum-size properties such as blue-shifts in the UV-vis spectrum associated with decreasing particle size is not totally unexpected. Quantum size effects are expected when the Bohr radius of the first exciton in the semiconductor is either larger or about the same size as

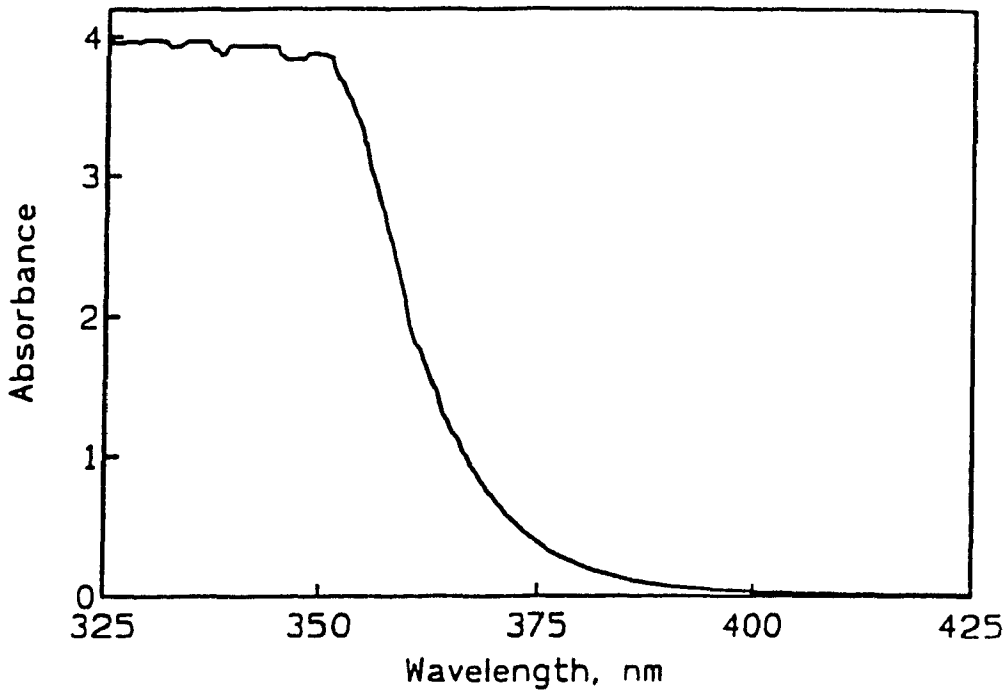

Figure 5.1 Absorption spectra of 23, 133 and 281 Å diameter colloidal TiO_2 particles. $[TiO_2]$ = 15 g/L; pH 2.6; optical path length 1 cm. All spectra are identical.

that of the particle.[21] The Bohr radius can be calculated from the effective mass of the charge carriers (equation 5.1):

$$r_B = \frac{h^2 \epsilon_0 \epsilon}{c^2 \pi^* m} \qquad (5.1)$$

where $\mathbf{r_B}$ is the Bohr radius, **h** is Planck's constant, ϵ_0 is the permittivity in vacuum and the product $\epsilon_0\epsilon$ is the relative permittivity or dielectric constant of the material, c is the speed of light and $^*\mathbf{m}$ is the effective mass of the charge carrier.

Using the values of $^*m_{e^-} = 30\ m_{e^-}$[21] and $\epsilon = 170\ C^2/N\ m^2$ [21] for TiO_2 and neglecting contributions from valence band holes, Grätzel[21] has calculated that quantum size effects should not be manifested in TiO_2 until the size of the particle is below 3 Å.

Although the results presented in Figure 5.1 are in good agreement with these predictions, they would appear to contradict a recent study[16] in which 20 Å diameter colloidal TiO_2 particles showed a bandgap shift of 0.15 eV relative to bulk TiO_2. A possible explanation for the discrepancy may reside in the concentration of the colloidal sol used to calculate the bandgap position. The absorption of colloidal TiO_2 is strongly concentration dependent and will, in fact, follow Beer-Lambert behaviour over a narrow concentration range (see Section 5.2.2). Eventually, a maximum absorption concentration will be reached. At this point, the absorption spectrum of the colloid should match the reflectance spectrum of the colloid removed from solution. This was observed when the 23, 133 and 281 Å colloids were removed from solution and reflectance spectra taken. The spectra were identical to that presented in Figure 5.1. The fact that the reflectance spectra agree with the observed absorption spectra of the concentrated (~5 g/L) colloids strongly supports the observation that there are no quantum-size effects in the size regime of the TiO_2 particles studied. In the case of the study in which 20 Å diameter TiO_2 particles were reported to have shown a 0.15 eV blueshift in the absorption spectrum, the colloid may not have been concentrated enough to accurately reflect the bandgap of the material.

5.2.2 Effect of [TiO_2] on the Absorption Spectrum of Colloidal TiO_2 Particles

The effect of TiO_2 concentration on the observed UV-vis spectra of 133 Å diameter colloidal TiO_2 particles is shown in Figure 5.2. The spectral changes observed when the concentration of TiO_2 was increased from 0.5 to 15 g/L stem from

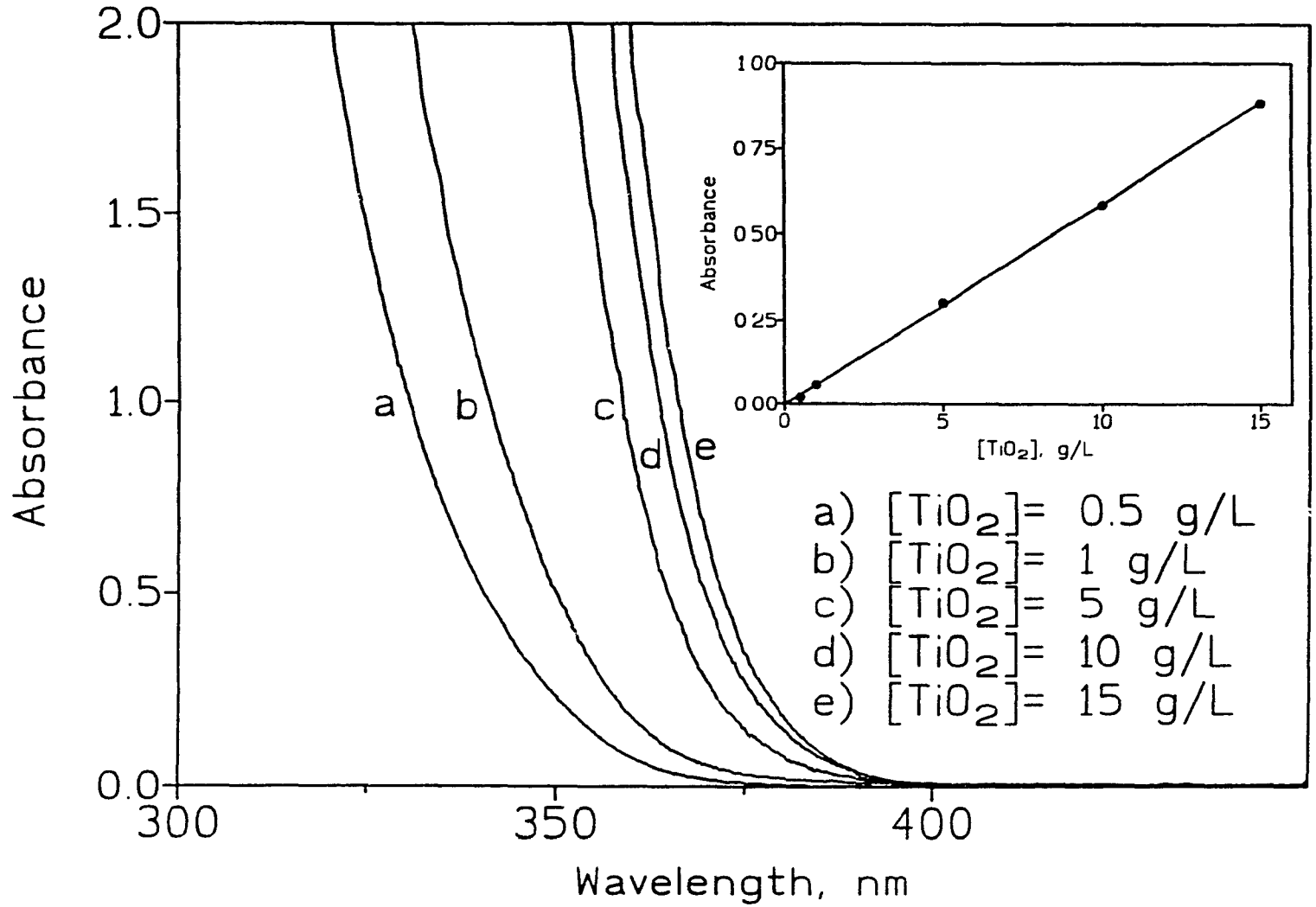

Figure 5.2 Absorption spectra of 13. Å TiO_2 particles; pH = 2.7; optical path length, 1 cm. Inset shows that the absorbance changes at 370 nm follow Beer-Lambert behaviour.

concentration effects associated with the increase of an absorbing species; that is, the spectral behaviour obeys the Beer-Lambert law (equation 5.2). This can be seen from the inset in Figure 5.2 which shows that the increase in absorption at 370 nm is linear over 0 to 15 g/L TiO_2.

$$A = \epsilon c l \tag{5.2}$$

where **A** is the absorption of the absorbing species, ϵ is the molar absorptivity coefficient, c is the concentration of absorbing species (in this case TiO_2 particles) and ℓ is the optical path length.

5.2.3 Growth of TiO_2 Particles

Figure 5.3 illustrates the spectral changes immediately observable when $TiCl_4$ was added to an aqueous solution. Initially a broad band forms whose maxima is centred at approximately 400 nm. This band was most pronounced when the initial temperature of the $TiCl_4$ was 0 °C, although it also appeared when room temperature $TiCl_4$ was added to cold water. Upon warming the solution to ambient temperature (20 °C), the band disappeared and the only absorption observed was the band edge absorption of the growing TiO_2 particles.

The presence of the initial absorption band at 400 nm is indicative that the formation of colloidal TiO_2 may be more complex than the simple hydrolysis of $TiCl_4$ (equation 5.3) and although the hydrolysis of titanium(IV) has been studied by a number of investigators, a number of uncertainties remain concerning the nature of the protolysis products.[22] However, the method of preparation of a semiconductor is known to affect

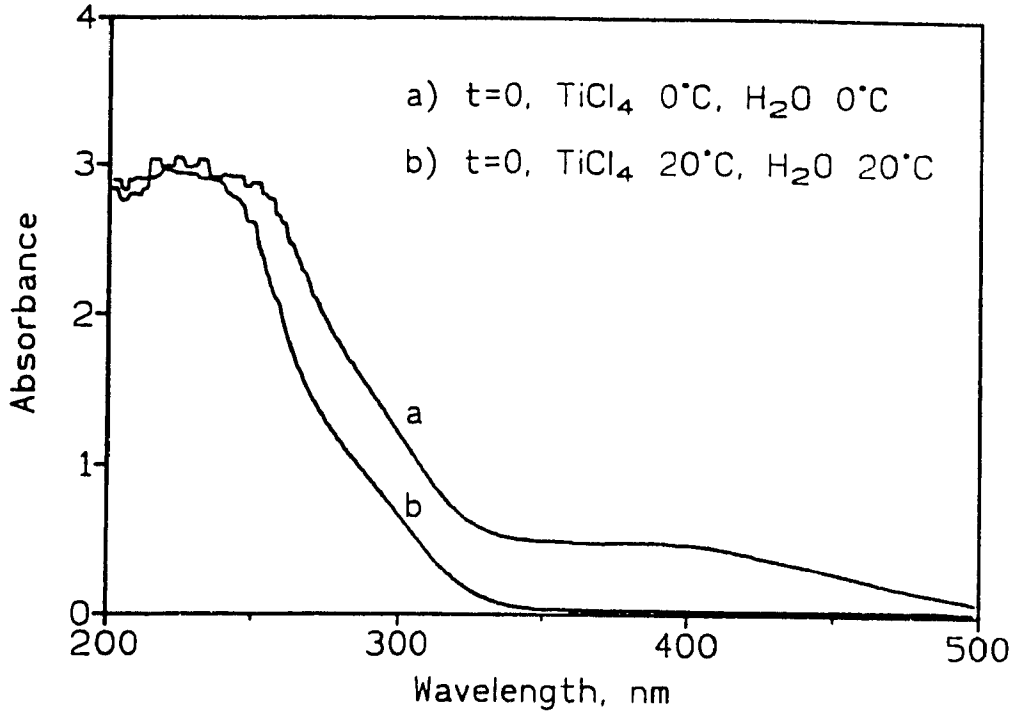

Figure 5.3 Spectral changes when (a) $TiCl_4$ (0 °C) is initially added to water and then (b) allowed to warm up to room temperature (20 °C).

its properties[23] and similarly the early stages of particle growth *may also* have significant influence on the photophysical and photocatalytic properties of TiO_2.

$$TiCl_4 + 2H_2O \rightarrow TiO_2 + 4H^+_{aq} + 4Cl^- \qquad (5.3)$$

A recent study has shown that under highly acidic conditions (0.5 M $\leq [H^+] \leq$ 2 M) and high chloride concentration, conditions which may prevail in the synthesis of colloidal TiO_2, such species as $Cl_n(H_2O)_{2-n}Ti(OH)_2^{2+}$ species may also be formed.[22] The band which appears at ~ 400 nm probably arises from a charge transfer transition from the chloride to Ti^{IV} in a species such as $Cl_n(H_2O)_{2-n}Ti(OH)_2^{2+}$. This assignment is

strengthened by recent observations by Serpone and Kennepohl[24] who looked at a mixture of $TiCl_4$ in ethanol (containing < 1% water) and saw a very strong band formed in the same spectral region. Given that there was insufficient water present to cause a complete hydrolysis of the $TiCl_4$, the observed absorption was attributed to a charge transfer event implicating the chloride and the titanium(IV) orbitals; the exact nature of this band is yet to be confirmed.

The observation that intermediates are formed in the hydrolysis of $TiCl_4$ and that the lifetimes of these species may be controlled by reaction conditions, such as the temperature at which the $TiCl_4$ is added to the water, could conceivably have implications in the observed photophysical and photocatalytic properties of the TiO_2. The presence and concentration of these intermediate species may control the level of defects within the TiO_2 structure. Alternatively, these species may slow the rate of hydrolysis of $TiCl_4$ sufficiently that a more "perfect" crystal structure formed. It is interesting to note that the hydrolysis of $TiCl_4$ in water yields anatase TiO_2 with a large amorphous component. Increasing the lifetime and concentration of intermediate hydrolysis species could lead to increased crystallinity. No doubt, the presence and concentration of these intermediate species may also bear on the particle size of the sol obtained. A more detailed study of the conditions under which $TiCl_4$ is hydrolysed and the resulting photophysical and photocatalytic properties of the TiO_2 produced is required before any definitive conclusions can be reached.

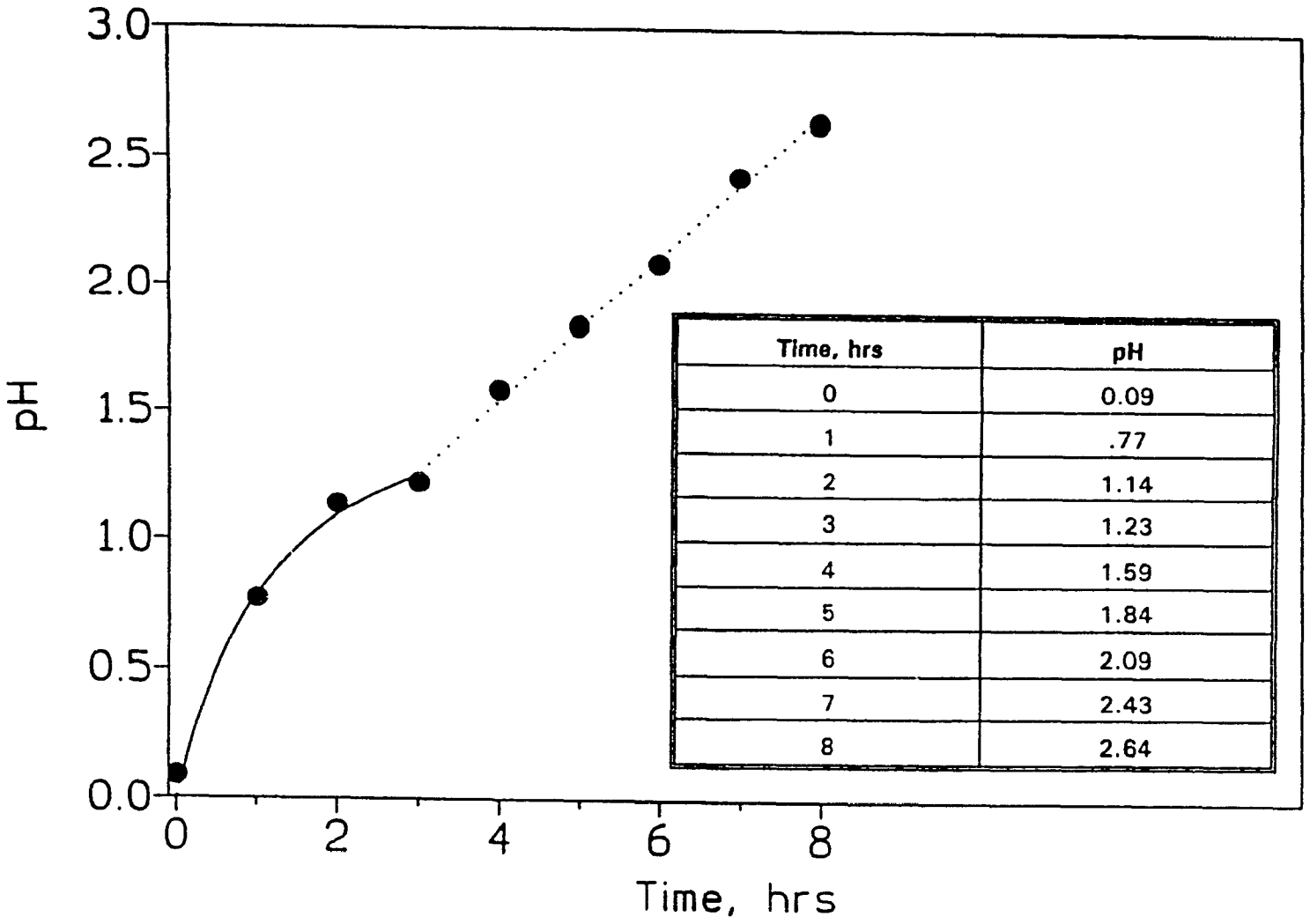

Time, hrs	pH
0	0.09
1	.77
2	1.14
3	1.23
4	1.59
5	1.84
6	2.09
7	2.43
8	2.64

Figure 5.4 pH changes as a function of time during the synthesis of 15 g/L 133 Å TiO_2 particles. Rapid non-linear pH changes occur during the first 3 hrs, after which the increase in pH is linear.

5.2.3.1 GROWTH OF 133 Å TiO_2 PARTICLES

Rapid spectral changes were observed when 15 g/L TiO_2 sols (all particle sizes) were synthesized. No further changes in the absorption spectra were observable after 3 hours. During the dialysis, the pH of the sol increased from 0.1 (t = 0) to 2.6 (t = 8 hrs) (Figure 5.4). The most rapid pH changes also occurred during the first 3 hrs which suggest that particle growth is likely finished by this time. Additional dialysis decreases the ionic strength of the sol and changes the surface charge of the colloid such that precipitation does not occur.

In order to better study the spectral changes which occur when 133 Å TiO_2 were synthesized, a more dilute colloid was prepared and the spectral changes with time followed. Figure 5.5 shows the spectral changes of 0.3 g/L TiO_2. No further spectral changes were observed after 30 minutes. The inset in Figure 5.5 shows that, during the first 20 minutes the absorbance increased linearly with time and then levelled off as maximum particle growth was reached. The linear increase in absorbance during the first 20 minutes is reminiscent of a Beer-Lambert plot (see inset to Figure 5.2) and suggests that the formation of small titania clusters $(TiO_2)_n$, the building blocks of the final $(TiO_2)_N$ lattice, occurred immediately upon addition of $TiCl_4$ to the water. The agglomeration of $(TiO_2)_n$ occurred linearly for approximately twenty minutes, after which particle growth slowed down and continued gradually until the final particle size was reached. The non-linearity in the absorbance changes between 20 and 30 minutes may suggest that the larger particles create a more viscous medium and as such diffusion of the smaller $(TiO_2)_n$ is slowed, effectively arresting particle growth.

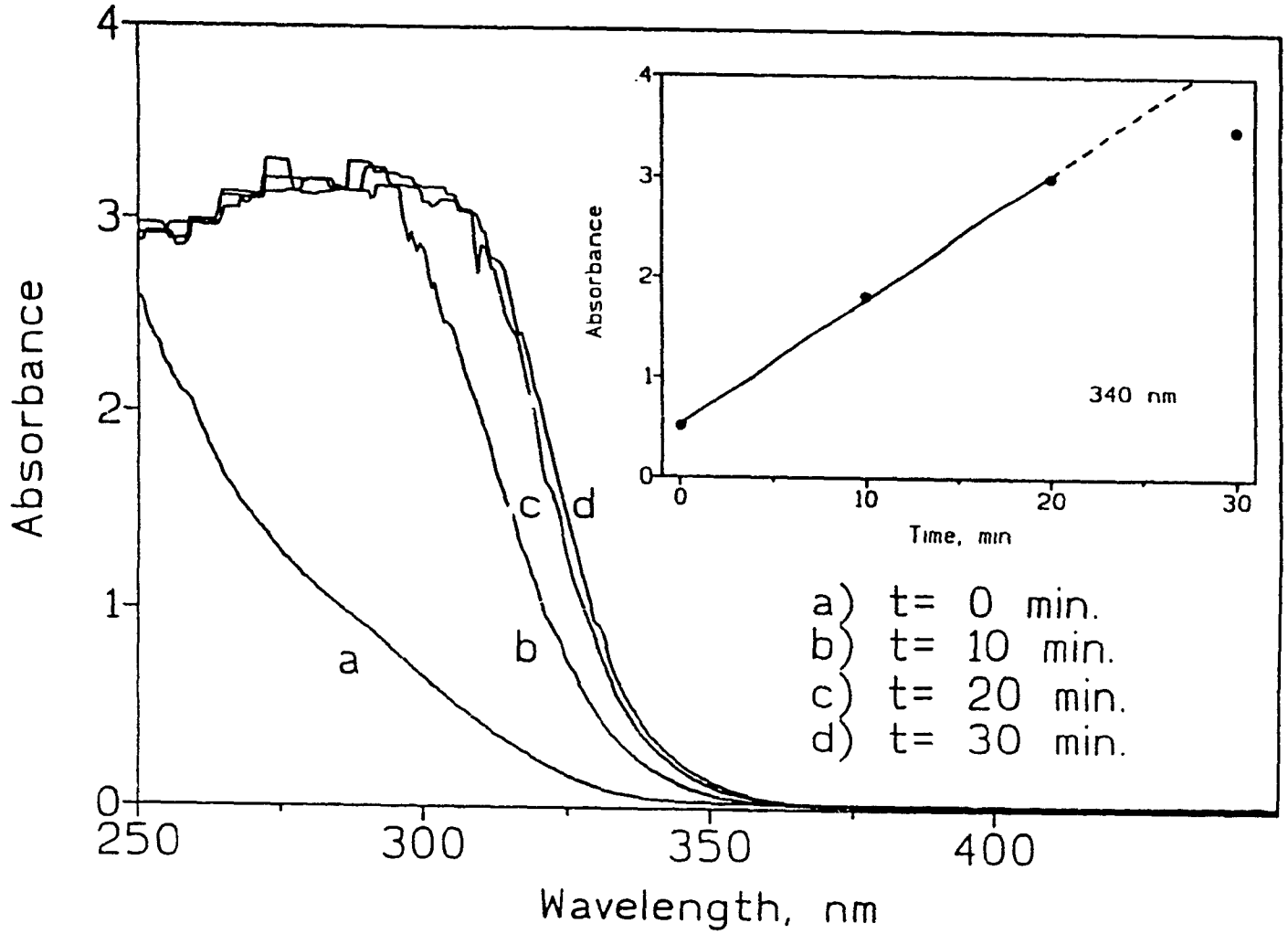

Figure 5.5 Changes in the absorption spectra of 133 Å TiO_2 particles (0.3 g/L) with time; pH_f = 2.7; optical path length, 1 cm. No further spectral changes occurred after 30 min. Inset shows that initially the 340 nm absorbance changes linearly with time.

5.2.3.2 GROWTH OF 23 Å TiO_2 PARTICLES

The growth of 23 Å TiO_2 particles (0.3 g/L) with time is shown in Figure 5.6. The inset illustrates the absorbance changes which occurred at 340 nm over 50 minutes. After 50 minutes there were no further spectral changes. Although the growth of the 23 and 133 Å TiO_2 particles were similar in nature, there are a number of fundamental differences. The time it took to form the smaller $(TiO_2)_N$ product is much longer (50 minutes) than for the larger particles (30 minutes). The behaviour in the early stages of growth of the 23 Å TiO_2 particles was also different. During the first 10 minutes, the change in absorbance was non-linear when compared to the subsequent absorbance changes. The low temperature of the $TiCl_4$ (used to synthesize the smaller particles, see chapter 2) may have resulted in the formation of additional chlorinated and hydroxylated titanium species. Under highly acidic and high concentrations of chloride, such species as $(H_2O)_5Ti(OH)^{3+}\bullet 3Cl^-$ and $(H_2O)_4Ti(OH)_2^{2+}\bullet 2Cl^-$ form in detectable amounts.[22] These species would also eventually lead to formation of $(TiO_2)_n$ clusters or possibly to defect sites within the $(TiO_2)_N$ lattice (see section 5.2.3). It is likely that the conditions used led to a decrease of the effective diffusion rate of the smaller $(TiO_2)_n$ clusters to form the larger particles $(TiO_2)_N$ (see chapter 3). The result was smaller TiO_2 particles. The inset of Figure 5.6 also indicates that the absorbance change is linear from 10 to 50 minutes after which time no further spectral changes occurred. The linearity of the absorbance changes from 10 to 50 minutes suggests that the diffusion and agglomeration of $(TiO_2)_n$ units control the particle growth process, and the presence (or formation) of additional hydroxylated titanium species is no longer important (or does not occur).

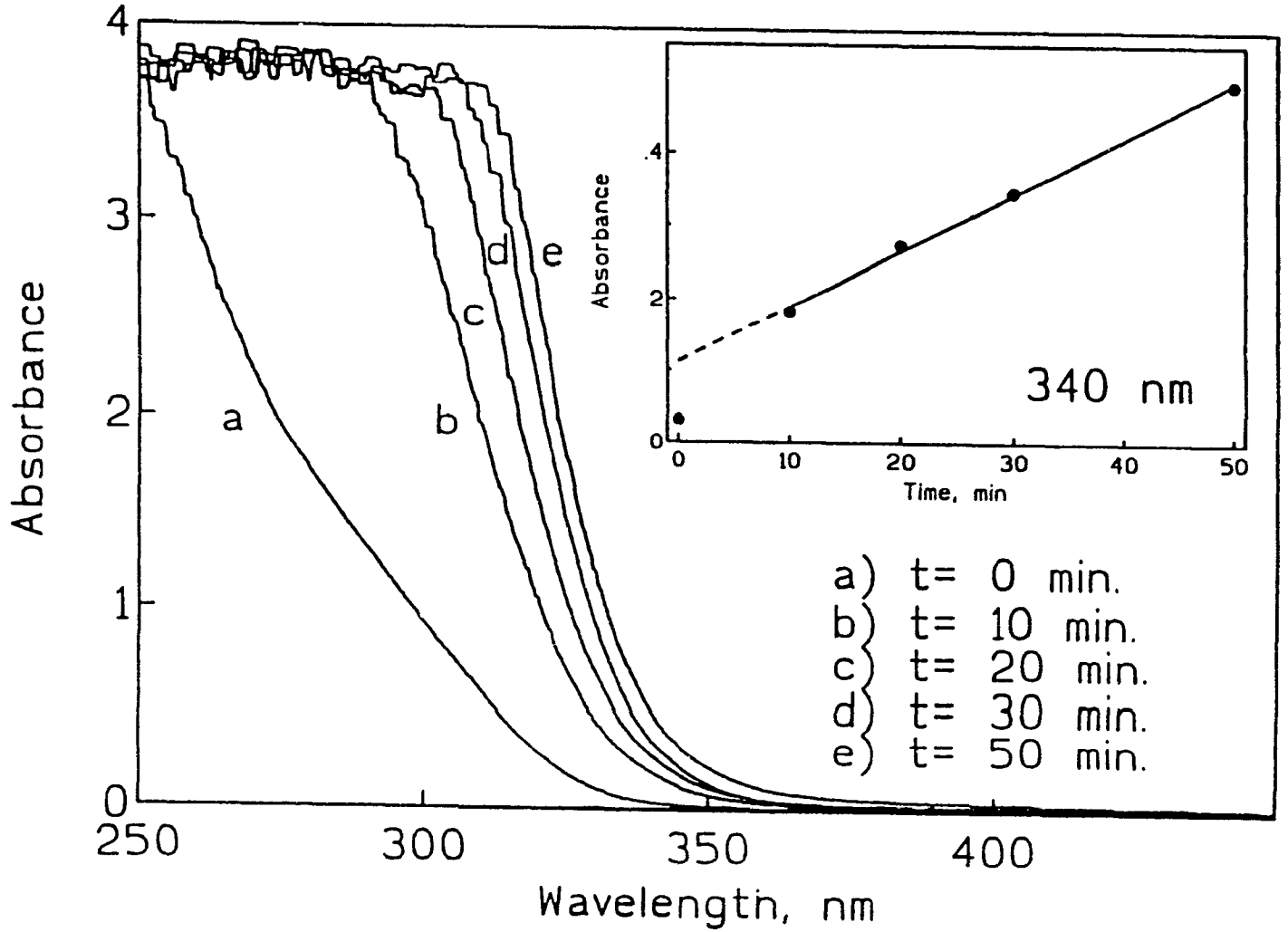

Figure 5.6 Changes in the absorption spectra of 23 Å TiO_2 particles (0.3 g/L) with time; pH_f = 2.7, optical path length, 1 cm. No further spectral changes occurred after 50 min. Inset shows that the 340 nm absorbance changes linearly with time.

5.2.3.3 GROWTH OF 281 Å TiO_2 PARTICLES

The growth of 281 Å TiO_2 was very rapid; no spectral changes were observed after ten minutes. This suggests that the hydrolysis of $TiCl_4$ occurred immediately upon addition of the $TiCl_4$ to the water (10 °C). The higher temperature of the water compared to that used (0 °C) in the synthesis of the 23 and 133 Å most likely increased the effective diffusion rate of the smaller $(TiO_2)_n$ clusters to form the larger particles $(TiO_2)_N$.

5.3 LUMINESCENCE OF COLLOIDAL TiO_2

The luminescence spectra of the 23, 133 and 281 Å diameter TiO_2 particles, run under otherwise identical conditions, is shown in Figure 5.7. To minimize the possibility of inner filter effects#, very dilute colloidal sols were used (0.015 g/L for the 23 and 133 Å TiO_2; 0.3 g/L 281 Å TiO_2). Changing the wavelength of excitation did not cause shifts in the observed emission spectra, indicating that the emission was real and was neither an artifact nor scattered light. Distilled water run under the same conditions showed no "emission" thereby ruling out the observed spectra as a Raman band of water or any other type of artifact.

The particle concentration of the different sized TiO_2 colloids was deduced from equation 5.4. Taking the average particle diameters of the TiO_2 particles as 23 Å, 133 Å and 281 Å, the concentration of TiO_2 as 0.015 g/L for the 23 and 133 Å TiO_2 particles

---

inner filter effects refer to absorption of emitted light by particles in solution; scattering of light under these effects is also included.

and 0.3 g/L for the 281 Å TiO_2 particles, the particle concentration of the three different sized TiO_2 is calculated to be 1.03 x 10^{-6} M, 5.26 x 10^{-9} M and 1.13 x 10^{-8} M respectively.

$$[TiO_2]_p = \frac{3w}{4\pi N\delta R^3} \tag{5.4}$$

where w is the total TiO_2 concentration in g/L, N is Avogadro's number, δ is the density of the material (= 3.84 g/cm^3; anatase TiO_2) and **R** is the average radius of the particle.

The luminescence maxima of all three rather broad spectra correspond closely to the onset of absorption indicating that the observed bands originate from the band edge fluorescence or from recombination of shallowly trapped electrons and holes. A weak broad emission is also observed in the 450-500 nm region. This emission is probably due to radiative recombination from more deeply trapped electrons and holes and thus infers the existence of surface states/energy levels within the forbidden gap of TiO_2. The emission was strongest for the 133 Å particles (Figure 5.7b).

The band-edge fluorescence of the 23 Å TiO_2 particles (Figure 5.7a) was approximately 50% weaker than that of the 133 Å particles. Since the absorption of both samples was nearly identical at 270 nm (the excitation wavelength), the differences in fluorescence yield between the two samples must arise from differences in the surface properties of the particles. The decrease in band-edge fluorescence could arise from increased quenching by the relatively larger number of surface states/energy levels expected to be greatest in the smaller particles,[1c] thereby increasing the non-radiative component of e^-/h^+ recombination. Decreasing the particle size might force

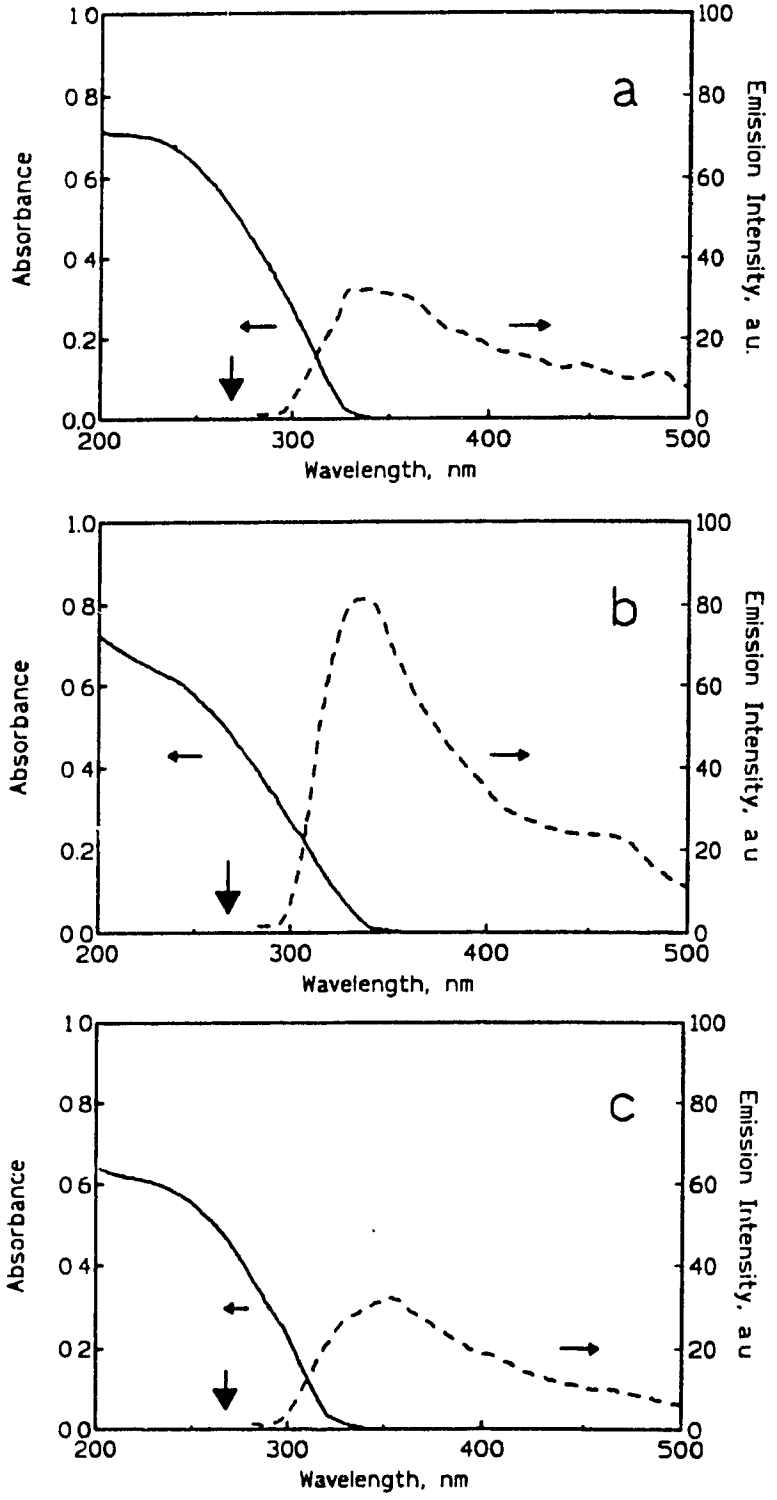

Figure 5.7 Absorption and fluorescence spectra of (a) 23 Å, (b) 133 Å and (c) 281 Å colloidal TiO_2 sols. $[TiO_2]$ = 0.015 g/L for (a) and (b), 0.3 g/L for (c), pH 2.7 in all cases. λ_{exc} = 270 nm, 290 nm (Corning 0-54) filter, slit widths 16/16 (excitation/emission).

recombination to favour a non-radiative route.

The near band edge fluorescence of the larger (281 Å) particles was also weak. The absorption and subsequent fluorescence of the larger particles were too weak to be observable at 0.015 g/L; the concentration of the colloid was therefore increased to 0.3 g/L. At this concentration, the absorption of the larger particles at 270 nm was similar to that of the 133 and 23 Å TiO_2 particles. Increasing the TiO_2 concentration increased the 281 Å TiO_2 particle concentration such that it was approximately twice that of the 133 Å TiO_2 particles (11.3 and 5.26 nM, respectively). However, the observed emission was approximately half that of the 133 Å TiO_2 particles.

5.4 TRANSIENT EMISSION STUDIES OF COLLOIDAL TiO_2

The effect of TiO_2 particle size on the dynamics of charge carrier recombination was also examined using picosecond laser transient emission spectroscopy. The relevant transient emission decay traces obtained for the different TiO_2 samples are reported in Figure 5.8. The emission decay followed good single exponential kinetics: τ_{decay} = 86 ± 2 ps (23 Å, Figure 5.8a), τ_{decay} = 417 ± 14 ps (133 Å, Figure 5.8b), τ_{decay} = 71 ± 5 ps (281 Å, Figure 5.8c). The decay is attributed to band edge luminescence arising from conduction band electron and valence band hole recombination. These decay times parallel the fluorescence data and indicate that recombination of the charge carrier species is slowest in the 133 Å TiO_2 particles. The weaker emissions seen for the 23 Å and 281 Å particles (Figures 5.7a and 5.7c, respectively) reflect emission quantum yields which scale with $k_{rad}\tau_{decay}$, where τ_{decay} denotes the emission lifetime; k_{rad} is not expected to be

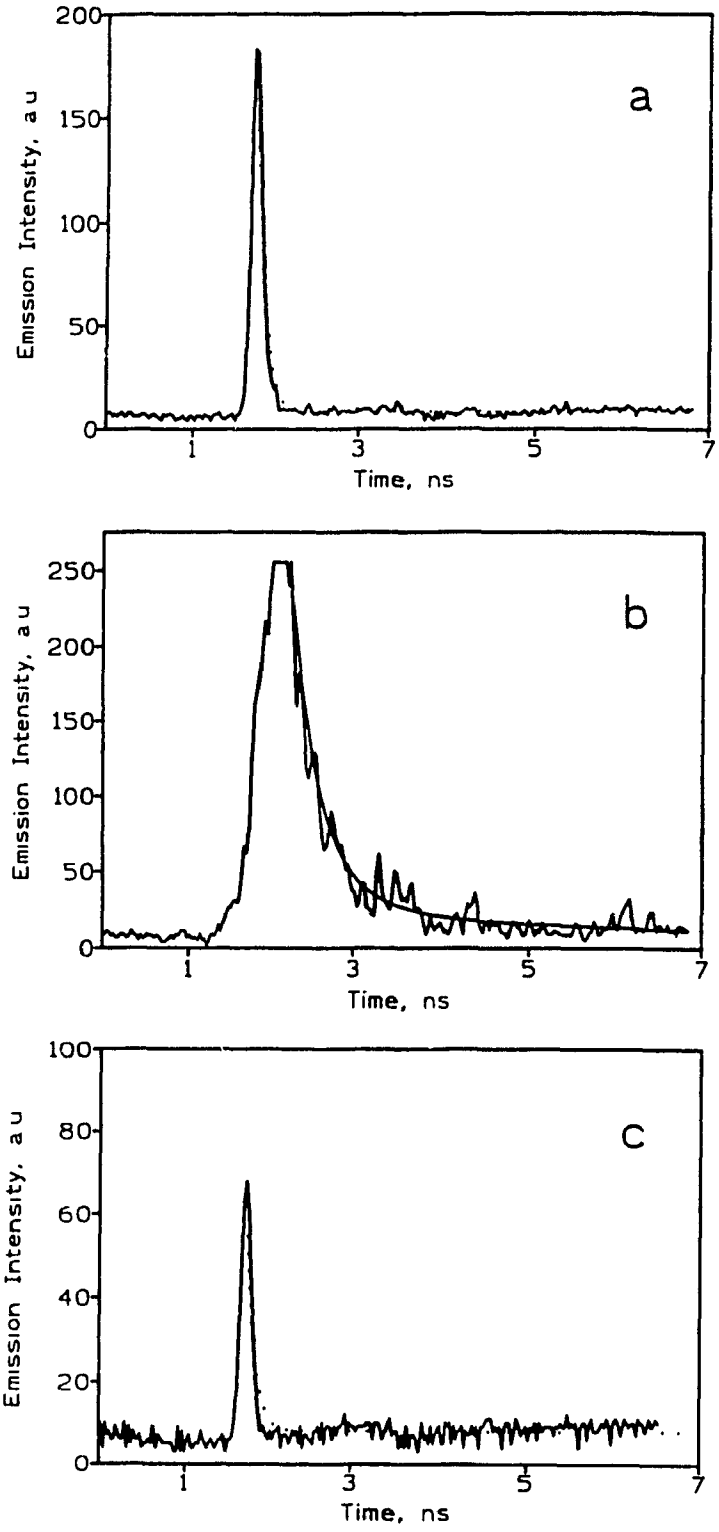

Figure 5.8 Transient emission decay for the luminescence of 15 g/L colloidal TiO_2 at wavelengths greater than 400 nm; (a) 23 Å diameter particles (b) 133 Å diameter particles and (c) 281 Å diameter particles.

affected by the particle size.

5.5 TRANSIENT ABSORPTION STUDIES OF COLLOIDAL TiO_2

The temporal evolution of the transient spectra in the picosecond and nanosecond time domains are illustrated in Figures 5.9 through 5.11 for the 23 Å, 133 Å and 281 Å TiO_2 particles, respectively.

Excitation of the TiO_2 sols with a 30-ps, 355-nm laser pulse generates electron/hole pairs in the particle (equation 5.5).

$$TiO_2 \xrightarrow{h\nu} TiO_2\,(e^-_{cb},\ h^+_{VB}) \rightarrow e^-_{CB} + h^+_{VB} \qquad (5.5)$$

Following charge separation, in competition with recombination, the e^- and h^+ can migrate to the surface, can be trapped at defect sites in the lattice and can also be trapped at surface sites as Ti^{III} for the electron and as $\{Ti^{IV}\text{-}O^{\bullet}\text{-}Ti^{IV}\}\text{-}OH^- \leftrightarrow \{Ti^{IV}\text{-}O^{2}\text{-}Ti^{IV}\}\text{-}^{\bullet}OH$ for the hole. The average diffusion time (θ) of the charge carrier from the bulk to the surface can be estimated by the relationship 5.6:[25]

$$\theta = \frac{r^2}{\pi^2 D} \qquad (5.6)$$

where **r** is the particle radius and **D** the diffusion coefficient of the carrier; for TiO_2, D is 2×10^{-2} cm^2/s.[14] The average transit time of the electron from the bulk to the surface is ~ 50 fs for 23 Å sized TiO_2 particles, ~ 1.8 ps for 133 Å TiO_2 particles and ~ 9.9 ps for 281 Å TiO_2 particles. The 20-ps transient spectra of all three different sized TiO_2

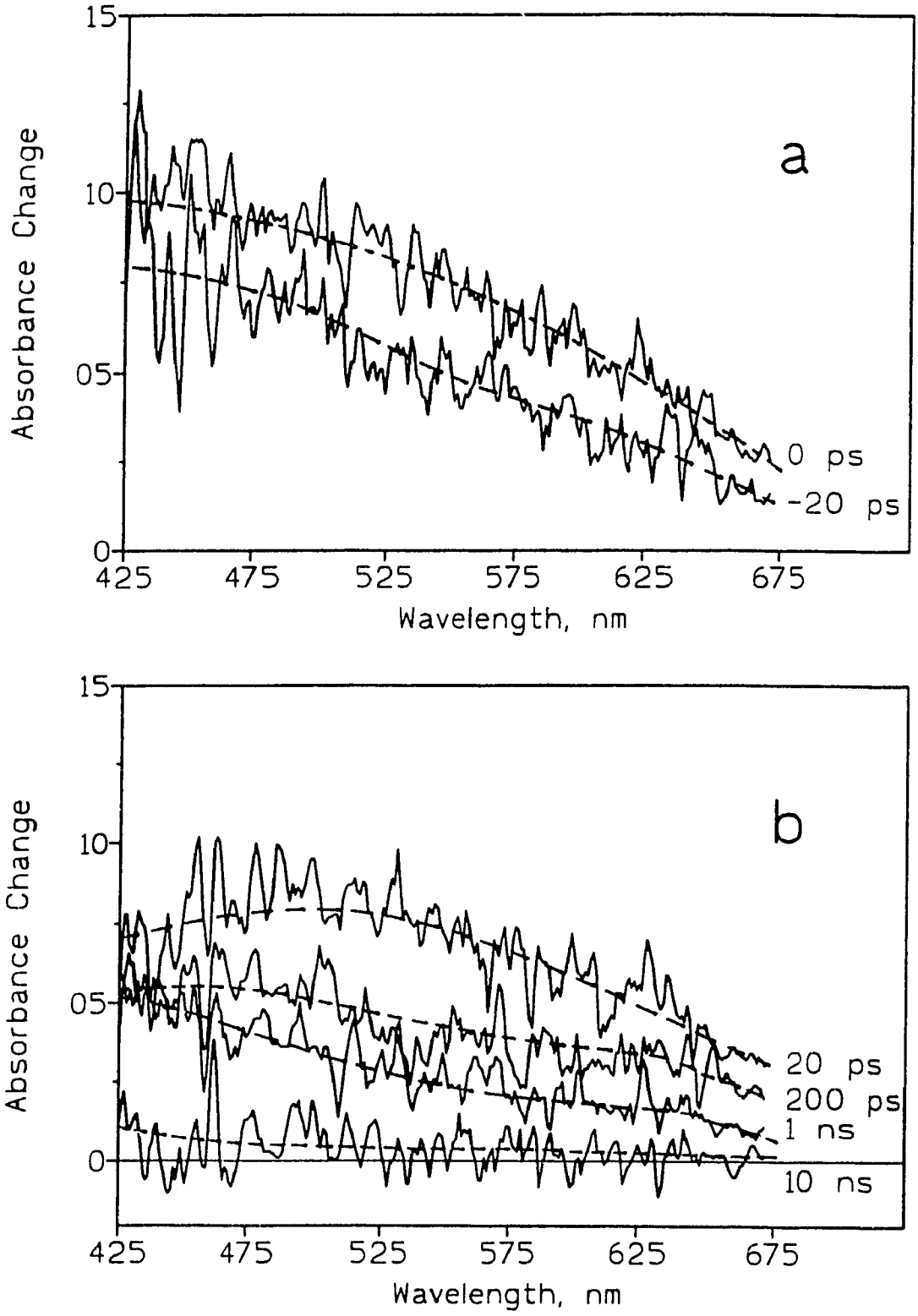

Figure 5.9 Transient spectra observed at various time intervals after picosecond excitation of colloidal 23 Å sized TiO_2. $[TiO_2]$ = 15 g/L; pH 2.7; optical path length 0.2 cm.

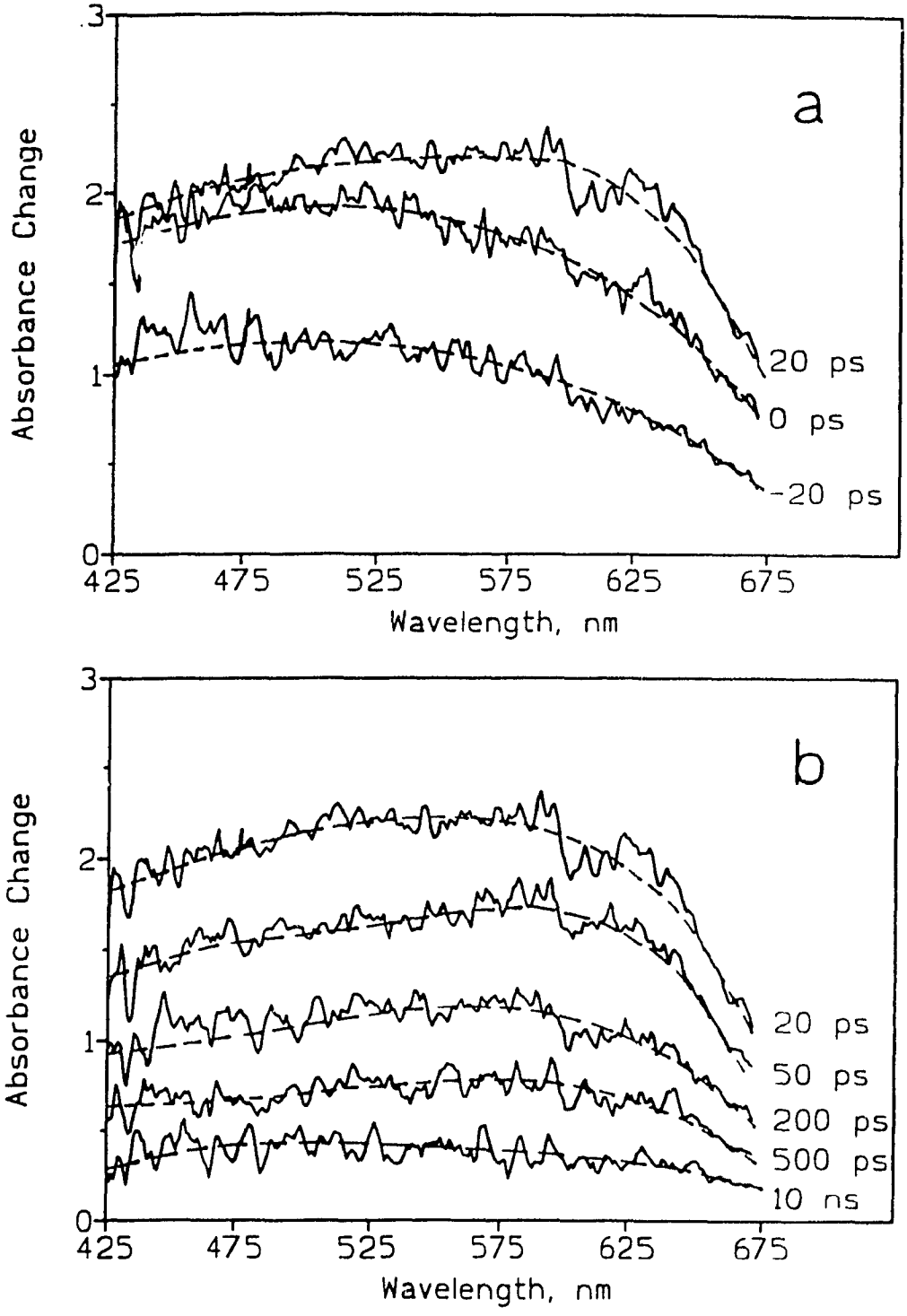

Figure 5.10 Transient spectra observed at various time intervals after picosecond excitation of colloidal 133 Å sized TiO_2. $[TiO_2]$ = 15 g/L; pH 2.7; optical path length 0.2 cm.

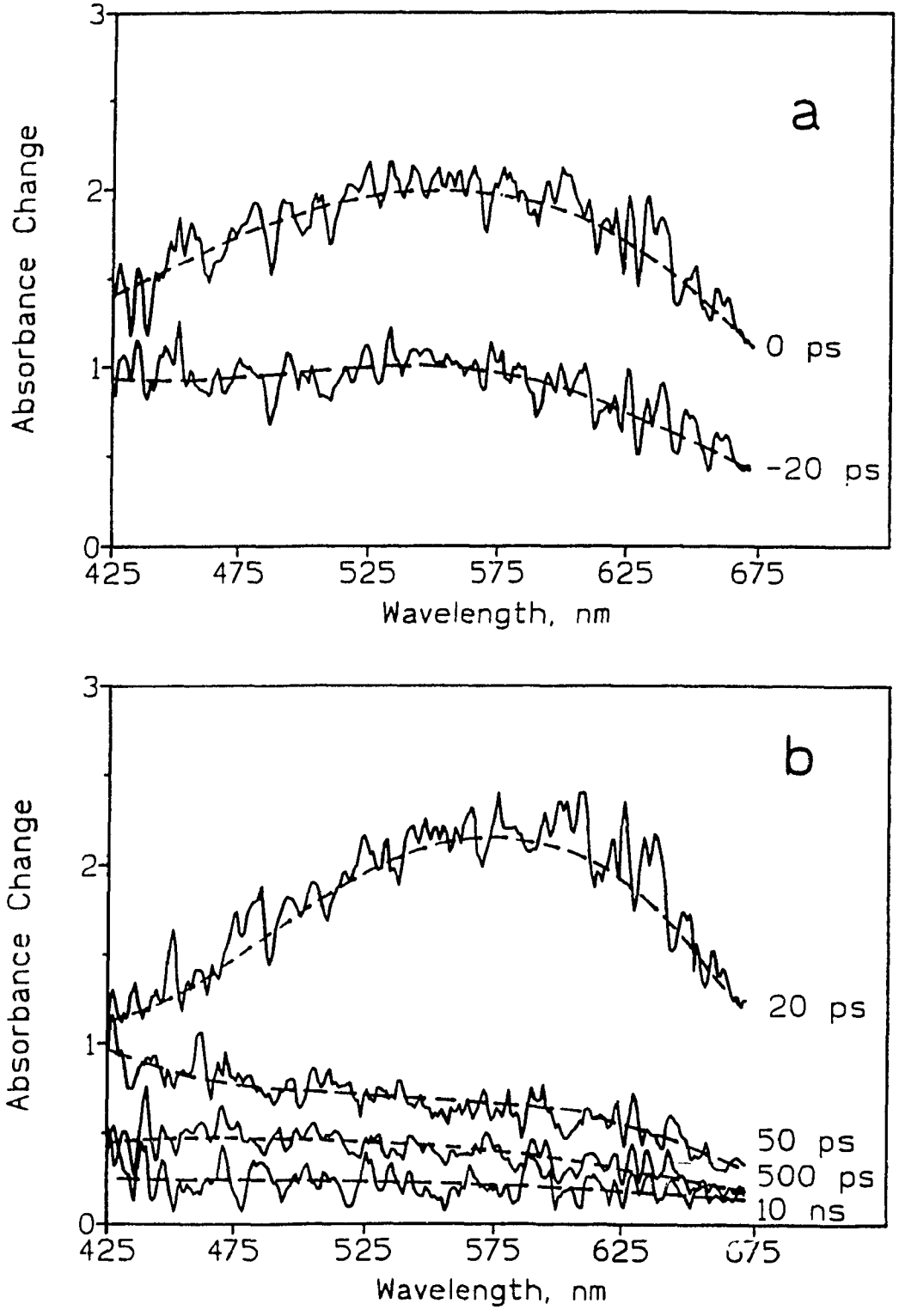

Figure 5.11 Transient spectra observed at various time intervals after picosecond excitation of colloidal 281 Å sized TiO_2. $[TiO_2]$ = 15 g/L; pH 2.7; optical path length 0.2 cm.

show that the transients were fully developed at the end of the 30 ps excitation pulse (Figures 5.9a to 5.11a). It is inferred that in all cases the electron gets trapped in less than 30 ps (pulse-width limited), consistent with the predictions of equation 5.6. This puts a lower limit for the e^- trapping rate: $k_{tr} \geq 3 \times 10^{10}\ s^{-1}$.

The number of electron/hole pairs per TiO_2 particle, $< x >_0$, immediately present after the excitation laser pulse (i.e. at the end of the laser pulse (20 ps)) was estimated from the TiO_2 particle concentration using Beer's law and the extinction coefficient of the loosely bound electron ($Ti^{IV}...e^-$) taken at 600 nm as $\epsilon_{600} = 1200\ M^{-1}\ cm^{-1}$.[20,26] For example, for the 133 Å TiO_2 particles the absorbance at 600 nm in a 0.2 cm cell is 0.198. The concentration of the absorbing species, in this case the electron, is therefore 0.198/(1200*0.2) = 8.25×10^{-4} M. The number of electron/hole pairs is thus simply this concentration divided by the particle concentration: 8.25×10^{-4} M / 5.26×10^{-6} M or 157 pairs. Similarly for the 23 Å and 281 Å TiO_2 particles, $< x >_0$ is estimated to be 0.3 and 1754 pairs, respectively. Note that the estimate for the 23 Å TiO_2 particles must be considered a lower limit since the electron is more likely localized at a surface state or an energy level at the surface of the particle (for example, as Ti^{III}). The number of photons in the laser pulse impinging onto a 2 mm spot was determined using equation 5.7. For an average pulse energy of 2.5 mJ, the photon flux is estimated to be ~ 1.4×10^{17} photons/cm^2.

$$E = \frac{Nhc}{\lambda} \tag{5.7}$$

where E is the energy in joules/einstein, h is Plank's constant (= 6.626×10^{-34} J s), c

is the speed of light (= 2.998 x 10^8 m/s) and λ the wavelength of excitation (= 355 x 10^{-9} m). Based on the TiO_2 particle concentration in the 0.2 cm cell, the number of photons per particle may be obtained. For example, the particle molar concentration for 15 g/L 133 Å TiO_2 is 5.26 x 10^{-6} M or 5.26 x 10^{-9} moles particles/cm^3 which in a 0.2 cm cell yields 6.3 x 10^{14} particles/cm^2 (multiplying the particle concentration by Avogadro's number, 6.023 x 10^{23}). For an average laser energy of 2.5 mJ, the average number of photons per particle of TiO_2 is then ~ 224. Similarly, the number of photons per particle is calculated to be ~ 1 and ~ 2116 for the 23 and 281 Å TiO_2 particles, respectively. Table 5.1 presents a summary of the relevant data. It is interesting to note that the smaller the particle is, the greater the fraction of e^-/h^+ that have recombined at 20 ps (last column of Table 5.1).

Table 5.1 Number of Photons per TiO_2 Particle

Size TiO_2 [a]	$[TiO_2]_p$* mol/L	Abs. at 600 nm	$[e^-]$[b] mol/L	$<x>_0$[c]	# photons per particle[d]	% e^-/h^+ recomb
23	1.02 x 10^{-3}	0.065	2.77 x 10^{-4}	0.3	1	70
133	5.26 x 10^{-6}	0.198	8.25 x 10^{-4}	157	224	30
281	5.58 x 10^{-7}	0.235	9.79 x 10^{-4}	1754	2116	17

* based on 15 g/L and using equation 5.4.

[b] based on ϵ = 1200, l = 0.2 cm and using equation 5.2; at 20 ps delay.

[c] $<x>_0 = [e^-] / [TiO_2]_p$.

[d] based on photon flux of 1.42 x 10^{17} photons/cm^2 (2.5 mJ).

[e] By 20 ps (i.e. by the end of 30 ps (FWHM) laser pulse). By 1 ns, the fraction of e^-/h^+ pairs that have recombined are: 91% (23 Å); 86% (133 Å); and 91% for the 281 Å TiO_2.

The transient spectra observed for 133 Å sized TiO_2 particles and illustrated in Figure 5.10 are in excellent agreement with the spectra previously reported by Rothenberger and co-workers.[14] These authors attributed the transient absorption to trapping of the electron by titanium(IV) ions near or at the surface resulting in the formation of Ti^{+3} centres.[26] Supportive of this assignment of the transient spectra as that of a trapped electron was the fact that the 20 ps transient spectrum was identical to an absorption spectrum of electrons produced in acidic (pH 3) TiO_2 sols by continuous illumination in the presence of hole scavengers.[27] Several reports[9,10,12,13,28] detailing the optical characteristics of the photogenerated electron are also consistent with the transient spectra being those of the fully or partially trapped electron. Figure 5.10 shows that the spectra may be composites of the spectrum of the trapped e^- as Ti^{III} ($\sim$ 500 nm), the trapped h^+ as $\{Ti^{IV}\text{-}O^{-\bullet}\text{-}Ti^{IV}\}\text{-}OH^- \leftrightarrow \{Ti^{IV}\text{-}O^{2-}\text{-}Ti^{IV}\}\text{-}^{\bullet}OH$ at $\sim$ 350-360 nm which shows an onset of absorption at approximately 470 nm (see chapter 4), and that of the loosely bound electron ($Ti^{IV}\ldots e^-$) with a maximum at $\sim$ 600 nm. A weak transient absorption remained after 10 ns which suggests that under the conditions of the experiment complete electron/hole recombination must occur at times longer than 10 ns. The lifetime of the minority carrier (h^+) in 120-Å size TiO_2 was estimated as $\sim 30 \pm 15$ ns.[14]

In the 23 Å TiO_2 particles (Figure 5.9), the electron and hole are also trapped within the pulse. However, the spectra differ from those of the 133 Å TiO_2 particles in that the apparent absorption maximum appears blueshifted. This feature probably arises, in part, from a greater component due to the trapped hole which absorbs at wavelengths below 425 nm (see chapter 4). A spectral maximum forms at $\sim$ 500 nm after 20 ps;

there is weaker absorption in the 600 nm region. It is inferred that a larger fraction of the electrons surface localized as a Ti^{III} site. Very little transient absorption remains after 10 ns suggesting that electron/hole recombination is nearly complete by this time.

The transient absorption spectra of the 281 Å TiO_2 particles at delay times below 20 ps are very similar to those of the 133 Å particles; however, the absorption maximum at ~ 600 nm is more pronounced at the end of the laser pulse (20 ps). This inters that a larger fraction of the electrons may be loosely bound than is the case in the 23 and 133 Å TiO_2 particles. The transient absorption decayed very rapidly initially (τ ~ 50 ps; Table 5.2) as shown by the sharp decrease in the broad absorption from 20 to 50 ps delay. The rapid decay may be explained by the following consideration. The electron in the 281 Å TiO_2 particles may be delocalized more than in the 23 and 133 Å particles and therefore more likely to migrate on the surface of the particle. This should increase the likelihood of electrons recombining with a trapped hole at some non-radiative recombination centre.

The change in absorbance with time at various wavelengths for the different sized TiO_2 particulates is given in Figure 5.12. The absorbance changes show biphasic decay kinetics at all wavelengths (see Table 5.2) with the slow and fast components showing some dependence on the monitoring wavelength (see Figure 5.13). The increased scatter at the different wavelengths in the slower τ component simply reflect the complexity of the broad transient spectra.

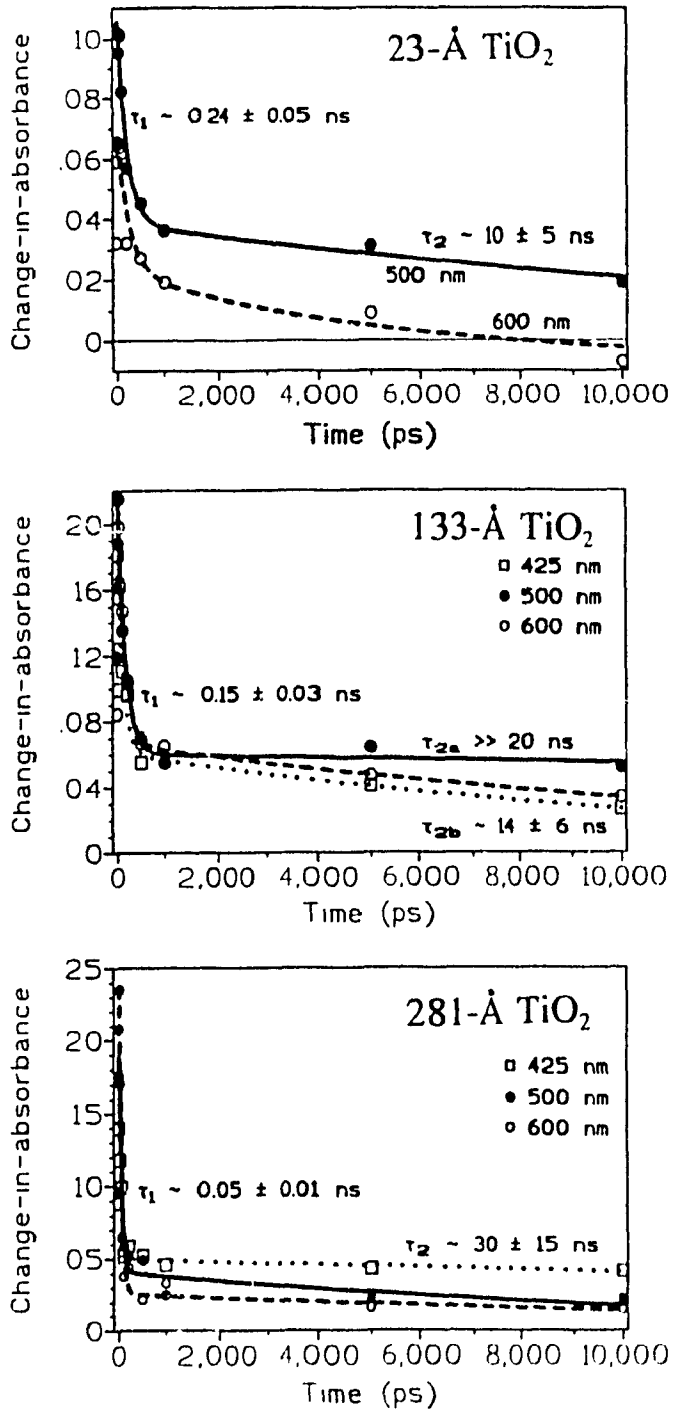

Figure 5.12 Change-in-absorbance with time at various wavelengths for the 23, 133 and 281 Å TiO_2 particles. The solid and dashed lines are fits of the data to a double exponential decay.

Table 5.2 Average Lifetimes Obtained From a Computer Fit of the Change-in-Absorbance versus Time for the Different Sized TiO_2.

TiO_2 size, Å	τ_{fast}, ns	τ_{slow}, ns
23	0.24 ± 0.05	10 ± 5
133	0.15 ± 0.03	14 ± 6
281	0.05 ± 0.01	30 ± 15

The components for the absorption decay at the different wavelengths do not follow the same behaviour as the transient emission decay times (inset Figure 5.13) suggesting that the transient absorption and emission features have different origins. The emission is attributed to electron/hole recombination, and absorption originates with the different photochemical events following light absorption. Whatever the precise nature of the two decay components, particle size seems to have an opposite effect on the two components (Figure 5.13). The lifetime of the fast decay component decreases with increasing particle size; that of the slower decay component seems to increase with increasing particle size. The two processes may be rationalized in the following manner. The fast component originates with recombination of "free" electron/hole pairs or recombination of electrons or holes trapped in shallow traps on the surface. The slow component must have its origins with a surface trapped electron ($Ti^{IV}...e^-$) and a surface trapped hole in a deep energy trap: as $\{Ti^{IV}\text{-}O^{2-}\text{-}Ti^{IV}\}\text{-}\bullet OH$; alternatively or concomitantly, it may also reflect the reaction of trapped electrons with a reducible impurity centre such as oxygen (reactions 5.8).

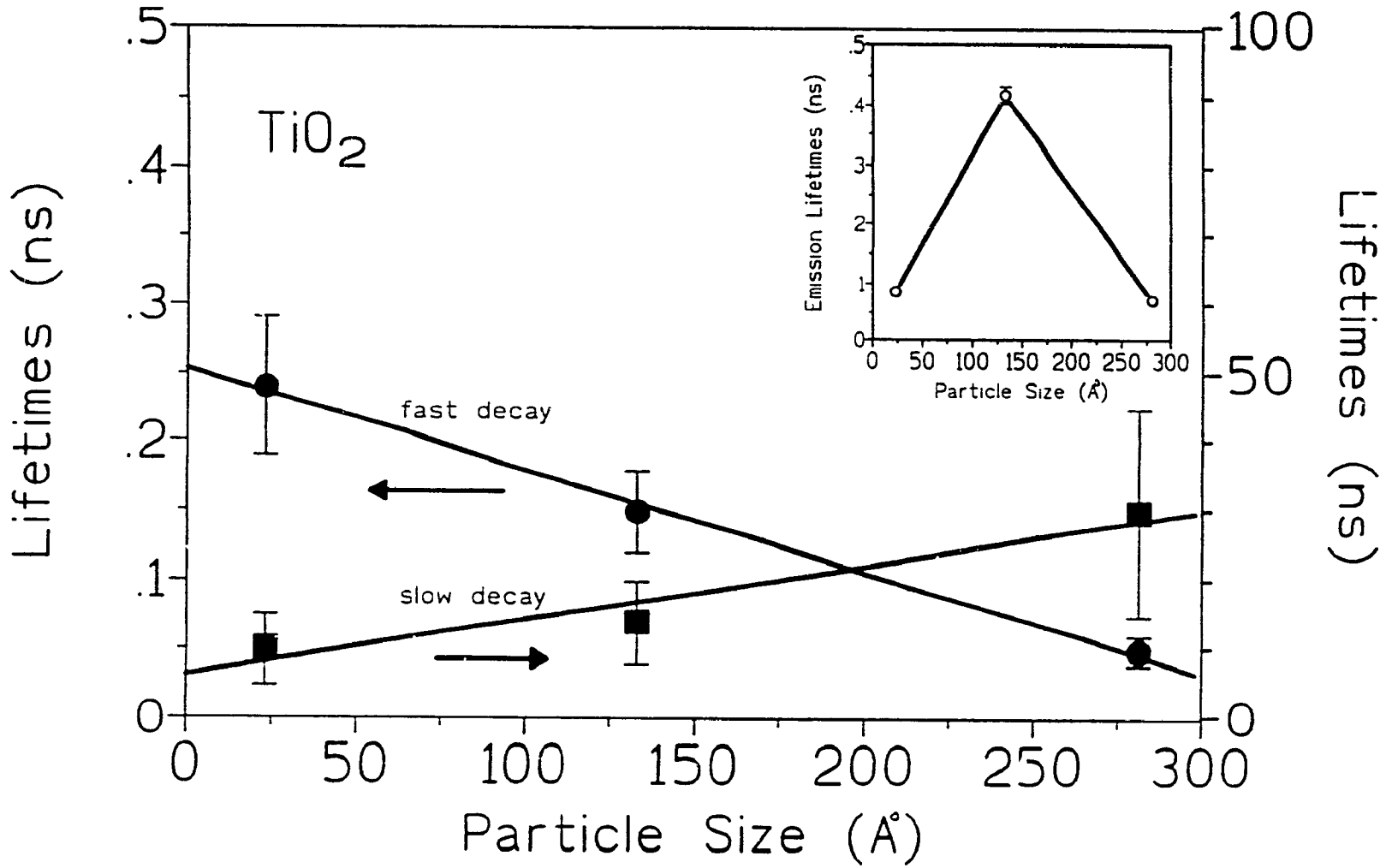

Figure 5.13 Effect of TiO_2 particle size on the lifetimes of the fast and slow components of the biphasic kinetics of the change-in-absorbance at various wavelengths with time (see Figure 5.12). Inset shows the effect of particle size on the emission lifetimes.

$$e_{tr}^{-}\ (TiO_2) + h_{tr}^{+}\ (TiO_2) \rightarrow TiO_2 \qquad \textbf{(5.8a)}$$

$$e_{tr}^{-}\ (TiO_2) + \textit{impurity species (e.g. } O_2) \rightarrow \textit{products} \qquad \textbf{(5.8b)}$$

The electron in the 23 Å TiO_2 particles is likely more localized than in the 133 and 281 Å particles and therefore there would be greater resistance for it to diffuse along the particle surface. Its lifetime at a particular trap site would therefore be expected to be greater than in the larger particles. Similarly, the probability of a trapped electron encountering a trapped hole should be smaller in the larger particle than in the smaller particle. The lower the probability of the electron and hole encountering each other, the higher is the expected lifetime of the trapped charge carrier; as such, the lifetimes of the trapped carriers are therefore expected to increase with increasing particle size.

When the number of photons impinging on a target system far exceeds the number of particles, an Auger process could be a predominant mechanism in the fate of the electron/hole pairs (bound excitons), as might be the case for the 133 Å and 281 Å TiO_2 particulates (Table 5.1). Relaxation of the multiexcitonic excited state, $TiO_2\{e^-/h^+\}_m$, can lead to electron (or hole) ejection (reaction 5.9).

$$TiO_2\{e^-/h^+\}_n \rightarrow TiO_2\{nh_{tr}^{+}\} + ne^- \qquad \textbf{(5.9a)}$$

$$TiO_2\{ne^-/h^+\}_n \rightarrow TiO_2\{ne_{tr}^{-}\} + nh^+ \qquad \textbf{(5.9b)}$$

As well, interaction of excitonic excited states with trapped electrons (or trapped holes) can detrap them. Thus,

$$TiO_2\{e^-/h^+\}_{1\ or\ n} + e^-_{tr} \rightarrow e^-_{detrapped} \qquad \textbf{(5.10a)}$$

$$TiO_2\{e^-/h^+\}_{1\ or\ n} + h^+_{tr} \rightarrow h^+_{detrapped} \qquad \textbf{(5.10b)}$$

The outcome of the Auger process is that, under conditions of multiphotonic excitation at high laser fluence, electron and hole recombination is facilitated by detrapping and the rate at which this recombination occurs should scale with the density of electron hole pairs per particle which scales with particle size (Table 5.1). The larger particles have a higher charge carrier density and thus a faster recombination rate (lower lifetime; see Figure 5.13).

5.6 CONCLUSIONS

The present study has examined the absorption, fluorescence, and picosecond transient absorption and emission of 23, 133 and 281 Å diameter TiO_2 colloidal particles. No differences between the different particle sizes of TiO_2 was noted in the absorption properties; however, significant variations in the dynamics of charge carrier recombination were noted. Colloidal sols of 23, 133 and 281 Å diameter TiO_2 particles do not display typical quantum-size properties such as blue shifts in the UV-vis spectrum associated with decreasing particle size. The absorption depends on particle concentration and follows a Beer-Lambert behaviour in the 0 to 15 g/L concentration

range. The band edge luminescence was strongest in the 133 Å TiO_2 particles. Further, transient emission studies indicated that the radiative electron/hole recombination is slowest in the 133 Å TiO_2 particles. Interestingly, this particle size of TiO_2 was recently shown by Grätzel and co-workers to be optimal in the derivatization of TiO_2 with ruthenium complexes for use in photovoltaic devices.[29] The picosecond transient absorption spectra indicated that the localization of the electron as a Ti^{III} species was strongest in the 23 Å TiO_2 particles and decreased with increasing particle size. The fast component of the transient absorption decay was smallest in the 281 Å particles, contrary to the slow component which is somewhat larger in these particles. It is tempting to suggest that an optimal TiO_2 particle size exists for efficient electron transfer reactions at the particle/solution interface. Such a notion could have interesting implications in photocatalytic applications.

References

1. For some recent reviews see:
(a) *"Photochemical Energy Conversion"*; Norris, J.R. & Meisel, D. (Eds.), Elsevier, New York, 1989;
(b) Harriman, A., *Photochemistry*, **1986**, 17, 601;
(c) *"Homogenous and Heterogenous Photocatalysis"*, Pelizzetti, E. & Serpone, N. (Eds.), Reidel, Dordrecht, The Netherlands, **1986.**

2. Grätzel, M., *Acc. Chem. Res.*, **1981**, 41, 376.

3. Grätzel, M., *"Heterogeneous Photochemical Electron Transfer"*, CRC Press, Boca Raton, **1989**.

4. Kalyansundaram, K., Grätzel, M. and Pelizzetti, E., *Coord. Chem. Rev.*, **1986**, 69, 57.

5. (a) Henglein, A., *Top. Curr. Chem.*, **1988**, 143, 113.
(b) Henglein, A., *Chem. Rev.*, **1989**, 89, 1861.

6. Kamat, P.V. and Dimitrijevic, N.M., *Sol. Energy*, **1990**, 44, 83.

7. Brus, L., *J. Phys. Chem.*, **1986**, 90, 2555.

8. Völz, H.G., Kämpf, G., and Fitzky, H.G., *Farbe Lack*, **1972**, 78, 1037.

9. Henglein, A., *Topics Curr. Chem.*, **1988**, 143, 113.

10. Henglein, A., *Ber. Bunsenges Phys. Chem.*, **1982**, 86, 241.

11. Duonghong, D., Ramsden, J. and Grätzel, M., *J. Am. Chem. Soc.*, **1982**, 104, 2977.

12. Bahnemann, D., Henglein, A., Lillie, J. and Spanhel, L., *J. Phys. Chem.*, **1984**, 88, 709.

13. Bahnemann, D., Henglein, A. and Spanhel, L., *Faraday Disc. Chem. Soc.*, **1984**, 78, 151.

14. Rothenberger, G., Moser, J., Grätzel, M., Serpone, N. and Sharma, D.K., *J. Am. Chem. Soc.*, **1985**, 107, 8054.

15. Howe R.F. and Grätzel, M., *J. Phys. Chem.*, **1985**, 89, 4495.

16. Kormann, C., Bahnemann, D.W. and Hoffmann, M.R., *J. Phys. Chem.*, **1988**, 92, 5196.

17. As an example, see: Haase, M., Weller, H. and Henglein, A., *J. Phys. Chem.*, **1988**, 92, 4706.

18. As an example, see: Rossetti, R., Ellison, J.L., Gibson, J.M. and Brus, L.E., *J. Phys. Chem.*, **1984**, 80, 4403.

19. As an example, see: Micic, O.I., Meglic, M., Lawless, D., Sharma, D.K. and Serpone, N., *Langmuir*, **1990**, 6, 487.

20. Moser, J., PhD dissertation, Thesis No. 616, Ecole Polytechnique Fédérale de Lausanne, Lausanne, Switzerland, **1986**.

21. Grätzel, M., *"Heterogenous Photochemical Electron Transfer"*, CRC Press, Boca Raton, Fl., **1987**.

22. Ciavatta, L., Ferri, D. and Riccio, G., *Polyhedron*, **1985**, 4(1), 15.

23. Sclafani, A., Palmisano, L. and Schiavello, M., *J. Phys. Chem.*, **1990**, 94, 829.

24. Serpone, N. and Kennepohl, P., unpublished observations, December 1992.

25. Grätzel, M. and Frank, A.J., *J. Phys. Chem.*, **1982**, 86, 2964.

26. Howe R.F. and Grätzel, M., *J. Phys. Chem.*, **1985**, 89, 4495.

27. Kolle, U., Moser, J. and Grätzel, M., *Inorg. Chem.*, **1985**, 24, 2253.

28. Duonghong, D., Ramsden, J. and Grätzel, M., *J. Am. Chem. Soc.*, **1982**, 104, 2977.

29. (a) Grätzel, M., work presented at the 1991 ACS meeting, New York.
(b) Grätzel, M., in *"Photochemical Energy Conversion"*, Norris, J.R. and Meisel, D. (Eds.), Elsevier, New York, **1989**.
(c) Vlacopoulus, N., Liska, P., Augustinski, J. and Grätzel, M., *J. Am. Chem. Soc.*, **1988**, 110, 1216.

PAGINATION ERROR.

TEXT COMPLETE.

ERREUR DE PAGINATION.

LE TEXTE EST COMPLET.

NATIONAL LIBRARY OF CANADA.

CANADIAN THESES SERVICE.

BIBLIOTHEQUE NATIONALE DU CANADA.

SERVICE DES THESES CANADIENNES.

CHAPTER 6

PHOTOPHYSICAL STUDIES OF TRANSITION METAL DOPED COLLOIDAL TiO_2

6.1 INTRODUCTION

Titanium dioxide is a stable, highly active semiconductor often used in photocatalysis applications. Recently, much interest has been expressed in using TiO_2 as a photocatalyst in combination with solar or near-UV light to mineralize a number of organic wastewater contaminants. The efficiency of this process to solar energy applications is limited by the near UV ($\lambda \leq 400$ nm) absorption of TiO_2, which uses only a small fraction ($\sim$ 3% [1]) of the solar spectrum (Figure 6.1). Considering the charge carrier species generated, only a small fraction of the charge carrier density will actually be utilized in surface oxidation and reduction processes. This must be considered a fundamental drawback for solar energy applications. Further, interfacial kinetics are limited by rapid electron/hole recombination on the semiconductor, which occurs in nanoseconds time in TiO_2.[2] One potential way to circumvent both limitations is to add dopants into the lattice, which could increase the light absorption properties of TiO_2 into the visible region and which could act as either hole and/or electron traps.

The anatase TiO_2 structure (Figure 6.2a) is made up of four tetragonal TiO_2 units per unit cell which contains slightly distorted TiO_6 octahedra.[3] Three oblong channels,

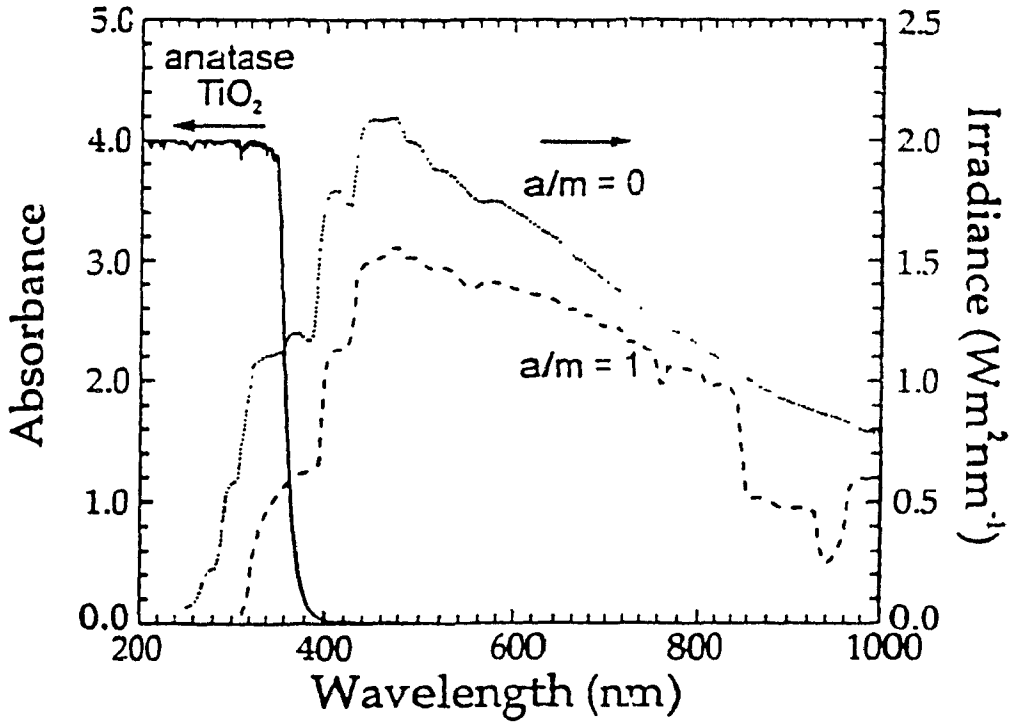

Figure 6.1 Absorption spectra of anatase TiO_2 superimposed upon the irradiance spectrum of sunlight. The spectra of sunlight before entering Earth's atmosphere (a/m=0)# and at the surface with the sun normal to the earth's surface (a/m=1) are shown.

with a diameter ≥ 0.7 Å, penetrate the (010) and (100) faces of anatase in bulk TiO_2. Dopants added to anatase TiO_2 may, therefore, either occupy substitutional lattice positions or, if sufficiently small, interstitial locations.

The type of doping and method of inserting dopants into the TiO_2 lattice should affect the behaviour of TiO_2 as a photocatalyst in solar energy applications. Very little attention has been paid to this aspect.[4,5] Substitutional doping implies that the doping species is added during the TiO_2 synthesis and is not part of electrode preparation [3] All

The a/m ratio is referred to as the air-to-mass ratio and is a means of measuring the intensity of the solar radiation received at the earth's surface.

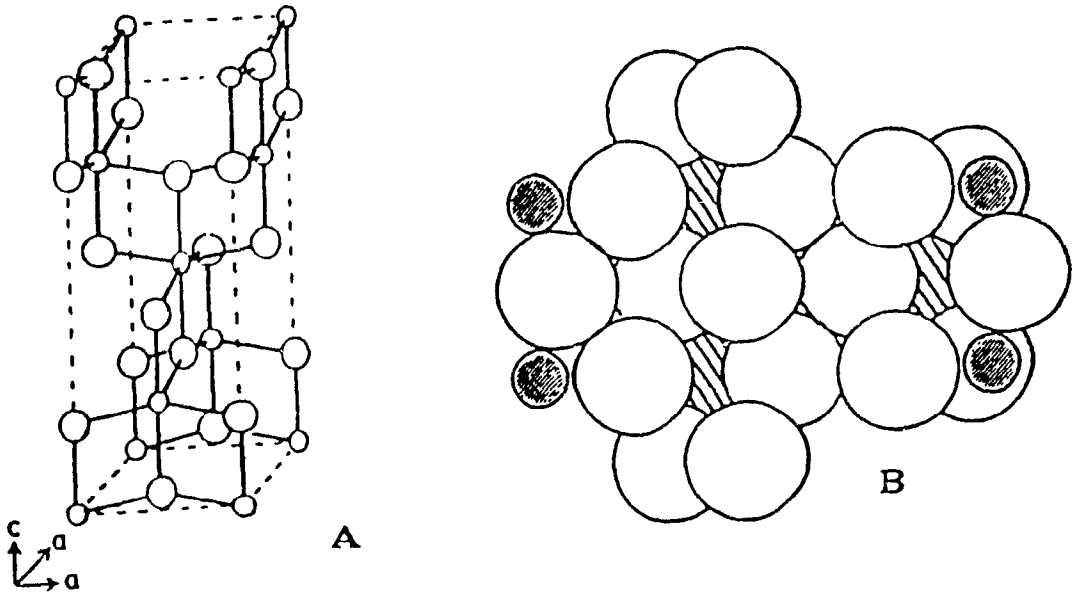

Figure 6.2 (a) the unit cell for anatase; (b) channels available in the (100) face of anatase (crossed region). Adapted from ref. 3.

iron-group elements may conveniently be substituted into the TiO_2 lattice; a number of dopants (e.g. iron and vanadium) have been found to greatly affect the photophysical properties of TiO_2.[6] For example, substitutionally doping the TiO_2 lattice with Fe^{+3} can extend the lifetime of the minority charge carrier to minutes or hours.[7] In addition to increasing carrier lifetime,[8] vanadium doping has shown promise in extending the absorptive range of TiO_2.[9] A number of other metals have also been added to TiO_2 both in the bulk and at the surface for solar energy applications.[3,5,10]

The majority of studies on transition metal doped TiO_2 have focused on the photocatalytic properties of the solid material and only a few photophysical investigations have been carried out.[7-9] Preparation of optically transparent doped TiO_2 colloidal solutions has permitted the use of fast optical techniques to examine the effect the nature of the

dopant and the dopant concentration have on the absorption properties and on the charge carrier recombination dynamics. This chapter reports on the absorption, fluorescence, and picosecond transient absorption and emission of transition metal doped TiO_2 colloidal particles.

6.2 SPECTRAL PROPERTIES OF TRANSITION METAL DOPED TiO_2

Several of the transition metal dopants added to the bulk of anatase TiO_2 significantly affected the absorption characteristics of TiO_2; these spectra are presented in Figures 6.3 to 6.8 for systems doped with (i) Cr^{+3}, (ii) Rh^{+3}, (iii) Fe^{+3}, (iv) Ru^{+3} and mixed Ru^{+3}/Pt^{+4}, (v) V^{+5}, V^{+3} and mixed V^{+5}/V^{+3}, (vi) Pd^{+2}, (vii) Re^{+7} and/or Re^{+3}, and finally (viii) mixed Cr^{+3}/Fe^{+3}. For example, vanadium(V) doped samples (Figure 6.7a) *appear* to extend the fundamental band edge absorption into the visible region of the spectrum. One possible explanation for this behaviour is that a dopant energy level is formed within the bandgap of TiO_2. As the concentration of vanadium is increased, the absorption arising from transitions from the valence band to this dopant energy level (if an electron acceptor) would be expected to increase and the effective absorption threshold would thus appear to be redshifted. A similar behaviour is observed with increasing iron(III) concentration (Figure 6.5), except that an absorbance band centred at approximately 475 nm appears to grow-in at higher ($\geq$ 5 weight percent) dopant levels. Chromium(III) (Figure 6.3), rhodium(III) (Figure 6.4), rhenium(III) (Figure 6.8b) and palladium(II) (Figure 6.8a) do not appear to affect the fundamental band edge

absorption threshold of TiO_2; rather, they appear to sensitize the material through formation of a broad band within the visible region of the spectrum. This effect is most pronounced for low doping ($\leq 1\%$ by weight) levels for the ruthenium(III) (Figure 6.6a) and for a mixture (1:1) of platinum(IV)/ruthenium(III)-doped titania systems. At 5 and 10% by weight of Ru^{+3} dopant, absorption has become so intense that in fact the absorption threshold seems to occur in the near infrared region, inaccessible under our experimental conditions; the TiO_2/Ru^{+3} systems appear black at these high dopant levels.

The concentration and the oxidation state of the dopant also appear to have a marked effect on the absorption properties of TiO_2 sols. Increasing the metal dopant concentration increased the spectral features observed. For example, increasing the chromium concentration led to a linear increase in the absorption band at 600 nm (see inset, Figure 6.3). Figure 6.7b illustrates that the addition of V^{+5}, V^{+3}, or a combination of both V^{+5} and V^{+3} (1:1) had different effects on the absorption spectrum of TiO_2. Addition of V^{+5} caused a redshift of the onset of absorption, whereas the addition of V^{+3} resulted in the formation of a broad absorption band centred at approximately 450 nm. Interestingly, a combination (1:1) of V^{+3} and V^{+5} resulted in non-linear optical changes; that is, the spectrum obtained for TiO_2 doped with 1 wt.% V^{+3} and 1 wt.% V^{+5} is not simply the addition spectrum of TiO_2/1 wt.% V^{+3} + TiO_2/1 wt.% V^{+5}. Another example of the effect of the dopant oxidation state can be seen in the rhenium-doped TiO_2 samples. Addition of Re^{+7} seems to have no effect on the absorption properties of TiO_2, while addition of Re^{+3} caused the formation of two absorption bands to appear centred at ~ 600 and 410 nm. A combination of 1 wt.% Re^{+3} and 1 wt.% Re^{+7} resulted in no

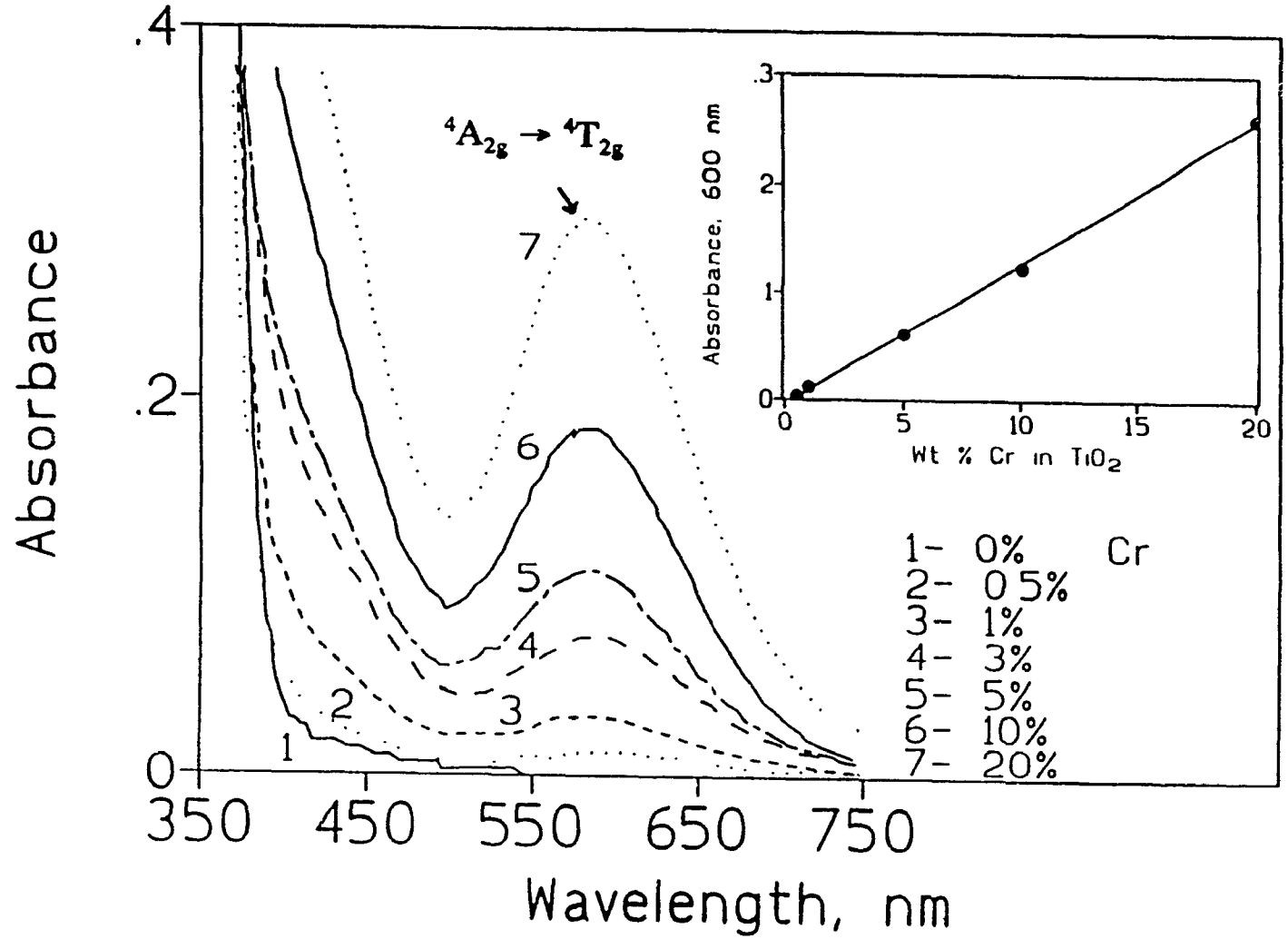

Figure 6.3 Absorption spectra of TiO_2 particles doped with chromium(III); pH = 2.7; optical path length, 1 cm. Inset shows that the changes in absorbance at 600 nm follow Beer-Lambert behaviour.

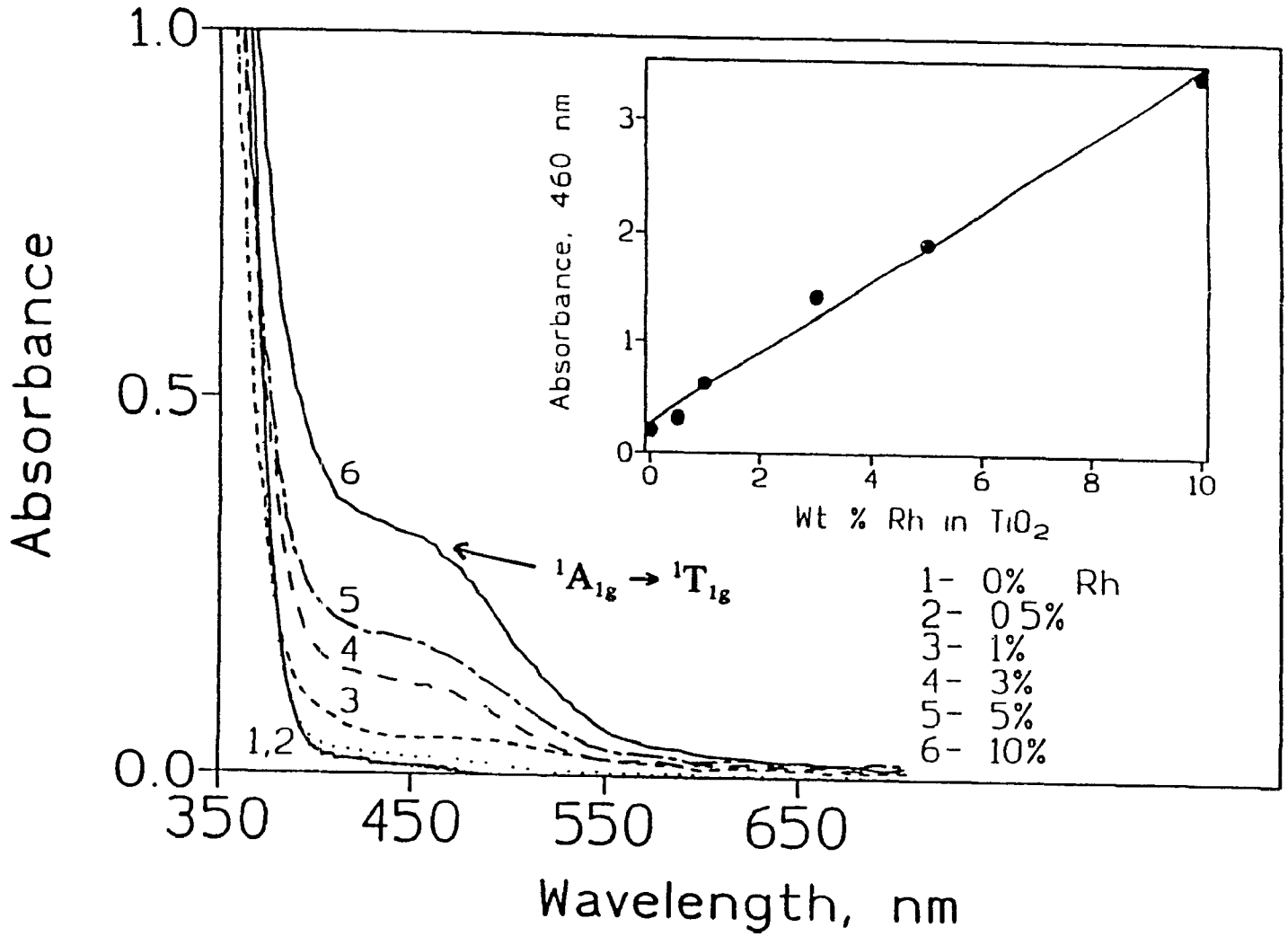

Figure 6.4 Absorption spectra of TiO_2 particles doped with rhodium(III); pH = 2.7; optical path length, 1 cm. Inset shows that the changes in absorbance at 460 nm follow Beer-Lambert behaviour.

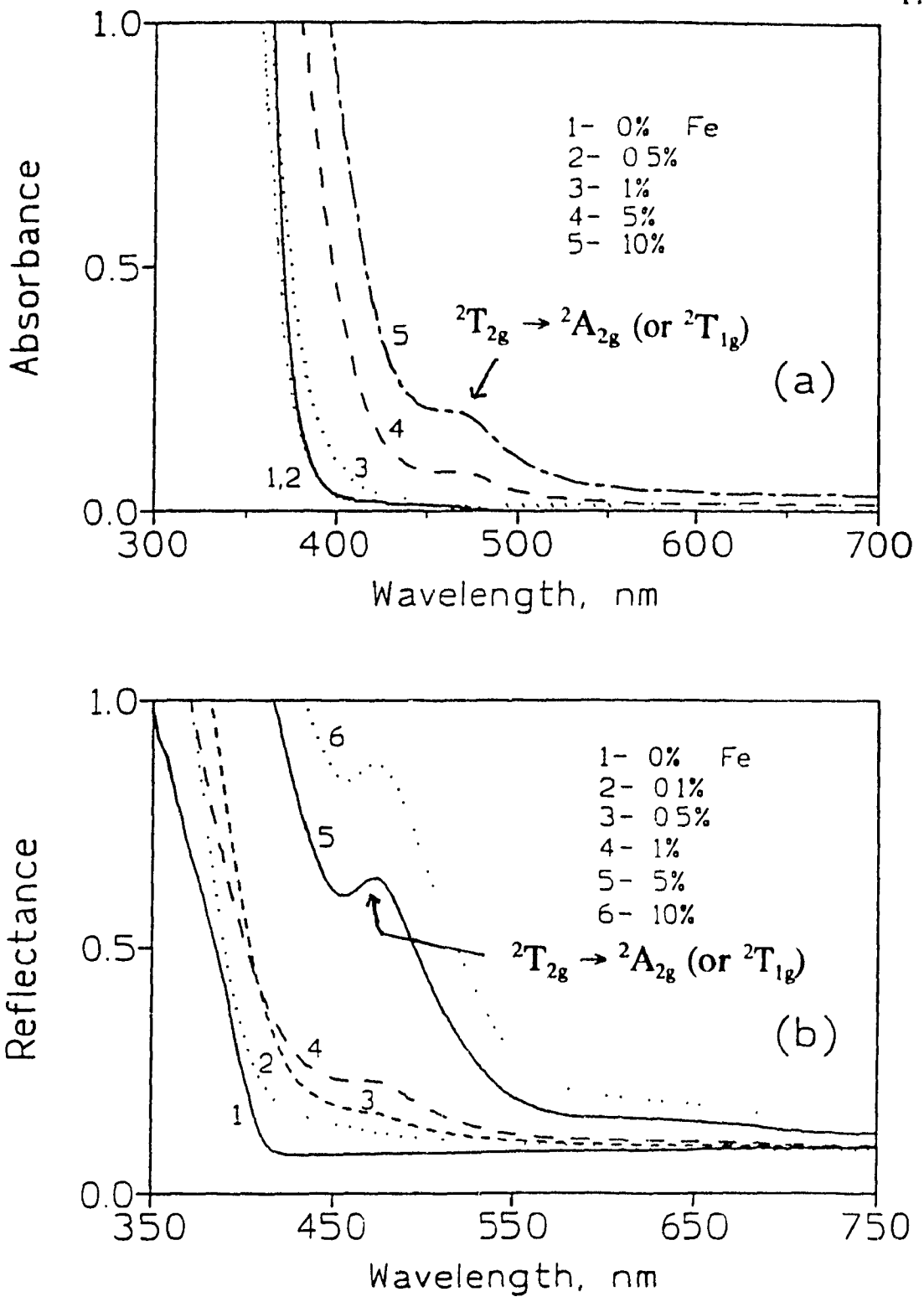

Figure 6.5 (a) Absorption spectra of TiO_2 particles doped with iron(III); pH = 2.7; optical path length, 1 cm. (b) Reflectance spectra of TiO_2/x wt.% Fe(III) particulates on MSI nylon 66 filter paper.

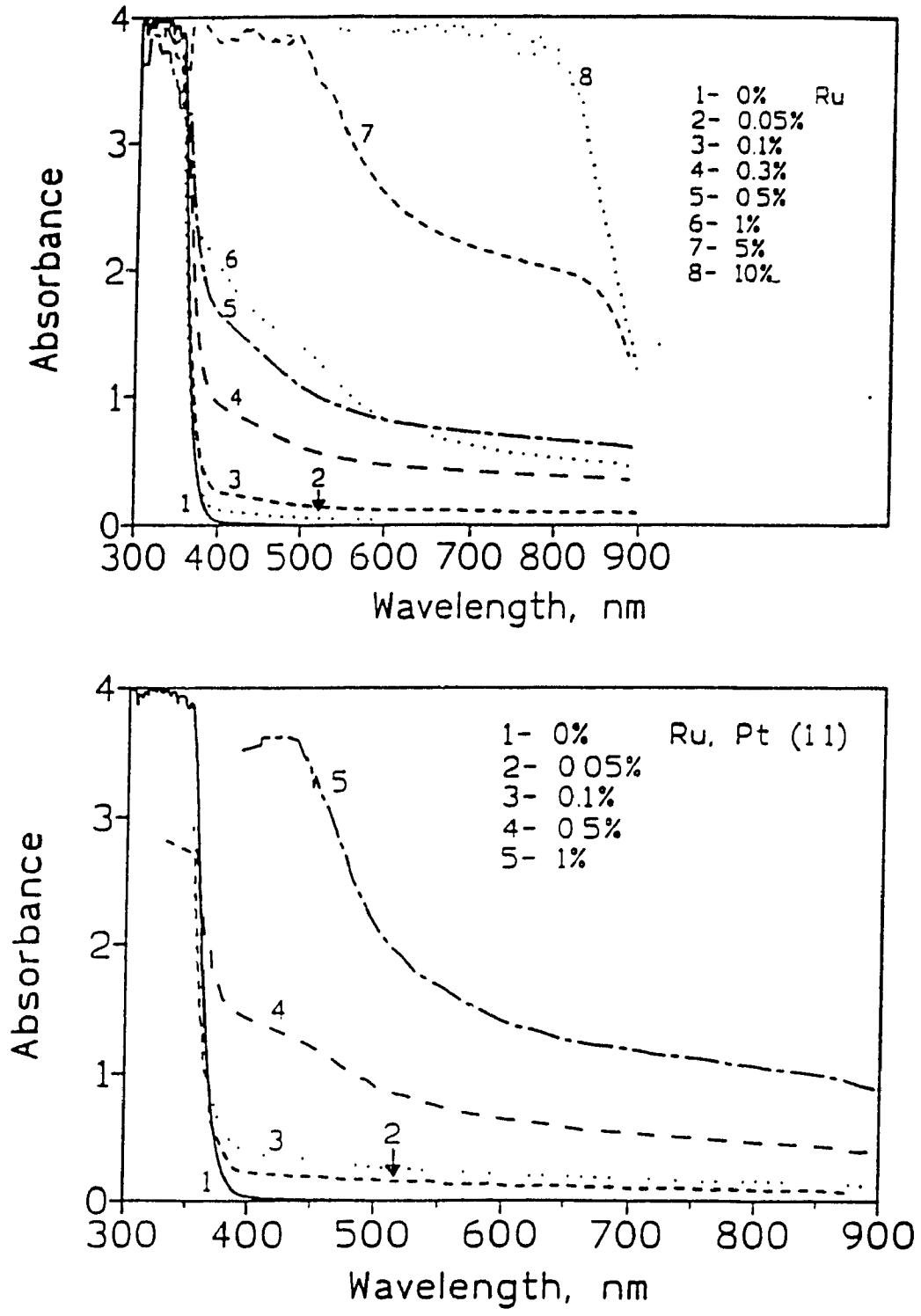

Figure 6.6 (a) Absorption spectra of TiO_2 particles doped with ruthenium(III); pH = 2.7; optical path length, 1 cm. (b) Absorption spectra of TiO_2 particles doped with a mixture of ruthenium(III) and platinum(IV) (1:1); pH 2.5; optical path length, 1 cm. (No assignment of the transitions was made here as the nature of the Ru and Pt is unknown in this material.)

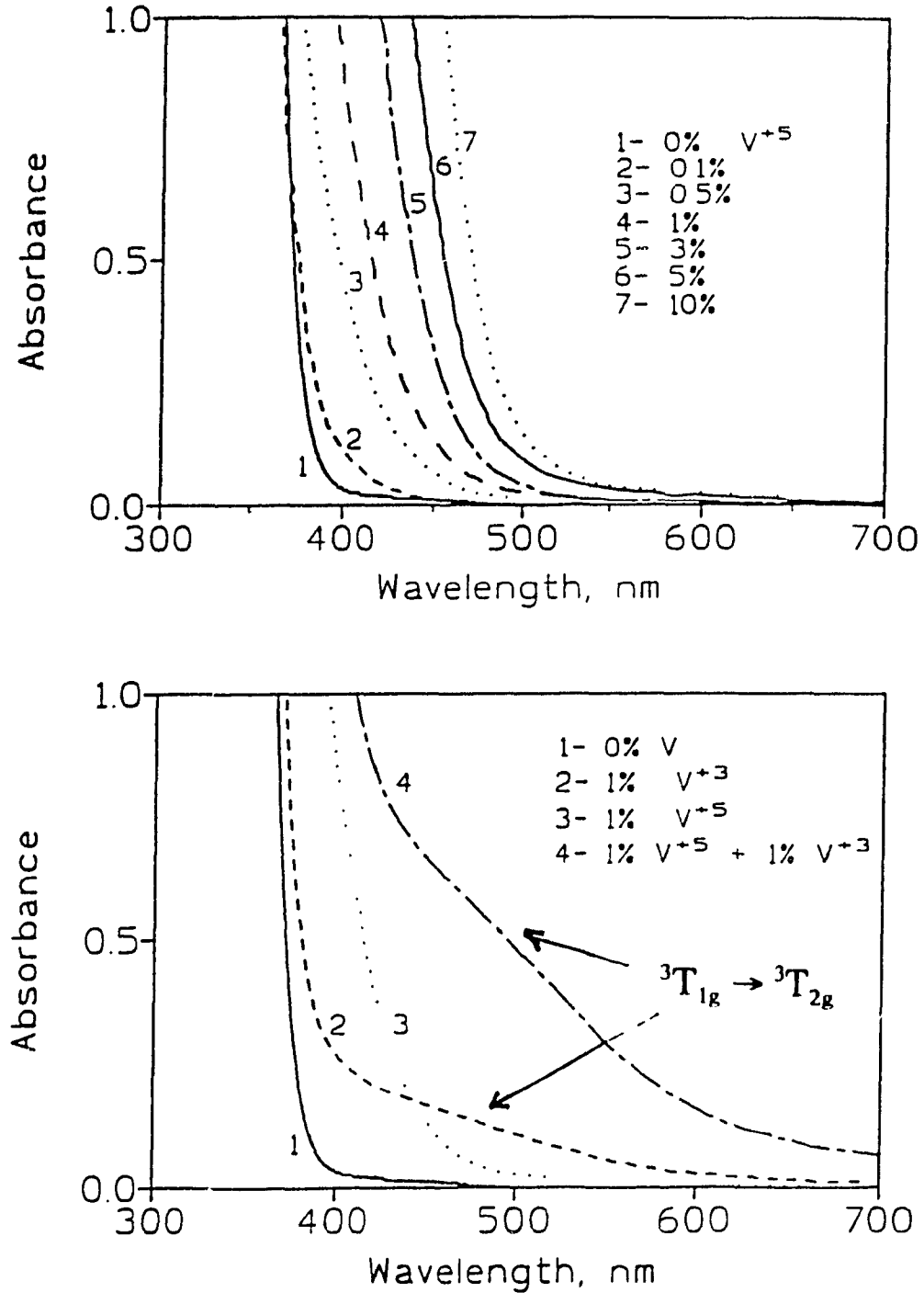

Figure 6.7 (a) Absorption spectra of TiO_2 particles doped with vanadium(V); pH = 2.7; optical path length, 1 cm. (b) Absorption spectra of TiO_2 particles doped with V^{+3}, V^{+5} and V^{+3} and V^{+5} (1:1); pH 2.6; optical path length, 1 cm.

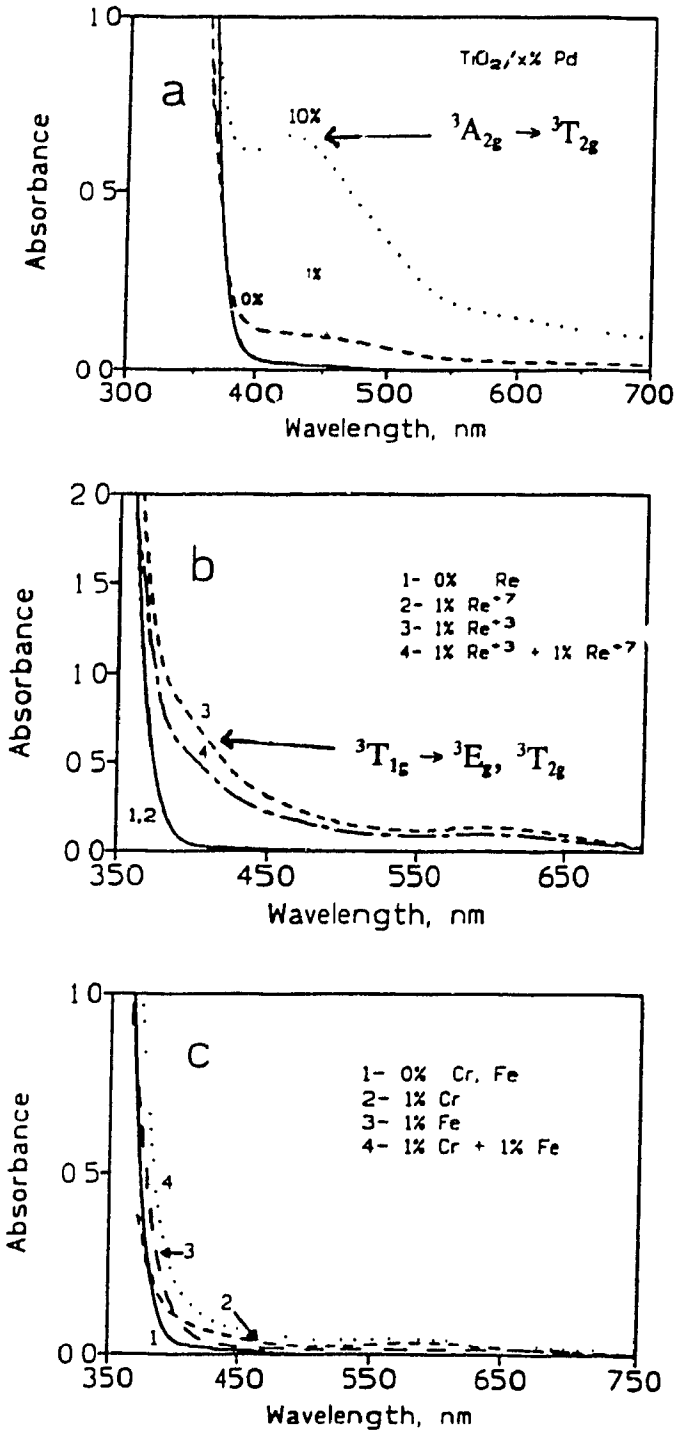

Figure 6.8 (a) Absorption spectra of TiO_2 particles doped with palladium(II); pH = 2.5; optical path length, 1 cm. (b) Absorption spectra of TiO_2 particles doped with Rhenium(III), Rhenium(VII) and Rhenium(III) and Rhenium(VII); pH 2.6; optical path length, 1 cm. (c) Absorption spectra of TiO_2 particles doped with chromium(III), iron(III) and a mixture of the two; pH = 2.5; optical path length, 1 cm.

new spectral features although a small, but finite, decrease in the absorption relative to that of the TiO_2/1 wt.% Re^{+3} was observed.

Although the absolute dopant levels were not determined, there are indications that increasing the dopant concentration led to a proportional increase in the amount of the dopant entering the TiO_2 lattice; i.e., although 5 weight % M may not be exactly 5.00% by weight of TiO_2, it is half the weight percent of a sample containing 10 wt.% of the same dopant. There are two main pieces of evidence which substantiate this hypothesis:

(1) The absorbance spectra of the doped materials, as indicated by a Beer's law type plot (see inserts to Figures 6.3 and 6.4)

(2) An E.D.A.X. (Energy Dispersive Analysis of X-ray fluorescence) study of chromium doped TiO_2 (see below).

The inset of Figure 6.3 shows how the absorbance of various chromium(III)-doped colloids change with chromium concentration at 600 nm. Similarly, the inset of Figure 6.4 shows how the absorbance of various rhodium(III)-doped TiO_2 colloids change with rhodium concentration at 460 nm. As can be seen from both graphs, the behaviour is Beer-Lambert in nature and is a strong indication that increasing the dopant concentration leads to a proportional increase in the amount of the material in the TiO_2 lattice. A similar behaviour is also observable for a number of the other doped materials. Although the possibility that the metal dopant co-exists in solution with the TiO_2 cannot be precluded entirely, this is considered unlikely for two reasons. First, the summation of the absorption spectrum of naked TiO_2 with that of the starting material at their respective concentrations does not correspond to the spectrum obtained for the doped

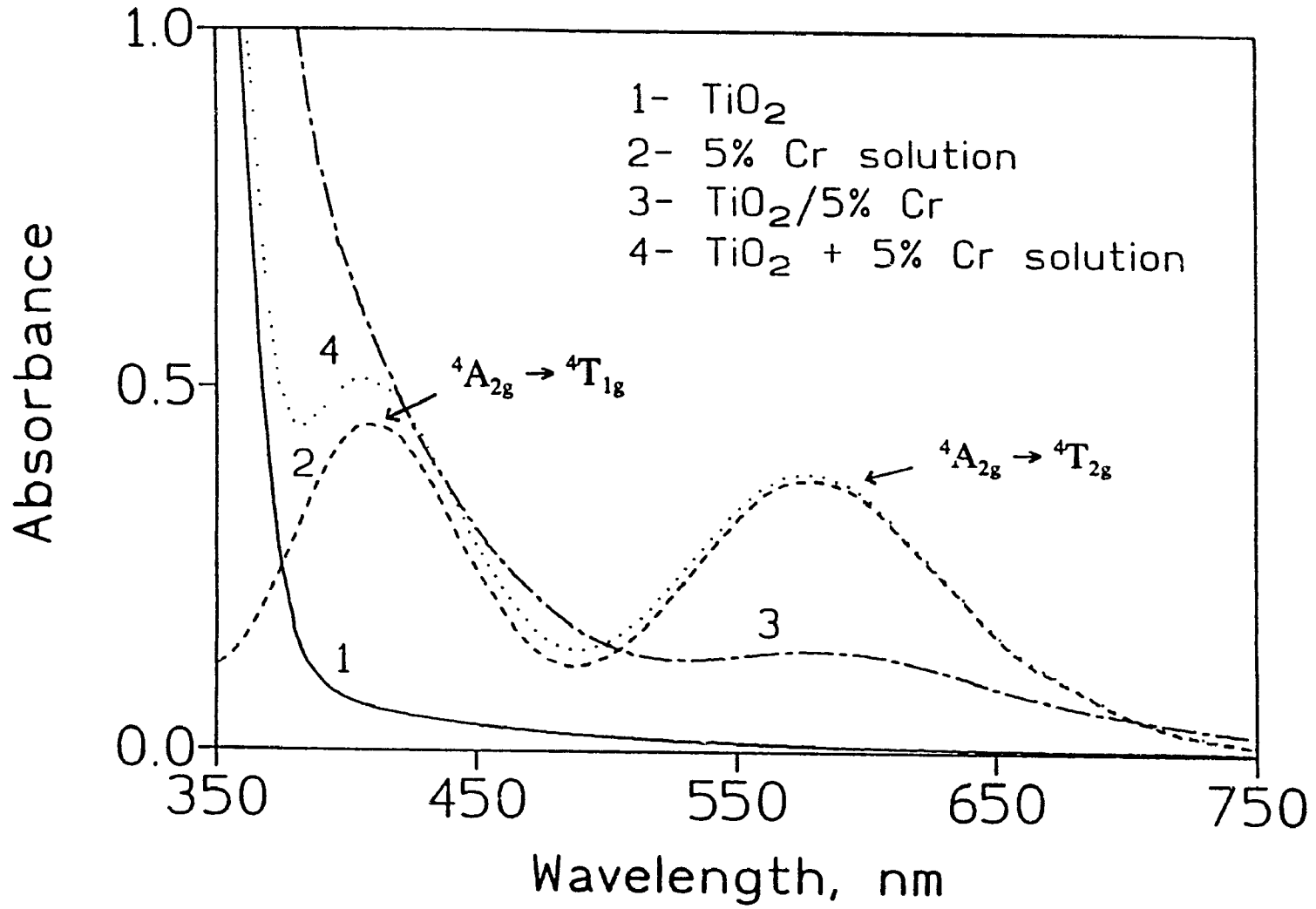

Figure 6.9 Absorption spectra of (1) 13.5 g/L TiO_2 particles, pH 2.8; (2) a pH 2.8 solution containing the same concentration of chromium(III) as would be expected in TiO_2 doped with 5 wt.% Cr; (3) 13.5 g/L TiO_2/5 wt.% Cr(III), pH 2.8; (4) the addition spectrum of (1) and (2).

material (Figure 6.9). Second, when a solution containing only the metal dopant (pH adjusted to that of the undoped material; i.e. pH 2 to 3) was added to a solution containing only TiO_2, precipitation occurred immediately, suggesting that co-existence of the starting material and colloidal TiO_2 is not possible. Further, the transmission electron microscopy micrographs (see chapter 3) of the doped materials revealed only one particulate species.

Energy dispersive analysis of x-ray fluorescence (E.D.A.X.) is a very sensitive technique for detecting the elemental composition of a material. Essentially a high energy beam of electrons is used to remove a core electron of the element with a subsequent release of energy in the form of fluorescence. Since the energy of the valence shell electrons is unique to each element, the technique can unambiguously identify which elements are present in the material. Although the technique is dependent upon the sample concentration, an internal standard could be used to compare the metal concentration between a series of similar samples. Figure 6.10 shows the results obtained from E.D.A.X. studies done on chromium(III)-doped TiO_2. In order to compensate for differences in sample preparation and hence concentration, the ratio of chromium to titanium in each of the doped materials was used as a standard of comparison since the ratio of titanium to chromium should be concentration independent; i.e., as the amount of chromium introduced into the lattice is increased the relative amount of titanium should decrease. The E.D.A.X. measurements were not calibrated because a homogenous sample containing known amounts of chromium and titanium was unavailable; thus, the results cannot be directly compared to the theoretical values

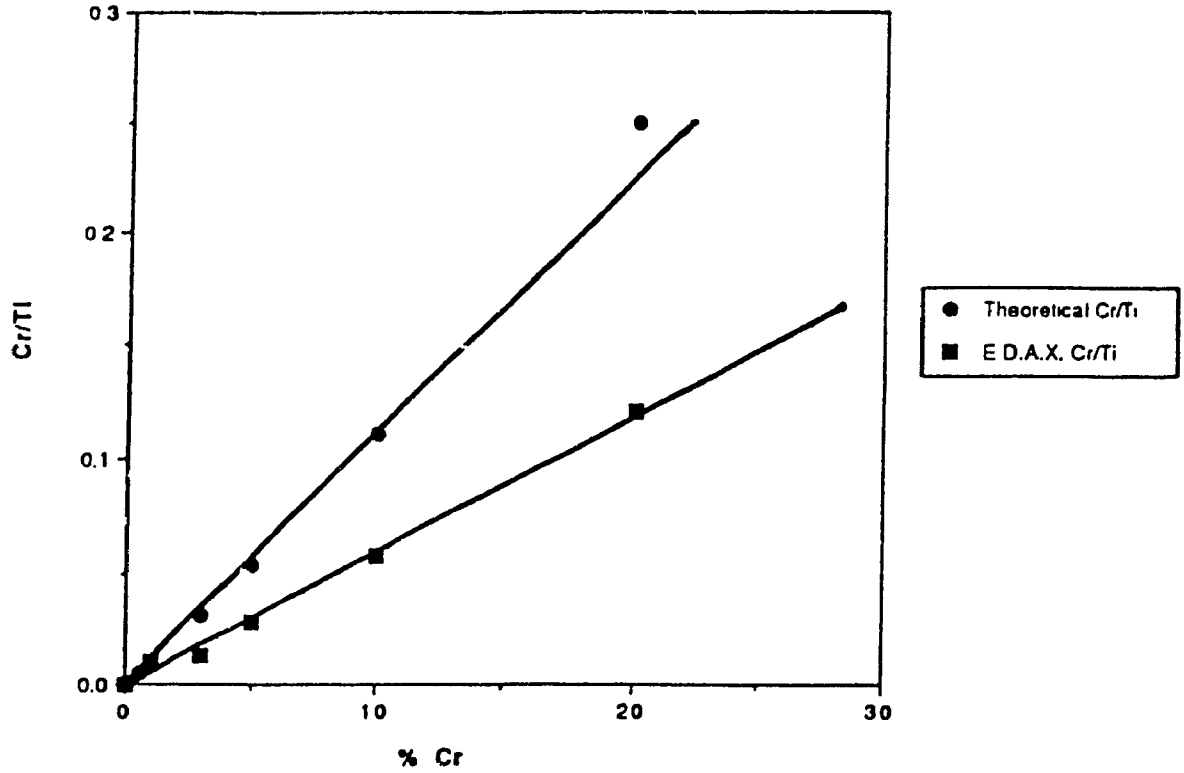

Figure 6.10 Chromium-to-titanium ratio as a function of the chromium concentration in TiO_2/x wt.% Cr and as measured by E.D.A.X. measurements.

indicated in Figure 6.10. However, the linearity of the line strongly suggests that a direct proportional relationship exists between the amount of chromium added and the amount entering the lattice; if this were not the case, then one would expect to see large scatter in the data illustrated in the graph. It is not unreasonable to expect that the other dopants behave in a similar fashion. It is inferred from these observations that the concentration noted for the dopants is that indicated.

6.3 LUMINESCENCE OF TRANSITION METAL DOPED TiO_2

The effect of the dopant concentration on the band edge emission intensity of TiO_2 is illustrated in Figures 6.11 to 6.15. Figure 6.16 summarizes the effect of 1 wt.% metal dopant on the emission of TiO_2, under otherwise identical conditions. All the spectra have been corrected so that the emission corresponds to 100% absorbance of light by the sample. The graphs indicate that there is a wide variation in the way that the different metal dopants affect the band edge emission characteristics of TiO_2. For example, in the cases of vanadium- and chromium-doped systems, increasing the metal concentration leads to a rapid quenching of the emission, followed by a recovery (i.e. increase in the emission) which then levels off at a level lower than that for undoped TiO_2. For the ruthenium(III)-doped TiO_2 systems, the extent of quenching appears to be independent of the ruthenium concentration at all concentrations examined. The emission originated with the TiO_2 doped systems and is not a scatter artifact, nor is it a Raman band of water (see chapter 5). Since the TiO_2 particle size is known to affect band edge luminescence (cf. section 5.3), the question as to the "quenching" of the luminescence is enigmatic. The observed decreases may be due to variations in particle size, quenching by the dopant and/or perhaps by additional surface states introduced by the presence of the dopant(s). However, the presence of the dopant is probably the single most important factor responsible for the quenching.

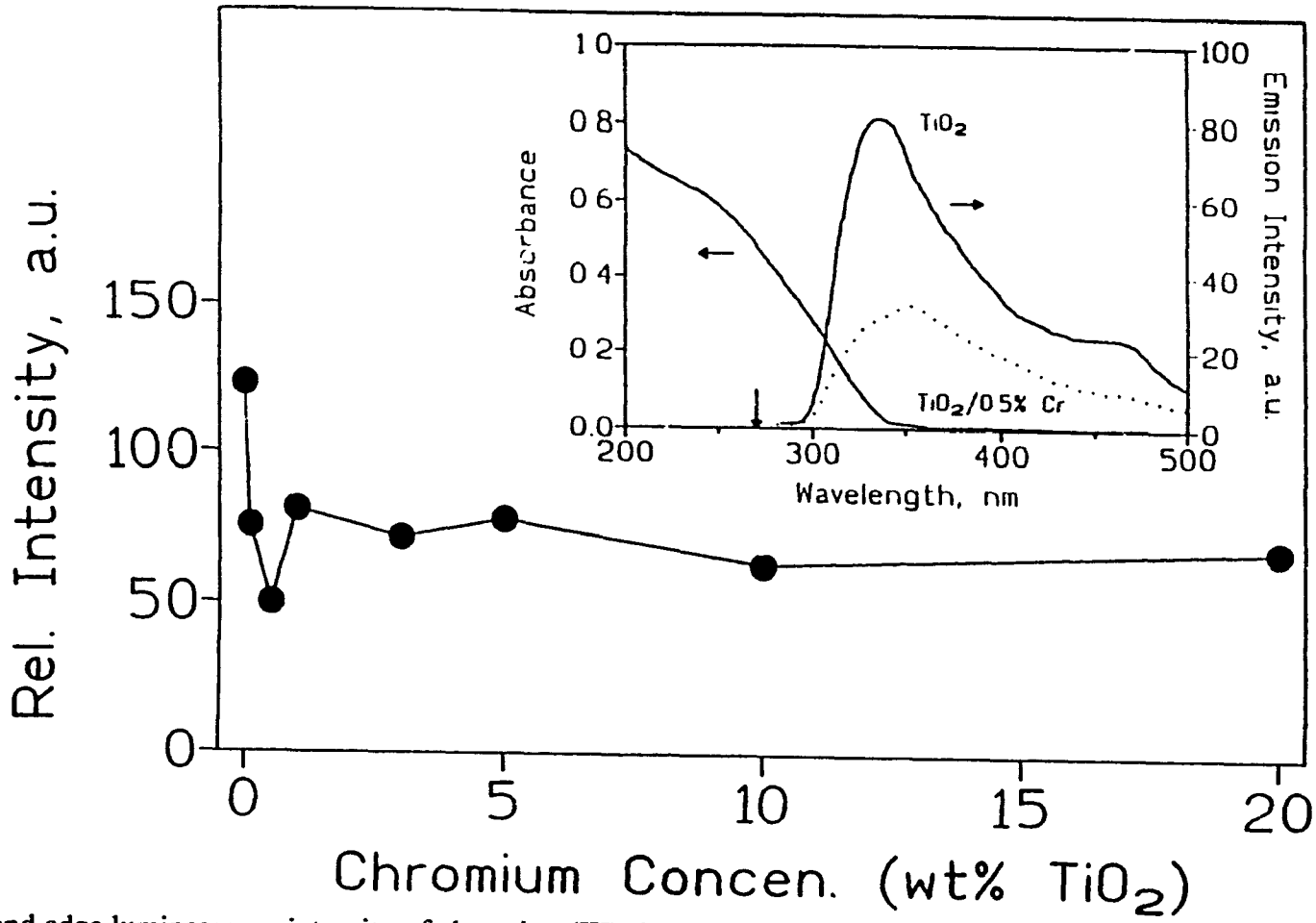

Figure 6.11 Band edge luminescence intensity of chromium(III)-doped TiO_2 as a function of chromium concentration. [TiO_2/x wt.% Cr] = 0.015 g/L, pH 2.7; the absorption at 270 nm was identical in all cases. λ_{exc} = 270 nm with 290 nm (Corning 0-54) filter; slit widths 16/16 (excitation/emission). Inset shows absorption and fluorescence spectra of TiO_2 and the emission of TiO_2 doped with 0.5 wt.% Cr.

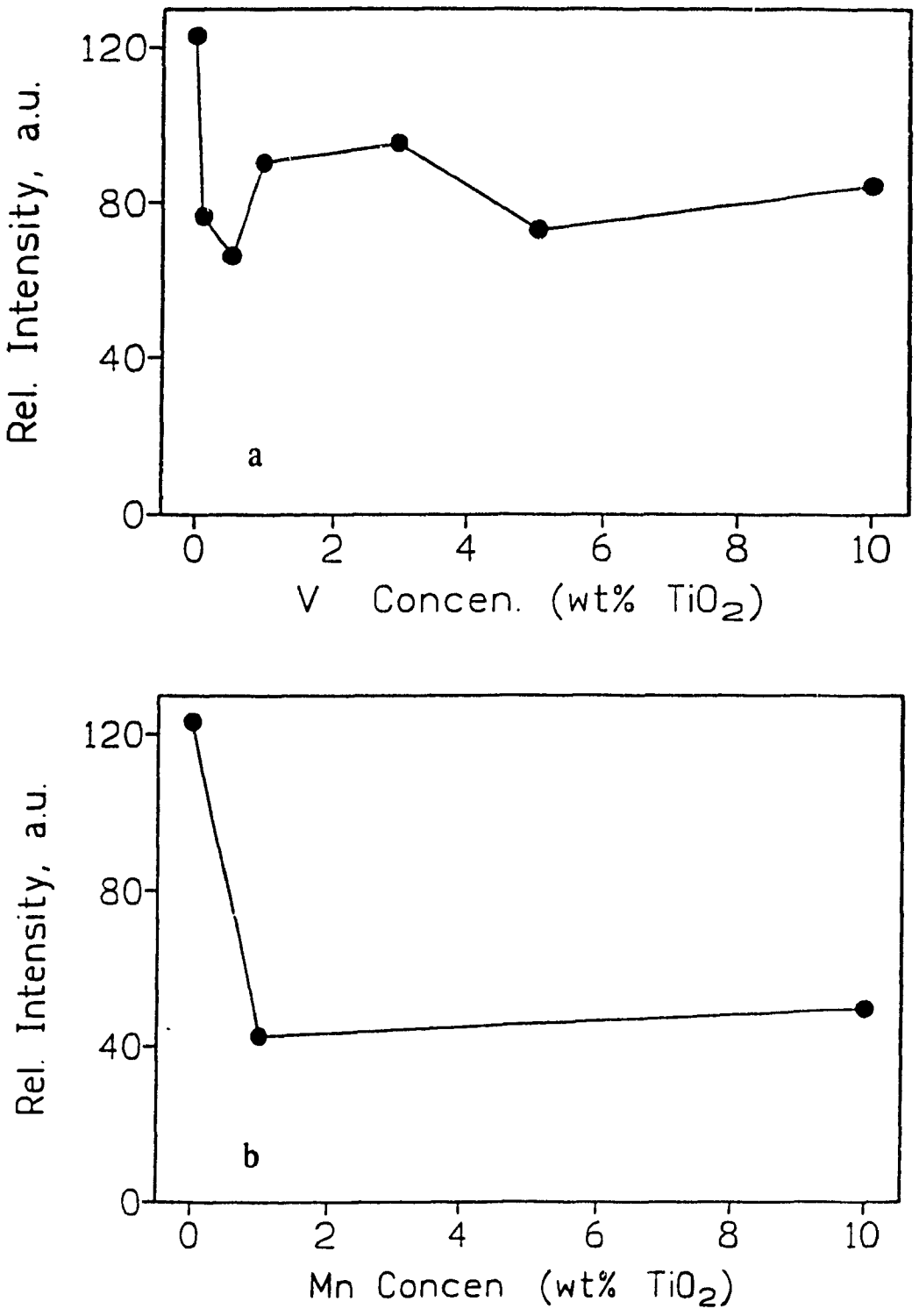

Figure 6.12 (a) Band edge luminescence of vanadium(V)-doped TiO_2 as a function of vanadium concentration (b) Band edge luminescence of manganese(II)-doped TiO_2 as a function of manganese concentration. The absorption at 270 nm was identical in all cases. All other conditions as in Figure 6.11.

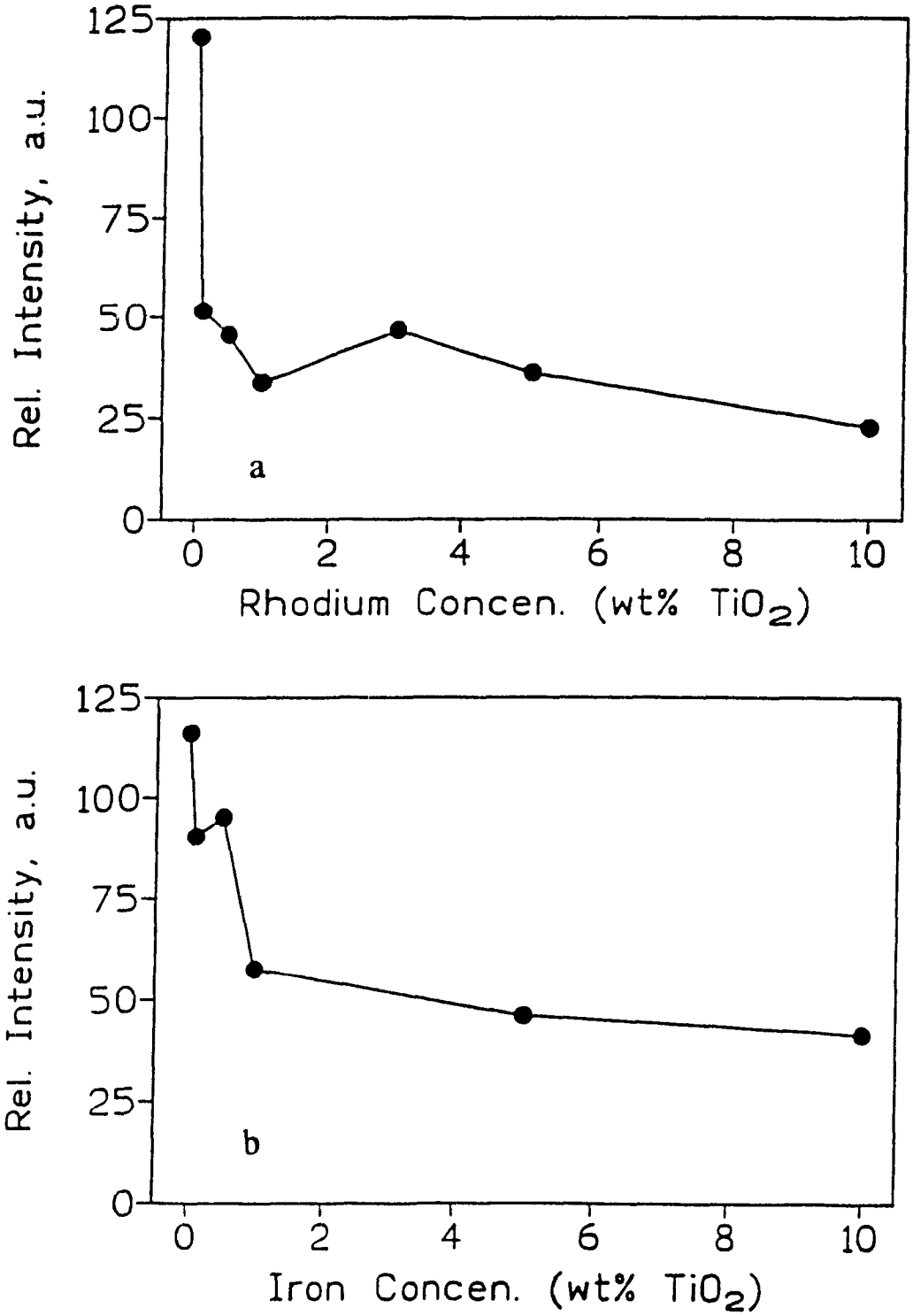

Figure 6.13 (a) Band edge luminescence of rhodium doped TiO_2 as a function of rhodium(III) concentration (b) Band edge luminescence of iron doped TiO_2 as a function of iron(III) concentration. The absorption at 270 nm was identical in all cases. All other conditions as in Figure 6.11.

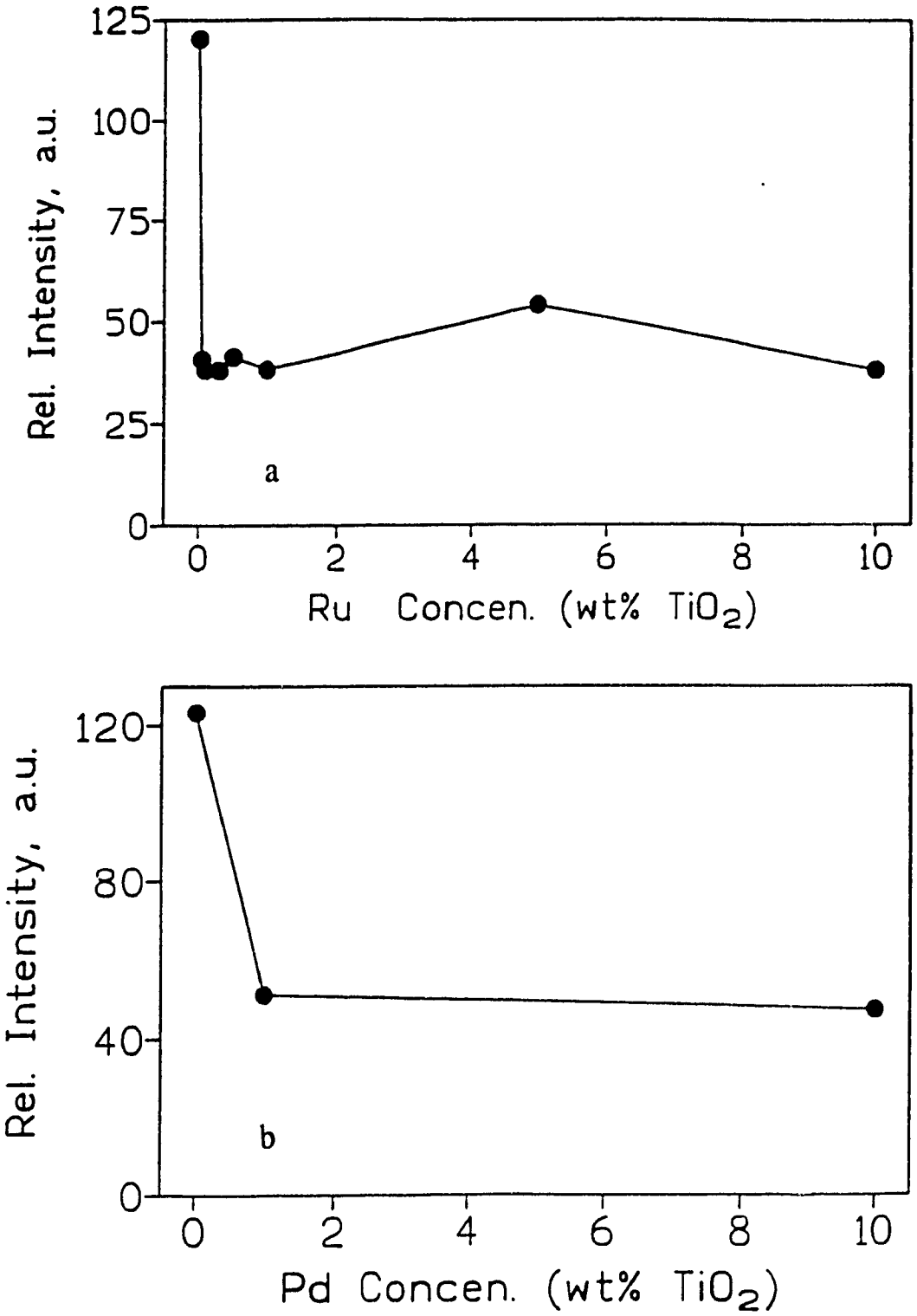

Figure 6.14 (a) Band edge luminescence of ruthenium doped TiO_2 as a function of ruthenium(III) concentration (b) Band edge luminescence of palladium doped TiO_2 as a function of palladium(II) concentration. The absorption at 270 nm was identical in all cases. All other conditions as in Figure 6.11.

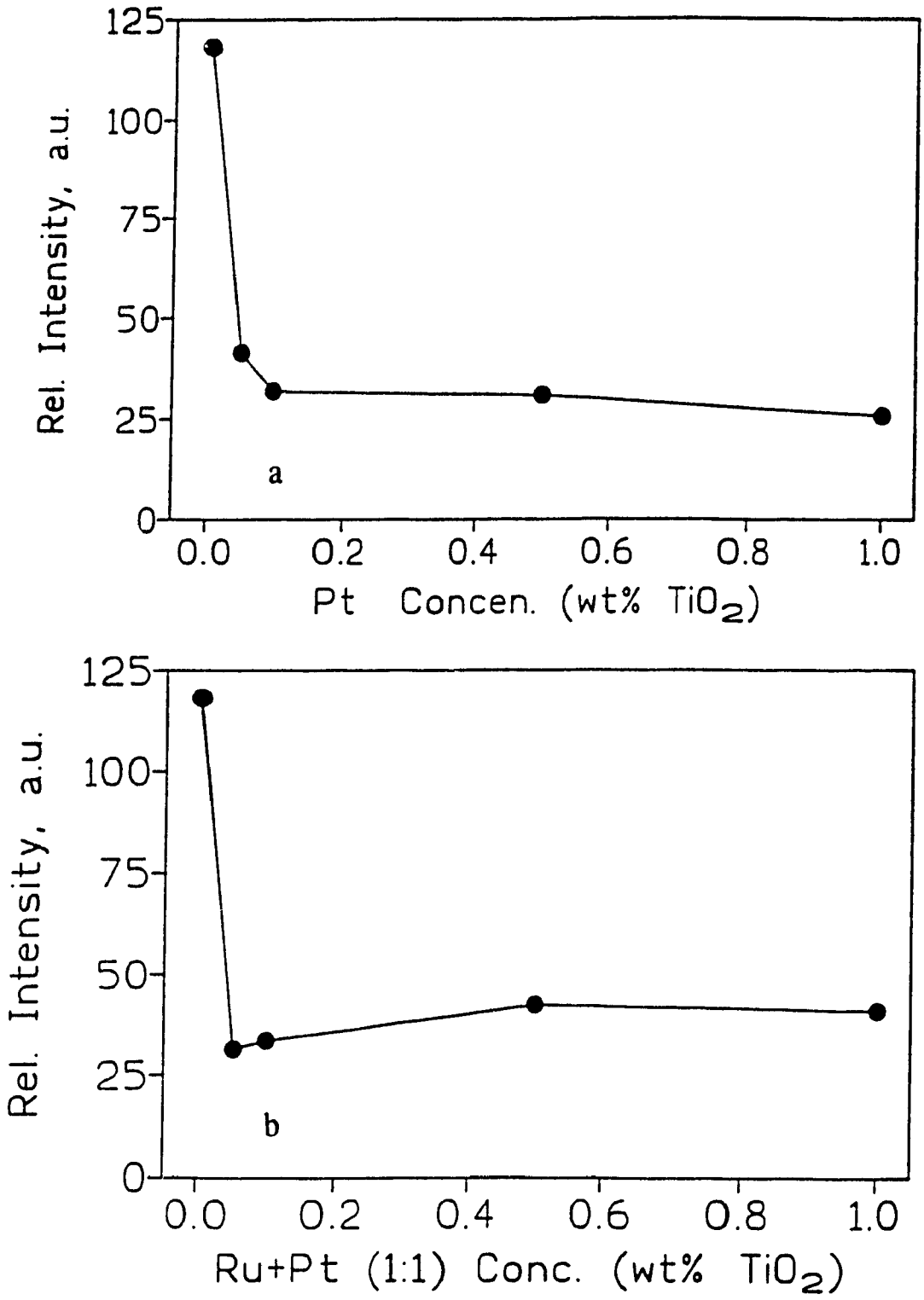

Figure 6.15 (a) Band edge luminescence of platinum doped TiO_2 as a function of platinum(IV) concentration (b) Band edge luminescence of ruthenium(III) and platinum(IV) (1:1) doped TiO_2 as a function of platinum(IV) and ruthenium(III) (1:1) concentration. The absorption at 270 nm was identical in all cases. All other conditions as in Figure 6.11.

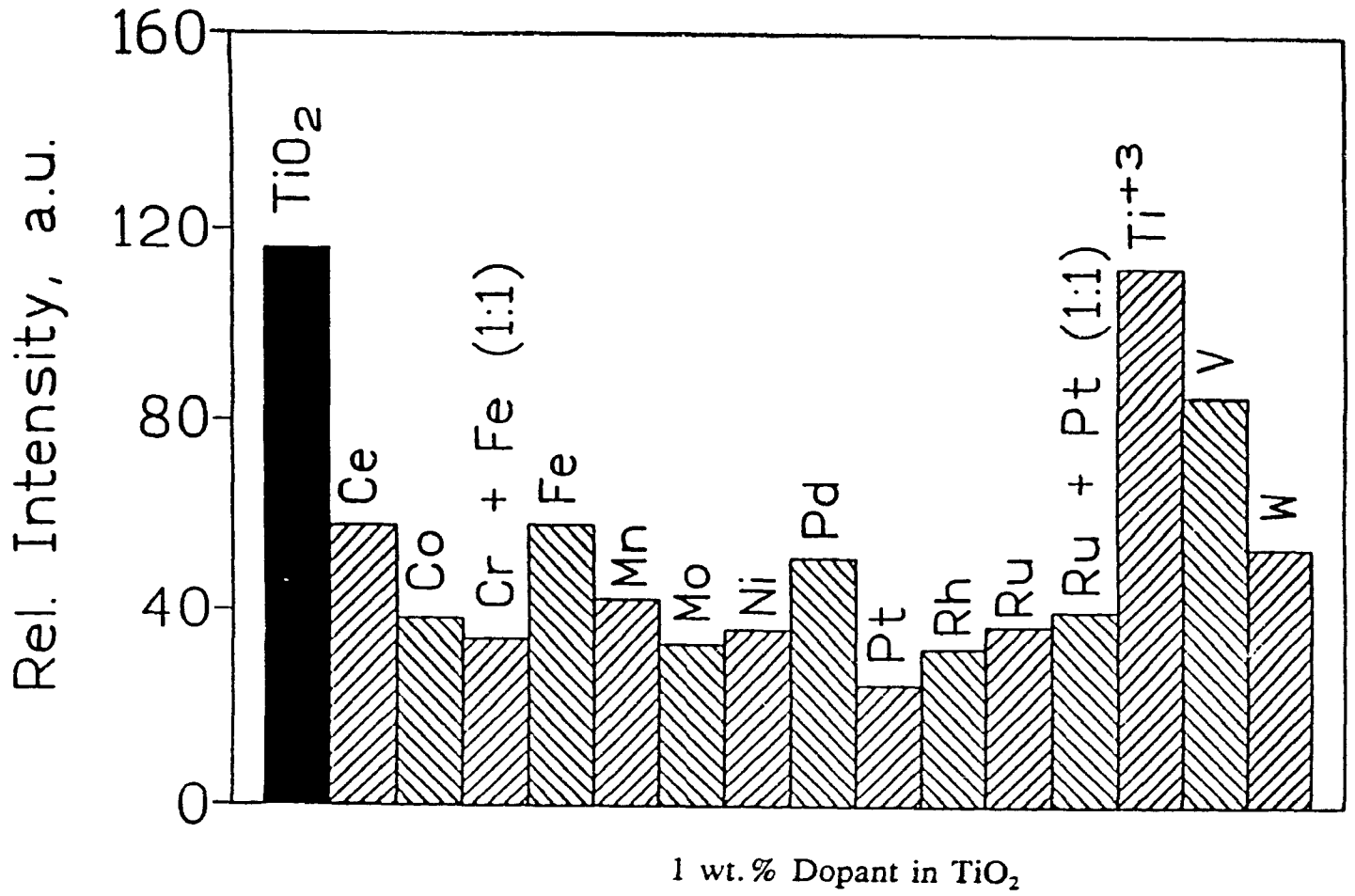

Figure 6.16 Band edge luminescence of TiO_2 doped with 1 wt.% of a variety of different transition metal dopants; Ce(VI), Co(II), Cr(III) and Fe(III), Fe(III), Mn(II), Mo(VI), Ni(II), Pd(II), Pt(IV), Rh(III), Ru(III), Ru(III) and Pt(IV), Ti(III), V(V) and W(VI). The absorption at 270 nm was identical in all cases. All other conditions as in Figure 6.11.

6.4 TRANSIENT EMISSION STUDIES OF TRANSITION METAL DOPED COLLOIDAL TiO_2

The effect of the different dopants on the dynamics of charge carrier recombination was examined using picosecond laser transient emission spectroscopy. Representative transient emission decay traces obtained for the different metal doped TiO_2 are reported in Figure 6.17. In all cases the emission decayed via excellent single exponential decay kinetics; a summary of the different decay times obtained for the various systems is presented in Table 6.1. As was the case for the naked TiO_2 systems, the decay may be attributed to band-edge luminescence arising from conduction band electron and valence band hole recombination.

Dopant concentration has a significant influence on the observed emission decay. In the case of chromium, the emission lifetime of colloidal TiO_2 is first quenched at low levels of chromium(III), and subsequently appears to increase until approximately 3 wt% in Cr^{+3} after which the decay lifetime begins to decrease. This may suggest that at low (1 and 3 wt%) dopant concentrations, chromium acts as an electron or hole trap but with increasing chromium concentration the chromium centres become recombination sites, thereby decreasing the emission lifetimes. For the other systems noted in Table 6.1, the decay time data are rather scattered; nevertheless, a general decreasing trend is seen with increase in the concentrations.

Table 6.1 Transient Emission Decay Lifetimes of Transition Metal Doped TiO_2 electron/hole recombination rate.

Dopant Added to TiO_2	Dopant concentration, wt/wt% TiO_2	τ_{decay} (ps)
- (TiO_2 - 23 Å)	-	86 ± 2
- (TiO_2 - 133 Å)		417 ± 14
- (TiO_2 - 281 Å)		71 ± 5
Cr^{+3}	0.1	337 ± 15
	0.5	297 ± 9
	1	444 ± 14
	3	457 ± 20
	5	325 ± 8
	10	250 ± 12
	20	165 ± 8
Fe^{+3}	0.1	291 ± 11
	0.5	302 ± 14
	1	309 ± 11
	5	136 ± 9
	10	109 ± 7
Cr^{+3} + Fe^{+3} (1:1)	1 (each dopant)	431 ± 37
V^{+5}	0.1	293 ± 9
	0.5	228 ± 9
	1	279 ± 10
	3	267 ± 16
	5	242 ± 14
	10	164 ± 8
Rh^{+3}	0.1	348 ± 13
	0.5	382 ± 11
	1	289 ± 10
	3	422 ± 17
	5	275 ± 12
	10	354 ± 15

Dopant Added to TiO_2	Dopant concentration, wt/wt% TiO_2	τ_{decay} (ps)
Ru^{+3}	0.05	347 ± 15
	0.1	454 ± 14
	0.3	430 ± 15
	0.5	391 ± 14
	1	334 ± 20
	5	543 ± 46
Pt^{+4}	0.05	641 ± 32
	0.1	525 ± 19
	0.5	439 ± 17
	1	525 ± 24
Ru^{+3} + Pt^{+4} (1:1)	0.05 (each dopant)	653 ± 31
	0.1	618 ± 28
	0.5	388 ± 24
	1	292 ± 29
Pd^{+2}	1	446 ± 15
	10	537 ± 16
Cu^{+2}	1	373 ± 18
	10	368 ± 13
Co^{+2}	1	453 ± 25
W^{+6}	1	416 ± 20
Mo^{+6}	1	377 ± 23
Ni^{+2}	1	522 ± 19
Ce^{+6}	1	546 ± 27
Ti^{+3}	1	400 ± 16

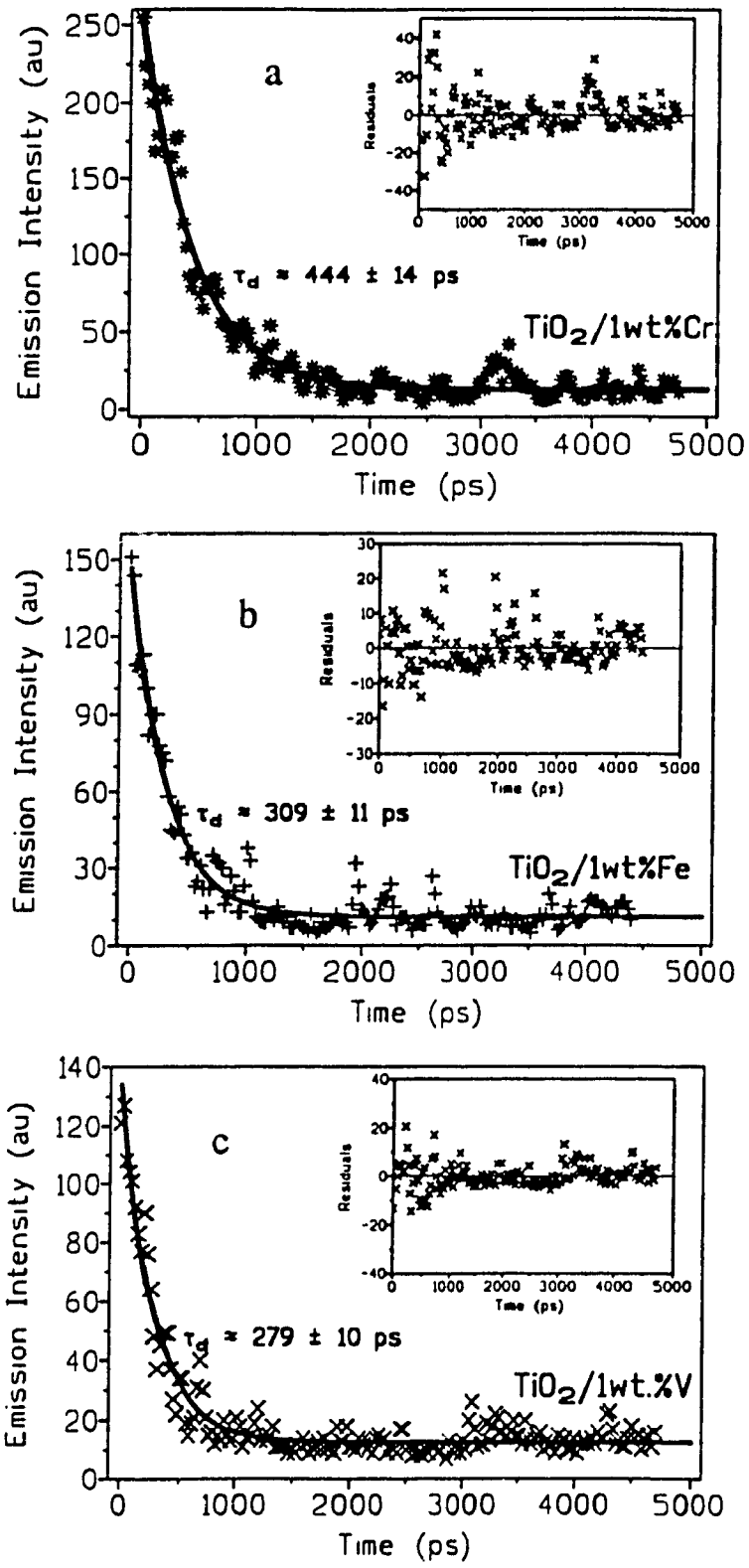

Figure 6.17 Transient emission decay for the luminescence of 15 g/L colloidal TiO_2 doped with (a) 1% Cr^{+3} (b) 1% Fe^{+3} and (c) 1% V^{+5}.

6.5 TRANSIENT ABSORPTION STUDIES OF TRANSITION METAL DOPED COLLOIDAL TiO_2

The transient absorption behaviour of a number of different metal doped TiO_2 systems were investigated in order to gain insight into the way dopants affect the initial electron trapping process and to note whether these dopants have any effect on the electron/hole recombination rate. Additional spectra for TiO_2/0.1 wt.% Rh^{+3}, TiO_2/10 wt.% Cr^{+3}, TiO_2/0.1 wt.% V^{+5}, TiO_2/1 w t.% V^{+5}, TiO_2/10 wt.% Fe^{+3}, TiO_2/0.1 wt.% Ru^{+3}, TiO_2/1 wt.% Ru^{+3} and TiO_2/(1 wt.% Ru^{+3} and 1 wt.% Pt^{+4}), not specifically discussed here, are presented in Appendix D.

6.5.1 TiO_2 Doped with 3 wt.% Rhodium

The temporal evolution of the transient absorption spectra in the picosecond and nanosecond time domains are illustrated in Figure 6.18 for TiO_2 doped with 3 wt.% rhodium. A kinetic analysis of the absorbance decay at 430 nm and 575 nm is shown in Figure 6.19. At -20 ps delay time, a broad transient absorption already formed which grew-in further by 20 ps (upper part of Figure 6.18); subsequently, transient absorption decay ensues to 10 ns (lower part of the Figure). However, note that residual absorption remains at 10 ns, suggesting that whatever the nature of the transient(s) it decays at times longer (ns or μs) than our time window permitted to observe. The broad absorption is reminiscent of those observed for naked TiO_2 colloidal sols seen earlier by Serpone and Grätzel and coworkers.[2] Two spectral regions are relevant in Figure 6.18: the region around 600 nm and the region at wavelengths below ca. 500 nm. The former is the

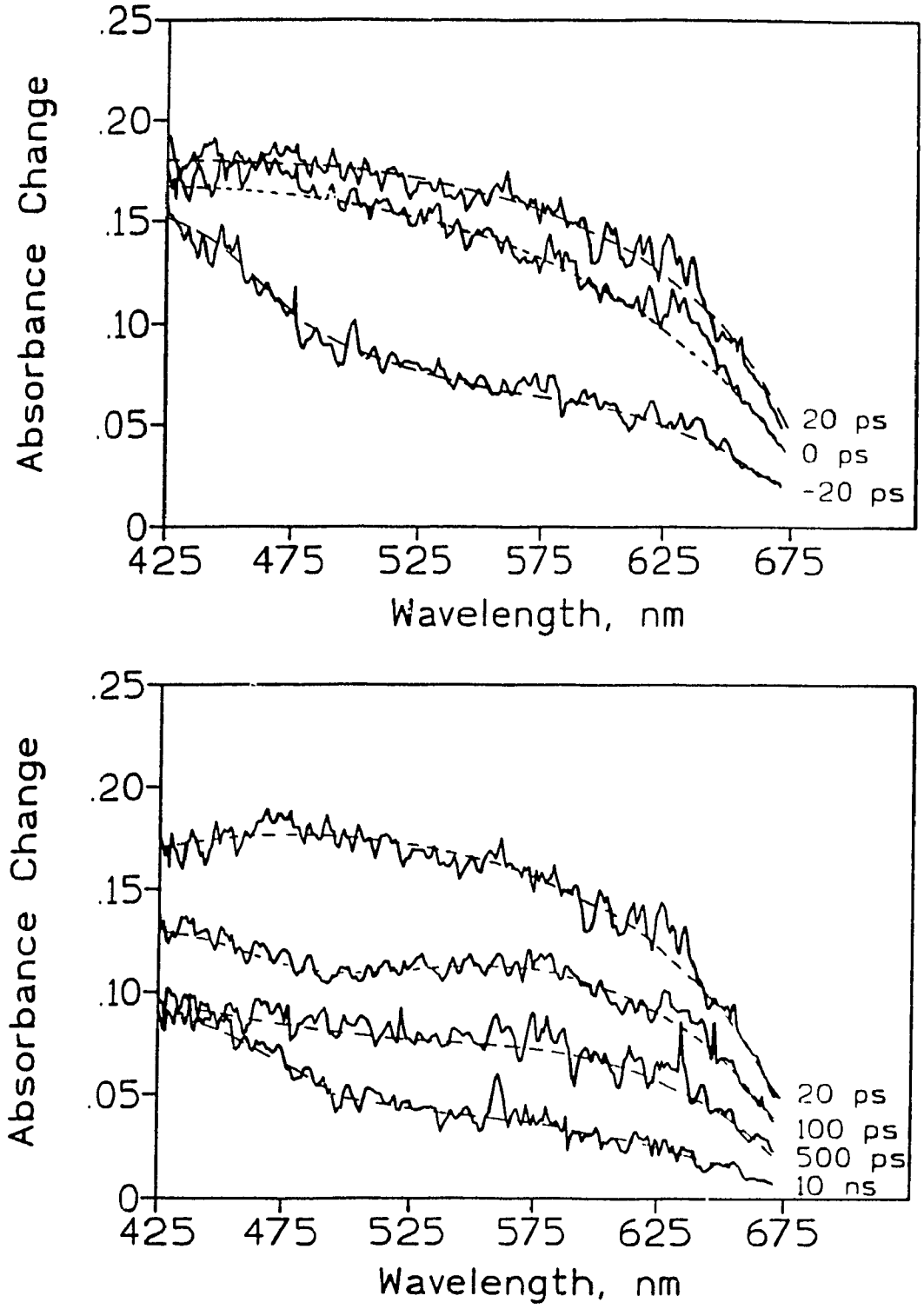

Figure 6.18 Transient absorption spectra observed at various delay times after picosecond excitation (355 nm) of colloidal TiO_2 doped with 3 wt.% Rh^{+3}. [TiO_2/3 wt.% Rh^{+3}] = 15 g/L; pH 2.7; optical path length 0.2 cm.

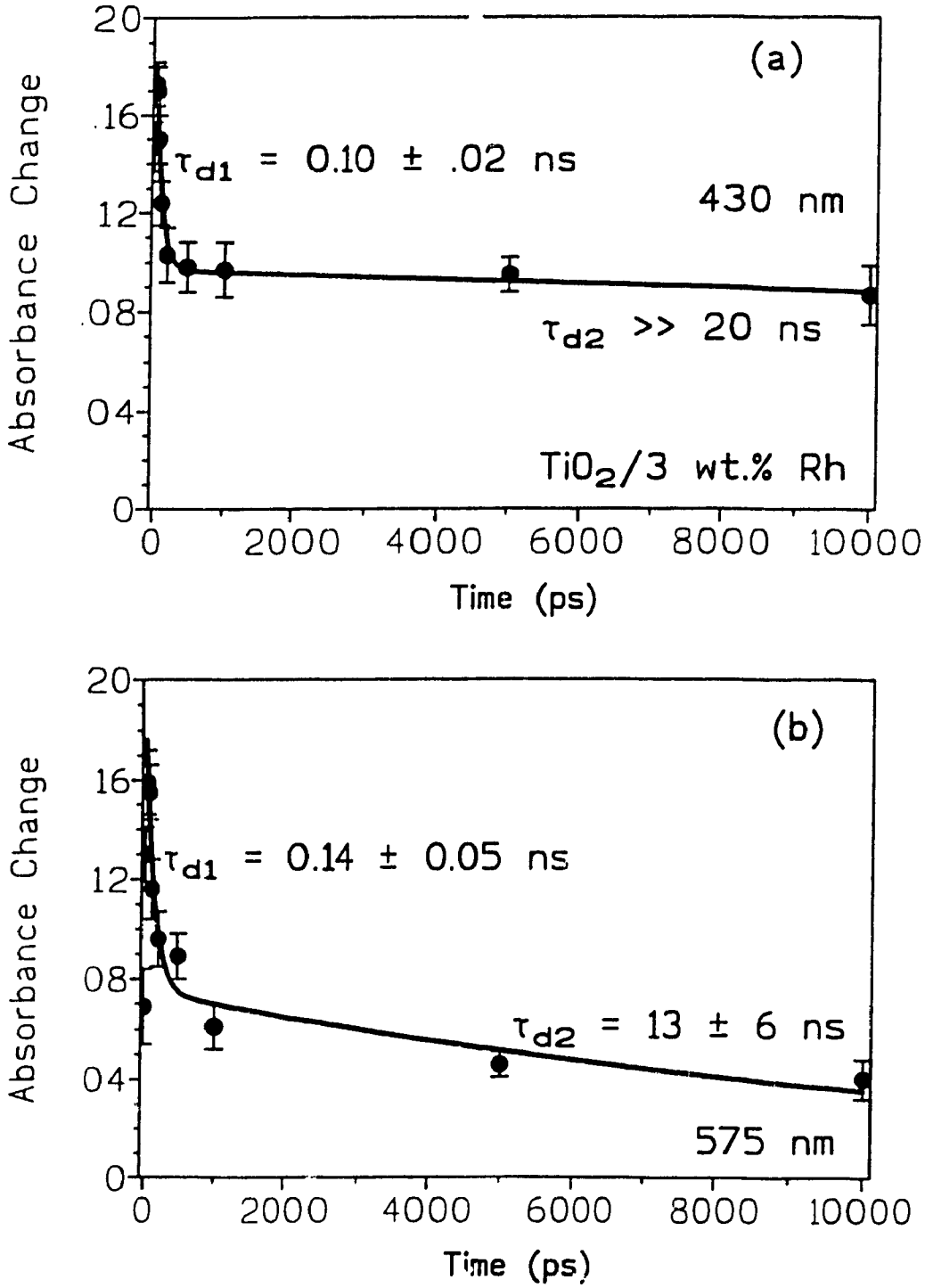

Figure 6.19 Kinetic analysis of the absorbance decay at (a) 430 nm and (b) 575 nm for colloidal TiO_2 doped with 3 wt.% Rh^{+3}. [TiO_2/3 wt.% Rh^{+3}] = 15 g/L; pH 2.7; optical path length 0.2 cm.

region where a *loosely* trapped electron (either as Ti^{IV}...e or as Rh^{III}...e) is expected to have absorption,[9] while the trapped hole is known to absorb at ca. 350 nm with an absorption onset at ~ 470 nm.[11] It is relevant to point out that the ≤ 500 nm transient has practically reached its maximal absorption at ~20 ps, unlike the 600 nm transient. Also, as the latter decays to near zero absorption, significant absorption remains for the former transient at 10 ns. It is tempting to suggest that this decay is connected with formation of Rh^{II} or with a further reduced species such as metallic Rh^{o} islands on the TiO_2 particle. Metallic deposits at the surface of TiO_2 are known to show broad absorption bands in the visible region of the spectrum.[12]

The data in Figure 6.18 were obtained for sols under air-equilibrated conditions. We thought it relevant to also examine the sols under anaerobic conditions using argon purging. Figure 6.20a illustrates the transient spectra observed for TiO_2/3 wt.% Rh sols in the absence of oxygen (argon atmosphere), while Figure 6.20b depicts transient absorption spectra recorded at the same delay times for a pre-irradiated (for 3 hrs with a 1000 W Hg/Xe lamp) sample in an argon atmosphere. Following illumination in the absence of oxygen, the sample was black indicating that metallic rhodium had formed at the surface of the TiO_2 particulates. Despite the fact that the irradiated sample contained preformed rhodium(0) centres, the two sets of spectra in Figure 6.19 show remarkably similar, if not identical, spectral features although the transient(s) in the pre-irradiated sample seems to decay faster. Presumably, the metallic rhodium deposits also can act as electron traps. This has consequences in heterogeneous photocatalysis whereby reduced metallic islands on TiO_2 particulates can induce formation of dihydrogen in the photo-

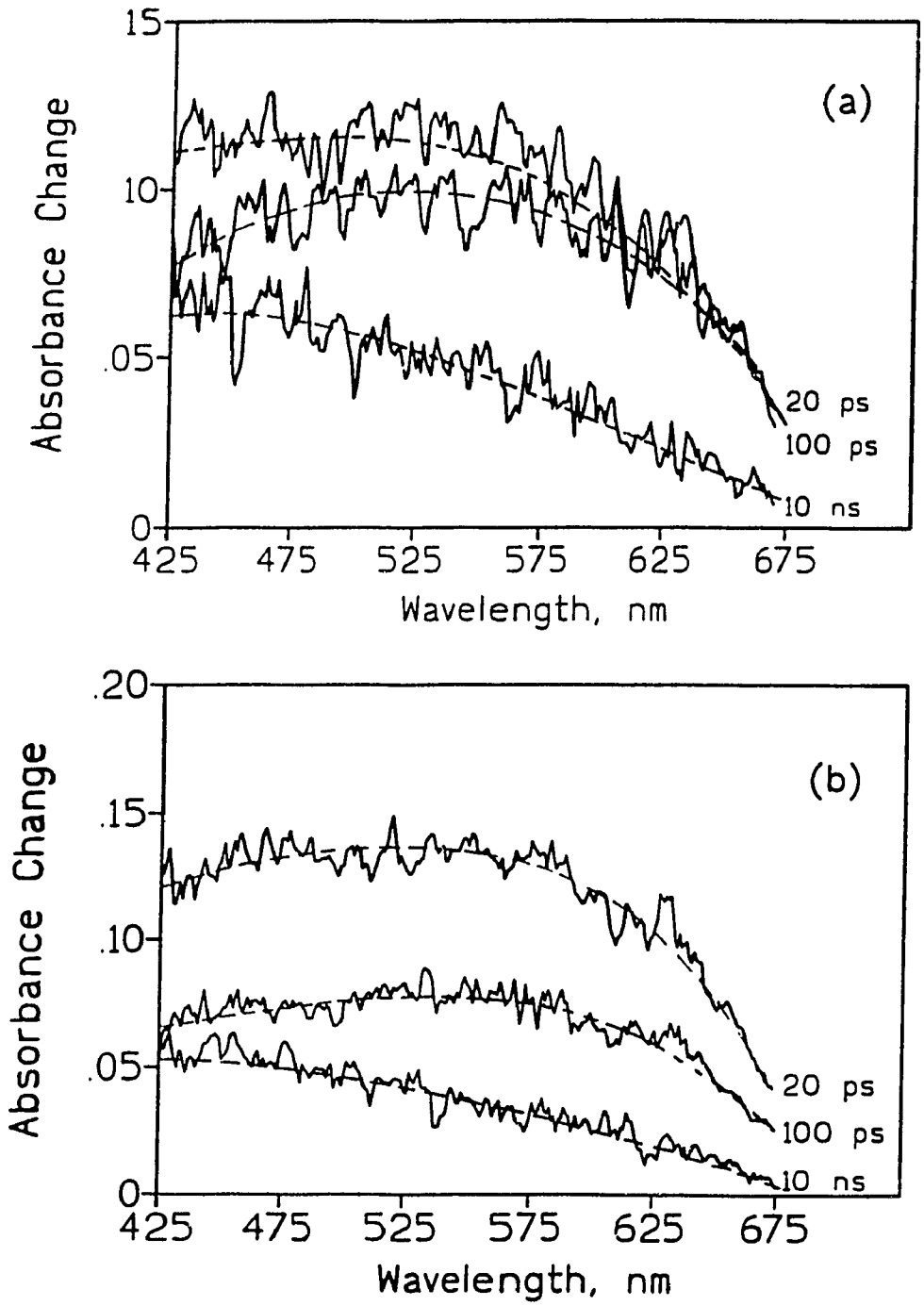

Figure 6.20 Transient absorption spectra observed at various delay times after picosecond excitation of a colloidal TiO_2/3 wt.% Rh^{+3} system under an argon atmosphere. [TiO_2/3 wt.% Rh^{+3}] = 15 g/L; pH 2.7; optical path length 0.2 cm. Lower figure: the sols had been pre-irradiated for 3 hrs under argon using a 1000 W Hg/Xe lamp.

reduction of water. The photoformed holes may decay via regression of the metallic centre back to the ionic form.

6.5.2 TiO_2 Doped with 1 wt.% Platinum

The temporal evolution of the transient absorption spectra of TiO_2 doped with 1 wt.% platinum is shown in Figure 6.21. A kinetic analysis of the absorbance decay at 430 nm and 575 nm is shown in Figure 6.22. Formation and possibly trapping the electrons and holes occur within the laser pulse, at the end of which, a rapid decrease in absorption is noted at 425 nm. The transients show broad absorption over the whole visible region. Again, this may be due to a reduced form of (probably metallic) platinum together with contributions from the trapped hole; the latter could decay via oxidation of the reduced dopant. These events are nothing more than electron/hole recombination, albeit trapped in deep traps.

6.5.3 TiO_2 doped with Iron and Chromium

Finally, in order to study the effect of doping the lattice of TiO_2 with two different metals on the dynamics of charge carrier trapping, TiO_2 doped with 1 wt.% Fe (Figure 6.23), 1 wt.% Cr (Figure 6.25) and a 1:1 mixture of 1 wt.% Cr/1 wt.% Fe (Figure 6.27) were also examined. The kinetic analysis at 430 and 575 nm for 1 wt.% Fe, 1 wt.% Cr and a mixture of 1 wt.% Cr/ 1 wt.% Fe are given in Figures 6.24, 6.26 and 6.28, respectively. In all three cases, the electron and hole are trapped in less than 20 ps. However, the transient spectral features produced in the three systems show some

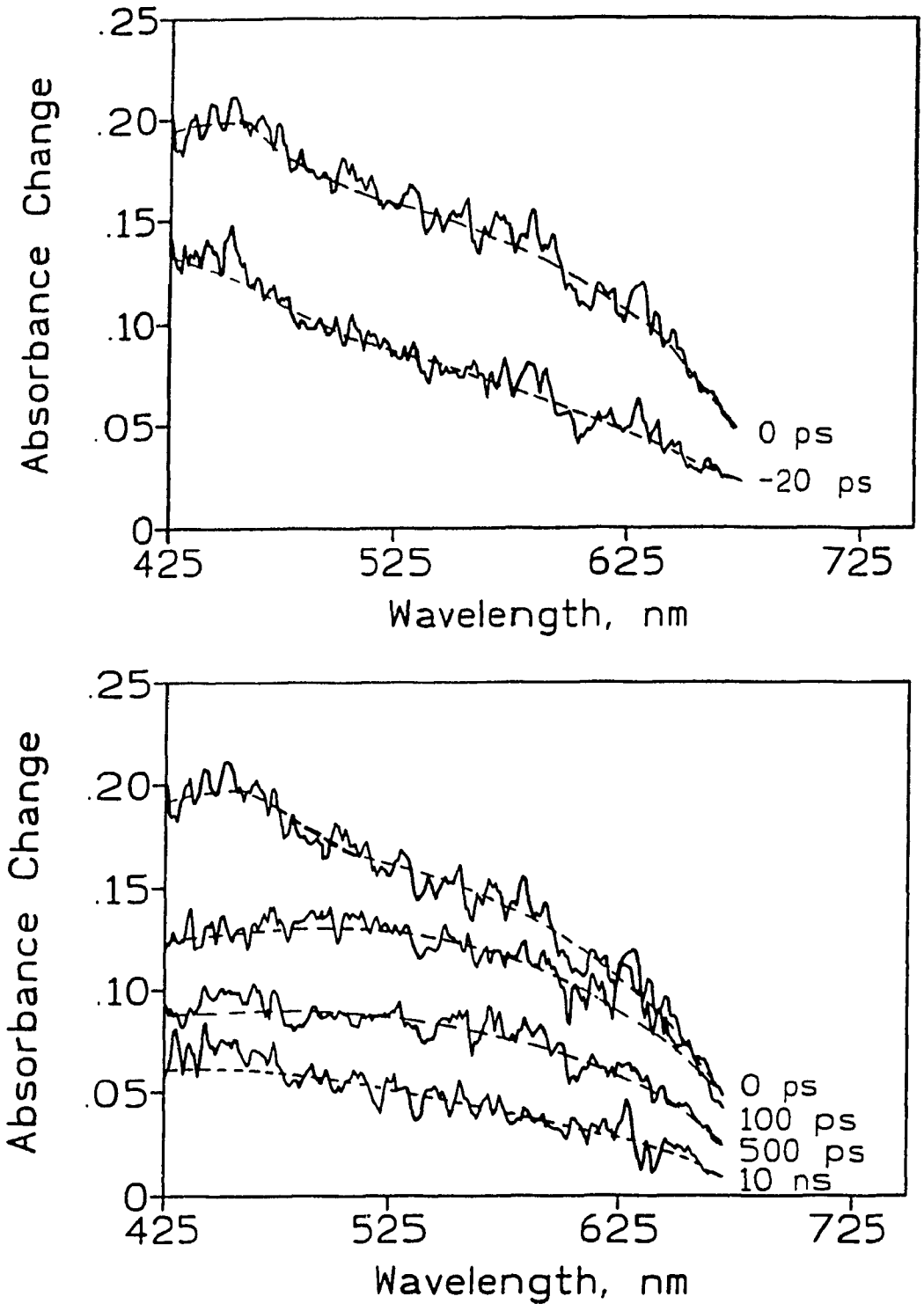

Figure 6.21 Transient absorption spectra observed at various delay times after picosecond excitation (355 nm) of colloidal TiO_2 doped with 1 wt. % Pt^{+4}. [TiO_2/1 wt. % Pt^{+4}] = 15 g/L; pH 2.7; optical path length 0.2 cm.

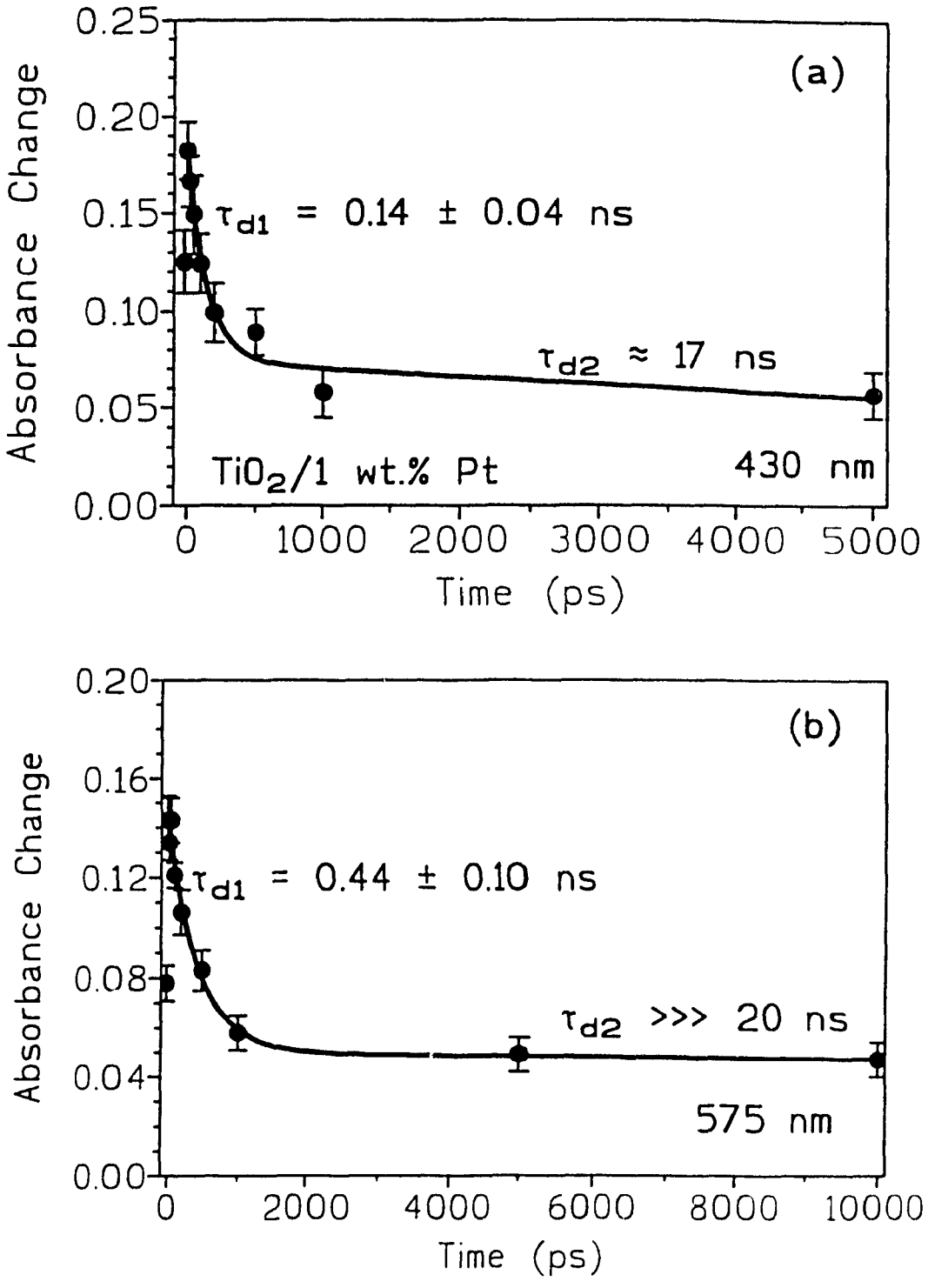

Figure 6.22 Kinetic analysis of the absorbance decay at (a) 430 nm and (b) 575 nm for colloidal TiO_2 doped with 1 wt.% Pt^{+4}. [TiO_2/1 wt.% Pt^{+4}] = 15 g/L; pH 2.7; optical path length 0.2 cm.

variations. In the case of chromium(III)-doped TiO_2, a pronounced maximum at ~ 600 nm is observable immediately following the pulse (20 ps delay). The strong maximum infers a larger fraction of $\{Cr^{III}...e\}$ transients, than seems to be the case in the iron(III)-doped and mixture of iron(III)- and chromium(III)-doped TiO_2 particulates. Interestingly, the small residual absorption at 10 ns in Figure 6.22 shows no significant spectral features, unlike the spectra of the iron-doped TiO_2 system (Figure 6.21) which shows two fairly well resolved spectral features even at 10 ns.

The transient absorptions illustrated in Figure 6.23 for the mixed Fe^{III}/Cr^{III}-doped titania particles are rather revealing. Unlike the spectra seen in Figures 6.21 and 6.22, a significant transient absorption is evident at -20 ps delay time and at wavelengths below 500 nm; there is no significant absorption at ~ 600 nm. Notable residual absorption is observed at 10 ns. Presumably the transient responsible for the near-uv absorption decays very slowly for several tens of nanoseconds. We infer that this transient reflects a trapped hole whose nature might be connected with $\{Fe^{III}...h^+\}$ or with Fe^{IV},[13] a well-known oxidation state for iron.

6.6 CONCLUSIONS

A number of transition metal dopants added to the lattice of TiO_2 appears to extend the absorption characteristics of TiO_2 into the visible part of the spectrum. A number of the metal dopants examined do not seem to affect the band-edge absorption of TiO_2, but rather seem to sensitize the material through illumination into the broad band seen in the visible region. The concentration and the oxidation state of the dopant

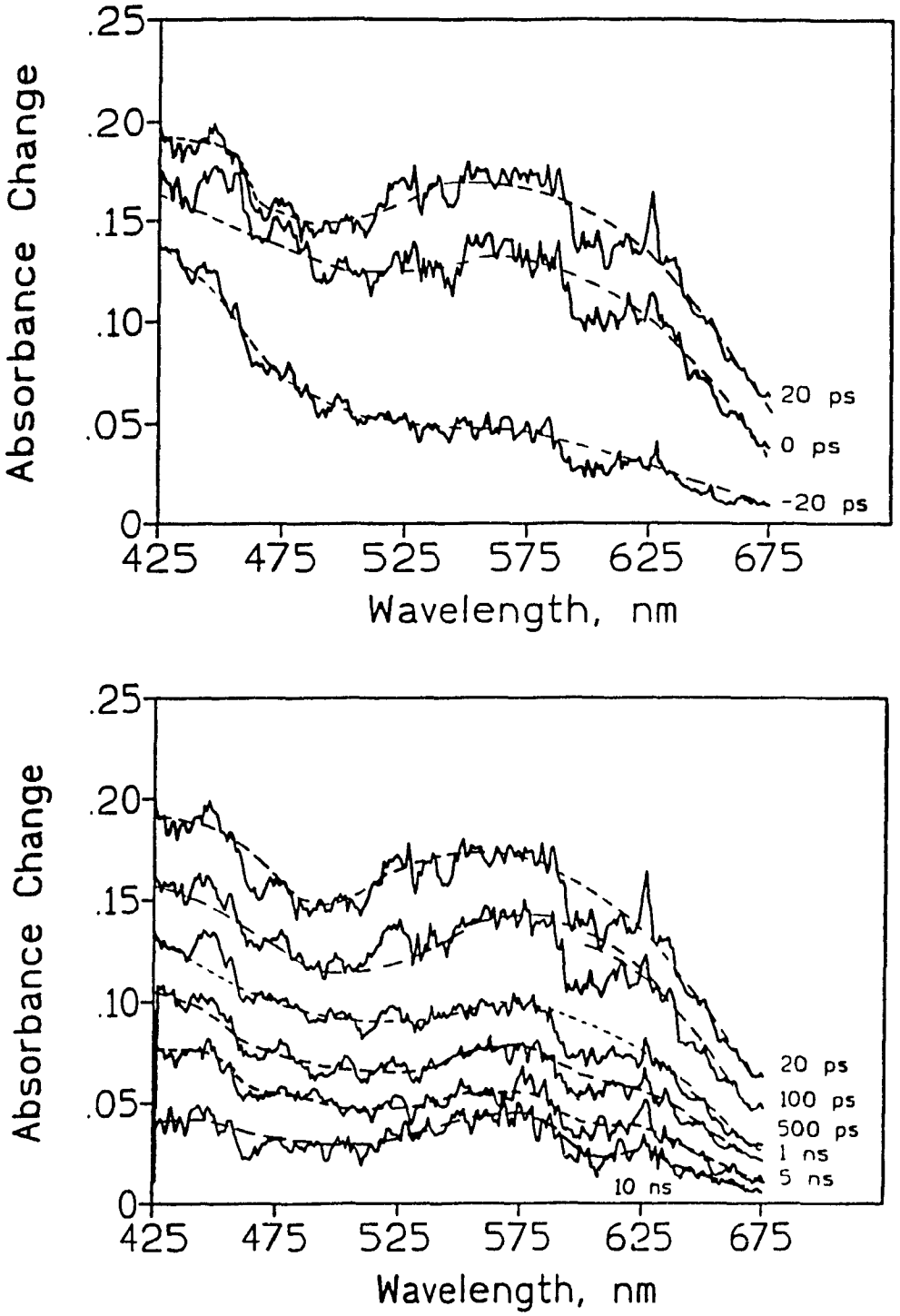

Figure 6.23 Transient absorption spectra observed at various delay times after picosecond excitation (355 nm) of colloidal TiO_2 doped with 1 wt.% Fe^{+3}. [TiO_2/1 wt.% Fe^{+3}] = 15 g/L; pH 2.7; optical path length 0.2 cm.

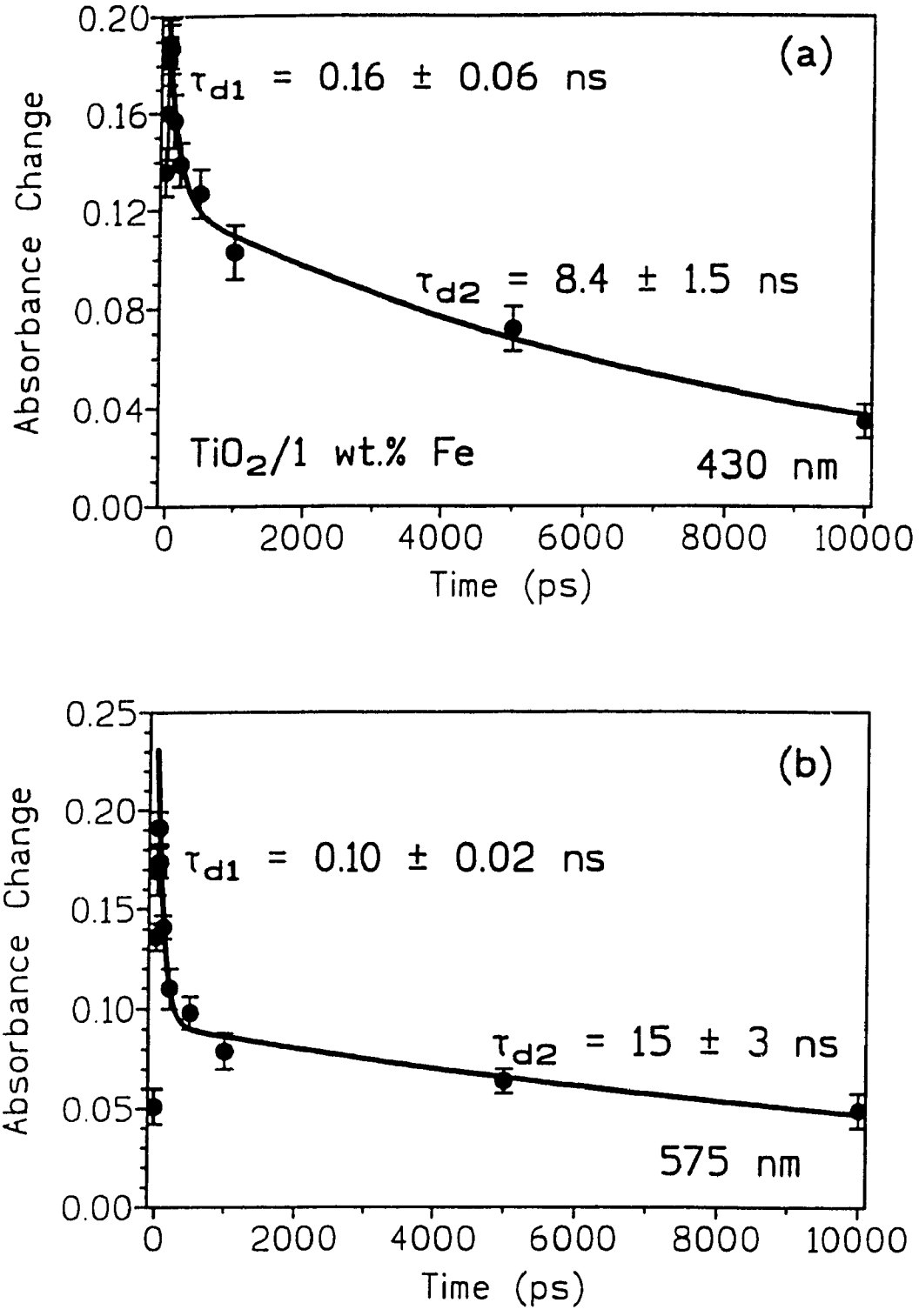

Figure 6.24 Kinetic analysis of the absorbance decay at (a) 430 nm and (b) 575 nm for colloidal TiO_2 doped with 1 wt.% Fe^{+3}. [TiO_2/1 wt.% Fe^{+3}] = 15 g/L; pH 2.7; optical path length 0.2 cm.

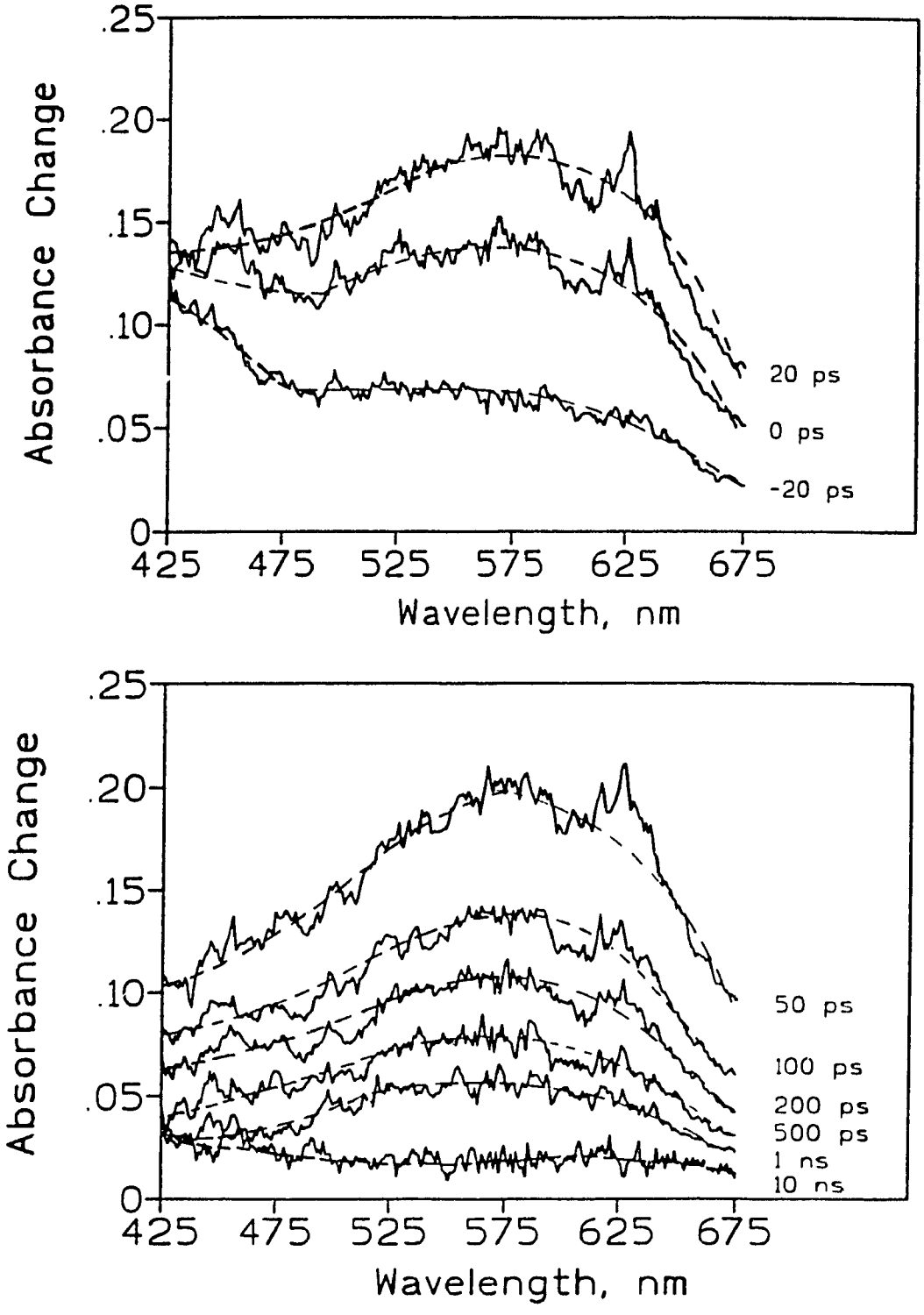

Figure 6.25 Transient absorption spectra observed at various time delays after picosecond excitation (355 nm) of colloidal TiO_2 doped with 1 wt.% Cr^{+3}. [TiO_2/1 wt.% Cr^{+3}] = 15 g/L; pH 2.7; optical path length 0.2 cm.

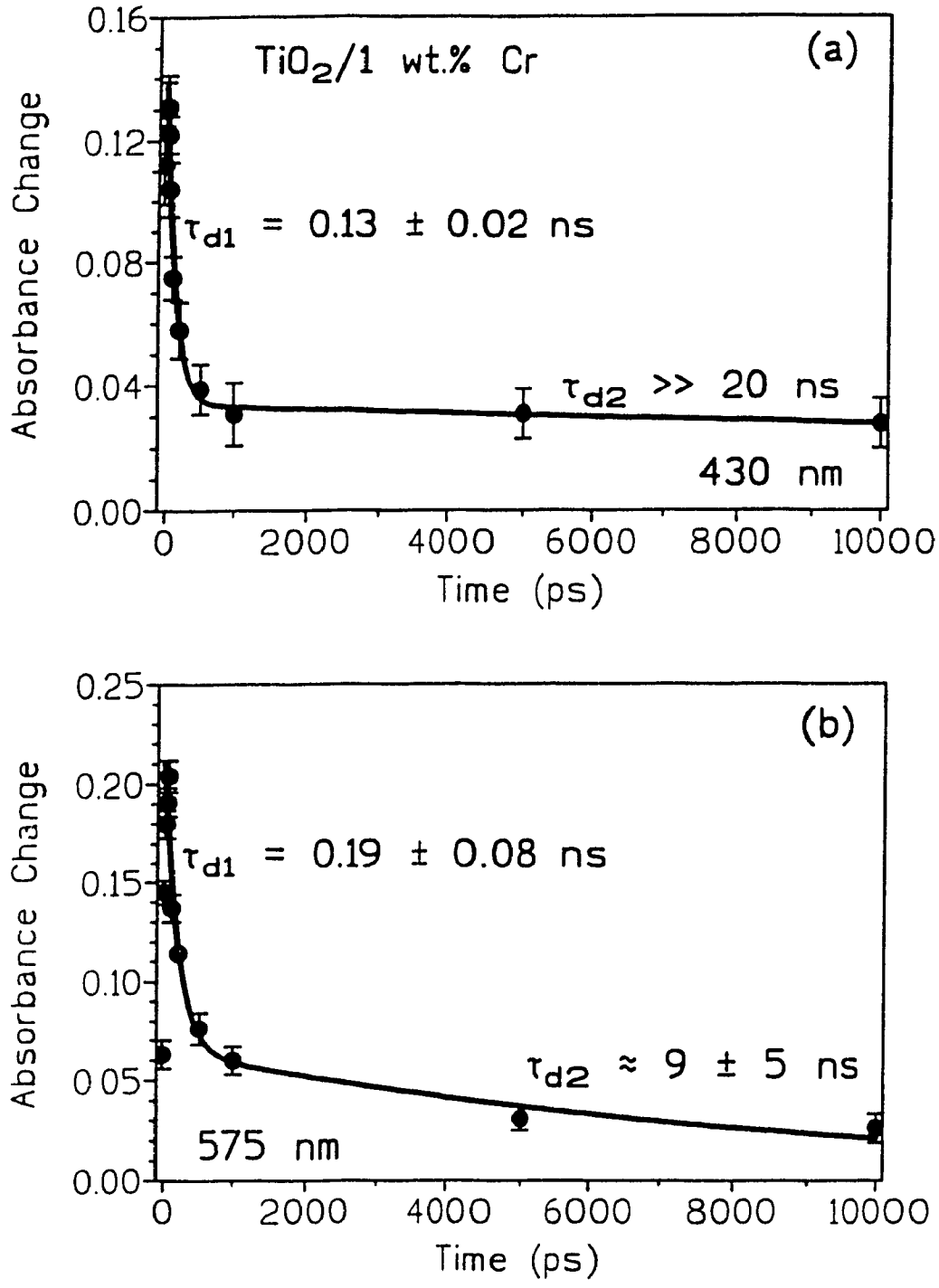

Figure 6.26 Kinetic analysis of the absorbance decay at (a) 430 nm and (b) 575 nm for colloidal TiO_2 doped with 1 wt.% Cr^{+3}. [TiO_2/1 wt.% Cr^{+3}] = 15 g/L; pH 2.7; optical path length 0.2 cm.

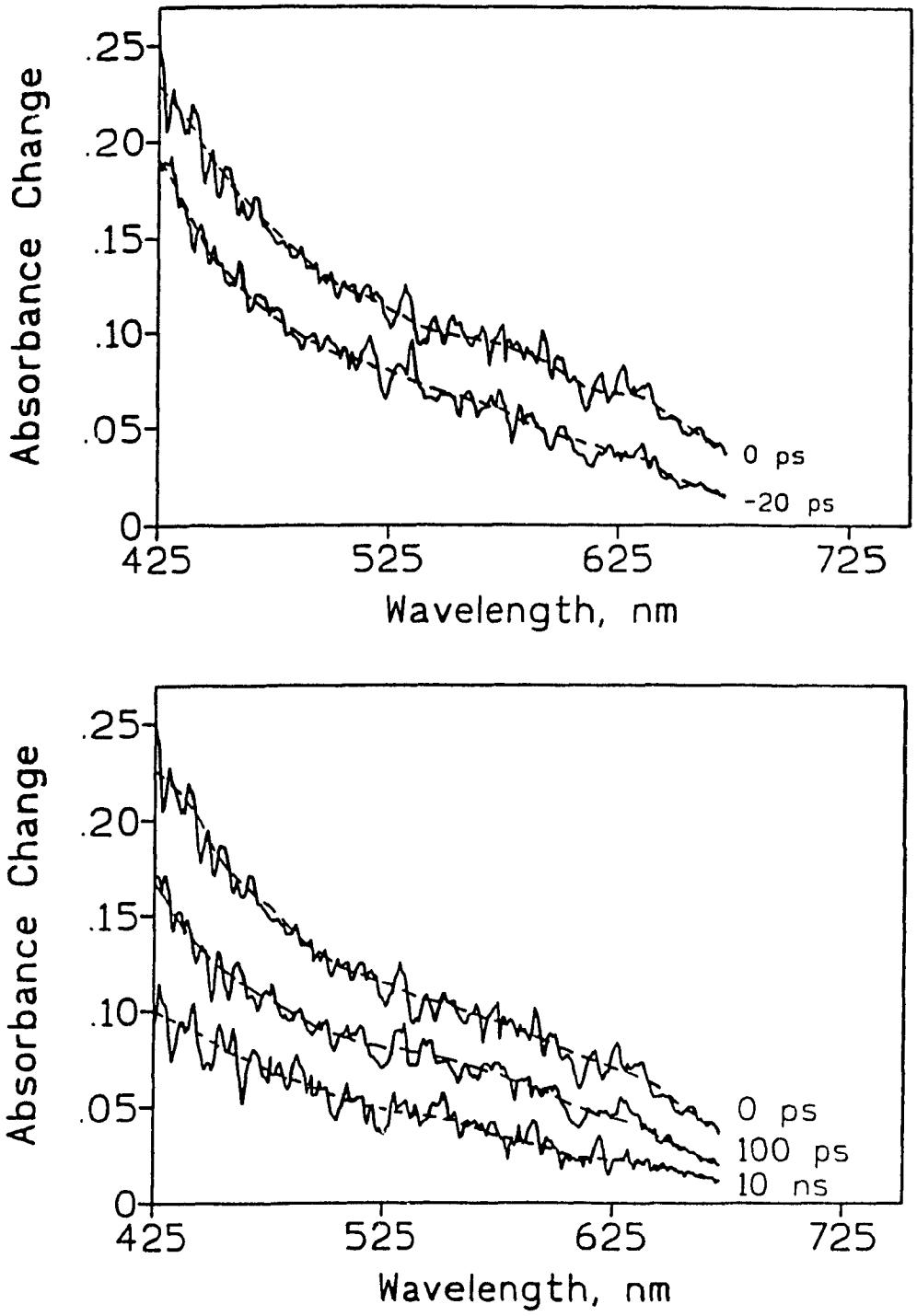

Figure 6.27 Transient absorption spectra observed at various time delays after picosecond excitation (355 nm) of colloidal TiO_2 doped with 1 wt.% Fe^{+3} and 1 wt.% Cr^{+3}. [TiO_2/(1 wt.% Fe^{+3}, 1 wt.% Cr^{+3})] = 15 g/L; pH 2.7; optical path length 0.2 cm.

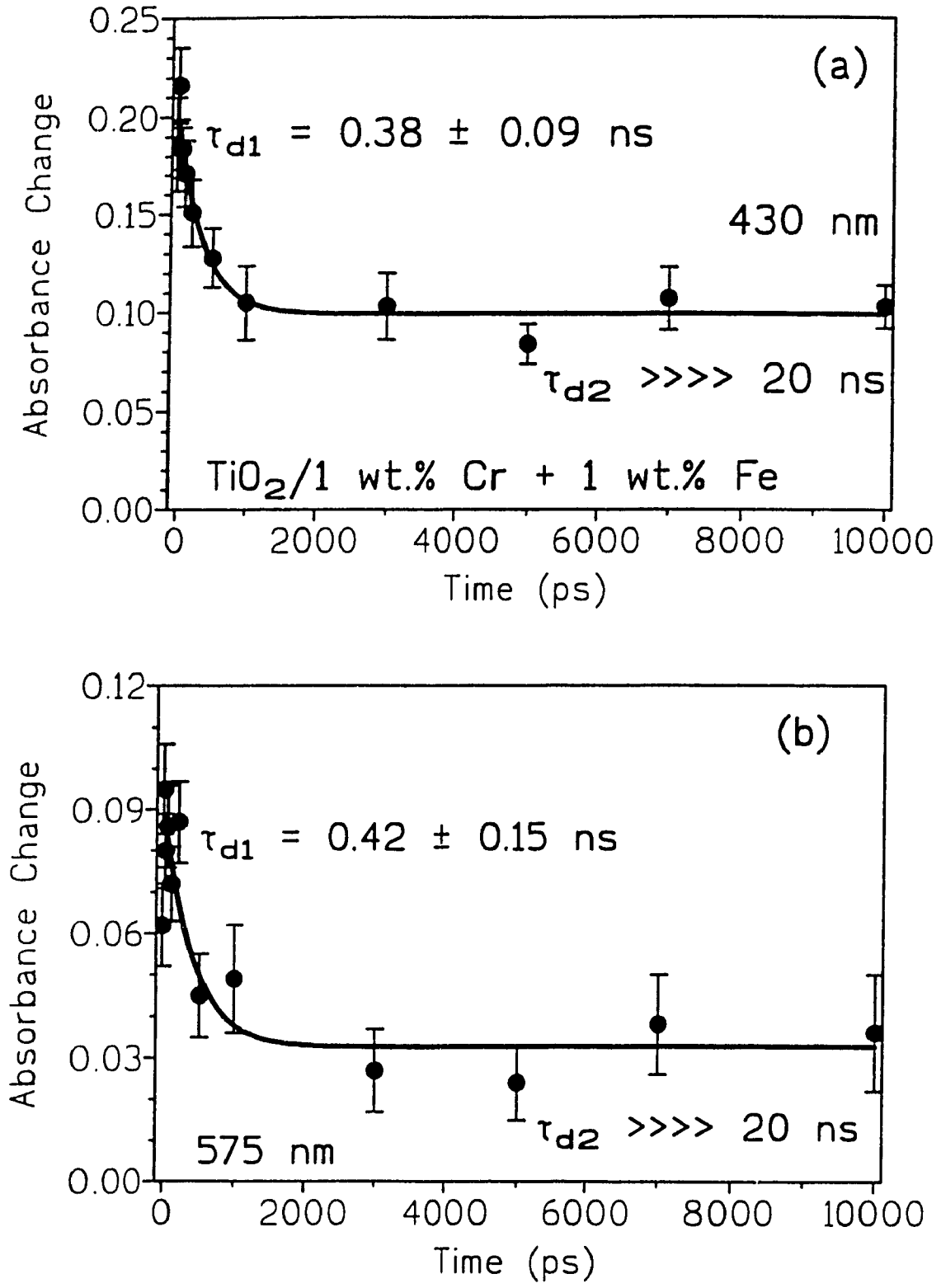

Figure 6.28 Kinetic analysis of the absorbance decay at (a) 430 nm and (b) 575 nm for colloidal TiO_2 doped with 1 wt.% Cr^{+3} and 1 wt.% Fe^{+3}. [TiO_2/(1 wt.% Cr^{+3}, 1 wt.% Fe^{+3}] = 15 g/L; pH 2.7; optical path length 0.2 cm.

have a marked effect on the absorption properties. Increasing the metal dopant concentration increases the absorption spectral features observed. The effect of the dopant concentration on the band edge emission intensity of TiO_2 is non-linear. In many cases, low dopant concentrations cause increased quenching of the band-edge emission, as compared to the higher dopant concentrations. Variations in the extent of what appears to be emission quenching on particle size cannot be ruled out; however, the presence of dopants is perhaps the major factor. Transient emission studies indicate that the different dopants have small but finite effects on the band-edge emission decay times. Finally, transient absorption studies infer that the different dopants may act as either electron or hole traps.

References

1. Archer, M.D., *J. Appl. Electrochem.*, **1975**, 5, 17.

2. Rothenberger, G., Moser, J., Grätzel, M., Serpone, N. and Sharma, D.K., *J. Am. Chem. Soc.*, **1985**, 107, 8054.

3. Finklea, H.O. in *"Semiconductor Electrodes"*, Studies in physical and theoretical chemistry 55, Elsevier, Amsterdam, **1980**, p. 43 and references therein.

4. Malati, M.A. and Wong, W.K., *Surf. Technol.*, **1984**, 22, 305.

5. Wong, W.K and Malati, M.A., *Sol. Energy*, **1986**, 36 (2), 163.

6. Mizushima, K., Tanaka, M., Asai, A, Iida, S and Goodenough, J.B., *J. Phys Chem Solids*, **1979**, 40, 1129.

7. Moser, J., Grätzel, M. and Galloy, R., *Helv. Chim. Acta.*, **1987**, 70, 1596.

8. Grätzel, M. and Howe, R.F., *J. Phys. Chem.*, **1990**, 94, 2566.

9. Moser J., Ph.D. disscrtation, Thesis no. 616, Ecole Polytechnique Fédérale de Lausanne, Switzerland, **1986**.

10. Goodenough, J.B., *Studies in Inorganic Chemistry, vol. 3. **1983;*** Proceedings of the Second European Conference, Velhoven, The Netherlands, 7-9 June, 1982.

11. Lawless, D., Serpone, N and Meisel, D., *J.Phys.Chem.*, **1991**, 95, 5166.

12. Williams, C. and Serpone, N. unpublished observations, December 1990.

13. Moser, J., Grätzel, M and Gallay, R., *Helv. Chim. Acta.*, **1987**, 70, 1596.

CHAPTER 7

PHOTOCATALYTIC STUDIES OF NAKED AND TRANSITION METAL DOPED TiO_2

7.1 INTRODUCTION

Illumination of semiconductor particulates with sufficient energy ($\geq E_{BG}$) results in the creation of conduction band electrons and valence band holes. These charge carriers rapidly diffuse to the surface where oxidation and reduction processes may occur. By far, the most widely studied semiconductor for photocatalytic applications has been anatase titanium dioxide; in particular P25 Degussa TiO_2 has shown the greatest potential for use in the environmental mineralization of a number of organic wastewater pollutants[1] as well as the removal of toxic metals,[2] such as lead and mercury, from solution. However, as discussed in chapter 6, the effectiveness of TiO_2 is restricted by the relatively fast electron/hole recombination and by the fact that TiO_2, whose band gap energy is in the near UV ($E_{BG} \sim 3.2$ eV) can only absorb a small ($\sim 3\%$ [3]) fraction of the solar irradiance.

A number of questions regarding the photocatalytic properties of TiO_2 may be raised. (1) Why is P25 Degussa TiO_2 far superior to other commercially available samples of TiO_2? A recent report[4] has suggested that the method of preparation may be the determining factor in the photocatalytic activity. Schindler and Kunst[4] proposed that

the enhanced photocatalytic activity of P25 Degussa TiO_2 is due to the fact that this material is made up of a mixture of anatase and rutile TiO_2. They suggest that the enhanced photocatalytic activity arises from an interparticle electron transfer between the two forms of TiO_2; the result is efficient charge carrier separation and subsequent reduction and oxidation processes at the particle surface. The enhanced catalytic activity may also be due to impurities ($< 0.3\%$ Al_2O_3, $< 0.2\%$ SiO_2, $< 0.01\%$ Fe_2O_3, $< 0.3\%$ HCl) present in Degussa TiO_2. (2) What effect will TiO_2 particle size have on the photocatalytic properties? (3) Can the addition of various transition metal ion dopants to the bulk of TiO_2 extend charge carrier lifetime and thus enhance redox processes? (4) Will the addition of these dopants extend the absorptive properties further into the visible part of the spectrum without loss of and perhaps improve the photocatalytic properties? (5) What effect will dopant concentration have on the photocatalytic properties?

This chapter addresses a number of these questions and reports the results of experiments aimed at (a) assessing the effect of anatase/rutile concentration in P25 Degussa TiO_2, (b) the effect of anatase TiO_2 particle size, and (c) the effect of adding various transition metal dopants at various concentrations to the bulk of anatase TiO_2 on the photocatalytic activity. The photooxidation of phenol (at pH 3) was used as a target molecule to assess the effect of varying the anatase/rutile concentration in P-25 Degussa TiO_2 and to assess the effect of anatase TiO_2 particle size. The photooxidation of phenol by irradiated TiO_2 has been examined extensively and the reaction is well characterized.[5] It has recently been proposed that the oxidation of phenol by illuminated Degussa P-25 TiO_2 be considered a standard reaction when comparing photoreactor efficiencies between

different laboratories.[6] The photooxidative activity of the transition metal doped TiO_2 was assessed by the oxidation of oxalic acid; the photocleavage of water was used to evaluate the photoreductive properties of the materials.

7.2 EFFECT OF ANATASE CONCENTRATION IN P-25 DEGUSSA TiO_2 ON THE PHOTOOXIDATION OF PHENOL

It is relevant to recall the proposal of Schindler and Kunst[4] that the photooactivity of P-25 Degussa TiO_2, relative to other commercial samples, is due to interparticle electron transfer[7,8] between the anatase and rutile components of the material (~ 80% anatase and ~ 20% rutile, see chapter 2). In their model, electrons created in the anatase part of the powder should be transferred to the rutile part because the conduction band of the anatase is more positive than the one of rutile. However, deep trapping of the photoholes formed in the anatase part would prevent their transfer to the rutile phase. The charge carriers generated in the anatase part of the powder would therefore be separated; the electron trapped in the rutile part of the powder and the hole in the anatase part of the powder. Increasing the rutile component might be expected to enhance this interparticle electron transfer and therefore enhance the photooxidative activity of P-25 Degussa TiO_2.

The photocatalyzed oxidation of phenol is often considered a model reaction in heterogenous photocatalytic studies; its mineralization is known to proceed through several hydroxylated intermediates including catechol and hydroquinone (Figure 7.1).[8] In the present study, no attempt was made to follow or detect the intermediates formed

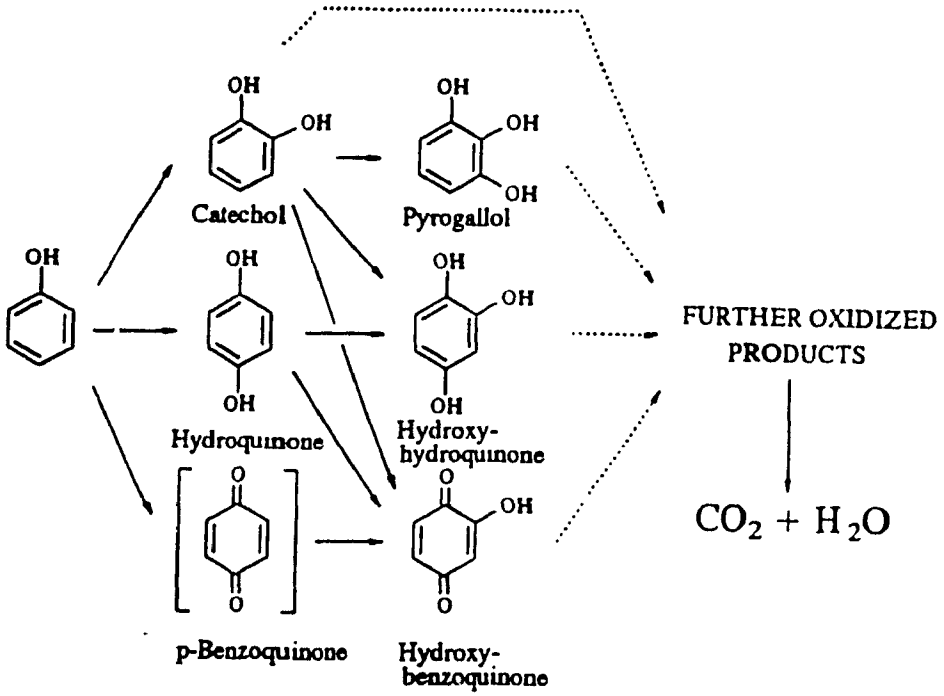

Figure 7.1 Intermediates formed in the mineralization of phenol by TiO_2 (from ref. 8)

in the reaction; instead, only the decrease in phenol concentration was monitored. The normalized phenol concentration versus reaction time for the various anatase/rutile P-25 Degussa TiO_2 samples is presented in Figure 7.2. In all cases, the degradation of the phenol was zero order and decreased with decreasing anatase concentration and with decreasing surface area (Table 7.1).

The correlations between the rate of degradation of phenol with the surface area and with the quantity of anatase TiO_2 is illustrated in Figure 7.3. The rate of degradation of phenol increased with increasing anatase concentration and with increase in surface area. This strong dependence suggests that either interparticle electron transfer between the anatase and rutile parts of P-25 Degussa TiO_2 is not important, or else its effect is

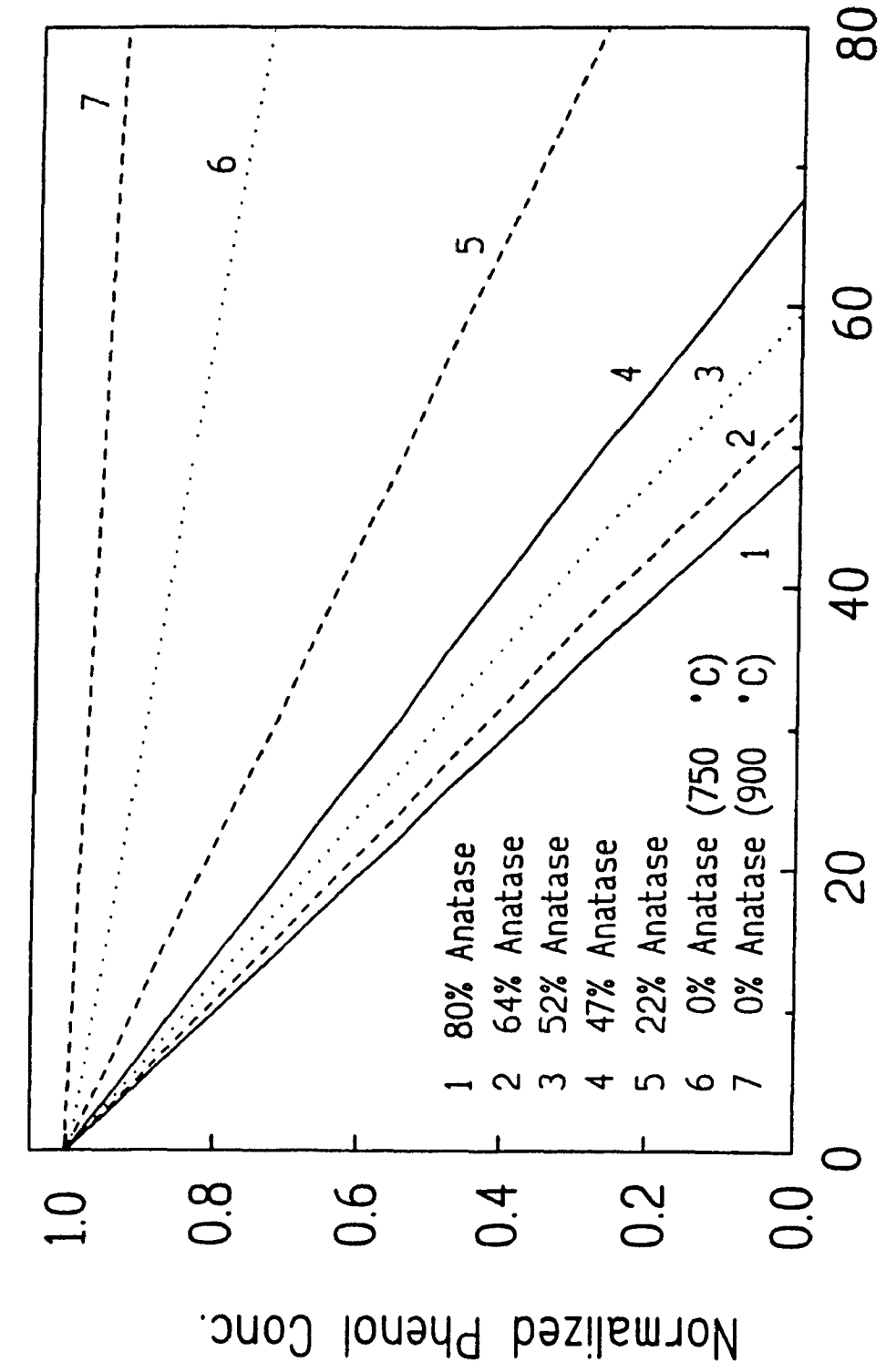

Figure 7.2 Decrease in phenol concentration with time for various anatase/rutile concentration in P25 Degussa TiO_2.

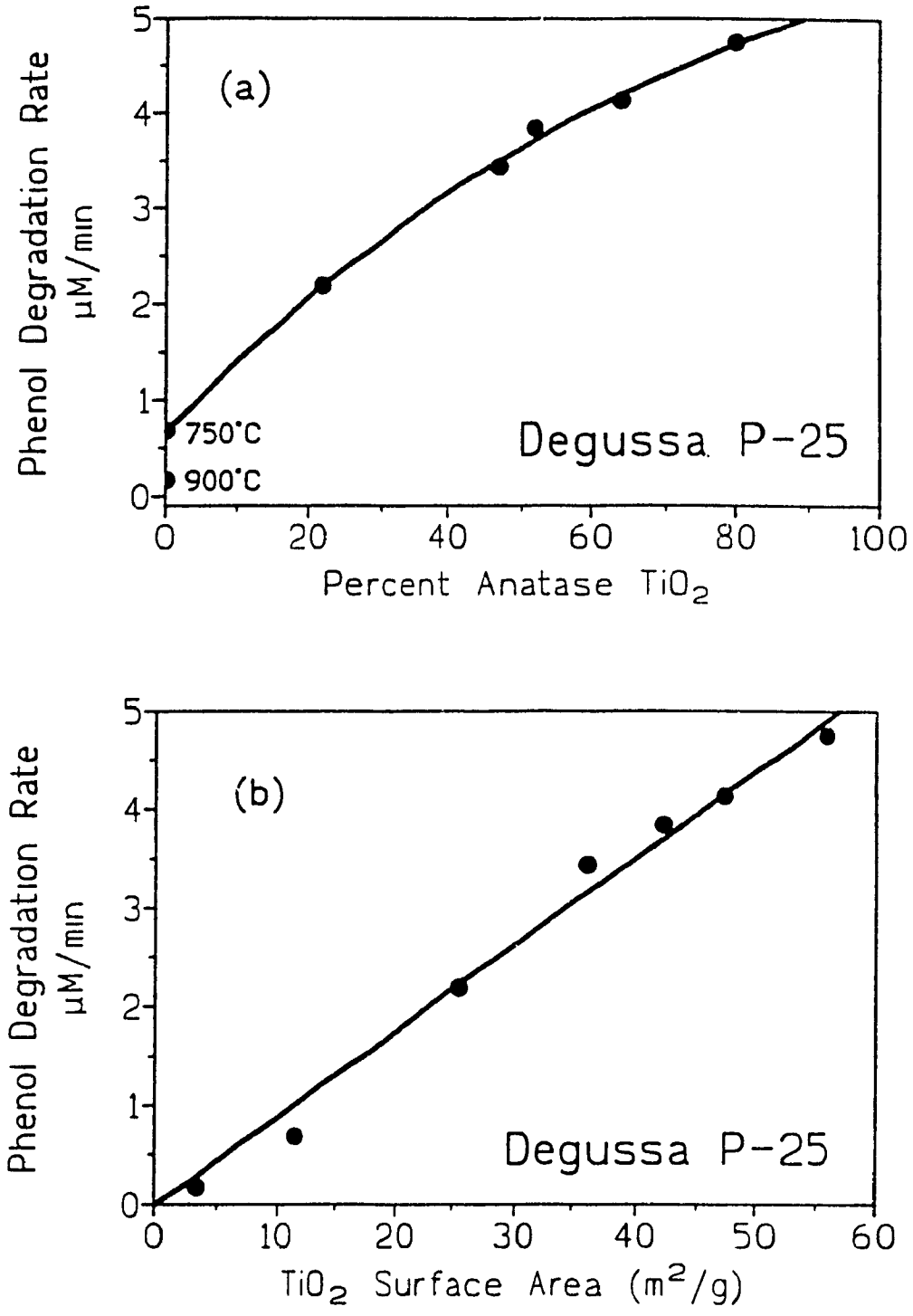

Figure 7.3 Correlation of surface area and phenol degradation to anatase concentration in P25 Degussa TiO_2.

Table 7.1 Surface Area and Rate of Phenol Degradation of Various Heat-treated P-25 Degussa TiO_2 Samples.

% Anatase	Surface Area m^2/g	Rate of Phenol Degradation, $\mu M\ min^{-1}$
80	56	4.75
64	47.4	4.13
52	42.2	3.84
47	36.1	3.44
22	25.5	2.19
0 (750 °C heat treatment)	11.5	0.68
0 (900 °C heat treatment)	3.2	0.17

less than that of surface area. If interparticle electron transfer were of greater importance, the rutile concentration should have a greater influence on the photooxidation of the phenol. Between ~ 20 to 80 % anatase the phenol degradation rate increased non-linearly with anatase concentration. By contrast, the rate varied linearly with the surface area. The results are also consistent with observations that the photoactivity of rutile is dependent upon the method of preparation;[9,10] the 100% rutile sample of P-25 obtained by heat treatment at 750 °C showed higher photooxidative ability than did the sample heated at 900 °C. Other factors, such as the presence of impurities, the method by which P-25 is prepared, surface treatment, etc., may be responsible for the high photooxidative ability of untreated P-25 Degussa TiO_2.

The importance of factors other than interparticle electron transfer in P-25 TiO_2 is strengthened by recent observations by Serpone and Pelletier[11] who looked at the

photoactivity of partially dehydroxylated P-25 TiO_2. In their study, partial dehydroxylation of the particle surface was achieved by alternate cycles of soaking the sample in water during the day and heating in a vacuum oven at 380 °C overnight. After 5 cycles, no change in the anatase/rutile concentration was noted but infrared measurements noted a decrease in the intensity in the water stretching frequency. The degradation of phenol under identical conditions as used to evaluate the different TiO_2 samples yielded a phenol degradation rate 27% slower (3.43 ± 0.2 μM min^{-1}) than the untreated sample. If interparticle electron transfer were mainly responsible for the catalytic activity of P-25 Degussa, then changing the nature of the surface should have had no effect on the degradation rate. Clearly, surface properties are the primary factors affecting redox chemistry at the semiconductor particle. One of these is the density of the surface OH^- groups.

7.3 EFFECT OF PARTICLE SIZE (ANATASE TiO_2) ON THE PHOTOOXIDATION OF PHENOL

The effect of TiO_2 particle size (23, 133 and 281 Å diameter particles) on the photooxidation of phenol was examined. The degradation of phenol in all three cases obeyed reasonably good zero order kinetics (Figure 7.4a-c) to about 75 minutes of illumination and yielded degradation rates of 2.77 ± 0.12, 2.56 ± 0.12 and 2.95 ± 0.09 μM min^{-1} for the 23, 133 and 281 Å TiO_2 particles, respectively. Within experimental error, particle size has a small but finite effect on the photooxidation of phenol. This result would appear, at first glance, to contradict the results presented in Section 7.2.

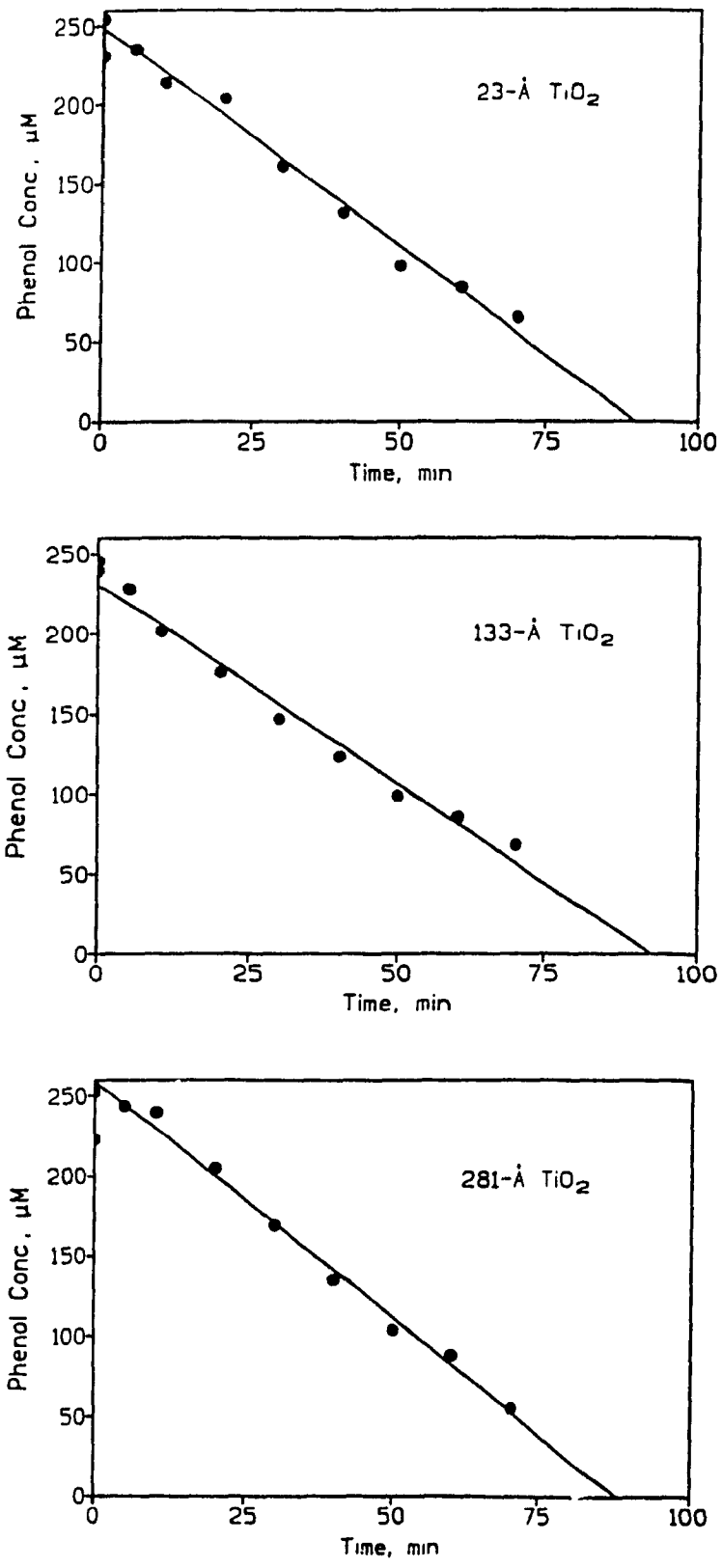

Figure 7.4 Degradation of phenol by 23 (upper) 133 (middle) and 281 (lower) Å TiO_2 particles; pH 3; 2 g/L catalyst concentration, air, UV illumination.

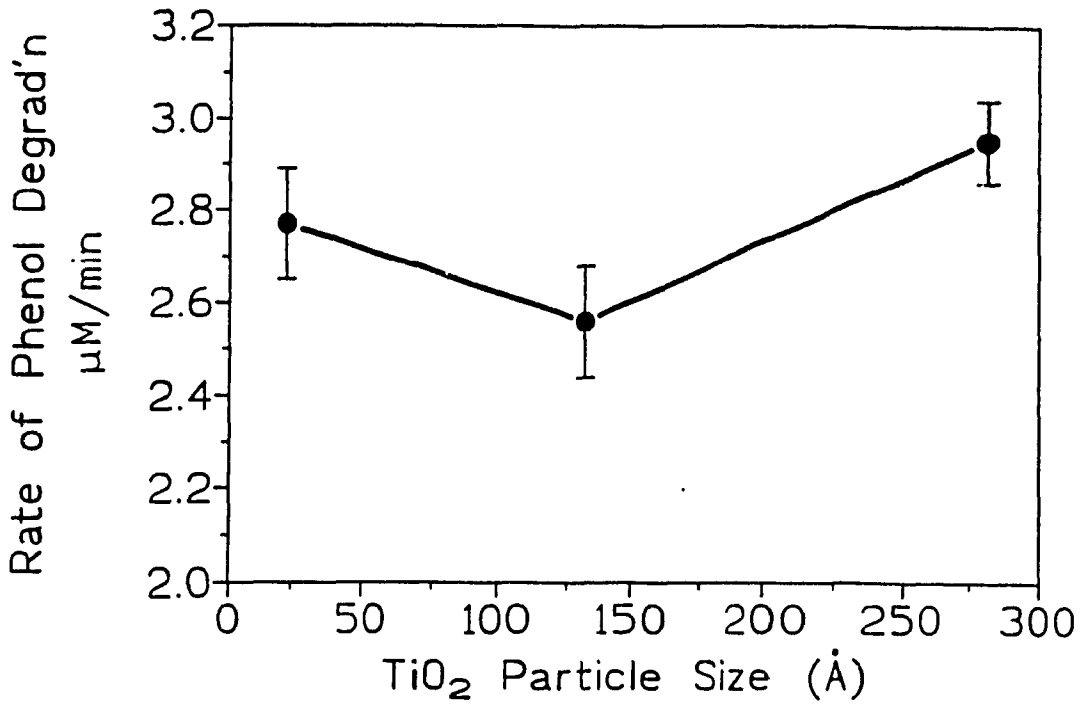

Figure 7.5 Rate of degradation of phenol as a function of TiO_2 particle size.

The smaller particles should have a higher surface area (eq 7.1) and as such the phenol degradation rate should have shown a linear dependence on particle size, definitely not the case here (Figure 7.5).

$$surface\ area = 4\pi R^2 \tag{7.1}$$

where **R** is the particle radius. However, many materials fail to show good correlation between BET area and catalytic activity.[12] Further, all three samples contained a large amorphous fraction and the exact concentration of anatase in the materials was not accessible. Nevertheless, from Figure 7.3a an anatase concentration of ~ 30-40 % is inferred. It is conceivable that the three samples contained different amounts of anatase thereby making assessment of the effect of particle size difficult.

7.4 EFFECT OF TRANSITION METAL DOPANTS IN THE BULK OF ANATASE TiO_2 ON THE PHOTO-CATALYTIC PROPERTIES OF TiO_2

In order to assess the effect of doping the bulk of anatase with various transition metal dopants and, in two cases, a combination of two metal dopants, the materials were tested using standard oxidation and reduction reactions.

The oxidation of oxalic acid was selected as a standard reaction to measure the relative photooxidative activity of the various materials based on several considerations. First, the oxidation of oxalic acid by illuminated suspensions of TiO_2 has been studied extensively and the mechanistic details of the process are well characterized.[13] Second, the redox couple $H_2C_2O_4(aq)/CO_2$ (E^0 = -0.49 V) is small and as such even weakly oxidizing semiconducting materials should be able to transform it.[13] Third, the photooxidation of oxalic acid to CO_2 gas proceeds through a minimum of intermediate products (equation 7.2) and therefore competing reaction pathways would be minimized.

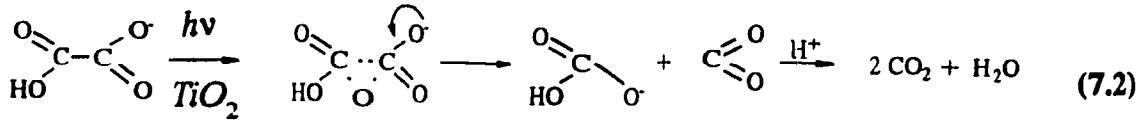

(7.2)

Competing reaction pathways would complicate evaluation of the relative photooxidative ability of the materials. In fact, the conversion of isopropanol to acetone was originally considered as a possible standard reaction to compare the photooxidative activity of the various materials. However, preliminary experiments, in which the conversion of anhydrous isopropanol to acetone using UV illuminated 2 g/L P-25 Degussa TiO_2 suspensions was monitored using gas chromatography, indicated that a number of

intermediate products were formed in the reaction. This raised the possibility that the addition of the dopant *might* favour the formation of particular intermediates and thereby complicate assessment of the photooxidative activity of the material. Lastly, the analytical procedure for determining the amount of oxalic acid left in solution following irradiation was conducive to screen a large number of samples. The reaction was not followed to complete mineralization; the net conversion, namely its transformation to intermediate products, was calculated by determining the quantity of unreacted oxalic acid using the permanganate titration method as described in Chapter 2. The formation of gaseous CO_2 was detected qualitatively by purging the headspace gases into an alkaline solution of barium nitrate; the presence of CO_2 was noted by the formation of the white ($BaCO_3$) precipitate.

The photoreductive activity of the different materials was evaluated by examining the photoreduction of water into dihydrogen gas (equation 7.3).

$$TiO_2 + h\nu \rightarrow e^-(TiO_2) + h^+(TiO_2) \qquad (7.3a)$$

$$2\,e^-(TiO_2) + 2\,H_2O \rightarrow H_2\uparrow + 2\,OH^- \qquad (7.3b)$$

Initially, the photoreduction of silver ions from solution was considered as a possible means of testing the photoreductive activity of the samples. However, it was observed that upon stirring a 2 g/L suspension of the doped and naked homemade TiO_2 materials

in the presence of 50 ppm Ag^+ for 30 minutes in the dark, no silver ions were left in solution. Under identical conditions, with P-25 Degussa TiO_2 only 25% of the silver ions were adsorbed in the dark.

7.4.1 Photooxidative Tests

The results of the photooxidation of oxalic acid (at pH =2.25) by the various materials is summarized in Table 7.2. P-25 Degussa TiO_2 was included in the tests for comparative purposes; the net conversion of oxalic acid by P-25 Degussa TiO_2 was in excellent agreement with values previously reported by Herrmann and co-workers.[13]

The data in Table 7.2 show that, in general, the addition of a transition metal ion to the bulk of TiO_2 did not result in enhanced photooxidative activity. Rather, in many cases decreased photocatalytic activity was noted, and in certain cases illumination resulted in a reduced affinity of the material for the oxalic acid. This was manifested by negative net conversion (probably reflecting lower adsorption of oxalic acid after illumination of TiO_2 as compared to dark conditions) and suggests that rather than being photooxidized, some of the oxalic acid desorbed from the surface under illumination. It is inferred that illumination affects desorption more than adsorption. As shown in Figure 7.6, increasing the chromium concentration progressively decreased the amount of oxalic acid *removed* from solution. Addition of copper significantly improved the photooxidative activity of the home made TiO_2; at 10 wt.% Cu doping oxidation is enhanced such that the photoactivity was comparable to that of P-25 Degussa TiO_2. However, the improved catalytic activity is tempered by the observation of a significant

Table 7.2 Photoconversion of Oxalic acid (initial concentration = 5 x 10^{-3} M)

TiO_2, TiO_2/x% M	% Conversion dark	Net % Conversion UV light[a]	Net % Conversion Vis light[a]	ppm (%) M leached - UV illumin.	ppm (%) M leached -Vis illumin.
P-25 Degussa TiO_2	10.2	40.2	0.2	-	-
Home made TiO_2	13.4	25.7	3.6	-	-
0.1	18.3	13.2	-2.9	0 (0)	0 (0)
0.5	18.3	11.1	-2.4	0.09 (0.9)	0.08 (0.8)
1	17.6	8.9	1.6	0.33 (1.6)	0.28 (1.4)
3 % Cr^{+3}	21.3	1.4	-4.3	0.48 (0.8)	0.61 (1)
5	23.3	-0.6	-3.6	2.14 (1.2)	1.66 (1.7)
10	24.3	-3.7	-8.1	2.98 (1.5)	3.52 (1.8)
20	26	-5.0	-3.7	6.17 (1.5)	8.26 (2.1)
0.1	14.9	27.8	-0.9	0.19 (9.5)	0 (0)
0.5	19.4	26.9	1.3	0.88 (8.8)	0.39 (3.9)
1 % Fe^{+3}	19.6	23.1	-0.2	1.45 (7.2)	0.67 (3.4)
5	21.8	26.8	1.8	3.7 (3.7)	1.37 (1.4)
10	20.3	28.1	3.3	3.66 (1.8)	2.85 (1.4)
1% Cr^{+3}, 1% Fe^{+3}	19.6	20.1	-0.4	0.33 (Cr, 1.6) 1 03 (Fe, 5.2)	1.56 (Cr,7.8) 0.39 (Fe,2)
0.1	18.3	17.7	-1.0	0 (0)	0 (0)
0.5	19.8	6.9	-3	0 (0)	0 (0)
1	21.8	8	-5	1.89 (9.4)	2.34 (11.7)
3 % V^{+5}	14.2	3.8	3.9	1.89 (3.2)	2.73 (4.6)
5	15.1	4.7	2.5	3.77 (3.7)	2.73 (2.7)
10	17.3	-1.1	-3.5	8.96 (4.5)	11.3 (5.6)
1% V^{+3}	19.8	2.6	-0.7	0.94 (4.7)	0 (0)
1% V^{+5}, 1% V^{+3}	21.3	1.1	-2.2	2.83 (7.1)	2.73 (6.8)
0.1	20.0	22.4	0.3	0.17 (8.5)	0 (0)
0.5	22.3	11.9	-0.3	2.16 (21.6)	1.31 (13.1)
1	19.1	26.5	5.1	5.09 (25.4)	4.33 (21.6)
3 % Rh^{+3}	24.2	11.8	-0.6	7.93 (13.2)	7.85 (13.1)
5	18.1	15.4	8.0	12.93 (12.9)	12.02 (12)
10	16.6	19.4	8.2	15.78 (7.9)	16.92 (8.5)
0.05	18.6	24.3	4.7	0 (0)	0 (0)
0.1	25.7	10.9	-3.7	0 (0)	0 (0)
0.3 %	21.3	14.7	1.4	0 (0)	0 (0)
0.5 Ru^{+3}	25.2	3.4	0.6	0 (0)	0 (0)
1	21.6	8.8	3.5	0 (0)	0 (0)
5	15.3	10.2	7.7	0 (0)	0 (0)

TiO_2, TiO_2/x% M	% Conversion dark	Net % Conversion UV light[a]	Net % Conversion Vis light[a]	ppm (%) M leached - UV illumin.	ppm (%) M leached -Vis illumin.
0.05	19.8	33.4	1.7	0 (0)	0 (0)
0.1 %	19.6	18.7	2.0	0 (0)	0 (0)
0.5 Pt^{+4}	23.1	15.2	-1.9	0 (0)	0 (0)
1	18.5	24.4	4.2	0 (0)	0 (0)
0.05 %	22.6	21.4	0.1	0 (0)	0 (0)
0.1 Ru^{+3}	18.3	27.6	2.9	0 (0)	0 (0)
0.5 & Pt^{+4}	20.1	11.6	-0.7	0 (0)	0 (0)
1 (1:1)	20.1	9.1	2.3	0 (0)	0 (0)
1 % Pd^{+2}	24.8	23.4	-2.7	0.81 (4.1)	1.68 (8.4)
10	17.8	22.1	0.7	12.65 (6.3)	13.2 (6.6)
1 % Cu^{+2}	20.3	32.5	1.5	7.14 (35.17)	5.1 (25.5)
10	19.1	40.5	3.1	37.43 (18.7)	32 (16)
1% Re^{+3}	18.6	16.2	-1.3		
1% Re^{+7}	19.1	22.7	0		
1% Re^{+3}, 1% Re^{+7}	22.8	16.2	-1.6		
1% Y^{+3}	19.8	22.9	2.3		
1% Nd^{+3}	22.6	15.5	-3.5		
1% Co^{+2}	18.6	24.1	5.3	1.79 (9)	2.21 (11.1)
1% W^{+6}	18.6	23.8	4.7	0 (0)	0 (0)
1% Mo^{+6}	19.3	5.5	1.9	0.41 (2)	0 (0)
1% Ni^{+2}	19.3	17.3	1.9	2.19 (11)	2.23 (11.2)
1% Ce^{+6}	18.8	16	2.3		
1% Ti^{+3}	17.1	24	-0.7		

[a] Net % conversion = % conversion in UV or Vis light - % conversion in the dark

Note: Numbers in parenthesis refer to the percent M leached from the material

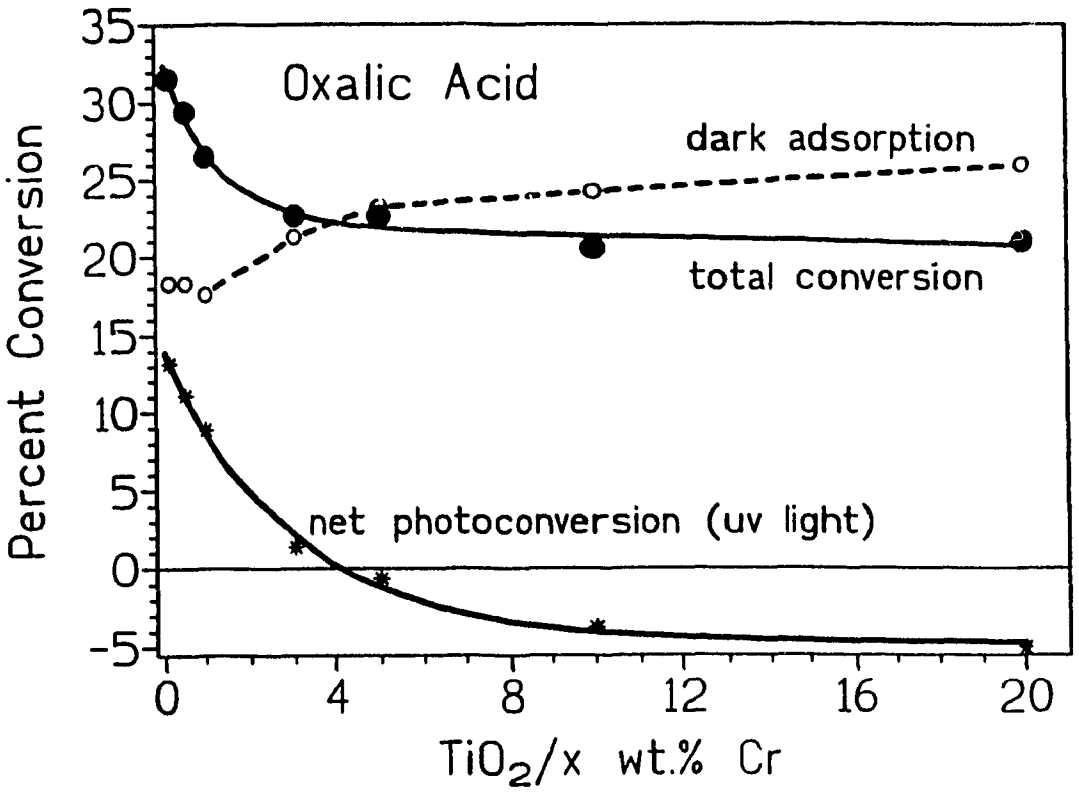

Figure 7.6 Net conversion of oxalic acid as a function of chromium concentration in TiO_2 (wt./wt.%)

fraction of the copper dopant that leached from the TiO_2. Possibly the Cu^{+2} traps photogenerated electrons from bandgap excitation of the TiO_2/x wt.% Cu^{II} material to become a Cu^0 species, leaving excess holes on the particles. This Cu^0 species could reduce the oxalic acid at the surface.

A number of materials showed poor stability; the metal dopant was detected in non-neglible amounts in solution following either visible or ultraviolet illumination. The amount of dopant dispelled from the lattice under both illumination conditions is comparable. In all of the home made samples, less than 0.3% titanium was detected in solution at the end of the reaction indicating that despite the removal of the dopant from

the TiO_2, the lattice was still relatively stable to photocorrosion.

In a number of cases, addition of the dopant resulted in an increased spectral response in the visible part of the solar spectrum (see Chapter 6). However, despite this increased visible light sensitivity, the photooxidative activity of TiO_2 was not extended by irradiation in the visible region (i.e wavelengths $\geq$ 400 nm). None of the dopants examined significantly enhanced the oxidation of oxalic acid when only visible light was used, although high doping levels of rhodium ($\geq$ 5%) showed a mild improvement in the net conversion of oxalic acid. Unfortunately, as was the case for copper, non-negligible concentrations of rhodium were also detected in solution following illumination.

7.4.1.1 Photoreduction of Oxalic Acid

After 30 minutes of illumination several of the filtrates of the TiO_2/M and oxalic acid mixtures were a light greenish yellow colour. Several observations precluded the colour being simply due to metal ions leached from the lattice. First, the colour of the filtrates obtained using differently doped TiO_2 materials was identical. Since the absorption spectra of the different metal ions are different, the colour of the filtrates was also expected to be different. Further, when the filtrates were analyzed the concentration of metal dopant present in solution was too low (ppm levels) to give such strongly coloured solutions. Second, acidification of the sample with concentrated H_2SO_4 caused the solution to become colourless. If the colour were due to metal ions in solution, acidification would not have shown such an effect. Lastly, the absorption spectra of

several filtrates, an example of which is the filtrate obtained following the reaction of TiO_2/0.5 wt.% Ru with oxalic acid (Figure 7.7b), differed from that of oxalic acid (Figure 7.7a); the spectral maximum at ~ 390 nm is evident which is not found in a 5 mM solution of oxalic acid; it is attributed to glyoxylic acid (see below).

Table 7.3 lists the final pHs and the absorbances of the various filtrates at 390 nm. It can be seen that the system containing P-25 Degussa TiO_2 also produced a very small absorbance at 390 nm indicating that this reaction also yielded a previously unreported side product. However, given that the solution was optically clear and that the small absorption is indicative of a small concentration of the product (assuming a reasonable ϵ for the product) it is not surprising that its presence was not detected previously.[13] Assuming that Beer's law is obeyed, Table 7.3 illustrates that the concentration of the product formed is affected by the dopant concentration. For example, in the case of TiO_2/x wt.% Cr increasing the chromium concentration results in a decrease in the absorption at 390 nm, and therefore in a decrease in the concentration of the product formed. No correlation between the final pH of the solution and product formation, or for that matter oxalic acid conversion, is evident.

An attempt was made to identify the product formed in the reaction. Since the oxidation of oxalic acid is believed[13] to proceed through an epoxide and bicarbonate intermediates, both of which are unstable[14] (equation 7.2), and thus not expected to show absorption in the visible region of the absorption spectrum, formation of a reduction product of oxalic acid was hypothesized. The first product considered was glycolic (or hydroxyacetic) acid ($OHCH_2COOH$) which is produced from the electrolytic reduction

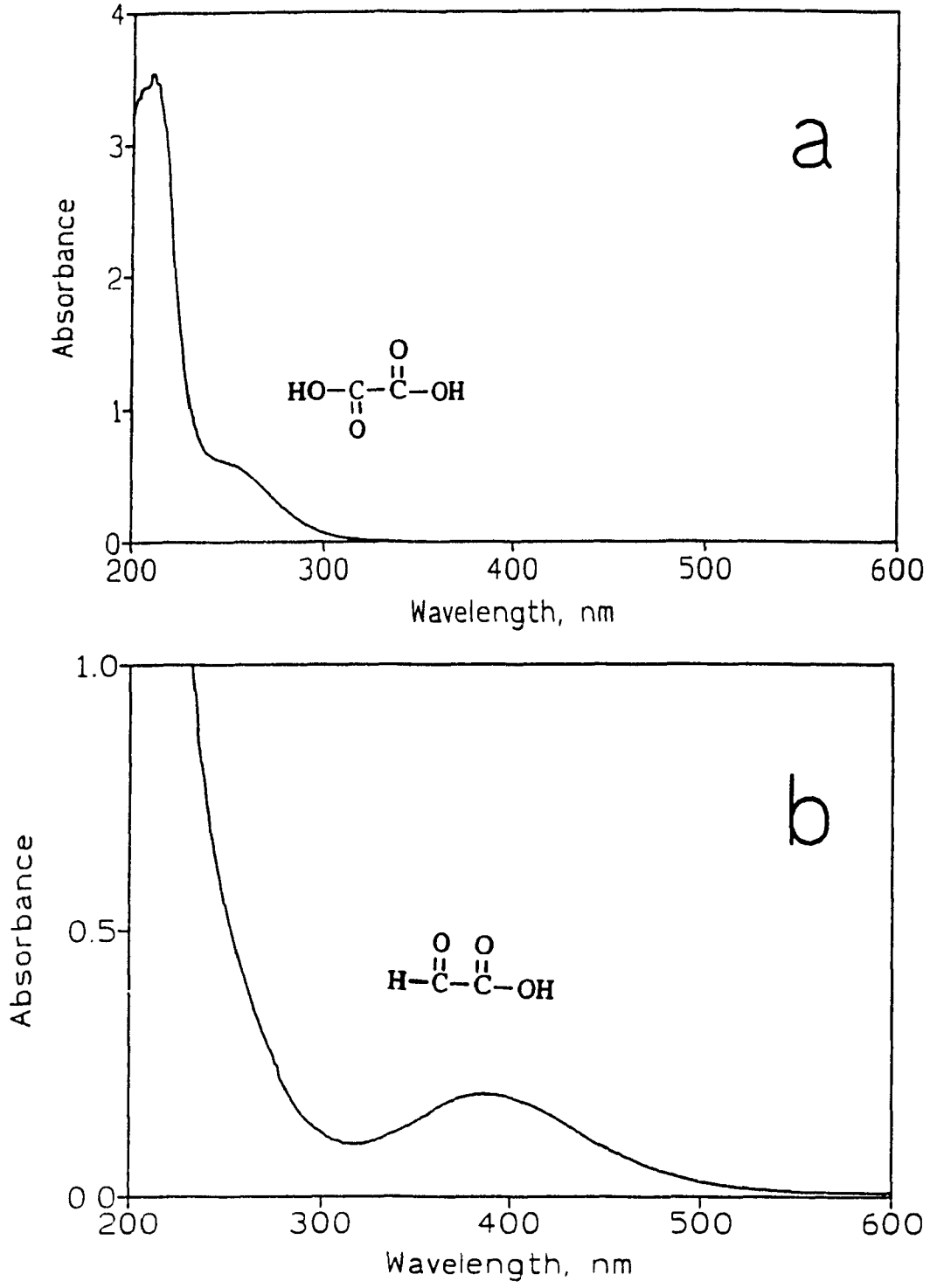

Figure 7.7 (a) Absorption spectrum of 5 mM oxalic acid. (b) Absorption spectrum of the filtrate of a slurry of 2 g/L TiO_2/0.5 wt % Ru in 5 mM oxalic acid after 30 min. irradiation. In both cases the optical path length was 1 cm.

Table 7.3 **Final pH and Absorbance at 390 nm of the Filtrate of the Reaction of 5 mM Oxalic acid and TiO_2/M Following 30 Min. UV Irradiation.**

Sample or Dopant Added to TiO_2	Dopant concentration, wt/wt% TiO_2	Final pH	Absorbance at 390 nm (UV illumin.)
Oxalic acid	-	2.32	0
P-25 Degussa TiO_2	-	2.51	0.016
Home made TiO_2	-	2.41	0.047
Cr^{+3}	0.1	2.27	0.099
	0.5	2.27	0.074
	1	2.25	0.074
	3	2.22	0.049
	5	2.23	0.045
	10	2.24	0.035
	20	2.12	0.018
Fe^{+3}	0.1	2.39	0.03
	0.5	2.00	0.01
	1	2.09	0.01
	5	2.38	0.019
	10	2.46	0.019
Cr^{+3} + Fe^{+3} (1:1)	1 (each dopant)	2.41	0.027
V^{+5}	0.1	2.36	0.026
	0.5	2.27	0.026
	1	2.39	0.011
	3	2.21	0.001
	5	2.12	0.001
	10	2.31	0.001
V^{+3}	1	2.19	0.033
V^{+5} + V^{+3} (1:1)	1 (each oxidation state)	2.20	0.007
Rh^{+3}	0.1	2.35	0.026
	0.5	2.05	0.061
	1	2.34	0.1
	3	2.28	0.087
	5	2.16	0.148
	10	2.27	0.137
Ru^{+3}	0.05	2.27	0.089
	0.1	2.00	0.1
	0.3	2.24	0.107
	0.5	1.73	0.182
	1	2.22	0.095
	5	2.19	0.047

Sample or Dopant Added to TiO_2	Dopant concentration, wt/wt% TiO_2	Final pH	Absorbance at 390 nm (UV illumin.)
Pt^{+4}	0.05 0.1 0.5 1	2.45 2.33 2.22 2.22	0.066 0.064 0.083 0.086
Ru^{+3} + Pt^{+4} (1:1)	0.05 (each dopant) 0.1 0.5 1	2.36 1.98 2.29 2.34	0.095 0.095 0.086 0.116
Pd^{+2}	1 10	2.43 2.31	0.120 0.109
Cu^{+2}	1 10	2.11 2.38	0.109 0.055
Re^{+3}	1	2.33	0.055
Re^{+7}	1	2.28	0.054
Re^{+3} + Re^{+7} (1:1)	1 (each oxidation state)	2.31	0.075
Y^{+3}	1	2.18	0.088
Nd^{+3}	1	1.86	0.073
Co^{+2}	1	2.26	0.073
W^{+6}	1	2.18	0.076
Mo^{+6}	1	2.26	0.076
Ni^{+2}	1	1.88	0.051
Ce^{+6}	1	1.77	0.088
Tl^{+3}	1	2.35	0.047

of oxalic acid.[15] A Fourier transform infrared (FTIR) spectrum of the most coloured filtrate (that from the reaction of oxalic acid with TiO_2/0.5 wt.% Ru) was inconclusive as to the precise nature and therefore confirmation of glycolic acid. This spectrum did not correlate with the FTIR spectrum reported for glycolic acid in the Sadtler IR catalog.[16] This may have been due to a low quantity of the presumed product in the filtrate, and to interference from the larger quantity of oxalic acid present in solution.

However, more convincing evidence that glycolic acid was not produced in the reaction comes from comparison of the absorption spectrum of the intermediate formed (Figure 7.7b) to that of a 2% (by weight) solution of glycolic acid (Figure 7.8a). There is no absorption in the area (~ 390 nm) where the intermediate showed an absorption band.

The second possibility was that glyoxylic acid (HOCCOOH), also produced by the electrolytic reduction of oxalic acid, was formed. A sample of glyoxylic acid was prepared from oxalic acid using a known procedure[17] and the absorption spectrum of the material is shown in Figure 7.8b. Both the colour and the spectral properties of the glyoxylic acid were in good agreement with those of the intermediate. The small spectral differences may have been due to the higher pH of the glyoxylic acid solution (~ 4.1) relative to that of the solution containing oxalic acid and the intermediate (~ 2.4). As well, the spectrum shown in Figure 7.8b was that of the mixture which also contained large quantities of unreacted oxalic acid. A sensitive colorimetric method of determination for glyoxylic acid, the details of which may be found elsewhere,[18] was employed in order to verify that the product formed was in fact glyoxylic acid. In essence, the procedure involved reacting the solution to be tested with phenylhydrazine in a high ionic strength medium. The glyoxylic acid reacts with the phenylhydrazine to produce a phenylyhydrazone which is oxidized by potassium ferricyanide to yield a complex which has an absorption band at ~ 517 nm. The technique can detect concentrations as low as 0.5 to 8 μg/mL of glyoxylic acid.[18] A typical absorption spectrum obtained from the testing of the various filtrates, in this case the filtrate obtained from the reaction of oxalic acid with TiO_2/1 wt.% Pd, is shown in Figure 7.9.

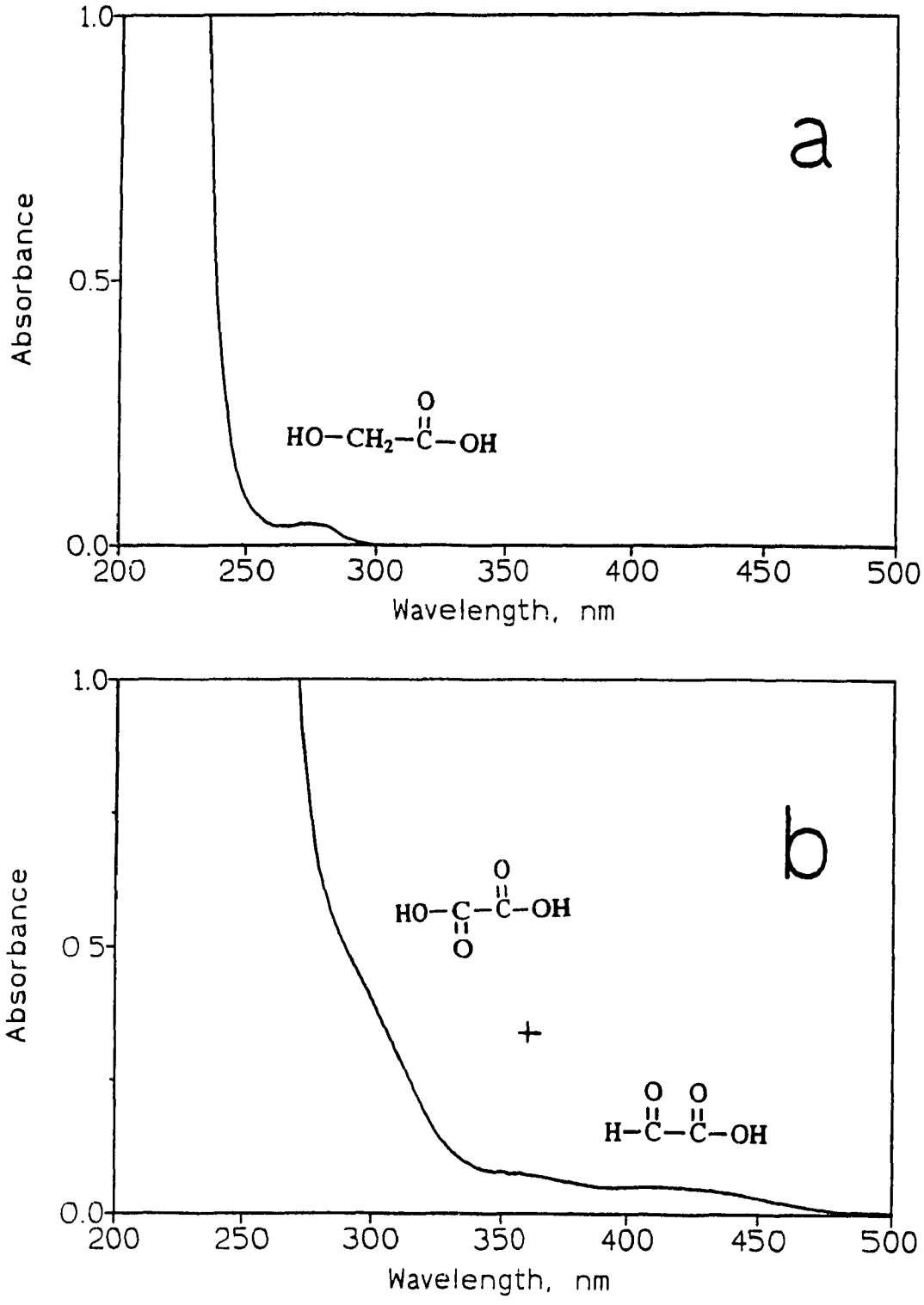

Figure 7.8 (a) absorption spectrum of a 2 % by weight solution of glycolic acid. (b) A solution of glyoxylic acid and oxalic acid prepared according to ref. 17. In both cases, the optical path length was 1 cm.

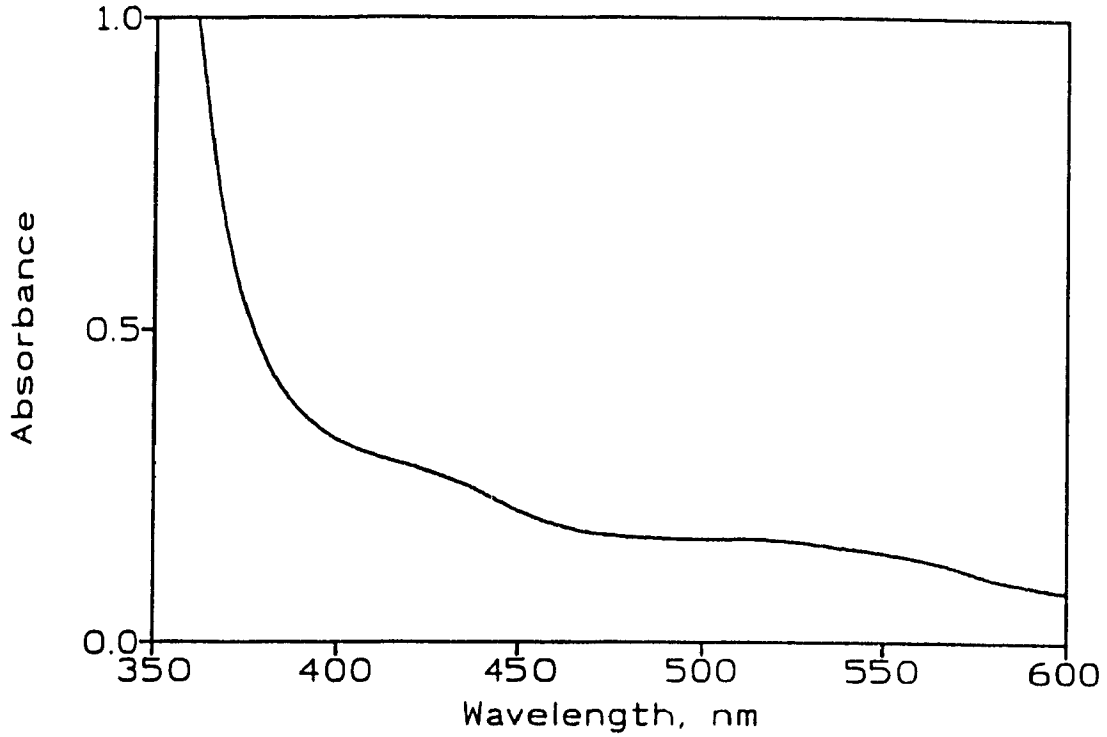

Figure 7.9 Absorption spectra of the filtrate of TiO2/ 1 wt% Pd tested using Lui and Roels technique [Ref. 18]. See text for details, (optical path length = 1 cm).

The spectrum is in good agreement with the spectrum reported for the phenylhydrazone complex by Lui and Roels.[18] The test indicated that all the samples showing absorption at 390 nm contained glyoxylic acid, thereby confirming that the reaction product formed was in fact glyoxylic acid.

Glyoxylic acid formation was also produced as a byproduct in several of the "oxidation" reactions carried out under visible excitation conditions. The systems which showed conversion of oxalic acid to glyoxylic acid were TiO_2 materials doped with: Rhodium (1 to 10 wt%), Ruthenium (5 wt% only), Platinum and Ruthenium (1 wt% only), Palladium (1 and 10 wt%) and Cerium.

7.4.2 Photoreductive Tests

The amount of hydrogen gas produced from the photocleavage of H_2O at pH 3 by the various materials tested is shown in Table 7.4. Figure 7.10 illustrates representative plots of the amount of hydrogen gas produced with time. In all cases where hydrogen gas was produced, the increase was linear with time and the rate of hydrogen gas produced (μL/hr) was taken as the slope of a plot of hydrogen gas produced versus time.

As noted in Table 7.4, doping TiO_2 with platinum enhanced the photoreductive properties of TiO_2. Increasing the platinum concentration beyond 0.1 wt %, however, did not result in a significant improvement in the rate of hydrogen produced. Commensurate with the hydrogen production, the material became silvery grey in colour (see below). This indicates that the Pt^{+4} ions on the surface were reduced to platinum metal (probably also in the bulk of the material); platinized TiO_2 is known to reduce water to hydrogen gas.[20] The dopant concentration affected the amount of hydrogen gas produced. For example, increasing the chromium dopant concentration from 0.1 to 5 % effectively eliminated the ability of TiO_2 to produce H_2 gas. Similarly, small doping levels ($\leq$ 1%) of rhodium were beneficial whereas the TiO_2 samples containing higher concentrations of rhodium ($\geq$ 3%) showed no photoreductive activity. A similar behaviour was also shown by varying the dopant level of palladium. Moreover, it is interesting that P25 TiO_2 is inactive towards H_2 production under the conditions used; it compared to homemade TiO_2 which shows a small but nevertheless finite quantity of H_2 formed.

Table 7.4 Rate of Hydrogen Gas Produced

Sample or Dopant Added to TiO_2	Dopant concentration, wt/wt% TiO_2	Rate of Hydrogen gas Produced, μL/hr
P-25 Degussa TiO_2	-	0
Home made TiO_2	-	3.6
Cr^{+3}	0.1 0.5 1 5	2.2 2.2 0.8 0
Fe^{+3}	0.1 0.5 5	0.7 1.1 0
Cr^{+3} + Fe^{+3} (1:1)	1 (each dopant)	0
V^{+5}	0.1 0.5 5	1.5 0 0
V^{+3}	1	0
V^{+5} + V^{+3} (1:1)	1 (each oxidation state)	0
Rh^{+3}	0.1 0.5 1 3 5	10.5 9.4 6.5 0 0
Ru^{+3}	0.05 0.1 0.3 0.5	5.5 6.6 0 0
Pt^{+4}	0.05 0.1 0.5 1	14.9 21.6 19.9 21.5
Ru^{+3} + Pt^{+4} (1:1)	0.05 (each dopant) 0.1 0.5 1	4.2 8.3 0.9 0
Pd^{+2}	1 10	13.1 0
Cu^{+2}	1	2.3
Re^{+3}	1	0

Sample or Dopant Added to TiO_2	Dopant concentration, wt/wt% TiO_2	Rate of Hydrogen gas Produced, μL/hr
Re^{+7}	1	0.6
Re^{+3} + Re^{+7} (1:1)	1 (each oxidation state)	0
Y^{+3}	1	4.4
Nd^{+3}	1	1.1
Co^{+2}	1	0
W^{+6}	1	2.0
Mo^{+6}	1	0
Ni^{+2}	1	1.0
Ce^{+4}	1	0
Tl^{+3}	1	0

7.4.3 Spectral Changes

Several of the materials tested showed pronounced colour changes following UV, and, to a lesser extent, visible illumination. A summary of these changes is summarized in Table 7.5.

TiO_2 doped with 10% Pd (by weight) is a good example of the colour changes which were observed. The colour of the material changed from a brass button colour to a silvery colour. This is most likely due to the formation of palladium metal at the surface (and to some extent within the bulk of TiO_2). The reflectance spectrum (see Figure 7.11) of the material (following illumination showed a broad structureless absorption band in the visible part of the spectrum, consistent with the absorption spectrum of metallic particle deposits at the surface of TiO_2.[19] The fact that the absorption band (at ~ 480 nm) initially present in the reflectance spectrum prior to

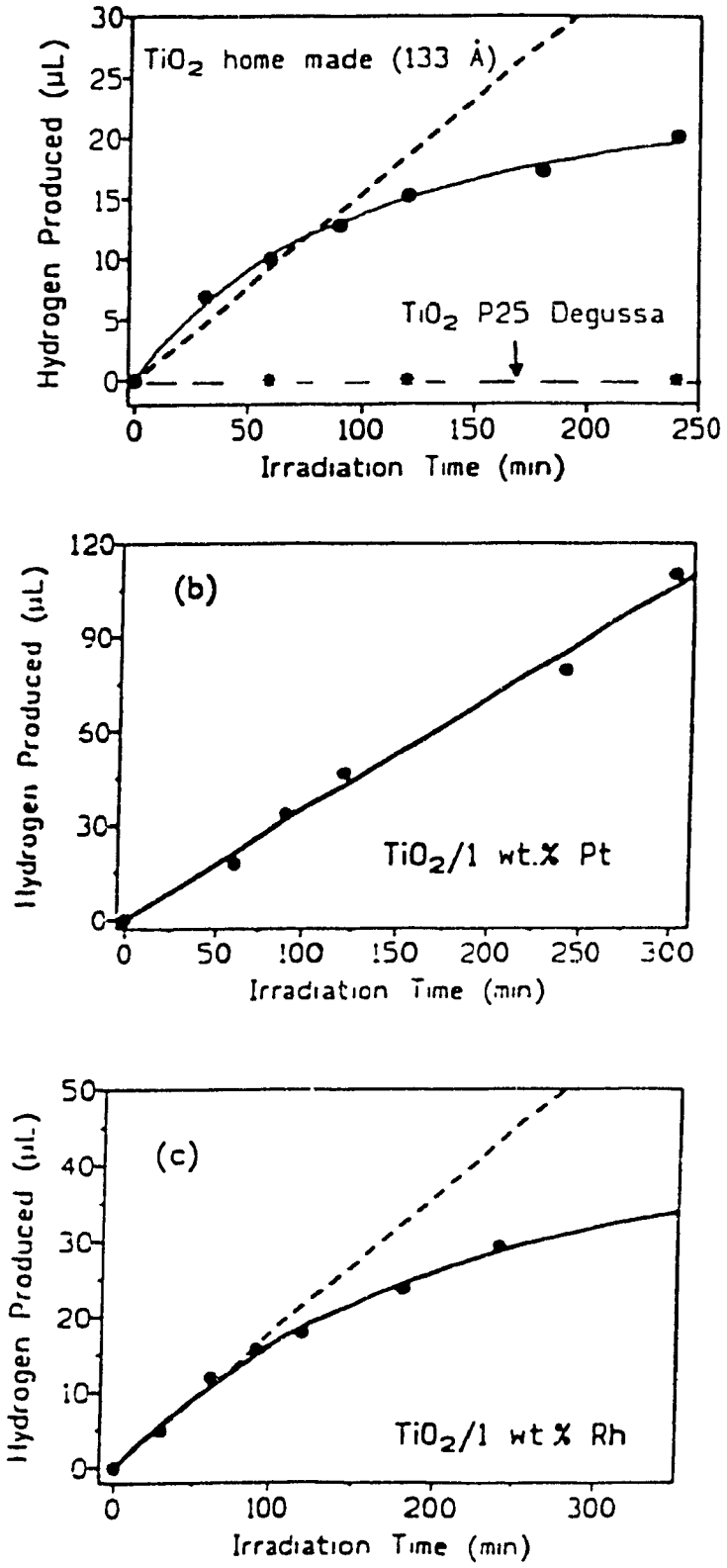

Figure 7.10 a) Representative calibration curve for H_2 detection. b) H_2 produced from reaction of TiO_2/ 1 wt.%Pt in pH 3 H_2O. c) H_2 produced from reaction of TiO_2/ 1 wt.% Rh in pH 3 H_2O.

Table 7.5 Spectral Changes Observed Upon UV (or Visible) Illumination of the Catalyst in Water under Anaerobic Conditions.

Dopant	Original Colour	Colour following illumin.
0.05 0.1 % Pt 0.5 1	yellow reed sunlight yellow spring yellow yellow	pale yellow light grey grey silver (black)
0.1 0.5 % V^{+5} 5	honey cream beige chamoline bronze brown	greyish brown greyish brown no colour change
1 % V^{+3}	beige	greyish brown
1 % V^{+3} & V^{+5} (1:1)	cinnamon sand	greyish brown
0.1 0.5 1 % Rh 3 5	custard corn husk orange mellow orange hearthside orange nishi orange	slightly grey light grey ash grey dark grey black
1 % Pd 10	light sphinx brown brass button	light grey charcoal grey
1 % Cu	arizona sand	light grey
1 % Nd	dirty white	pale yellow
1 % Co	beige	beige
1 % W	dirty white	slightly yellow
1 % Ni	dirty white	yellow green

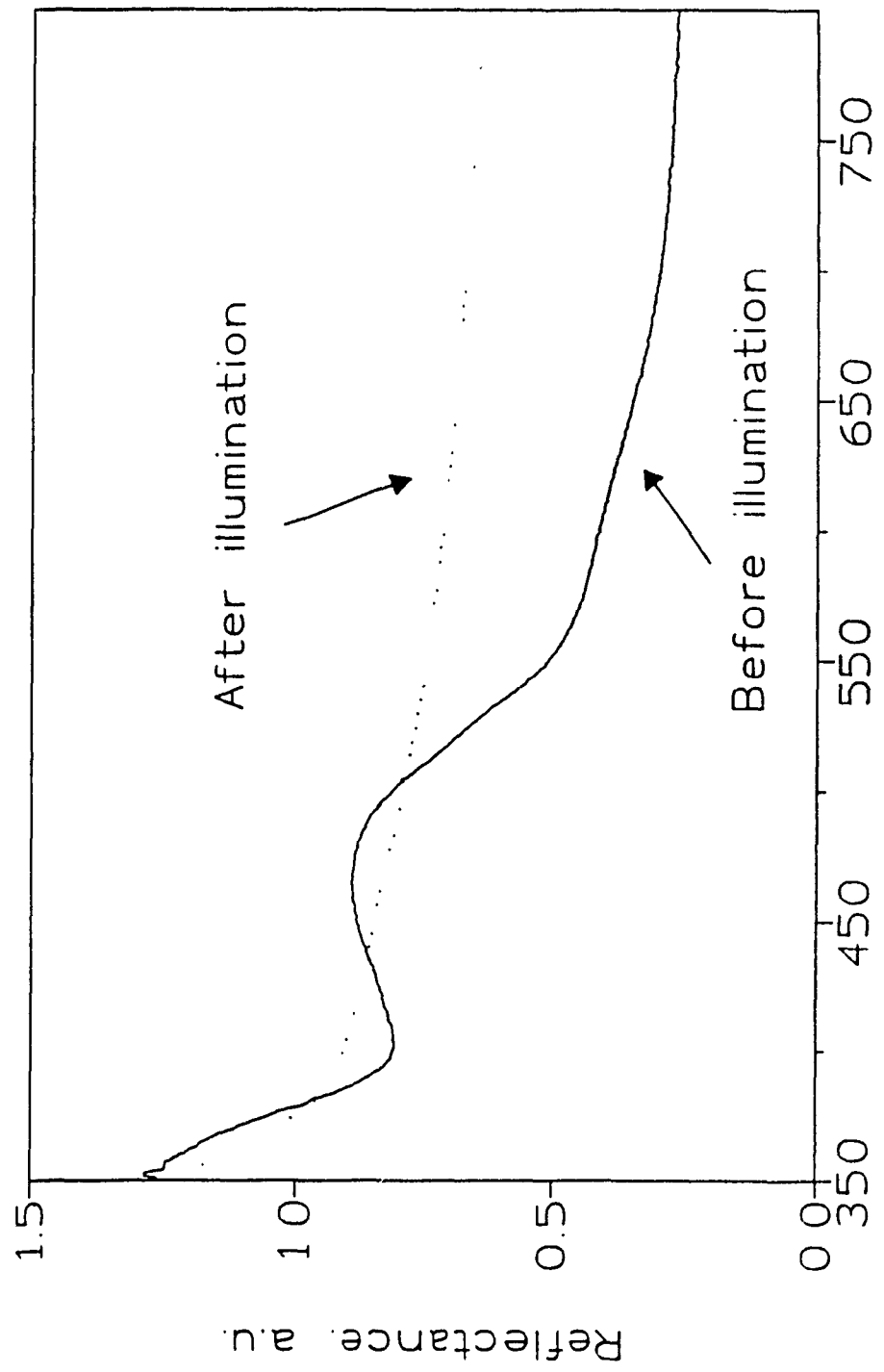

Figure 7.11 Reflectance spectrum of TiO_2/10 wt.% Pd prior to illumination and following 30 min UV illumination.

illumination disappears and is replaced by a broad absorption band strongly suggests that the initial Pd^{+2} ions are reduced to palladium metal(0). These metallic deposits are not affected by exposure to oxygen, indicative of an irreversible photoreductive process.

Rhodium-doped TiO_2 also displayed interesting spectral changes highly dependent upon the atmospheric environment under illumination. In an aerated or slightly enriched oxygen atmosphere, no colour changes were visible for the TiO_2 doped with 3 wt% Rh following UV illumination; the reflectance spectrum of the material (Figure 7.12b) remained unchanged. However, illumination in an argon atmosphere for ~ 30 min. caused the material to become black and a broad band to form in the visible part of the spectrum (Figure 7.12c). This suggests that rhodium metal formed at the surface. Purging an aqueous mixture of the material with oxygen gas did not lighten the colour of the catalyst. Illumination of TiO_2/3 wt.% Rh in an oxygen-saturated solution caused the material to turn from orange to olive green; this suggests that $RhO_2 \bullet 2H_2O$ formed.[19b] In conjunction with this colour change, spectral changes also occurred; the band formed by doping TiO_2 with Rh^{+3} shifted towards the blue (Figure 7.12a). With time (several days) the olive green colour faded back to the original orange colour. Clearly, under anaerobic conditions rhodium(III) acts as an electron trap and is reduced rhodium(0). Under an oxidizing atmosphere (saturated with O_2), electrons are preferentially trapped by O_2 to give the superoxide radical anion $O_2^{\bullet}$, thereby increasing the concentration of holes to oxidize rhodium(III) via a complex, but yet unknown, series of events to rhodium(IV) in the form of $RhO_2 \bullet 2H_2O$.

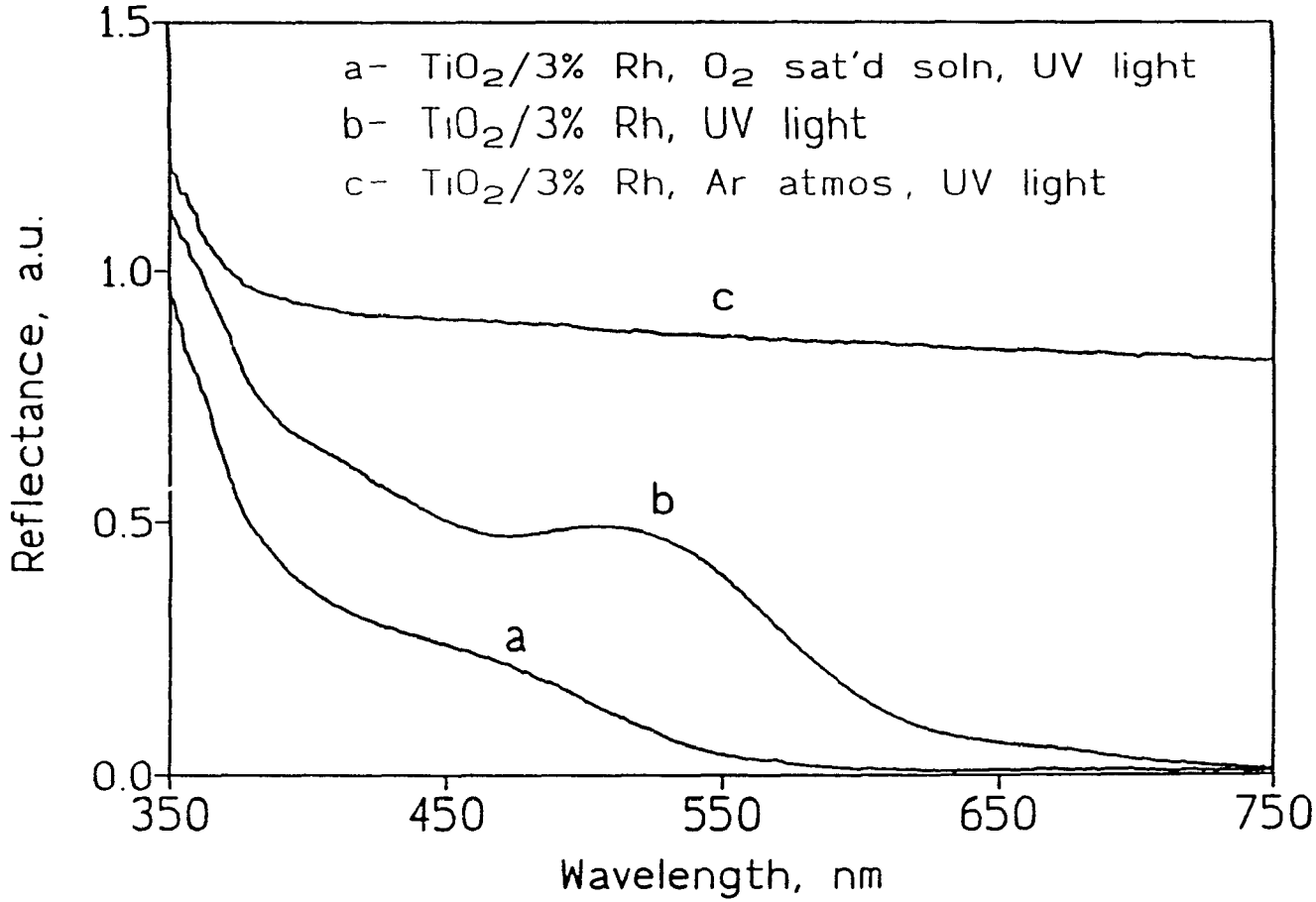

Figure 7.12 Reflectance spectrum of TiO_2/ 3 wt.% Rh following UV illumination in (a) O_2-saturated solutions (b) air-saturated solution (c) inert atmosphere (Ar).

7.4.4 Concluding Remarks

The addition of transition metal dopants to the bulk of anatase TiO_2 does not seem to enhance the photooxidative activity of TiO_2. In many cases it tends to decrease the photocatalytic activity. This is especially true when one considers that the values for the oxidative conversion of oxalic acid must be considered an upper limit, since some of the oxalic acid is in fact reduced to glyoxylic acid. Nevertheless, some of the metal dopants, (e.g., platinum), improve the photoreductive activity of the TiO_2. This was manifested not only in increased rates of hydrogen production from the photoreduction of water but also in the fact that a number of the doped catalysts **reduced** oxalic acid to glyoxylic acid. However, the imp oved photoreductive activity is tempered by the fact that the changes to the catalyst are irreversible, thereby changing the very nature of the doped TiO_2 material. The data suggest that upon band-gap excitation of TiO_2, the electrons reduce the metal dopants to the corresponding metallic form; this can be seen from the colour changes observed when the materials are illuminated. Hence, the dopants behave as electron traps. Unfortunately, some of the reduced metallic deposits are evidently poor catalysts towards reduction of water. As well, the dopants may also be acting as electron/hole recombination centres. This hypothesis is supported by the observation that increasing the dopant concentration often leads to decreased photocatalytic activity (see Tables 7.2 and 7.4), consistent with an increase in recombination centres.

Finally, one last issue needs to be addressed. What happens to the photogenerated holes in the cases where the metal dopant is reduced from its cationic state to the metallic

form? From the data presented in Table 7.2, it can be seen that increased oxidative activity towards oxalic acid conversion does not occur. This suggests that the trapped holes must oxidize water to dioxygen. Alternatively, the "trapping" of the electron by the metal may lead to a rapid build-up of holes at the surface. The large concentration of surface hydroxyl radicals (trapped holes) will lead either to formation of hydrogen peroxide or alternatively to formation of μ-peroxyl species at the surface.[20]

7.5 CONCLUSIONS

A number of conclusions may be reached regarding the photocatalytic activity of both naked and transition metal doped TiO_2. The high photocatalytic activity of P-25 Degussa TiO_2 is not simply related to the fact that the material is comprised of anatase and rutile fractions. Instead, it would appear that the method of preparation of the material and its surface properties are likely more important factors. Studies of these "dynamic" surface properties present formidable challenges. The particle size (23 to 281 Å) of TiO_2 (hence, surface area) appears to have a slight effect on the photooxidative activity of TiO_2. Finally, addition of transition metal dopants to the bulk of TiO_2 does not enhance the photooxidative activity of TiO_2; in some cases it does improve the reductive properties of the materials. Increasing the dopant concentration, in general, leads to decreased photocatalytic activity. The addition of the metal dopants examined in this study also does not extend the photo-action spectrum of TiO_2 into the visible region.

References

1. Ollis, D.F., Pelizzetti, E. and Serpone, N, *Environ. Sci. Technol.*, **1991**, 25, 1522 and references therein.

2. For examples, see
(a) Serpone, N., Ah-You, Y.K., Tran, T.P., Harris, R., Pelizzetti, E. and Hidaka, H., *Sol. Energy*, **1987**, 39, 491;
(b) Lawless, D., Res, A., Harris, R., Serpone, N., Minero,C., Pelizzetti, E. and Hidaka, H., *Chem. Ind. (Milano)*, **1990**, 72, 139;
(c) Domenech, J. and Munoz, J., *J. Electrochim. Acta*, **1987**, 32, 1383.

3. *"Semiconductor Electrodes"*, Finklea, H.O. (Ed.), Studies in Physical and Theoretical Chemistry 55, Elsevier, Amsterdam, **1988**.

4. Schindler, K-M and Kunst, M., *J. Phys. Chem.*, **1990**, 94, 8222.

5. Okamoto, K., Yamamoto, Y., Tanaka, H., Tanaka, M. and Itaya, A., *Bull. Chem. Soc. Jpn.*, **1985**, 58, 2015.

6. Matthews, R.W. and McEvoy, S.R, *J. Photochem. Photobiol. A: Chem.*, **1992**, 66, 355.

7. Spanhel, L, Weller, H and Henglein, A, *J. Am. Chem. Soc.*, **1987**, 109, 6632.

8. Serpone, N., Borgarello, E. and Pelizzetti, E., *J. Electrochem. Soc.*, **1988**, 135(11), 2760.

9. Sclafani, A., Palmisano, L. and Schiavello, M., *J. Phys. Chem.*, **1990**, 94, 829.

10. Davidson, R.S, Morrison, C.L and Abraham, J., *J. Photochem.*, **1984**, 24, 27.

11. Serpone, N and Pelletier, A-M, unpublished observations, March 2 1992.

12. Mulvaney, P., Greiser, F. and Meisel, D. in *"Kinetics and Catalysis in Microheterogenous Systems"*, Grätzel, M. and Kalyanasundaram, K., (Eds), Marcel Dekker Inc., New York, 1991.

13. Herrmann, J.-M., Mozzanega, M.-N. and Pichat, P, *J. Photochem.*, **1983**, 22, 333.

14. Primet, M., Pichat, P. and Mathieu, M.-V., *J. Phys. Chem.*, **1971**, 75, 1221.

15. *The Merck Index*, 9th ed., Merck & Co. Inc., Rathway, N.J., 1976, p. 501.

16. *Sadtler IR Standard Spectra*, Sadtler Research Laboratories Inc., Philadelphia, U.S.A., 1978.

17. *The Merck Index*, 9th ed., Merck & Co. Inc., Rathway, N.J., 1976, p. 503

18. Lui, N.S.T and Roels, O.A., *Anal. Biochem.*, **1970**, 38, 202.

19. (a) Serpone, N. and Williams, C. unpublished observations December 1990.
(b) Weast, R.C. (ED.), *CRC Handbook of Chemistry and Physics*, 51st Ed., The Chemical Rubber Co., Cleveland, 1970.

20. Serpone, N., Pelizzetti, E. and Grätzel, M., *Coord. Chem. Rev.*, **1985**, 64, 225.

21. Augustynski, J., *Structure and Bonding*, **1988**, 69, 3.

CHAPTER 8

CHARGE CARRIER TRAPPING IN ULTRASMALL SILVER IODIDE PARTICLES AND KINETICS OF SILVER ATOM CLUSTERS

8.1 INTRODUCTION

Size and concentration effects on the action and efficiency of photolytically produced silver aggregates (clusters) and on the action of the sensitivity centres have been recognized for some time in silver halide photographic imaging science; they are still matters of investigations and debates.[1-7] In particular, related to this is the finding that the photographic process is catalyzed by very small Ag_n clusters with a nuclearity n = 2-4 on silver halide grains.[1,8,9] As well, at least tetrameric silver atom clusters, Ag_4, are required for the heterogeneous catalytic silver ion reduction in solution.[1,10] Not least, several elegant attempts to model latent image formation in silver halide photographic processes are noteworthy[1,4,5] with considerations given to mixed silver halides such as Ag(BrI), where the iodide acts as a positive hole trap.[4] The propensity and uniqueness of the photographic system based on silver halide emulsions have been attributed to the exceptional ability of these emulsions to form, on light exposure, remarkably stable and catalytic silver clusters of atomic dimensions.

Size quantization effects in ultrasmall semiconductor particles (< 50 Å, depending on the semiconductor) dramatically alter their light absorption and emission characteristics, along with such other electronic properties as standard electrochemical

potentials, effective band gaps, and effective masses of electrons and holes.[11-15] Observations on AgI clusters have noted that very small colloidal particles can be synthesized and their properties examined.[14,16,17] Silver iodide is a direct band gap, ionic semiconductor; band gap ~ 2.75-3.0 eV.[14,18]

Radiolytic reduction of colloidal silver halides to metallic silver has been the focus of some attention.[17,19,20] Reduction of colloidal AgBr (average diameter, about 1000 Å) to Ag_n and HBr by organic reducing radicals has been demonstrated by electric conductivity.[19] This chapter reports additional studies on the pulse radiolytic (see ref. 17) reduction of colloidal, ultrasmall silver iodide particles (~ 25 Å) and compares the results with reduction of Ag^+ ions from a Ag_2SO_4 solution. A known number of electrons (~0.5 e^-/particle) was injected into $(AgI)_{coll}$ particles in aqueous acetonitrile media by using the reducing radicals generated by pulse radiolysis of acetonitrile. This solvent was used because extremely small particles can be prepared in it. This method of generating electrons on colloidal AgI particles allows the fate of excess charge carrier of one type to be examined. Also, the fate of the charge carriers (conduction band electrons and valence band holes) generated by irradiation with light of energy greater than 3 eV can also be examined by pulsed laser flash photolytic methods in the picosecond time domain. This latter technique can provide additional evidence for and can yield kinetics of formation of metallic silver atoms and/or their subsequent agglomeration to Ag_n° or Ag_n^{q+} clusters. Another aspect of this work was to explore potential size quantization effects on the photophysics of electron/hole separation/recombination events as part of the systematic studies into colloidal

semiconductor photophysics.[21-24]

8.2 PULSE RADIOLYSIS#

The major advantage of this technique for injecting electrons into colloidal AgI particles is that the negatively charged silver iodide particles, $(AgI)_{coll}^{p}$ (p is the average number of electrons per particle) can be examined without interference from positive holes, inherently present under optical irradiation of semiconductor particles.

In the 20-ns pulse of electrons, reducing and oxidizing species of equal concentration are produced upon radiolysis of acetonitrile. The argon-purged solution also contained 0.1 M triethanolamine (TEA) to scavenge all oxidizing species. The reducing species e_s^-, CH_3CN^-, and $(CH_3CN)_2^-$ formed with yield ~ 1.[25,26] The transient spectrum of the electron-rich $(AgI)_{coll}^{p-}$ was recorded following electron injection (see Figure 8.1). In the absence of $(AgI)_{coll}$, an identical argon-purged or N_2O-purged solution containing 0.1 M TEA, 0.01% Polybrene, and 3% water showed negligible absorption in the time scale of the experiment.

A previous study[17] reported on the reduction of 100-Å AgI particles in aqueous media using 2-propanol radicals; the number of electrons injected into $(AgI)_{coll}$ was ~ 60 e^-/particles. Determination of the nature of the initially reduced species proved difficult under these conditions; after 500 μs, colloidal metallic silver was evident. In the present study, attention was focused on smaller AgI particles (average diameter ~

The author is grateful to Dr. O.I. Micic of the Boris Kidric Institute of Nuclear Sciences, Belgrade, Yugoslavia for assistance in the pulse radiolysis of the AgI clusters.

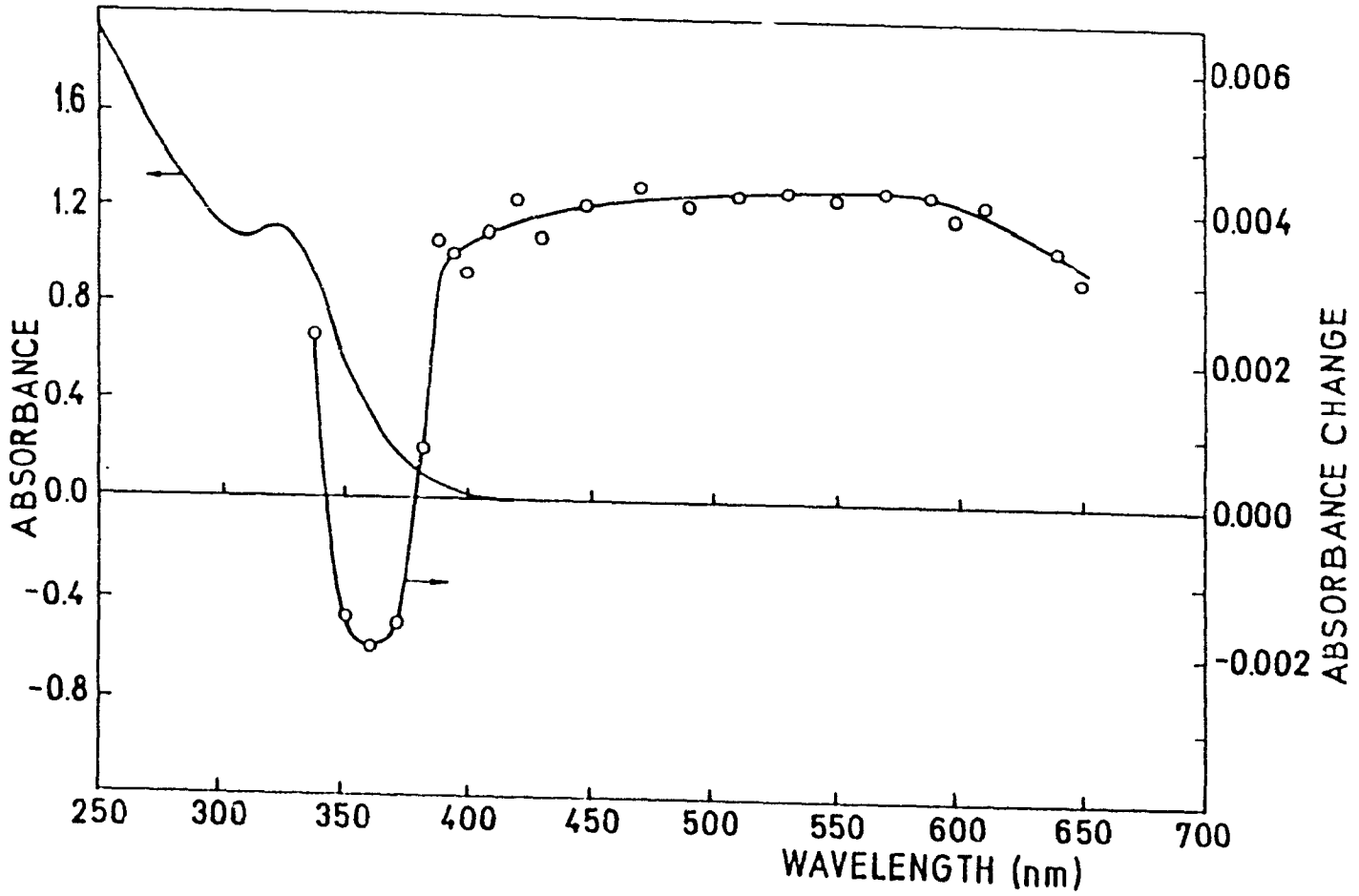

Figure 8.1 Absorption and difference spectra of AgI recorded 10 μs after the 20-ns electron pulse (dose, 9 Gy; concentration of reducing radicals, 9×10^{-7} M) in acetonitrile solution containing 2.0×10^{-4} M AgI colloids, 25 Å; mean agglomeration number, 120; particle concentration, 1.7×10^{-6} M. The argon-saturated solution also contained 0.1 M TEA, 0.01% Polybrene, 3% v/v water.

25 Å), concentration of particles ~ 1.7 X 10^{-6} M. The concentration of the reducing species was ~ 1 x 10^{-6} M. Denoting these species simply as e^-, the fate of the electron on the AgI particle can be described (equations 8.1a and 8.1b):

$$pe^- + (AgI)_{coll} \rightarrow e_t^-(AgI)_{coll} \qquad (8.1a)$$

$$pe^- + (AgI)_{coll} \rightarrow Ag^0(AgI)_{coll} \qquad (8.1b)$$

On average, every second colloidal particle reacts with one electron, and the nature of the transient can be clarified.

The transient spectrum observed 10 μs after the pulse is depicted in Figure 8.1 which also shows the absorption spectrum of $(AgI)_{coll}$ before electron injection. It is inferred that the excess negative charge on $(AgI)_{coll}^{p-}$ is localized (trapped) on at least two sites: (i) a defect site on the particle surface which can trap the e^- (reaction 8.1a) and (ii) a silver atom in AgI, $Ag^0(AgI)_{coll}$ (reaction 8.1b). The transient bleaching of the exciton absorption of AgI at λ_{max} ~ 360 nm is attributed to the surface-trapped electron. Such transient bleaching has been observed in such other semiconductor colloids as CdS,[14b,27-30] CdO,[31] ZnO,[15b,32] CdSe,[33] and In_2S_3[34] by both pulse radiolysis and laser photolysis. It occurs in small quantized semiconductor particles as well as in larger particles.[27,28]

Earlier,[17] it was shown that, following electron injection into the 100-Å AgI particles, transient bleaching occurred at wavelengths below 450 nm (λ_{max} ~ 410 nm). The position of this bleaching maximum was blue-shifted to higher energy at 360 nm for

the 25-Å AgI particles investigated in the present study. It parallels the shift of the fundamental absorption edge of AgI particles resulting from the quantum confinement of charge carriers. The density of electrons injected is large: 6×10^{19} electrons/cm^3 of the semiconductor particle. During the lifetime of the transient, the excess electrons alter the optical absorption characteristics of the material (see below).

Various factors can lead to exciton bleaching in negatively charged semiconductor particles, the merits of each shall be discussed in the next chapter. They are: (i) the free negative charge carriers fill the lower energy levels of the conduction band, including the excitonic levels, thereby effectively blocking the exciton transition (this is the so-called band-filling mechanism or Burstein-Moss effect[35]); (ii) free charge carriers can screen the Coulomb interactions in the exciton (reducing the binding energies between the e^- and h^+), thereby reducing the probability of exciton formation;[35] (iii) carriers trapped at (surface) defect sites can interact with the exciton, thus reducing the oscillator strength of the exciton transition.[29] Factor (i) does not appear important in the present study, since this Burnstein-Moss mechanism necessitates the existence of free charge carriers (not the case here). Also, since the effective mass of the electron is $> 20\text{-}30m_0$,[36] the Burstein-Moss effect is not expected here. In any event, bleaching is *not* the result of the presence of Ag^o atoms (see below) in colloids, since following bleaching recovery the absorption spectrum of Ag^o remains. Trapped electrons lead to the bleaching.

Together with transient bleaching, there is a broad absorption at 400-650 nm (Figure 8.1). The bleaching decays in milliseconds, much shorter than the decay time of the 400-650 nm absorption, which shows only slight changes in the time scale of

seconds. This longer lived transient is attributed to silver atoms or silver atom clusters (reaction 8.1b). To confirm the nature of this transient, an additional experiment was carried out in which silver atoms were initially produced by reducing Ag^+ ions, present as undissociated (~ 99%) Ag_2SO_4 salt,[37] using reducing radicals from radiolysis of acetonitrile (Figure 8.2).

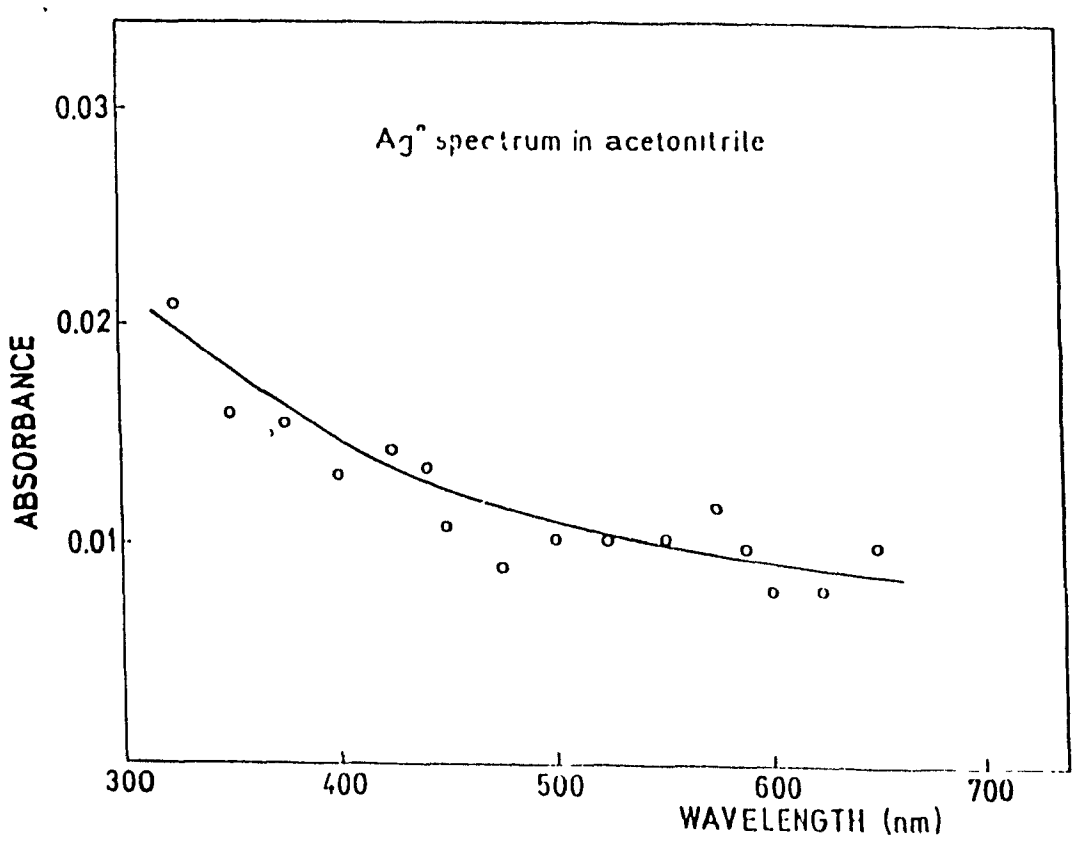

Figure 8.2 Absorption spectra of the intermediates of 5.0 x 10^{-6} M Ag_2SO_4, in argon-purged acetonitrile media in the presence of 0.1 M TEA containing 1% v/v water recorded 10 μs after the 20- ns electron pulse (dose, 120 Gy).

The concentration of silver sulphate was such (5.0 x 10^{-6} M) that the excess reducing radicals (1.2 x 10^{-5} M; dose 120 Gy) transfer electrons to convert all the Ag^+ ions to

Ag^{o}. These can subsequently agglomerate to form silver atom clusters (Ag_n) (eq 8.2a-c; $k \sim 10^{10}\ M^{-1}\ s^{-1}$). However, under our experimental time domain, n = 1 and/or 2, as mass transport is too slow for higher aggregates to form (equation 8.2):

$$Ag^0 + Ag^0 \rightarrow Ag_2^0 \qquad \textbf{(8.2a)}$$

$$Ag_2^0 + Ag^0 \rightarrow Ag_3^0 \qquad \textbf{(8.2b)}$$

$$Ag_3^0 + Ag^0 \rightarrow \ldots \rightarrow Ag_n^0 \qquad \textbf{(8.2c)}$$

Accordingly, the broad spectrum of Figure 8.2 must be due to silver atoms and/or, at best, to dimeric Ag_2 molecules. In solution, there are no free Ag^+ ions remaining that can complex Ag^o.[38]

8.3 PULSED LASER SPECTROSCOPY

The pulsed laser spectroscopy method permits recording transient spectra and a means for transient growth and/or transient decay kinetics to be examined.[21-24] In the present instance, the trapped charge carriers (or transients) are too long lived for us to follow their decay within the time window (30 ps to 12 ns) of the picosecond laser experiment. However, determination of transient growth kinetics could be realized as these are longer than the 30-ps time response of the laser system. Three different size $(AgI)_{coll}$ particles were investigated possessing an average diameter of ~ 100, 35, and 25 Å. To the author's knowledge, this was the first study to probe the rates of formation

of silver atoms, Ag°, silver atom clusters, Ag_n°, or silver cluster cations, Ag_n^{q+}, in a AgX colloidal sol by spectroscopic techniques under photolytic conditions (see also ref 39). Germane to the present study, Marquardt and Gliemeroth[39b] earlier examined the growth rate of photolytic silver in mixed $AgCl_{0.5}Br_{0.5}$ particles on photochromic glasses by nanosecond flash photolysis.

Figure 8.3 illustrates the transient absorption spectra as absorbance-change versus wavelength at seven delay times of 0 ps, 100 ps, 200 ps, 400 ps, 600 ps, 1 ns, and 3 ns for the 100-Å $(AgI)_{coll}$ particles in (aqueous) acetonitrile solution (the error bar represents plus/minus one standard deviation). The insert depicts the absorption spectrum of the AgI sol about 1 h after preparation; a spectral band is observed at 417 nm along with an unresolved band at ~328 nm. No further spectral changes were noted after several hours.

At 0 ps, transient absorption is barely noticeable above the zero base line; it grows at longer delay times reaching a plateau absorption by ~ 3-ns delay (Figure 8.4). In the system spectral window, limited to 425-675 nm, what appears to be the onset of "transient bleaching" is observed at the shorter wavelengths. Within experimental error, the increase in transient absorption follows simple exponential behaviour; average rise time ~ 0.5 ± 0.1 ns.

The absorption spectrum of the intermediate (35 Å) size $(AgI)_{coll}$ sols (insert in Figure 8.5) reveals a broad band at 334 nm and a shoulder at ~ 264 nm. The spectrum has blue shifted by some 80 nm to higher energy, paralleling the decrease in the size of the particle. The transient absorption spectra at several delay times following pulsed

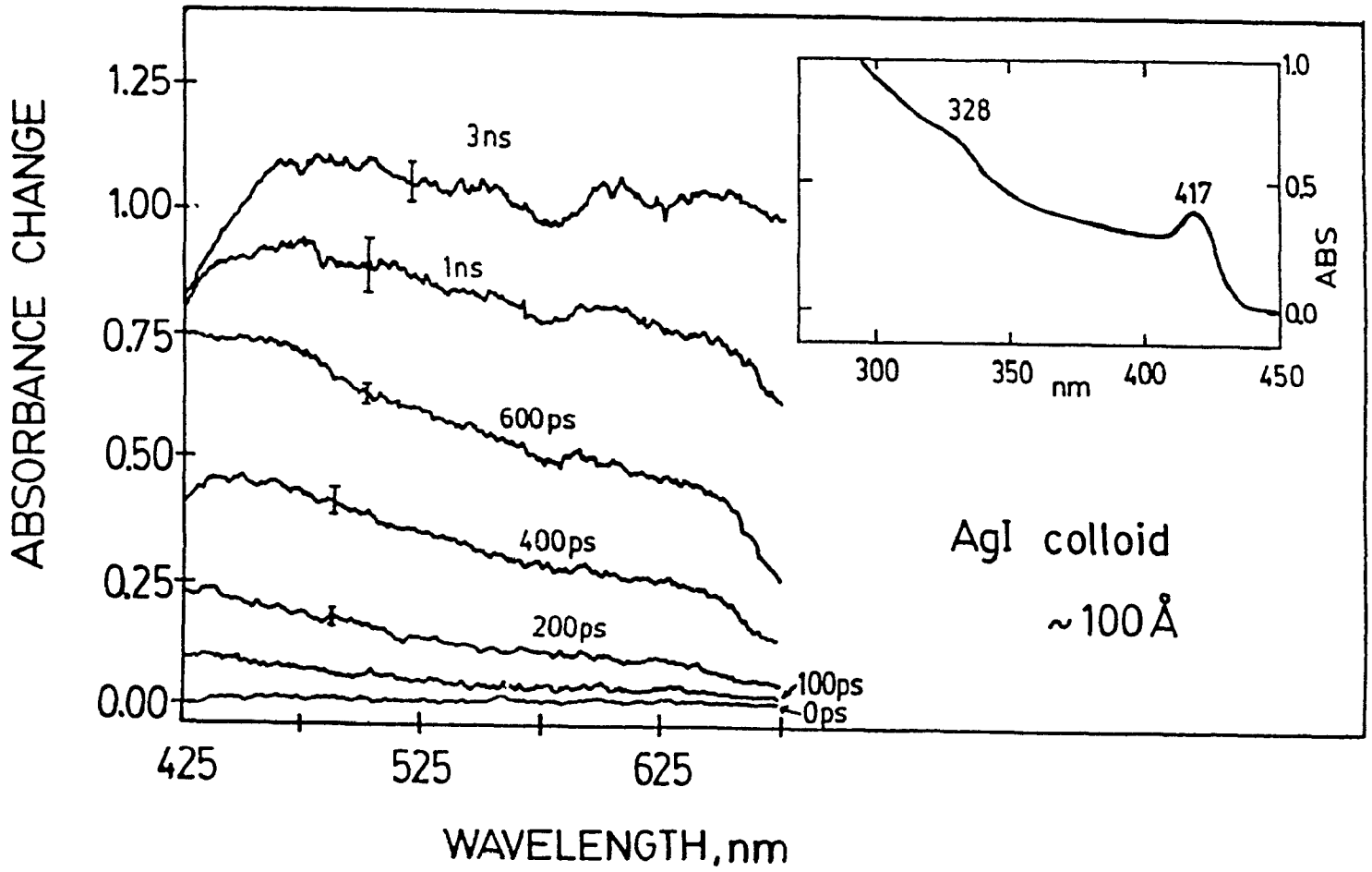

Figure 8.3 Transient absorption spectra as absorbance change versus wavelength (nm) for the 100-Å AgI colloids at several of the indicated delay times following 355-nm pulsed irradiation. The inset shows the absorption spectrum of the AgI colloidal solution in acetonitrile media (1% v/v water) 1 hr after preparation and before irradiation; light path length, 1 cm; [AgI] = 2×10^{-4} M; no stabilizer present.

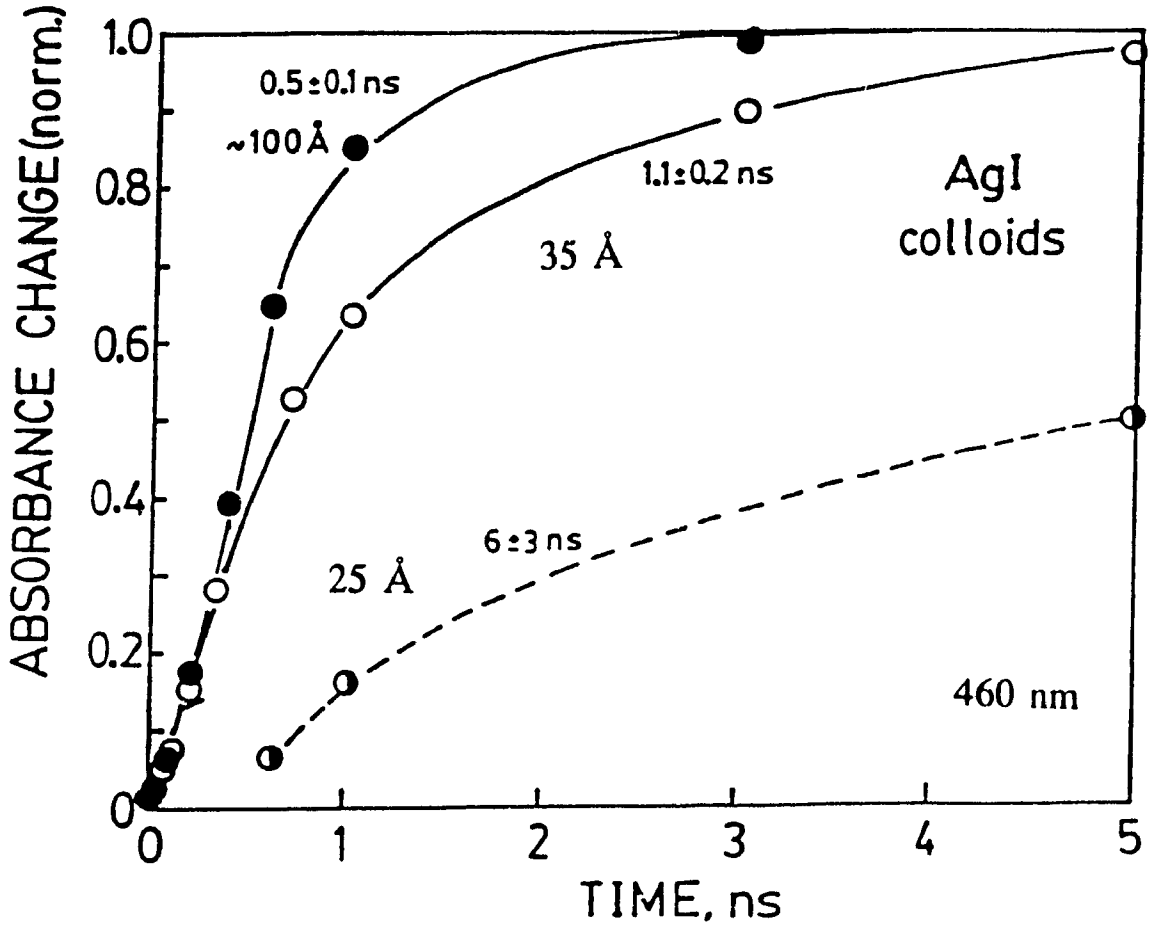

Figure 8.4 Normalized absorbance change versus time (ns) plots for the transient absorption growth of the three different size colloids of AgI.

laser excitation at 355 nm for the intermediate size colloids are also collected in Figure 8.5. At a 50-ps delay time, a slightly observable absorption appears at ~ 460 nm, which continues to grow at longer delay times to finally reach constant absorption growth by about 8-10 ns (Figure 8.4). Transient absorption growth also follows simple exponential kinetics; average rise time ~ 1.1 ± 0.2 ns.

The corresponding spectra for the smallest (25 Å) AgI particles are illustrated in

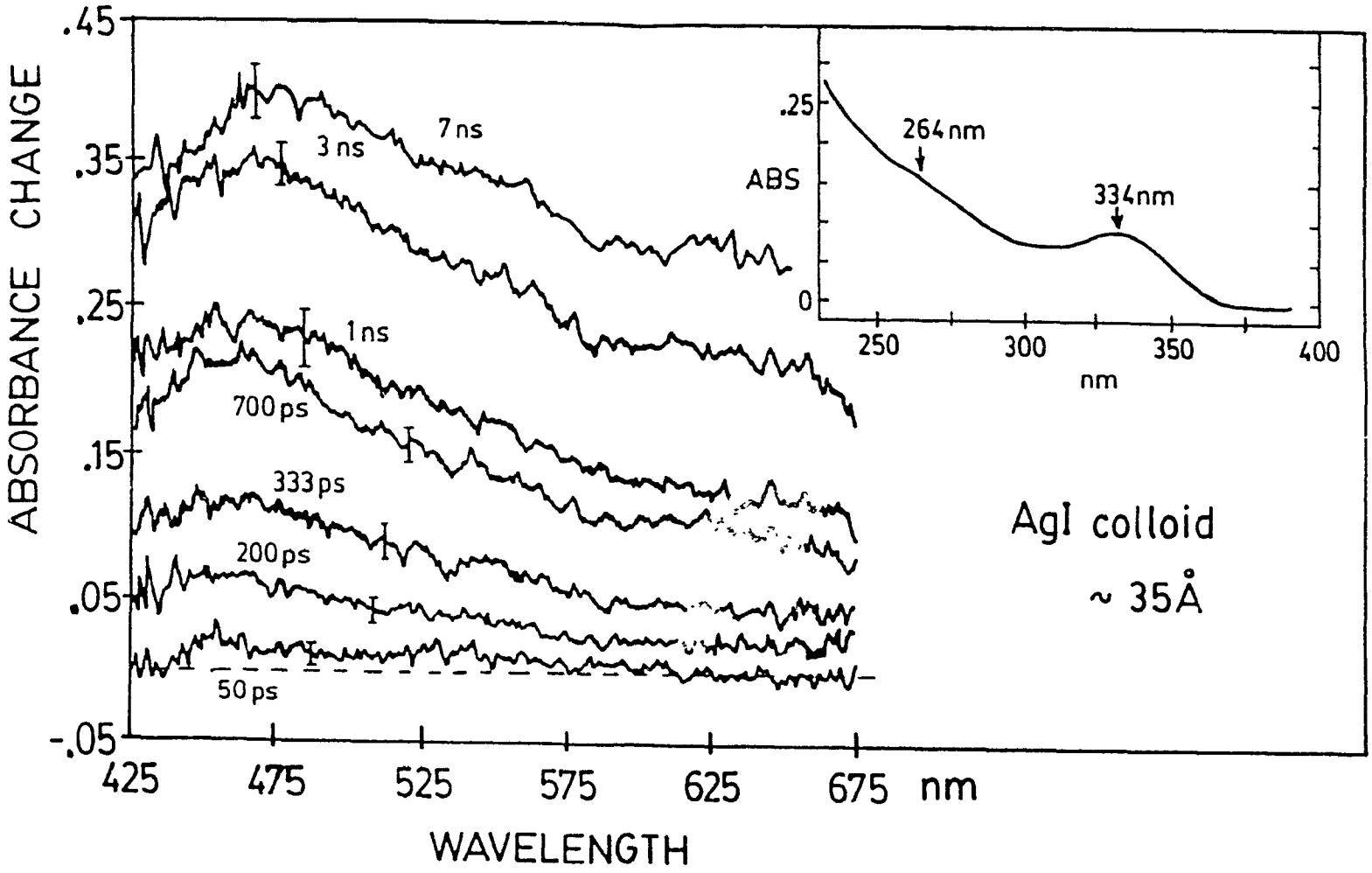

Figure 8.5 Transient absorption spectra as absorbance change versus wavelength (nm) for the 35-Å AgI colloids in water/acetonitrile media (24% v/v acetonitrile) at various indicated delay times: Polybrene is the stabilizer, [AgI] = 5.0×10^{-5} M. The inset shows the blue-shifted absorption spectrum of the AgI before irradiation; path length, 0.2 cm.

Figure 8.6, which shows the lowest energy band in the AgI absorption spectrum to have further blue-shifted to 303 nm (inset); note that no similar shift occurs for the 264-nm band between the two smaller size AgI colloids. Transient absorption growth is much slower (average rise time about 6 $\pm$ 3 ns); it has not reached a plateau by 10 ns. The onset of what appears to be "photobleaching" at wavelengths of 425-475 nm is more evident for the smallest particles. To the extent that there is no exciton absorption at these wavelengths (see insert), this bleaching is probably the onset of an emission from excited AgI particles (emission is observed for these AgI particles in this spectral range).

Figures 8.3, 8.5 and 8.6 demonstrate that the change-in-absorbance spectra are nearly identical, irrespective of the size of the $(AgI)_{coll}$ particles. More important, these spectra are essentially identical with the difference spectrum in Figure 8.1 in the 400-650-nm wavelength range. Evidently, the trapped positive hole, $I^{\bullet}$ atom, is not important in this spectral region. The $I_2^{\bullet-}$ radical, which shows spectral absorption bands at 400 and 700 nm,[34] is also inconsequential to the spectral observations in Figures 8.3, 8.5 and 8.6.

Absorption of light radiation of energy greater than the forbidden energy gap (band gap ~ 2.75-3.0 eV) of AgI semiconductor yields conduction band electrons (e_{cb}) and valence band holes (h_{vb}^+), along with an equal number of charge-compensating interstitial Ag_i^+ ions.[4] The immediate fate of the separated charge carriers in semiconductor particulates or colloid sols is radiative and/or nonradiative recombination, together with diffusion to the particle surface. At the surface, charge carriers may be trapped at various sites, including recombination centres, where the carriers can perform

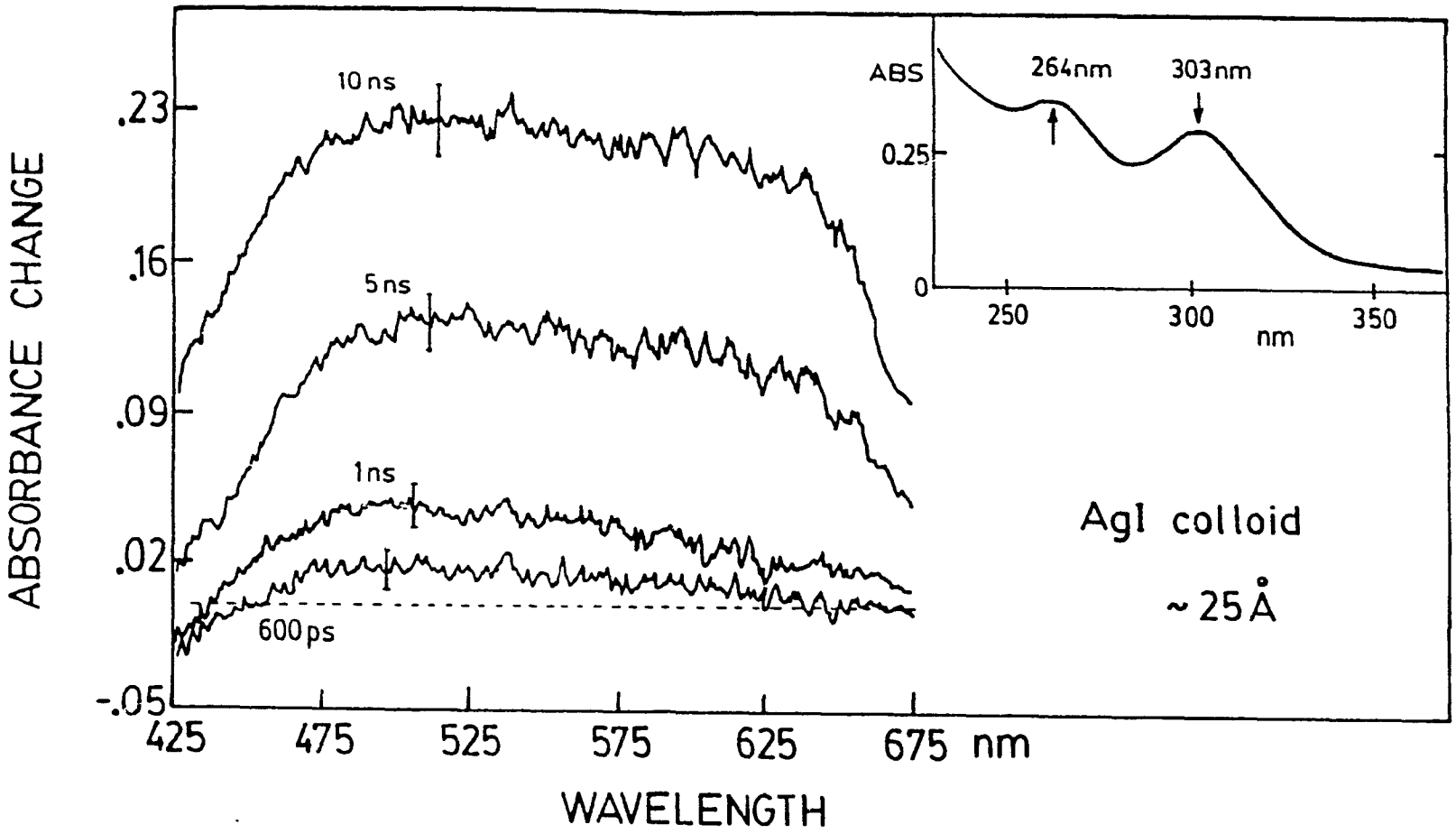

Figure 8.6 Absorbance-change versus wavelength spectra at various delay times following the 355-nm pulsed laser excitation of the 25-Å AgI colloids in aqueous (3.5% v/v) acetonitrile solution. Transient absorption growth is shown. The inset shows the absorption spectrum of the AgI before irradiation and 1 hr after preparation. Note the further blue-shift in the onset of absorption and the lowest energy absorption band (see text for details).

useful redox chemistry[40] and/or initiate corrosion of the semiconductor particles (eq 8.3):

$$(AgI)_{coll} \xrightarrow{h\nu} [e^- + h^+](AgI)_{coll} \rightarrow$$

$$[Ag^0, I\bullet, e_t^-, h_t^+, Ag^+, I^-](AgI)_{coll} \qquad (8.3)$$

Here e_t^- and h_t^+ are trapped carriers on different types of surface defects. Mitchell[4] has pointed out that the delocalization of the positive charge at the site where the electron formed, or at the trapping site of the hole, can lead to formation of Ag_i^+ interstitials. Subsequently, the electrons combine with Ag_i^+ ions at shallow positive potential wells to produce Ag atoms and ultimately dimeric Ag_2 or higher cluster Ag_n ($n > 2$) molecules. Malinowski[41] suggests that deep e^- traps exist only on the particle surface where Ag atoms and the subsequent latent image specks are formed via surface migration of silver on the silver halide microcrystals. The Ag atom does not seem to be a trap for a conduction band electron (neither is Ag_2[4,42]) and cannot adsorb a Ag^+ ion to become Ag_2^+ in thermodynamic equilibrium at room temperature.[42,43] Rather, the dimeric stable Ag_2 molecule probably forms according to reaction 8.4 or by a surface migration mechanism.[41]

$$Ag + e^- + Ag_i^+ \rightarrow Ag_2 \qquad (8.4)$$

A comparison of the transient absorption growths (normalized to their corresponding 10-ns spectra) is made in Figure 8.4. Whatever the nature of the transient(s), the bigger the particles are, the faster the transient(s) is (are) formed. The

large surface area-to-volume ratio in the smaller colloidal particles, in comparison to bulk particles, leads to a higher density of defects which can trap the free charge carriers. Subsequently, these carriers react with AgI to form, initially, Ag° and $I\bullet$.

Two additional, no less significant features are worth noting from the change-in-absorbance spectra following pulsed laser excitation. Figure 8.7 shows a linear correlation plot of (risetime)$^{-1}$ versus (size)$^{-1}$; $1/\tau_{rise} = k_{obs} = 2.6 \times 10^{9}$ s^{-1} to 6.0×10^{10} s^{-1} Å. The linear relationship extrapolates to a limiting rise time, $\tau_{lim} \sim 0.38$ ns, for

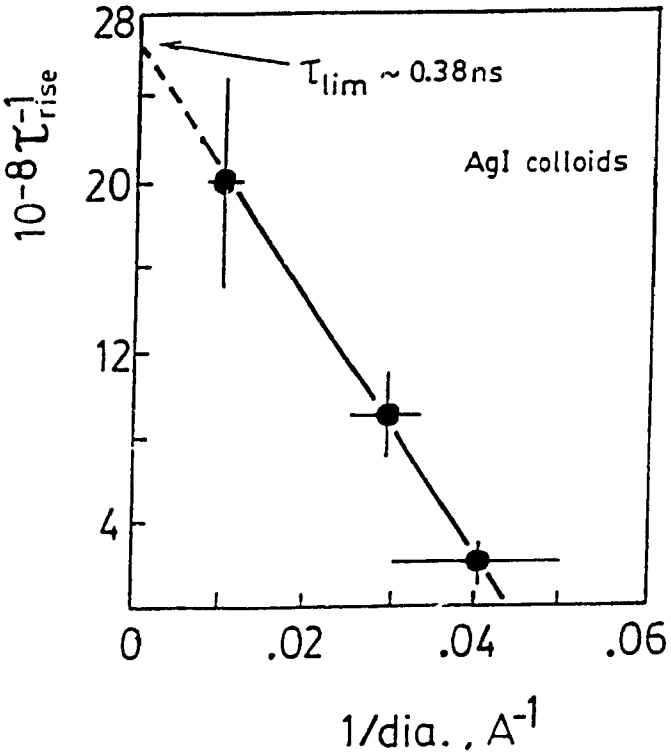

Figure 8.7 Linear correlation plot of $(\tau_{rise})^{-1}$ versus (size)$^{-1}$ for the three AgI colloid particles.

particles greater than 100 Å. This may bear on the photographic process(es), where silver halide grain sizes are several thousand angstroms.[1] Previous work[12] had inferred

cluster formation times on the order of microseconds for AgBr and Ag(ClBr). In particular, in mixed silver halide, Ag(ClBr), photochromic glasses, where particle size ranged from about 50 to 130 Å, these formation times varied linearly with size[19b] and contrast the present observations.

The absorbance change for the 35-Å AgI particles varies with the laser fluence (I, in mJ) as I^3 (Figure 8.8). Under the conditions of our laser photolysis, the photon flux per pulse was about 10^{16}-10^{17} photons/cm^2 against a particle flux of about 10^{14} particles/cm^2. This gives an electron density estimated at about 7 x 10^{20} to 7 x 10^{21}

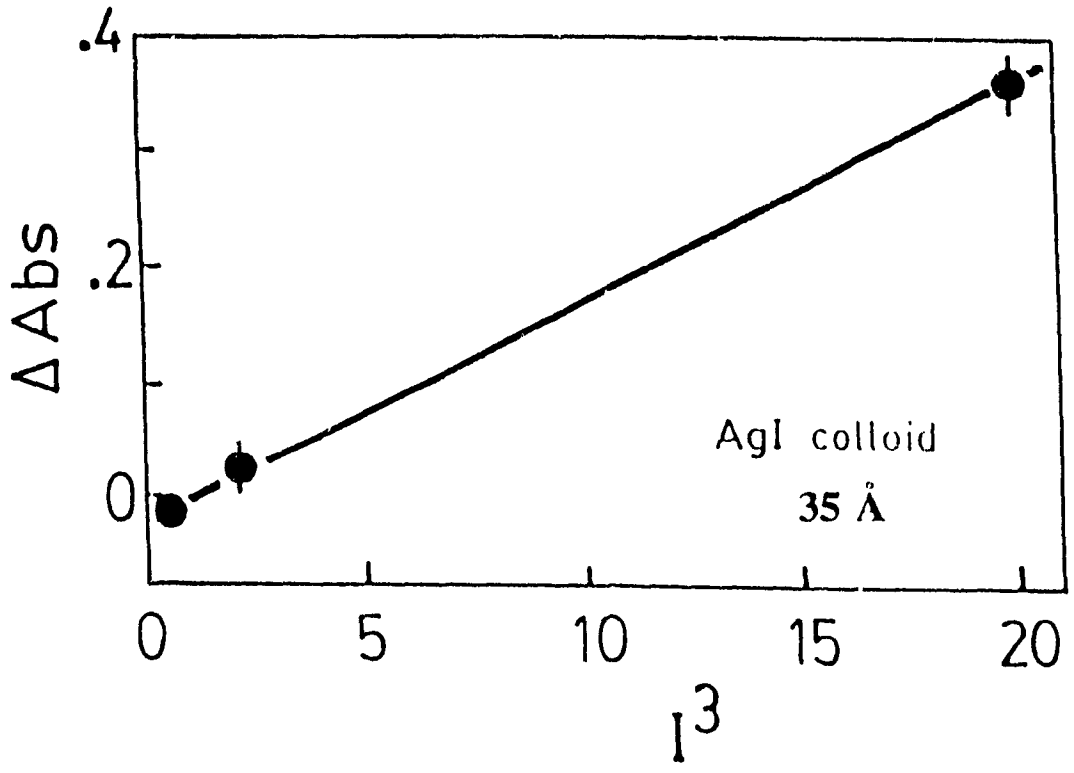

Figure 8.8 Linear plot showing the third-order dependence of the absorbance change at 1 ns delay times for the 35 Å AgI particles on the laser fluence (in mj) as I^3.

for all three sizes of AgI particles. Clearly, the Ag_n^0/Ag_n^{q+} transients affect the optical characteristics in a non-linear manner. The decrease in particle size for constant flux leads to the same effect as an increase in laser fluence for constant particle size.[35a]

8.4 NATURE OF TRANSIENTS

It is tempting to conclude that the nature of the transient absorption illustrated in Figures 8.3, 8.5 and 8.6 reflects the presence of silver atoms, silver atom clusters, and/or silver cluster cations.

The composite picture that has emerged from the cryophotoclustering studies of Ozin and co-workers[44] (along with stabilization of silver cluster cations Ag_n^{q+} in zeolite-Y supports[45,46]) to synthesize Ag_n is that there apparently exists a relatively smooth transition from discrete silver atoms to clusters of few atoms for n = 2 to 5 silver atoms having distinguishable molecular properties. Subsequently, progressively larger clusters containing 6 to 15 silver atoms form and exhibit both *bulk* and *molecular optical characteristics*, and then even larger silver aggregates form, which display effects associated with the bulk microcrystalline state.[44] Initially, Ag^0 and dimeric Ag_2 are produced; continued clustering generates the higher nuclearity Ag_n clusters with $n = 3$ to 6 along with still larger clusters. Optical absorption spectra show gradual broadening of the low-energy bands as the cluster size progresses for $n \geq 7$, along with a tendency for the band position(s) to red shift toward a limiting value to ~ 600 nm. In fact, as band-broadening effects become more pronounced with increasing cluster size, the optical spectra lose the fine structure evident in Ag^0 and in low nuclearity clusters (Ag_n; $n = 2$-6)

and resemble broad plasmon resonance-like absorptions (collective oscillations of conduction electrons) observed in massive silver aggregates.[44] This may indeed be what is observed in Figures 8.3, 8.5 and 8.6 from the reduction of AgI sols with the reducing conduction band electrons. Given the very short time scale of the experiments (< 10 ns), formation of these larger Ag_n species would most likely involve surface trapping of the electron by silver atoms at the surface of the crystal. Detrapping and or migration of surface silver atoms would lead to larger structures. Diffusion of silver atoms through the silver halide matrix is not considered likely in time frame of the picosecond experiments (< 10 ns). Finally, the onset from *molecular* to *bulk* optical transformations for silver clusters appears to occur around $n = 6$ and is nearly complete by $n \sim 10$ to 15.

Figure 8.9 illustrates, for comparison, the absorption spectrum of Ag_n^0 species[44] and the optical reflectance spectrum of silver cluster cations Ag_n^{q+} (n = 5-13) on silver zeolite-Y substrates, Ag_{55}-Y,[45,46] in the visible region (400-650 nm); the spectra are identical, displaying identical band positions. The spectra also bear somewhat similar features to our difference absorption spectra from pulse radiolysis (Figure 8.1) and laser photolysis (Figures 8.3, 8.5 and 8.6). Clearly, any conclusion as to the *precise* nature of the transients in the present work is made difficult by these spectral similarities: silver atom clusters versus silver cluster cations, not to mention the nuclearity of the various cluster species. In the time frame of the picosecond laser experiments (30 ps to 10 ns), formation of silver atom clusters and/or silver cluster cations with $n > 2$ at some surface defect site is not precluded by the present study, their formation being dependent on the

rate-determining surface migration of Ag^+ and Ag^o. Thus, while spectra of Figures 8.1 and 8.2 must be ascribed to silver atoms, Ag^o (and/or dimeric Ag_2 molecules) under the conditions of the experiment, the spectra of Figures 8.3, 8.5 and 8.6 may reflect those of higher silver clusters.

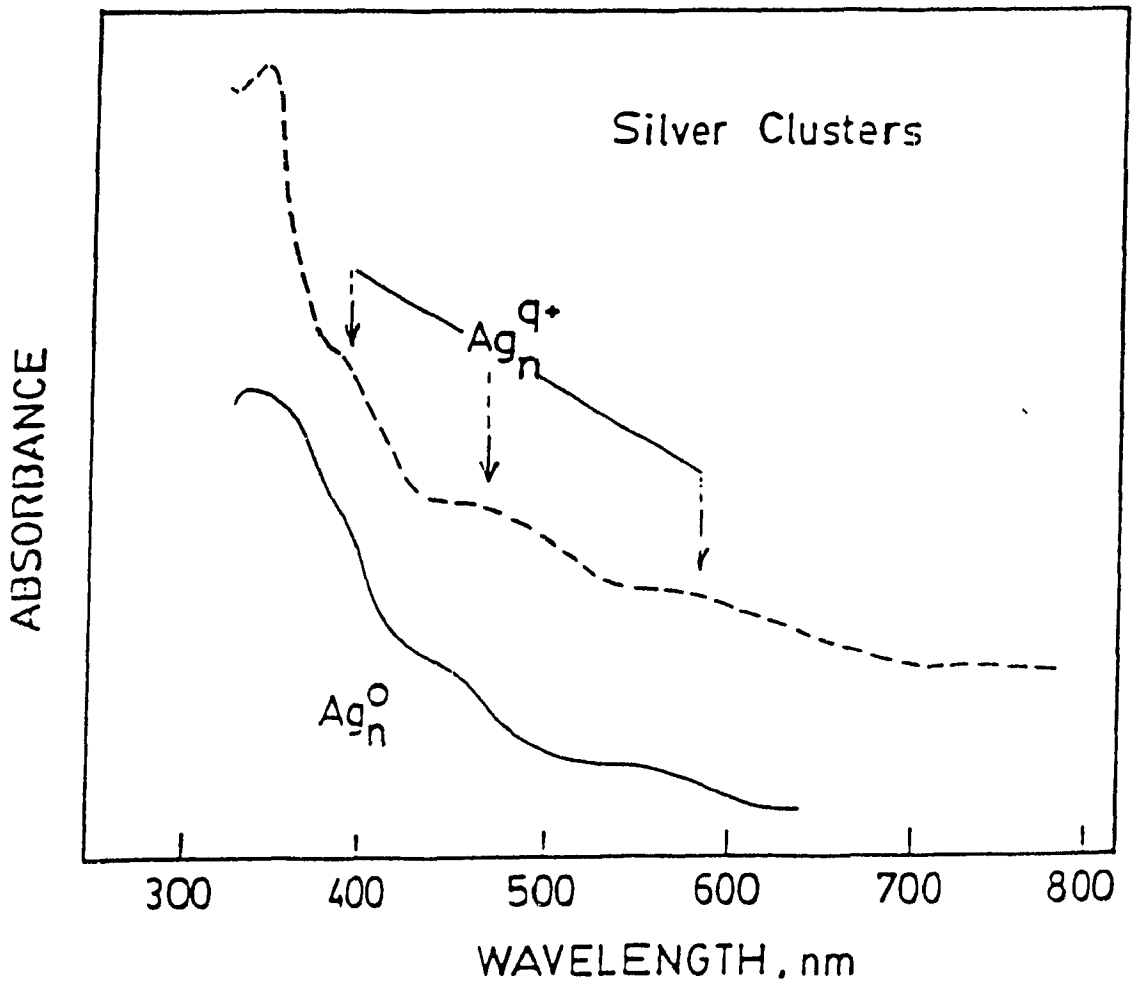

Figure 8.9 Comparison of the absorption spectra of silver cluster cations, Ag_n^{q+}, and silver atom clusters, Ag_n^0, in the 300-800 nm spectral region (where n ~ 55 - 60). For details of the experimental conditions, see the respective references (adapted from refs. 46 and 44, respectively).

8.5 CONCLUSIONS

Both pulse radiolysis and laser flash photolysis techniques have been employed to examine the behaviour of AgI colloids of small to very small dimensions (100, 35, and 25 Å) in acetonitrile media under conditions where Ag^+ ions are reduced to metallic silver by acetonitrile reducing radicals ($(CH_3CN)_2^-$, CH_3CN^-, and e_s^-) as well as by conduction band electrons under a 355-nm photolyzing laser pulse. The transient absorptions resulting from these redox conditions are those of silver atoms or dimeric Ag_2 silver molecules (pulse radiolysis) and probably higher Ag_n clusters ($n > 2$) under photolysis conditions. The absorption spectra of the AgI colloids exhibit bands that shift to higher energy (by about 0.7 and about 1 eV) as the particle size decrease from ~100 to ~25 Å consistent with the notion of increased effective band gap from the confinement of charge carriers in very small AgI semiconductor particles. The rates of formation of these silver clusters correlate inversely with size.

References

1. See *Proceedings of the International East-West Symposium II on the Factors Influencing the Efficiency of Photographic Imaging*, The Society for Imaging Science and Technology, Oct. 30- Nov. 4, 1988, Kona Hawaii.

2. Moisar, E., Dorf, R., Palm, E. and Yang, H., in ref 1, Paper B1.

3. Sahyun, M.R.V. in ref 1, Paper C14.

4. Mitchell, J.W., *Photogr. Sci. Eng.*, **1981**, 25, 170.

5. Hamilton, J.F., Baetzold, R.C., *Photogr. Sci. Eng.*, **1981**, 25, 189.

6. Sayhun, M.R.V., *Photogr. Sci. Eng.*, **1982**, 26, 211.

7. Mitchell, J.W., *Photogr. Sci. Eng.*, **1982**, 26, 211.

8. Hamilton, J.F., *J. Vac.Sci.Technol.*, **1976**, 13, 319.

9. Baetzold, R., *J. Appl. Phys.*, **1976**, 47, 3799.

10. Hamilton, J.F. and Logel, P.C., *Photogr. Sci. Eng.*, **1974**, 18, 507.

11. Brus. L., *J. Chem. Phys.*, **1983**, 79, 5566.

12. Fojtic, A., Weller, H., Koch, U. and Henglein, A., *J. Phys. Chem.*, **1984**, 88, 969.

13. Nozik, A.J.; Williams, F.; Nenadovic, M.T.; Rajh, T.; Micic, O. I. *J. Phys. Chem.*, **1985**, 89, 397.

14. (a) Schmidt, K.H., Patel, R. and Meisel, D., *J. Am. Chem. Soc.*, **1988**, 110, 4882.
(b) Hayes, D., Schmidt, K.H. and Meisel, D., *J. Phys. Chem.*, **1989**, 93, 6100.

15. (a) Henglein, A., *Top. Curr. Chem.*, **1988**, 143, 113.
(b) Koch, U., Fojtic, A., Weller, H. and Henglein, A., *Chem. Phys. Lett.*, **1985**, 122, 507.

16. Tanaka, T., Saigo, H. and Matsubara, T.J., *Photogr. Sci. Eng.*, **1982**, 26, 92.

17. Vucemilovic, M.I. and Micic, O.I., *Radiat. Phys. Chem.*, **1988**, 32, 79.

18. (a) Berry, C.R., *Phys. Rev.* **1967**, 161, 611.
(b) Bodikyan, L.D., Miloslovskii, V.K. and Ageev. A., *Opt. Spectrosc.*, **1979**, 47, 225.

19. Johnston, F.J. *Radiat. Res.*, **1978**, 75, 286.

20. Henglein, A., In *Baxendale Memorial Symposium Proceedings;* Consiglio Nazionale delle Ricerche, Laboratorio di Fotochimica e Radiazioni d'Alta Energia, Centro Stampa, Lo Scarabeo, Bologna, Italy, 1983; p 43.

21. Serpone, N., Sharma, D.K., Jamieson, M.A., Grätzel M. and Ramsden, J.J., *Chem. Phys. Lett.*, **1985**, 115, 473.

22. Moser, J., Grätzel, M., Sharma, D.K. and Serpone, N., *Helv. Chim. Acta*, **1985**, 68, 1686.

23. Rothenberger, G., Moser, J., Grätzel, M., Serpone, N. and Sharma, D.K., *J. Am. Chem. Soc.*, **1985**, 107, 8054.

24. Serpone, N., Sharma, D.K., Moser, J. and Grätzel, M., *Chem. Phys. Lett.*, **1987**, 136, 47.

25. Baptista, J.L. and Burrows, H.D., *J. Chem. Soc., Faraday Trans. 1*, **1974**, 70, 2066.

26. Bell, I.P. and Rodgers, M.A.J., *J. Chem. Soc., Faraday Trans. 1*, **1977**, 73, 315.

27. Albery, W.J., Brown, G.T., Darwent, J.R. and Saievar-Iranizad, E., *J. Chem. Soc., Faraday Trans. 1*, **1985**, 81, 1999.

28. (a) Baral, S., Fojtic, A., Weller, H. and Henglein, A., *J. Am. Chem. Soc.*, **1986**, 108, 375.
(b) Henglein, A., Kumar, A., Janata, E. and Weller, H., *Chem. Phys. Lett.*, **1986**, 132, 133.

29. Hilinski, E.F., Lucas, P.A. and Wang, Y., *J. Chem. Phys.*, **1988**, 89, 3435.

30. Kamat, P.V., Dimitrijevic, N.M. and Fessenden, R.W., *J. Phys. Chem.*, **1987**, 91, 396.

31. Fojtic, A., Henglein, A., Katsikas, L. and Weller, H., *Chem. Phys. Lett.*, **1987**, 138, 535.

32. Bahnemann, D.W., Kormann, C. and Hoffmann, M.R., *J. Phys. Chem.*, **1987**, 91, 3789.

33. Dimitrijevic, N.M. and Kamat, P.V., *J. Phys. Chem.*, **1987**, 91, 2096.

34. Kamat, P.V., Dimitrijevic, N.M. and Fessenden, R.W., *J. Phys. Chem.*, **1988**, 92, 2324.

35. (a) Kamat, P.V., Dimitrijevic, N.M. and Nozik, A.J., *J. Phys. Chem.*, **1989**, *93*, 2873.
(b) Pankove, J.I., *Optical Processes in Semiconductors*; Dover: New York, 1971.

36. Nozik, A.J., personal communication with Prof. Serpone, June 1989.

37. The solubility of Ag_2SO_4 in acetonitrile is 3.3 x 10^{-3} M. *Gmelins Handbuch der Anorganishe Chemie*, Verlag Chemie: Weinheim, 1973.

38. Tansch-Treml, R., Henglein, A. and Lilie, J., *Ber. Bunsenges. Phys. Chem.*, **1978**, 82, 1343.

39. (a) Levy, B., Chang, K.C. and Chen, F.P. in *Growth and Properties of Metal Clusters*; Bourdon, J., Ed.,; Elsevier: Amsterdam, 1980; pp 393-397.
(b) Marquardt, C.L. and Gliemeroth, G., *J. Appl. Phys.*, **1979**, 50, 4584.

40. Serpone, N., and Pelizzetti, E., Eds.; *Photocatalysis - Fundamentals and Applications;* Wiley-Interscience: New York, 1989.

41. Malinowski, J., in *Growth and Properties of Metal Clusters;* Bourdon, J., Ed.; Elsevier: Amsterdam, 1980; pp 303-320.

42. Sahyun, M.R.V., in *Growth and Properties of Metal Clusters;* Bourdon, J., Ed.; Elsevier: Amsterdam, 1980, pp 379-385.

43. Mitchell, J.W., *Photogr. Sci. Eng.*, **1978**, 22, 1.

44. Ozin, G.A. and Huber, H., *Inorg. Chem.*, **1978**, 17, 155.

45. Ozin, G.A. and Hughes, F., *J. Phys. Chem.*, **1983**, 87, 94.

46. Ozin, G.A., Hughes, F., Mattar, S.M. and McIntosh, D.F., *J. Phys. Chem.*, **1983**, 87, 3445.

CHAPTER 9

PHOTOLUMINESCENCE AND PICOSECOND CHARGE CARRIER DYNAMICS IN CdS QUANTUM DOTS CONFINED IN A SILICATE GLASS

9.1 INTRODUCTION

In recent investigations of nanometre-scale semiconductor clusters (quantum dots), much attention has been focused on their optical properties owing to their potential utilization in fast opto-electronics.[1-23] To understand the origin of the non-linear behaviour observed in these materials, the question of their recovery time following light excitation continues to be a matter of much current interest.[4,8,9,11,13 18,20,24,25] Amongst the various host materials (e.g., zeolites[4] and Nafion films[8,11a,16]) used to incorporate semiconductor clusters, glasses have provided an excellent medium in which to probe the optical effects of size quantization resulting from the three-dimensional confinement of excitons and/or electrons and holes.

Relevant to the present study, the related II-VI mixed chalcogenide semiconductor doped glasses (CdS_xSe_{1-x}) have proven to be efficient systems as third order non-linear optics.[2,19,23,26,27] Studies of absorption bleaching,[19,28 30] changes in the refractive index,[28,29,31] multiwave mixing,[32] and photoluminescence of semiconductor doped glasses have established some insights into the nature and origin(s) of the non-linearities in these systems. As well, improved preparations of semiconductor microcrystallites in a variety

of matrices, in which the sizes of the host sites can be controlled, have made it possible to examine the optical effects of size quantization of excitons and of charge carriers,[23,33,34] together with providing the stimuli for theoretical predictions[3,35,36] of non-linearities caused by the three-dimensional confinement.

Photogenerated charge carriers can be physically confined in a semiconductor cluster whose dimensions are smaller than the deBroglie wavelength of electrons and holes.[17] Unlike bulk materials, quantum size particles have no valence and conduction states near the Brillouin zone centre.[3,17,37,38] The energy levels are discrete and not band-like as in bulk semiconductor materials,[1,3,6,10,17,25,38,39] with the result that the oscillator strength is concentrated on the narrow, lower energy transitions. Exciton related optical non-linearity appears to have its origins with state-filling of the sharp excitonic transitions,[1,3] contrary to bulk materials where band-filling of continuum states has been inferred. Wang and co-workers[4,8,11,16] have examined exciton absorption bleaching in excited CdS microcrystallites in a Nafion film in the picosecond time domain. They showed that exciton bleaching originates with trapped charge carriers which interact with the excitons and reduce the oscillator strength of the exciton transition.[11]

Non-linear effects may have relatively little intensity in quantum dots as a result of (i) the inhomogeneity in the size of the quantized particles which leads to broadening of the excitonic absorption band, and (ii) the chemical nature of the surface which becomes increasingly important as the semiconductor particle size decreases and trapped electrons and holes, created on the crystal surface during the synthesis, can permanently reduce the excitonic absorption strength, manifested by the absence of a sharp exciton

peak.

The need to understand the effects of surfaces and the need to control the surface and interfacial chemistry on quantum dots by chemical agents [4,8,16,40,41] or laser illumination[42] was addressed only recently.[11] Passivation of surfaces has a dramatic influence on charge carrier dynamics in semiconductor quantum dots. Passivation of CdS particle surfaces with either alkyl amines,[43] NH_3 [8,16], OH^- [40,41] or by the host lattice atoms in optically inert materials[44] can quench the red luminescence and enhance the intra-band emission.

The contribution of excitons to the non-linearity in CdS quantum dots can only exist in the initial sub-picosecond time domain, since trapping times are in the femtosecond time regime.[10,13] Absorption recovery and the non-linearity observed in our experimental time domain must arise from trapped electron/hole pairs on the cluster surface. Under multiphoton excitation (present experiments), the generation of several such trapped charge carrier pairs within a single particle leads to electron ejection from the particle by an Auger-type recombination process which further initiates photocorrosion of the CdS quantum dots.

In this work, the photoluminescence of CdS microcrystallites in aqueous media and in a silicate matrix is examined and the effects of passivation by hydroxide ions and by the host environment (stabilizer/silicate glass) demonstrated. In most cases, the intra-band emission is enhanced at the expense of the red luminescence. The picosecond transient absorption spectra (-20 ps to 10 ns time window), emission decays, and charge carrier dynamics for CdS quantum dot systems stabilized with HMP (hexametaphosphate)

and PVA (polyvinyl alcohol) in acidic silicate hosts is also reported. The transient absorptions are rationalized in terms of photochemical events occurring on the microcrystallite surface.

9.2 ABSORPTION AND LUMINESCENCE SPECTRA

9.2.1 Aqueous CdS Colloidal Sols

The fluorescence properties of surface-modified CdS quantum dots in acidic glasses[#] were examined by steady-state and by time-resolved fluorescence spectroscopy. The results are compared with the fluorescence properties of CdS quantum dots in acidic and alkaline aqueous solutions, stabilized with the same surface-active materials. Absorption and emission spectra of aqueous HMP-stabilized CdS microcrystallites are depicted in Figure 9.1.[*] Luminescence properties of CdS colloids have already been examined in some detail.[45] Increasing the pH (to 10) of the aqueous CdS sols (2×10^{-4} M), originally synthesized at pH 6.5, had no effect on the exciton band position ($\sim$ 455 nm), but did increase slightly the absorption cross-section. However, a dramatic effect was seen on the emission characteristics when $CdSO_4$ (20 mM) was added to the CdS sols and the pH was brought to 10. Under these conditions, a layer(s) of cadmium hydroxide forms on the particle surface (surface passivation), effectively suppressing the number of surface recombination centres for the photogenerated electrons and holes.

[#] These glasses were kindly supplied by Drs. O.I. Micic and T. Rahj of the Boris Kidric Institute of Nuclear Sciences, Belgrade, Yugoslavia.

[*] Determined through the courtesy of Dr. T. Rajh.

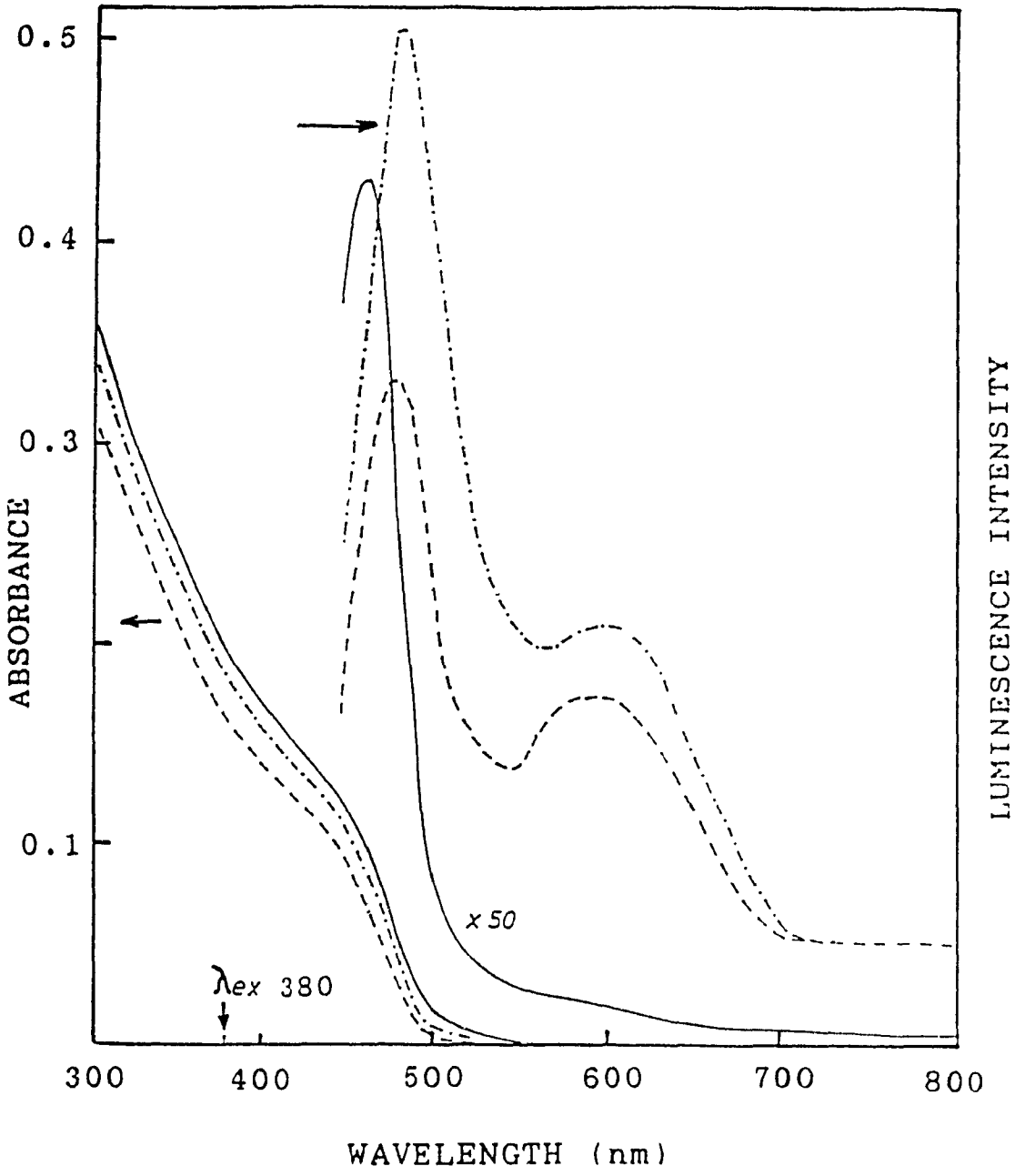

Figure 9.1 Optical absorption and emission spectra of colloidal CdS (2 x 10^{-4} M) prepared in the presence of 2 x 10^{-4} M HMP at pH 6.5: (---) no additives; (-•-) pH increased to 10; (—) added excess Cd^{+2} ions, 2 x 10^{-4} M, and pH brought to 10 (note that the emission is 50 times more intense than indicated in the Figure). Optical path length was 0.5 cm. In all cases, the excitation wavelength was 380 nm.

This leads to (i) an overlap of the exciton absorption band with the band-edge luminescence, (ii) a shift to lower wavelengths of the blue emission feature (471 nm to 454 nm), and (iii) partial quenching of the red emission at ~ 595 nm *vis-a-vis* the band-edge luminescence which shows a significant ca. 50-fold increase in intensity (Φ_{lum} = 0.7). Similar dramatic increases in the emission intensity were noted earlier by Henglein *et al.*[46] when CdS particle surfaces were passivated by a hydroxide layer. Suppression of radiative and non-radiative surface recombination sites (deep energy traps for electrons and holes) increases the quantum yield of the band-edge luminescence by about 1 to 2 orders of magnitude arising from free charge carrier recombination. The blue-shift of the emission from 471 nm to 454 nm and its overlap with the exciton band (Figure 9.1) suggests that the near band-edge, shallow energy traps for electrons and holes must also be suppressed by surface passivation. Clearly, the surface chemistry is a significant parameter in the optical properties of these CdS microcrystallites.

Attempts to prepare CdS colloidal particles embedded in the silicate glass matrix for which the exciton band and the emission band overlapped proved unsuccessful.[#] Apparently, difficulties arise from the inability to control the colloid's surface chemistry in the low-temperature prepared glasses. However, it should be noted that the orange-red luminescence intensity of the CdS quantum dots in acidic silicate glasses is several times more intense than that of CdS aqueous sols prepared under otherwise identical conditions. It is proposed that the increase in the intensities of the orange-red emission(s) in CdS doped glasses, relative to aqueous sols,[47] arises from the presence of excess Cd^{2+} ions

---

[#] O.I. Micic, personal communication to Professor Serpone (1990).

which increase the number of S^{2-} anion vacancies, V_S^{2+} (the origin of a radiative centre),[40] and from a lesser passivation of the surface defect sites by the silicate host atoms.

9.2.2 Acidic Glasses

Two acidic, CdS-doped silicate glasses were examined in which the CdS clusters were stabilized with HMP and PVA. The final concentrations of CdS in the silicate glasses are given in Table 9.1; their absorption and emission spectra are illustrated in Figure 9.2. The CdS/HMP glass shows a green luminescence at ~ 485 nm, an emission at ~ 550 nm, together with a broad weak feature spanning ~ 600 nm to ~ 750 nm.[48] Comparison of these features with those of aqueous CdS/HMP sols (cf., Figures 9.1 and 9.2) shows that the red emission is sensitive to the nature of the matrix. It also depends on the nature of the stabilizer used. Underlying these variations are the nature and the extent of surface defect sites on these CdS clusters, which are more pronounced here than in macrocrystals.[49]

The PVA-stabilized CdS glass shows weak emissions at ~ 485 nm (near band-edge), ~ 550-560 nm, and ~ 800 nm, together with a broad and more intense luminescence at ~ 660 nm. Little surface passivation occurs in acidic environments and, although no Φ_{lum} could be determined, HMP appears to be a better passivator than PVA. The reason for this assertion lies in the buffer properties of HMP which insures a micro-environment different from that prevailing in CdS/PVA glasses.

Table 9.1 Relevant Data of CdS Colloids Embedded in Acidic Silicate Glasses and Stabilized with HMP and PVA Stabilizers.

[CdS] M	stabi-lizer	[stabi-lizer] M	Wavelength, nm		$[CdSO_4]^c$ M	2R calc[d] Å	V_p Å^3	no. unit cells/p	no. molec CdS/p	[part] M	surface area cm^3	no. surface faces	no. Cd atoms on surface	Cd_{surf}/Cd_{total} %	[Cd] at surface M
			a	b											
$6x10^{-4}$	HMP	3.3×10^{-4}	500	450	$1.4x10^{-3}$	44	$4.5 x10^4$	227	908	$6.7 x10^{-7}$	$6.1 x10^{-13}$	115	345	38	$2.3 x10^{-4}$
$2x10^{-4}$	PVA	1.4×10^{-4}	475	435	$1.8x10^{-3}$	33	$1.9 x10^4$	96	384	$5.1 x10^{-7}$	$3.4 x10^{-13}$	65	195	51	$1.0 x10^{-4}$

[a] Threshold wavelength. [b] Exciton peak. [c] Remaining in excess after CdS formation was arrested.
[d] Based on the threshold wavelength.

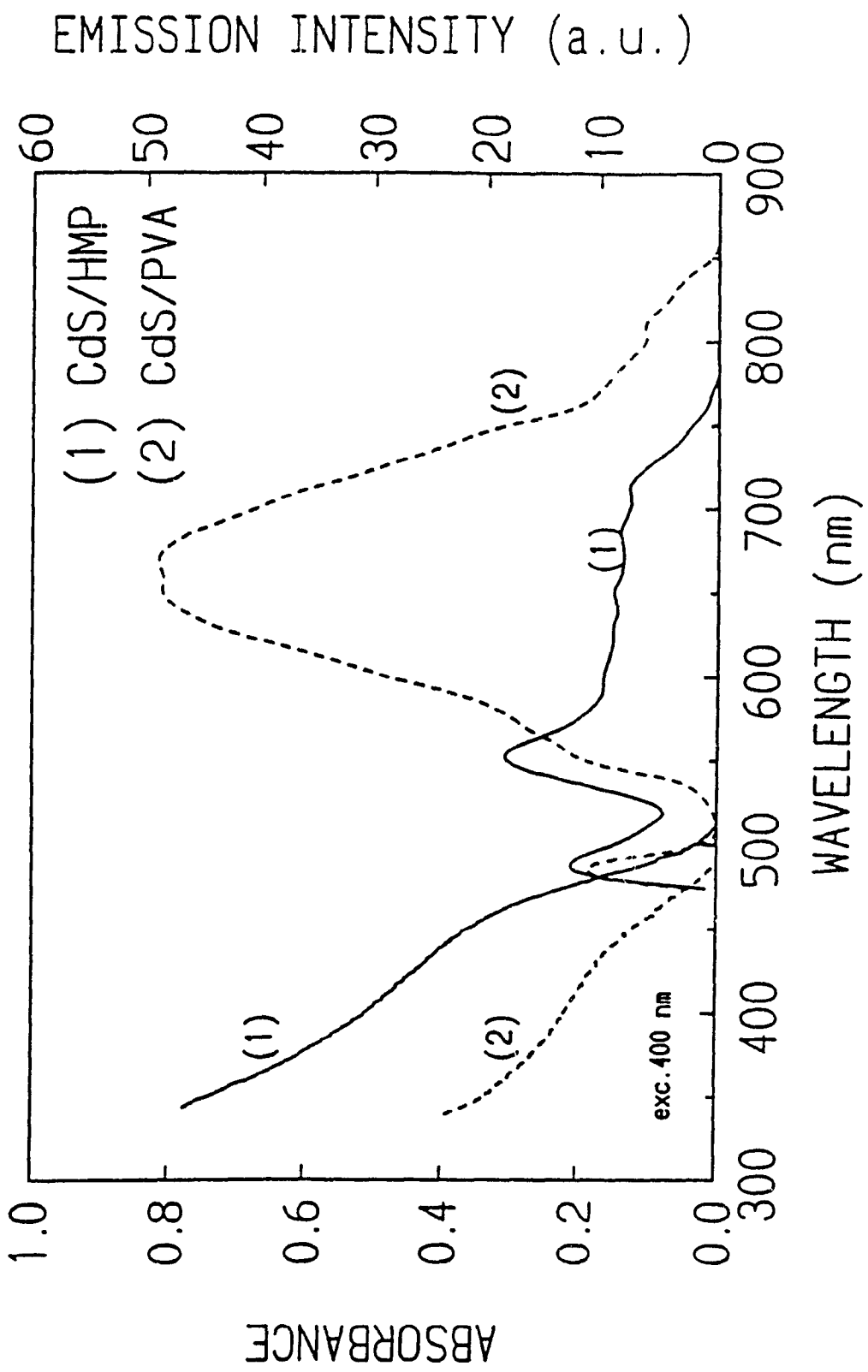

Figure 9.2 Absorption and emission spectra of CdS clusters embedded in an acidic silicate glass matrix, excitation wavelength 400 nm: (—) CdS clusters, 6×10^{-4} M, stabilized with 2×10^{-3} M HMP; (---) CdS colloids, 2×10^{-4} M, stabilized with 1 wt.% PVA.

9.3 PICOSECOND LASER SPECTROSCOPY

9.3.1 Primary Photochemistry

Optically transparent semiconductor doped glasses offer an excellent medium in which to examine these CdS quantum dots, in particular, since their dynamic behaviour can be monitored directly by time-resolved spectroscopic techniques. The use of glasses as the rigid matrix also provides an opportunity to examine photochemical processes without the interference of secondary events as often take place at liquid/solid interfaces. Under our conditions, photophysical events connected with light absorption and formation of excitons have terminated by the time our observations begin (> 20 ps).

Excitons are formed in the femtosecond time domain[10,13,15] at the instant the laser light pulse interacts with the CdS semiconductor clusters (eq. 9.1). They may be viewed as bound electron/hole pairs in the quantum confinement regime (CdS-doped glasses examined here) where the exciton diameter (40 A [50a]; 48 A [50b]) is comparable to or larger than the CdS cluster diameter (see Table 9.1). The lifetime of a free exciton (before trapping) is in the femtosecond time domain (30-150 fs).[10,13,15]

$$CdS \xrightarrow{h\nu} CdS[e^-/h^+] \tag{9.1}$$

$$CdS[e^-/h^+] \xrightarrow{10^{-14}-10^{-13}\ s} CdS[e^-/h^+]_{trapped} \tag{9.2}$$

The presence of at least two, $\{CdS(e^-/h^+)_2\}$, or more excitons, photogenerated in

the same CdS particle under multiphoton laser excitation, permits the excitons to interact, one manifestation of which is the appearance of Auger recombination and exciton-exciton annihilation.[13] Flytzanis and coworkers[19] have examined semiconductor doped glasses by time-resolved laser techniques and found a non-exponential intensity-dependent recombination of free carriers, which they ascribed to an Auger process. Auger recombination leads to electron emission by an interaction between either a primary (free) and a trapped e^-/h^+ pair, or between two trapped pairs (eq. 9.3),[10,13,14,18,19,21,25] with the expectation that the process will be even more efficient in quantum dots.[19a]

$$(e^-/h^+)_{free} + (e^-/h^+)_{trapped} \rightarrow CdS(h^+)_{trapped} + e^-_{ejected} \qquad \textbf{(9.3a)}$$

$$(e^-/h^+)_{trapped} + (e^-/h^+)_{trapped} \rightarrow CdS(h^+)_{trapped} + e^-_{ejected} \qquad \textbf{(9.3b)}$$

The precise fate of the ejected electron(s) is unknown. Possibly, (i) it may be trapped at different defect sites at the particle surface and in the bulk, $e^-_{trapped}$; or (ii) it may be trapped by surface Cd^{2+} ions to give $Cd^0_{surface}$ atoms and/or Cd^0_n clusters; or (iii) it can diffuse via trap to trap migration from the microcrystallite into the surrounding glass medium (photoionization) where it may be trapped at long-lived centres[21] (real defects or surface states [20]) in the host. The latter explains the photodarkening of the glass (noted here) and formation of permanent volume gratings in semiconductor-doped glasses.[17,20,21]

Once formed, the charge carriers in semiconductor particles can radiatively and/or non-radiatively recombine, together with being trapped at various sites available on the

CdS colloid (eq. 9.4):

$$CdS \xrightarrow{h\nu} (e^-/h^+), e_t^-, Cd^+, Cd^0, S^{\bullet -}, Cd^{2+}, S^{2-}, h\nu \text{ or } h\nu', \Delta \qquad (9.4)$$

The manner by which CdS doped glasses were prepared by the sol/gel method provides a variety of surface defects (intrinsic, stabilizer, silicate network, impurities), and additional defects generated by optical excitation. While the experimental conditions preclude a precise identification of the nature of trapped carriers in these various defect sites, observation of events in a wide time domain (20 ps to 10 ns), where the dynamics of localization are expected, allows a generalization to be made on some of the processes occurring when electrons and holes chemically interact with CdS.

9.3.2 HMP-Stabilized CdS Acidic Silicate Glasses

The transient absorption features for the HMP-stabilized CdS doped glass are illustrated in Figure 9.3. The number in each spectrum refers to delay times between the analytic (probe) and actinic (pump) pulses of the pump-and-probe technique used. The kinetic events were probed at 465, 506, and 670 nm from the plots of absorbance-change *versus* time (Figure 9.4a-c). The respective decay times and rise times are collected in Table 9.2. Transient bleaching of the exciton absorption in the CdS/HMP silicate glass occurs at 465 nm and is seen promptly (Figures 9.3 and 9.4a) at the leading edge of the actinic laser pulse. It is the result of a photoinduced shift of the CdS absorption to shorter wavelengths. Such hypsochromic shifts, also observed in CdS colloidal sols, can have

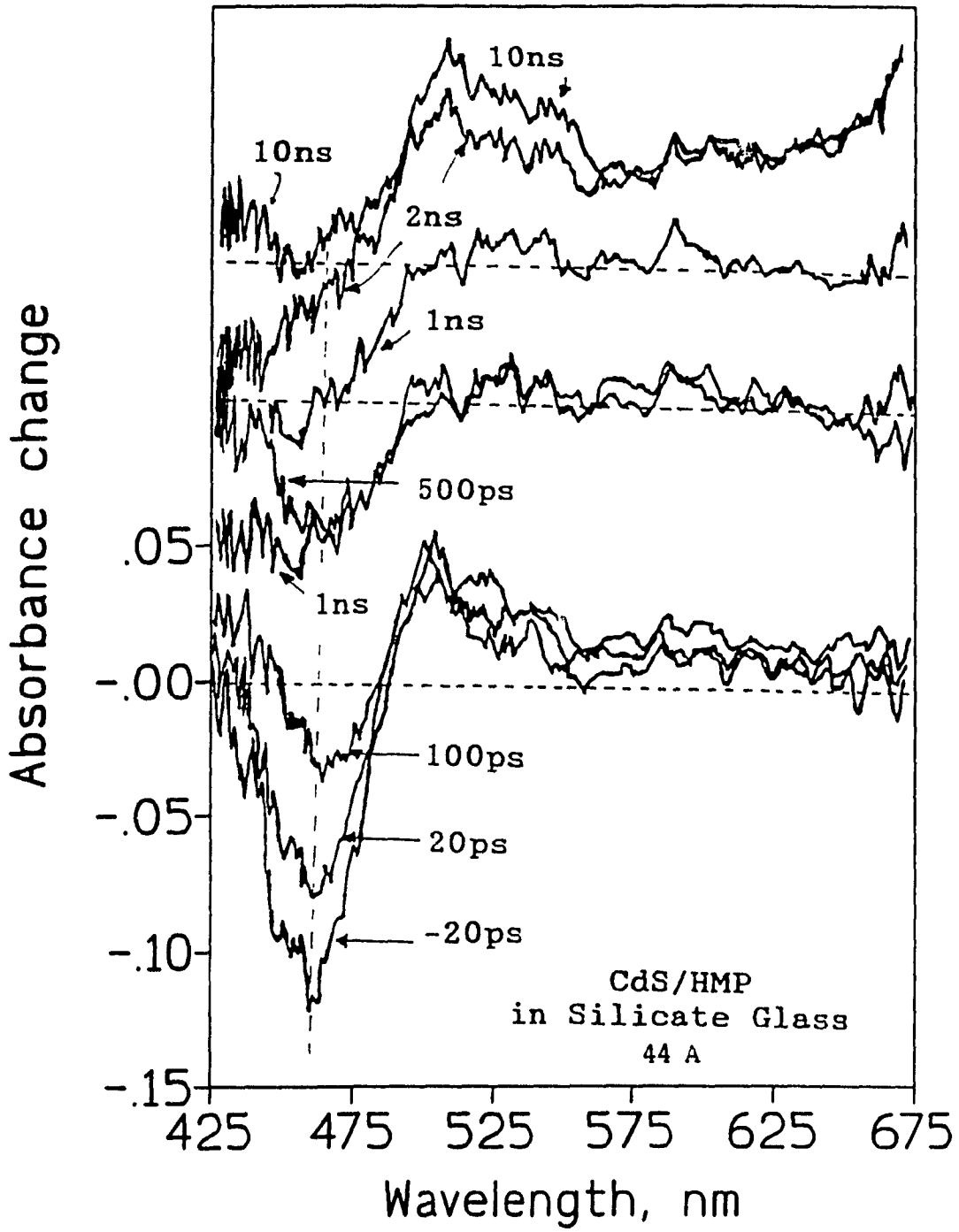

Figure 9.3 Transient absorption spectra (absorbance vs wavelength) in the range 425-675 nm of CdS colloids embedded in an acidic glass and stabilized with HMP. The glass samples were held against an appropriately built holder. The spectra are identified by the delay times which denote the time of arrival of the probe pulse after the pump pulse. The optical path length was 0.5 cm. The three horizontal lines denote the zero absorbance change baseline; spectra have been shifted for clarity.

Figure 9.4 Kinetic plots of absorbance change vs time (ns) at three selected wavelengths for CdS clusters (HMP stabilized) in an acidic silicate glass: (a) 465 nm, (b) 506 nm, and (c) 670 nm. Other conditions as in Figure 9.3.

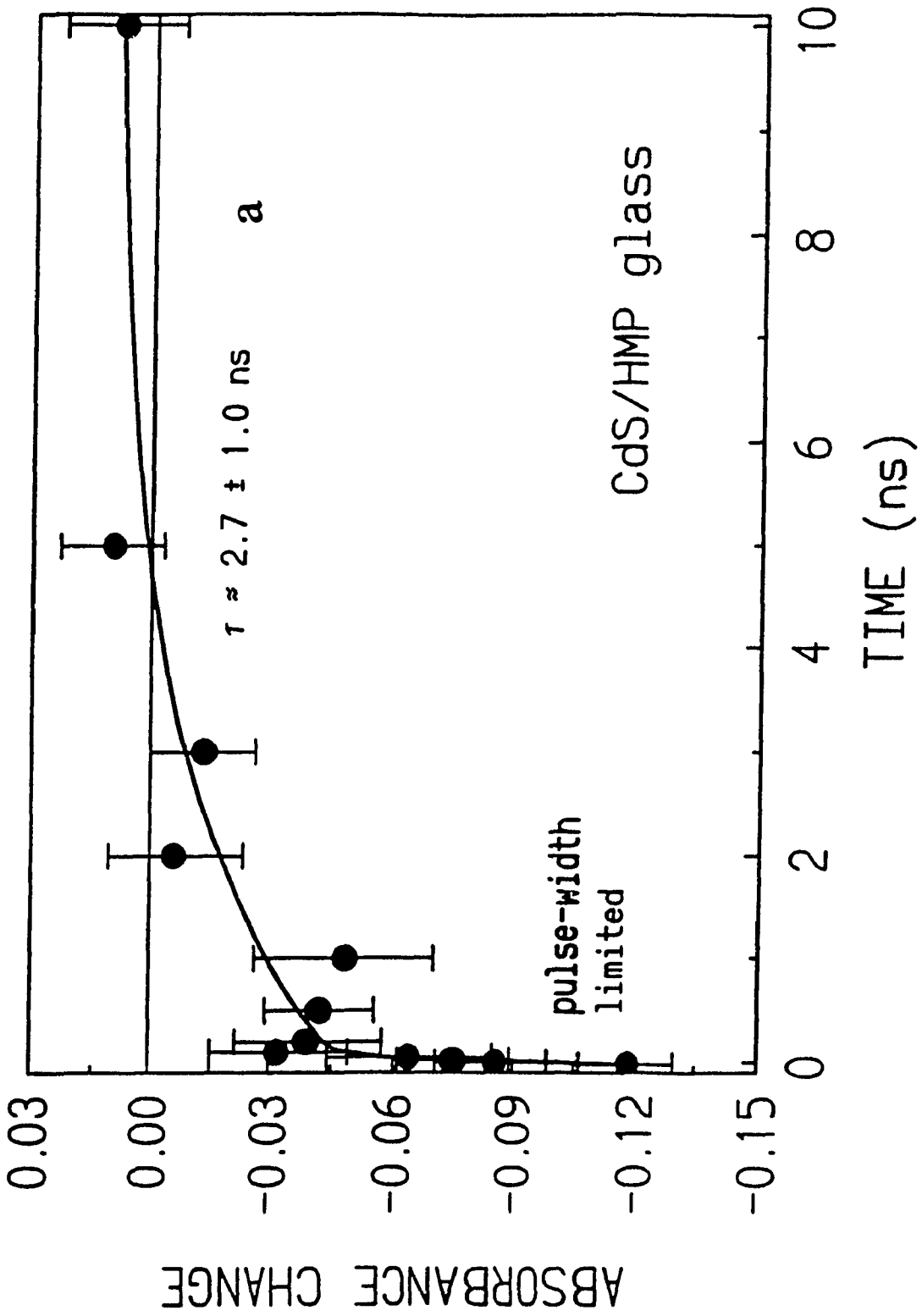
ABSORBANCE CHANGE
0.03
0.00
-0.03
-0.06
-0.09
-0.12
-0.15
0
2
4
6
8
10
TIME (ns)
CdS/HMP glass
τ ≈ 2.7 ± 1.0 ns
a
pulse-width
limited

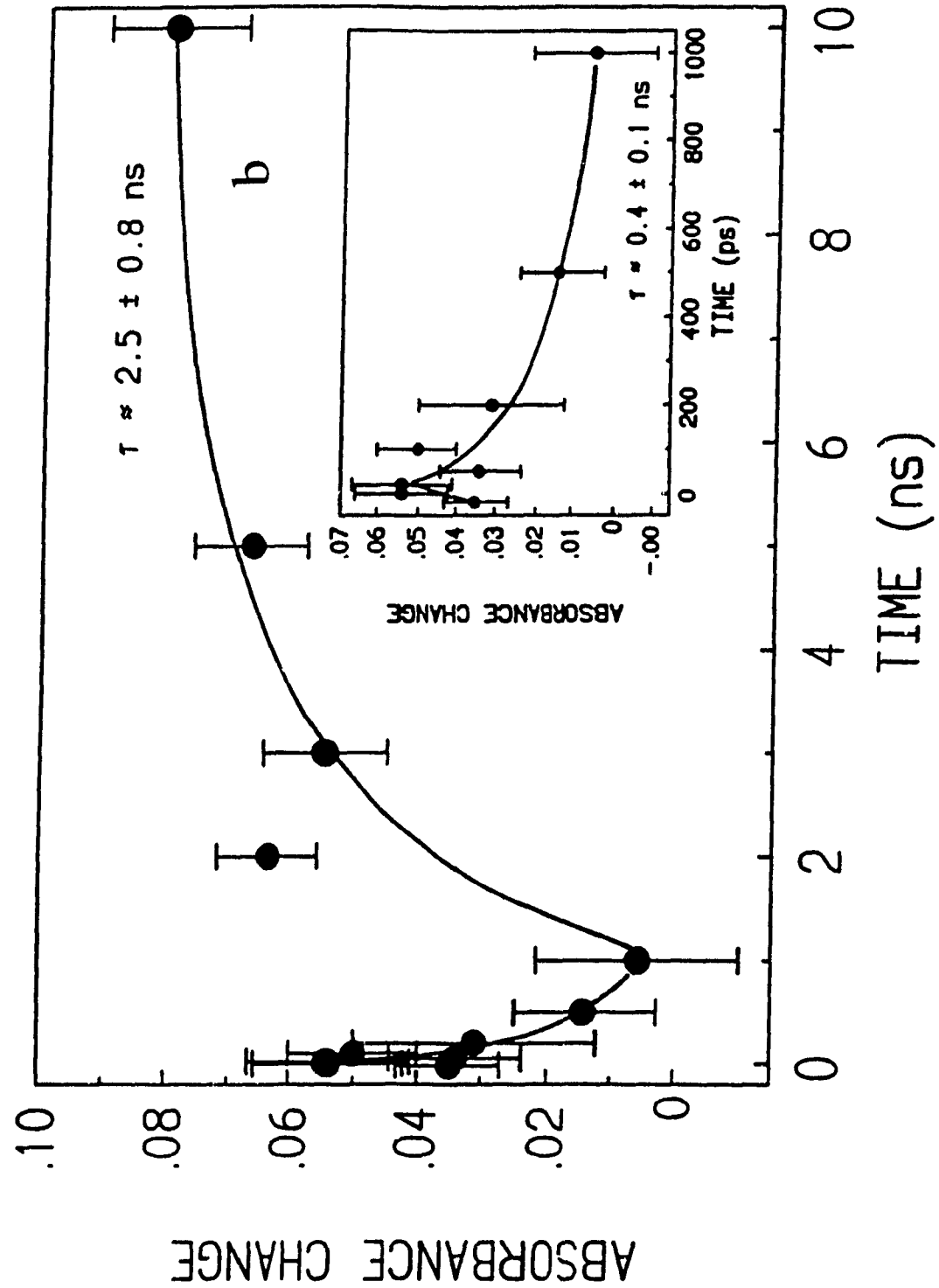
ABSORBANCE CHANGE
.10
.08
.06
.04
.02
0
0
2
4
6
8
10
TIME (ns)
τ ≈ 2.5 ± 0.8 ns
b
ABSORBANCE CHANGE
.07
.06
.05
.04
.03
.02
.01
0
-.00
0
200
400
600
800
1000
TIME (ps)
τ = 0.4 ± 0.1 ns

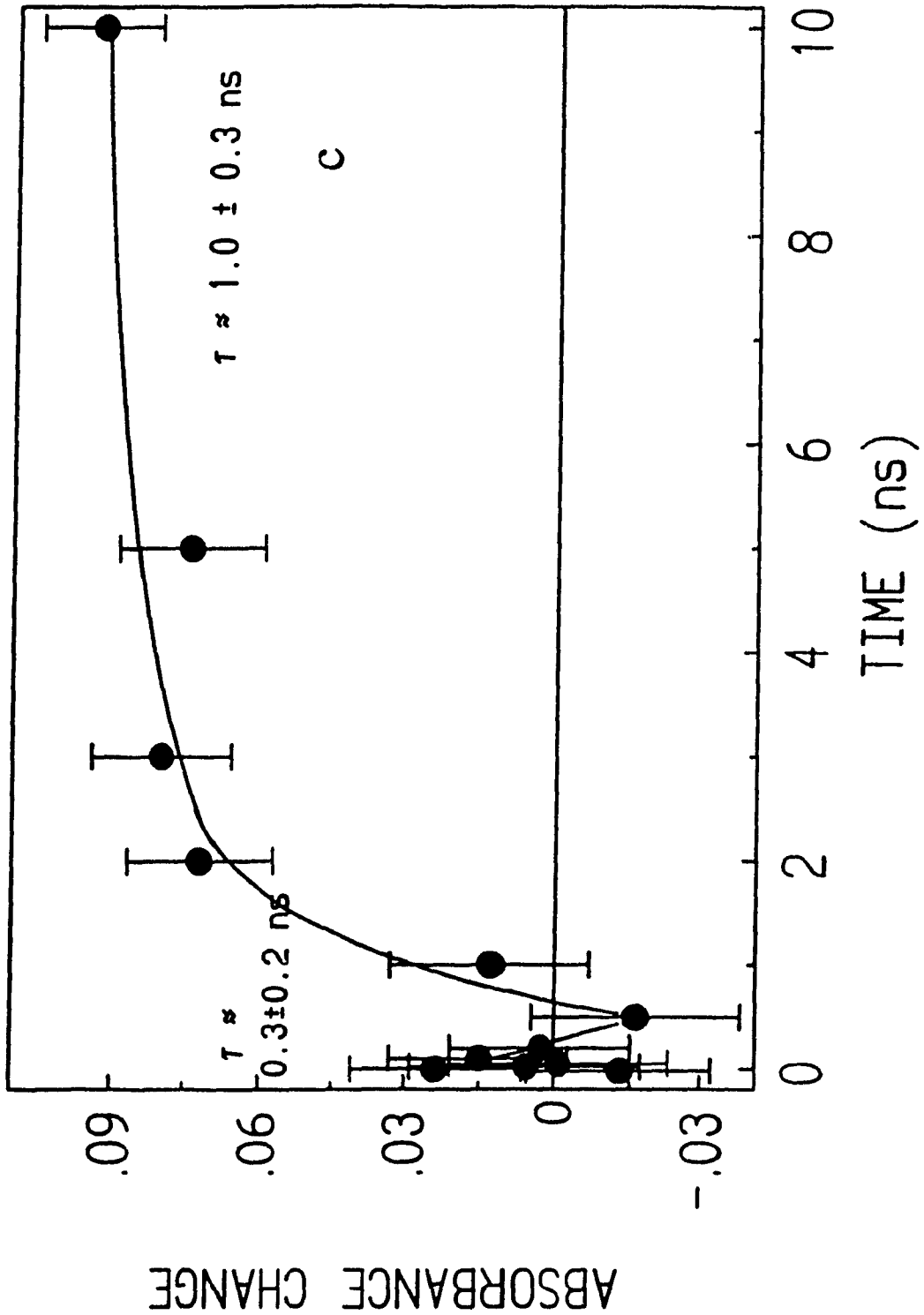
ABSORBANCE CHANGE
.09
.06
.03
0
-.03
0
2
4
6
8
10
TIME (ns)
τ ≈ 1.0 ± 0.3 ns
τ ≈ 0.3±0.2 ns
c

Table 9.2 Decay and Rise Times in the Transient Absorption and Transient Emission Spectra of HMP-Stabilized Cds Colloids in Silicate Glasses[a]

parameter	Wavelength nm			emission > 400 nm
	465	506	670	
$\tau^{(1)}_{(bleach)}$, ns	$\leq$ 40 ps			
$\tau^{(2)}_{(bleach)}$, ns	2.7 $\pm$ 1.0			
τ_{decay}, ns		0.4 $\pm$ 0.1	0.3 $\pm$ 0.2	(1) 0.4 $\pm$ 0.1
τ_{rise}, ns			1.0 $\pm$ 0.3	
τ_{rise}, ns		2.5 $\pm$ 0.8		(2) 3.5 $\pm$ 0.7

[a] Glass blanks gave no transient absorption at all the delay times examined.

different origins[7,9,11,18,22,50,51-56] and the four principal mechanisms which have been proposed to account for the observed blueshifts in the UV/Vis spectra are:

(1) band filling due to excess conduction band electrons (Burstein-Moss effect);

(2) increase in excitonic energy due to excess-surface trapped electrons;

(3) Coulombic screening by photogenerated free carriers;

(4) decrease in the oscillator strength of the excitonic transitions due to trapped electrons and holes.

These mechanisms are now briefly described.

The Burstein-Moss shift is based upon the creation of a very high density of electrons in the conduction band such that the energy levels closest to the bottom of the band fill up, thereby raising the Fermi level into the conduction band. Optical transitions must therefore involve higher energy levels causing a blue shift in the fundamental

absorption edge. However, for small particles this model becomes inefficient because of rapid charge carrier trapping at the particle surface.

Clusters contain many defects, mostly on the surface. Upon band gap excitation, free carriers or excitons are rapidly trapped by these sites. Interaction of these trapped charge carriers with excitons increases the energy necessary for optical excitation to occur and hence the absorption shifts to the blue.

Optical absorption may also be shifted to higher energies by the screening of excitons by free carriers. The screening reduces the binding energies of the exciton and as a result more energy must be provided in order for optical transitions to occur.

Finally, hypsochromic shifts can also be rationalized in terms of the exciton oscillator strength in the presence and absence of a trapped electron and hole pair. In the absence of such a trapped pair, there is strong overlap between the wavefunctions of the electron and hole. Introduction of a trapped pair decreases this overlap because the trapped electron localizes the hole's wavefunction at the surface of the particle. The oscillator strength of the exciton is thus decreased and as a result more energy is required for an optical transition to occur.

For the CdS quantum dots examined in this study, the transient bleaching is probably due to a decrease in the oscillator strength of the exciton transition caused by an interaction of surface-trapped excitons (or trapped electrons or holes) with other excitons (mechanism (4)).[50]

The decay of transient bleaching follows biphasic kinetics (Figure 9.4a); it is rapid initially (pulse-width limited; $\tau^{(1)}_{decay} \leq 40$ ps); later, bleaching decay occurs slowly

($\tau^{(2)}_{decay}$ = 2.7 ± 1.0 ns; Table 9.2). The faster process is due to a recombination of mobile, detrapped electrons with free holes or with shallow trapped holes. A small red shift (~ 2 to 4 nm) of the photobleaching maximum appears at delay times longer than ~ 20 ps (note the asymmetry of the bleach band). A pulse-width limited absorption feature also forms on the low energy side of the bleached exciton absorption, beginning at ~ 675 nm and rising slowly towards the UV with its maximum masked by the transient bleaching. This absorption persists for a short time (τ_{decay} ~ 0.4 ns at 506 nm and ~ 0.3 ns at 670 nm; Table 9.2) and by 500 ps it has decayed completely. This feature is believed to result from relaxation of a multi-excitonic excited state, $CdS(e^-/h^+)_{2n}$, from which electrons are ejected via an Auger mechanism (reactions 9.3) and are subsequently trapped by surface cadmium ions to give $(Cd_n^0)_{surface}$, reactions 9.5.

$$CdS(e^-/h^+)_{2n} \rightarrow CdS(h_t^+)_n + ne^- \qquad \textbf{(9.5a)}$$

and/or

$$CdS(e_t^-/h_t^+)_{2n} \rightarrow CdS(h_t^+)_n + ne^- \qquad \textbf{(9.5b)}$$

$$ne^- + CdS((n/2)Cd^{2+})_{surface} \rightarrow CdS(Cd_n^0)_{surface} \qquad \textbf{(9.5c)}$$

The 675-485 nm feature immediately formed is therefore attributed to cadmium atoms which evolve into Cd^0_n clusters on the CdS particle surface,[25] in accord with recent observations that such clusters absorb in this range (~ 430-540 nm) when only electrons are injected in CdS clusters.[4,54,55] More specifically, cadmium atom clusters have been

shown to absorb at about 480 nm.[56] Further support for this assignment emanates from spectral and kinetic considerations of other possible transient(s).

Every electron ejected from the particle leaves a trapped hole, $CdS(h^+_t)$, on the surface; this trapped hole is identified with the sulphide radical anion, $S^{\bullet-}$.[24,25,57] The 675-485 nm absorption at 10 ns in Figure 9.3 is unlike the one observed from the reaction of OH• radicals with CdS colloids which yields the $S^{-\bullet}$ species and which shows a broad absorption that extends far into the red region from 400 to 800 nm, with the maximum dependent on particle size.[25,58-60] The spectra at 2 ns and 10 ns of Figure 9.3 reflect in fact the overlap of two transient absorptions (see below). It should be noted here that electrons localized on cadmium ions as Cd^0 and holes localized on S^{2-} as $S^{-\bullet}$ absorb in the same wavelength region. However, any contribution by $S^{-\bullet}$ radicals to the absorption observed in the 30-500 ps time domain must be negligible, because of the relatively slow kinetics of formation[26,58] (and decay) of $S^{-\bullet}$ radicals in CdS sols: $k_f \sim 5 \times 10^8\ s^{-1}$;[26,58] ($k_d \sim$ 1-3 x $10^7\ s^{-1}$ [58,59]). Formation of the 675-485 nm feature in our experiments is pulse-width limited ($k \geq 3 \times 10^{10}\ s^{-1}$) which suggests it to be due to $(Cd_n^0)_{surface}$. Localization of electrons is known to be a fast process.[10,13] At longer times (1-10 ns), and after the complete decay of this 30-500 ps absorption via a non-radiative and/or radiative recombination of $(Cd_n^0)_{surface}$ with holes (reaction 9.6), the contribution of $S^{-\bullet}$ radicals to the absorption spectra could become significant.

$$CdS(Cd_n^0)_{surface} + nh^+(or\ h_t^+) \rightarrow CdS((n/2)Cd^{2+})_{surface} + \Delta + h\nu(550nm) \qquad (9.6)$$

The broad transient absorption growth around 510 nm and extending from ~ 470

nm to ~675 nm (overlaps extensively with the absorption at 670 nm) is formed in the 1 ns to 10 ns time window: τ_{rise} ~ 2.5 ns, identical to the transient bleaching decay at 465 nm ($\tau^{(2)}_{decay}$ ~ 2.7 ns; Table 9.2). This absorption is attributed to the formation of $S^{-\bullet}$ radical anions (eq. 9.7) on the basis of its rate of formation[58] and its spectroscopic behaviour.[18]

$$CdS(Cd^{2+}S^{2-}) + h^{+}(or\ h_t^{+}) \rightarrow CdS(Cd^{2+}S^{\bullet-}) \qquad (9.7)$$

The broad negative absorption seen at 1 and 2 ns delay times in Figure 9.3 may still be due to trapped electron/hole pairs or to different intermediates in the corrosion process known to occur in CdS particles.[24,25] The photochemical change that removes S^{2-} ions to give the $S^{\bullet}$ radicals would effectively reduce the particle size, decrease the absorption of CdS and displace the bleaching band maximum to shorter wavelengths, beyond our spectral window. It is therefore concluded that transient bleaching seen at times below 500 ps is due to electron trapping;[52,54] at times longer than 500 ps, hole trapping[53,57] is largely responsible for the bleaching. This is the first time that both pathways for transient bleacning have been seen for CdS in a single experiment.

The nature of the transient absorption feature at ca. 670 nm in Figure 9.3, which is seen to grow from 1 ns to 10 ns delay times, may now be addressed. This feature is attributed to long-lived trapped electrons in the silicate host. Since the $(Cd_n^{\circ})_{surface}$ absorption had completely decayed by 500 ps and the absorption at 670 nm was seen at times > 1 ns, electron transfer from the CdS quantum dots to the host is not mediated

by surface cadmium atoms. Rather, while the photogenerated holes are surface-trapped as $S^{-\bullet}$ species (τ_{rise} = 2.5 ns), the photogenerated electrons diffuse to the stabilizer/silicate network (τ_{rise} ~ 1.0 ns; Table 9.2) where they get trapped and cause photodarkening of the glass.[19]

The transient emission decays for the HMP/CdS glasses are presented in Figure 9.5. The decay data were computer-fitted to a sum of two exponentials: τ_{decay} = 0.4 ± 0.1 ns and 3.5 ± 0.7 ns. Although the multi-exponential nature[5,9,15,59] of the decay may arise from a distribution of particle size, and/or distribution of trap depths and to a spatial distribution of trap sites,[52] it does not preclude the fact that the emission decay may also have photochemical origins. It should be noted that where multi-exponential decay times have been reported, their origins have not been fully addressed. Under the conditions of the experiments, the decay curve in Figure 9.5 represents the sum of the decays of all the emissions monitored above 400 nm (cf., Figure 9.2). Recombination of photogenerated holes with the surface trapped electrons {$(Cd_n^o)_{surface}$; eqn. 9.6} is manifested by the 550-nm emission in the HMP/CdS glass sample. The decay time of 0.4 ns for this emission is identical to the decay time of the $(Cd_n^o)_{surface}$ absorption, as expected if both events have a common origin.

The decay of the near band-edge luminescence at ~ 485 nm, arising from the recombination of electrons and holes in shallow traps (a few meV) and recently described as *delayed fluorescence*,[15] is very rapid ($k >> 3 \times 10^{10} s^{-1}$ [10,15]), thus the failure to time-resolve the decay. Earlier, it was reported[60] that the decay of the green luminescence of aqueous CdS colloids (size, ~ 11 nm) was pulse-width limited ($k \geq 3 \times 10^{10} s^{-1}$); similar

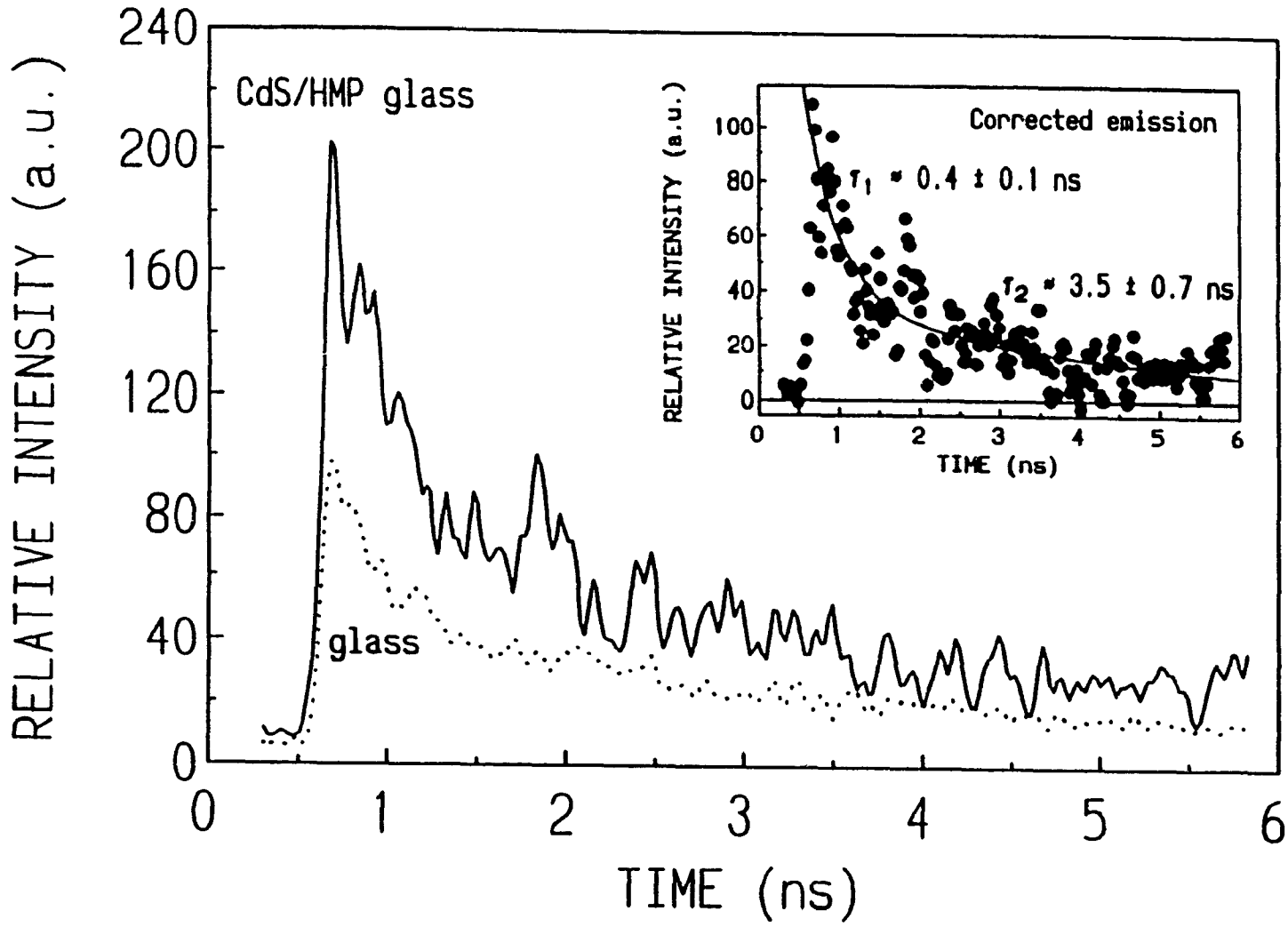

Figure 9.5 Transient emission decay for the luminescence(s) at wavelengths greater than 400 nm: (—) CdS colloids (HMP stabilized) in an acidic silicate glass; (•••) silicate glass only. Other conditions as in Figure 9.3 and in the text.

findings were noted recently by Morgan and Natarajan[5] and earlier by Harzion and coworkers[61] for untreated CdS bulk crystals ($k \geq 10^{11}$ s^{-1}), who also noted that the emission intensity depends quadratically on the laser fluence (intensity depended on the concentration of electrons and holes). When CdS quantum dots are confined in a glass, coupling of the host phonons and the CdS surface phonons increases the relaxation processes.

The second decay time ($\tau_{decay} \sim 3.5$ ns; Figure 9.5), attributed to the broad red emission spanning the range 580 to 750 nm, has its origins with the hole trapping event of eqn. 9.7. Since the photogenerated hole is trapped (i.e., S^{2-} acts as a quencher), it is unavailable to recombine with trapped electrons. Thus, the rate of emission decay is nearly identical to the rate of hole trapping, i.e. to the rate of formation of the $S^{-\bullet}$ radical species.[15] It is relevant that the photogenerated holes could, in principle, also be trapped by cadmium ion vacancies, V^{2-}_{Cd}:[51]

$$V_{Cd}^{2-} + h^{+}_{thermal} \rightarrow V_{Cd}^{-} \qquad \textbf{(9.8a)}$$

$$V_{Cd}^{-} + h^{+}_{photogenerated} \rightarrow V_{Cd}^{0} \qquad \textbf{(9.8b)}$$

an unlikely event here since the glasses contain residual excess of $CdSO_4$ (Table 9.1) after the formation of CdS was arrested.

9.3.3 Influence of Other Stabilizers

The optical behaviour of the transients formed in multiphoton excited CdS/PVA

Figure 9.6 Transient absorption spectra, as absorbance change vs wavelength, in the range 425-675 nm of CdS clusters embedded in an acidic silicate glass and stabilized with PVA. The spectra are identified by the delay times (see Figure 9.3 and text). The optical path length was 0.5 cm.

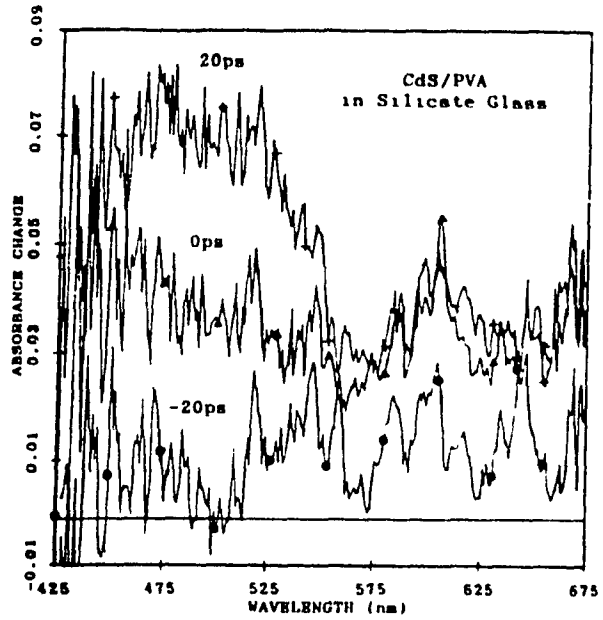
20ps
CdS/PVA
in Silicate Glass
0ps
-20ps
ABSORBANCE CHANGE
0.09
0.07
0.05
0.03
0.01
-0.01
425
475
525
575
625
675
WAVELENGTH (nm)

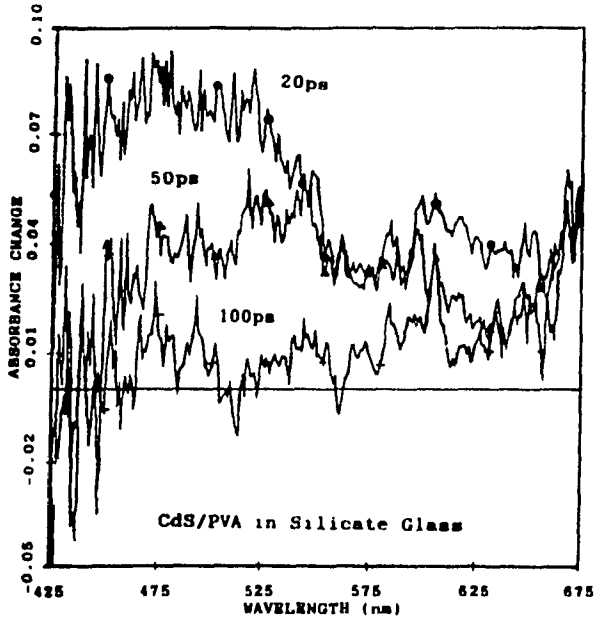
20ps
50ps
100ps
CdS/PVA in Silicate Glass
ABSORBANCE CHANGE
0.10
0.07
0.04
0.01
-0.02
-0.05
425
475
525
575
625
675
WAVELENGTH (nm)

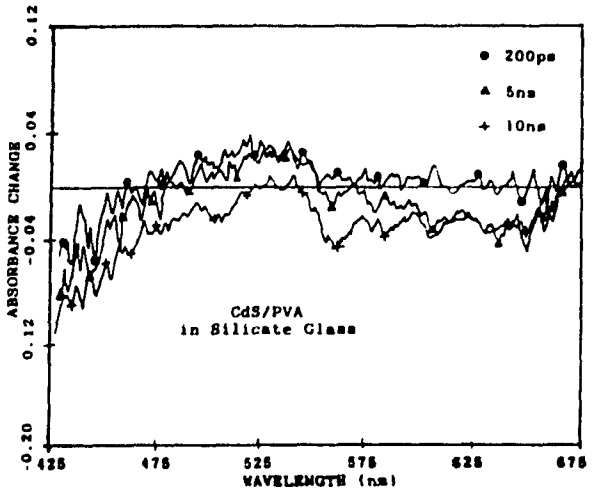
200ps
5ns
10ns
CdS/PVA
in Silicate Glass
ABSORBANCE CHANGE
0.12
0.04
-0.04
-0.12
-0.20
425
475
525
575
625
675
WAVELENGTH (nm)

glasses differs from that of CdS/HMP glasses. The transient absorption spectra at various delay times are illustrated in Figure 9.6. At -20 ps, absorptions are weak (absorbance change ~ 0.01). Subsequently, a broad (~ 425-550 nm) pulse-width limited transient absorption grows in ($\tau_{rise} \leq 30$ ps), which begins to decay at ~ 20 ps; decay is nearly complete by ~ 100 ps (τ_{decay} ~ 50 ps; Figure 9.7). Also evident in this short time are transient absorptions above 550 nm. Formation of $(Cd_n^{\circ})_{surface}$ species in this CdS/PVA sample is exhibited by the transient absorption growth at 425-550 nm, in keeping with the findings in the CdS/HMP glasses. The growth and decay kinetics of $(Cd_n^{\circ})_{surface}$ in the CdS/PVA glass differ from those in the CdS/HMP glass owing to the different nature of trap states and to a different interfacial chemistry.

The pulse-width limited transient growth observed at 100 ps and at wavelengths greater than 575 nm originates with trapped electrons on the silicate network (or on PVA) via the Auger process of multi-exciton interactions (eqn. 9.3). The observations, however, do not preclude an alternative source, namely trapped electrons in a S^{2-} anion vacancy, V^{+}_{S}, a rather deep trap (~ 0.7 eV; an F centre)[6] for conduction band electrons to give V°_{S} centres (eqn. 9.9; see also the scheme below):

$$e^{-} + V_S^{+} \xrightarrow{<30ps} V_S^{0} \qquad \textbf{(9.9)}$$

The emission which decays with τ_{decay} ~ 0.2 ns cannot involve V_S°. This centre can transfer the electron to a surface species, for example cadmium ions. In keeping with the findings for the CdS/HMP glass, the emission (560 nm; Figure 9.2) decay originates

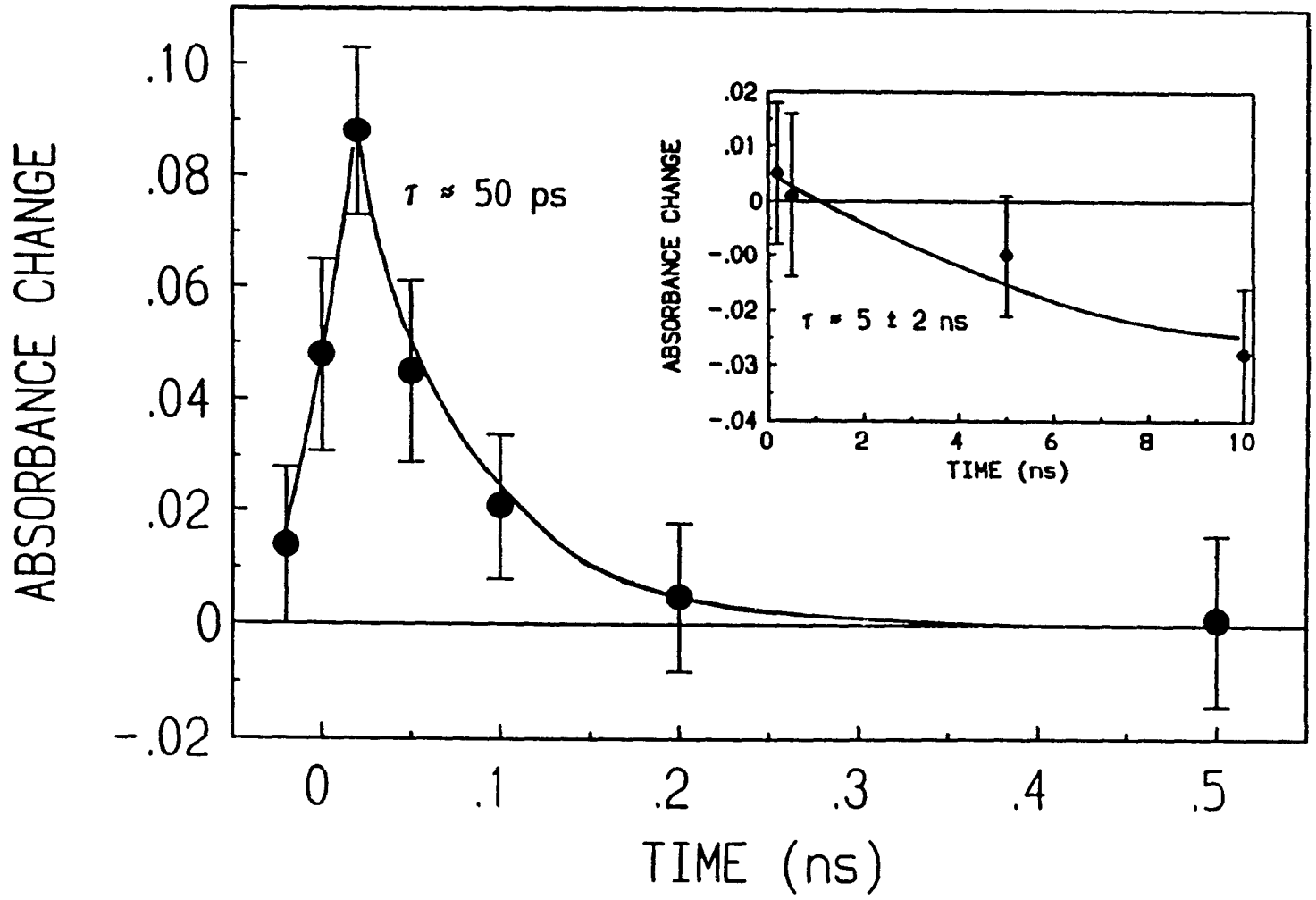

Figure 9.7 Kinetic plot of absorbance change vs time (ns) taken at 475 nm for the CdS colloids stabilized by PVA and embedded in an acidic silicate glass. Other conditions as in Figure 9.6

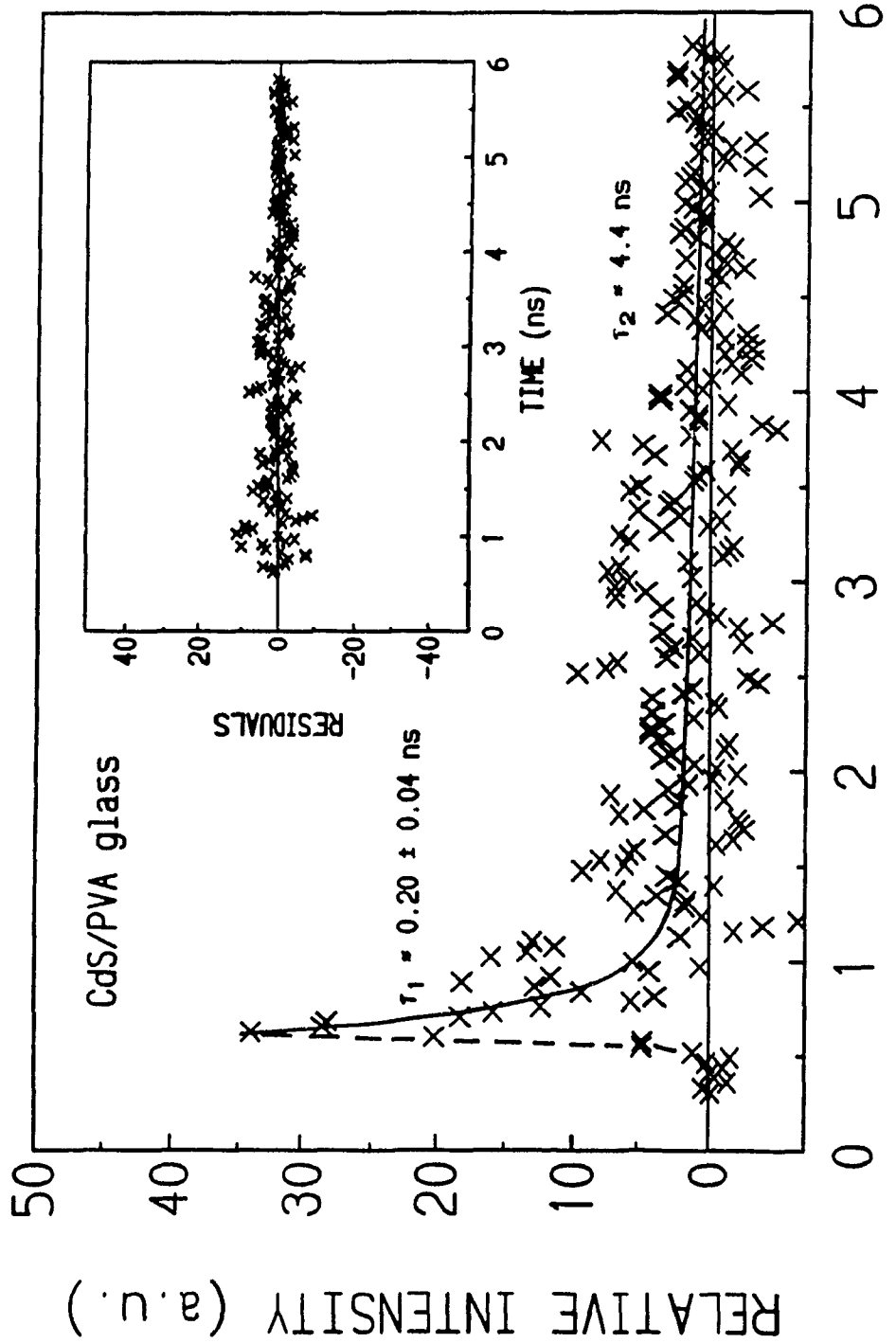

Figure 9.8 Transient emission decay for the CdS/PVA sample of Figure 9.6 taken at wavelengths greater than 400 nm. Other conditions as in text.

from a process which implicates $(Cd_n^0)_{surface}$ or its equivalent (eqn. 9.6) recombining with photogenerated holes. The decay time for the longer-lived emission is ~ 4-5 ns (Figure 9.8). The congruence of this decay time with that of the slower decaying transient absorption at 475 nm (τ_{decay} ~ 5 ± 2 ns) infers that both events may be related: formation of the sulphide radical anion (eqn. 9.7) does not lead to emission but quenches it.[40] At longer delay times (bottom of Figure 9.6), two apparent photobleachings appear at ~ 560 nm and at ~ 640 nm. The latter develops more rapidly than the former. The coincidence between these and the emission features seen in Figure 9.2 suggests a common origin, namely involvement of trapped electrons as cadmium atoms[4] (560 nm, eqn. 6) and as V^0_S [6] (640 nm; eqn. 9.10).

$$V_S^0 + h^+ (or\ h_t^+) \rightarrow h\nu\ (broad\ emission\ at\ \sim 640\ nm) \qquad (9.10)$$

The energy levels of the appropriate radiative recombination centres are portrayed in the scheme:[4]

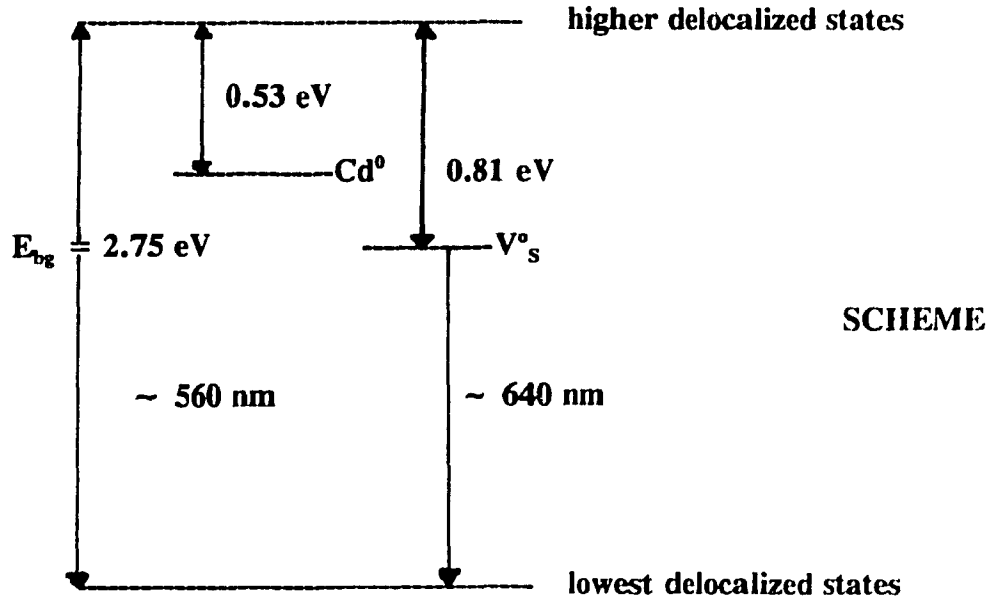

SCHEME

Direct electron/hole recombination from shallow traps no doubt does occur, unfortunately its manifestation is masked by an emission from the glass;

None of the alkaline glasses examined, in which CdS was stabilized with polyacrylic acid (PAA), polyvinyl alcohol (PVA), polyethylene glycol (PEG) and polystyrene sulphonate (PSS), showed transient bleaching of the exciton absorption. This accords with earlier observations by Albery and coworkers[52] and by Serpone *et al.*;[62] no long-lived transient bleaching of the exciton band was seen in the microsecond and picosecond time domains in alkaline colloidal CdS solutions. Evidently, emission spectra and transient bleaching are highly sensitive to the surface properties of the particles. In an alkaline medium, the small OH^- ions can bind to surface cadmium. The layer of cadmium hydroxide that forms on the CdS cluster passivates its surface by blocking or annihilating the defect sites.

9.4 CONCLUSIONS

Stabilized CdS quantum dots of very small dimensions (25-40 Å) have been incorporated in silicate glasses, prepared by a low-temperature sol/gel process, to examine the primary photochemical and photophysical processes by photoluminescence and picosecond laser techniques. Multiphoton laser excitation of these clusters (10 to 1000 photons absorbed per CdS cluster) generate multi-excitonic states, $\{CdS(e^-/h^+)_n; n = 2,...\}$, which upon relaxation lead to Auger ejection of electrons (i) to the particle surface/stabilizer/glass interface resulting in surface Cd° or Cd°_n species, and/or (ii) into the silicate network. The Auger process leaves excess positive charge on the CdS

particle yielding trapped holes that are identified with $S^{-\bullet}$ anion radicals. Collapse of two of these $S^{-\bullet}$ anions to give S and S^{2-} ultimately leads to photocorrosion of the CdS quantum dots.

The large surface-to-volume ratio in the CdS crystallites (Table 9.1) points to a high density of surface states, defects, and/or lattice imperfections at which photogenerated charge carriers can rapidly be trapped. The bulk of the non-linearity observed in this study arises from the presence of trapped carriers.[11b] On the time scale of picoseconds, surface trapped electron/hole pairs ($\leq$ 30 ps), together with surface trapped electrons first (as Cd_n°, below 500 ps) and with trapped holes later (as $S^{\bullet}$, above 1 ns), through their interaction with another exciton, are mostly responsible for transient bleaching of the exciton absorption which is particularly noticeable in the HMP-stabilized CdS acidic silicate glass, and to a lesser extent in the corresponding PVA-stabilized CdS glass. Variations in transient bleaching with time reflect the dynamics of trapped charge carriers.

The nature of the stabilizer/host environment plays a significant role on the optical behaviour of quantum-confined CdS microcrystallites and on the charge carrier dynamics. Quantum dots stabilized with HMP and PVA display different charge carrier dynamics. The reason for this is found in the different micro-environments created by the two stabilizers; in the case of HMP, its buffer properties show a more pronounced effect on the dynamics. CdS colloids in acidic aqueous media showed different optical behaviour from the corresponding systems in alkaline media. The presence of OH^- ions and added Cd^{2+} ions to the aqueous dispersions passivate the CdS particle surface resulting in a

dramatic ca. 50-fold increase in the band-edge luminescence at the expense of the red emission. The stabilizer/silicate host atoms also passivate the surface of the CdS quantum dots in the glass, but to a lesser extent as witnessed from their photoluminescence and to some extent from their transient absorptions.

Electron migration from its origins in the CdS quantum dots to the glass host probably takes place first via rapid electron trapping in shallow states, followed by a slower trap to trap diffusion across the CdS/host interface until a deep trap is encountered in the host lattice. Photodarkening of the glass was observed as a black dot along the path of the laser beam.

References

1. Takagahara, T. *Phys.Rev.,B,* **1987,** 36, 9293, and references therein.

2. Kull, M. and Coutaz, J.-L., *J.Opt.Soc.Am.,B,* **1990,** 7, 1463.

3. Schmitt-Rink, S., Miller, D.A.B. and Chemla, D.S. *Phys.Rev.,B,* **1987,** **35,** 8113.

4. Wang, Y. and Herron, N., *J.Phys.Chem.*, **1988,** 92, 4988.

5. Morgan, J.R. and Natarajan, L.V., *J.Phys.Chem.*, **1989,** 93, 5.

6. Chestnoy, N., Harris, T.D., Hull, R. and Brus, L.E., *J.Phys.Chem.*, **1986,** *90,* 3393.

7. Liu, C.-Y and Bard, A.J., *J.Phys.Chem.*, **1989,** 93, 3232.

8. Wang, Y., Herron, N., Mahler, W. and Suna, A., *J.Opt.Soc.Am.B,* **1989**, 6, 808.

9. Kamat, P.V., Dimitrijevic, N.M. and Nozik, A.J., *J.Phys.Chem.*, **1989,** 93, 2873.

10. Bawendi, M.G., Wilson, W.L., Rothnerg, L., Carroll, T.M., Jedjiu, T.M., Steigerwald, M.L. and Brus, L.E., *Phys.Rev.Lett.*, **1990,** 65, 1623.

11. (a) Hilinski, E.F., Lucas, P.A. and Wang, Y., *J.Chem.Phys.*, **1988,** 89, 3435.
    (b) Wang, Y., *Acc.Chem.Res.*, **1991**, 24, 133.

12. (a) O'Neil, M., Marohn, J. and McLendon, G., *Chem.Phys.Lett.*, **1990,** 168, 208.
    (b) O'Neil, M., Marohn, J. and McLendon, G., *J.Phys.Chem.*, **1990,** 94, 4356.

13. Ernsting, N.P., Kaschke, M., Weller, H. and Katsikas, L., *J. Opt. Soc. Am., B,* **1990,** 67, 1630.

14. Kaschke, M., Ernsting, N.P., Muller, U. and Weller, H., *Chem. Phys. Lett.*, **1990,** 168, 543.

15. Eychmuller, A., Hasselbarth, A., Katsikas, L. and Weller, H., *Ber. Bunsenges. Phys. Chem.*, **1991**, 95, 79.

16. Wang, Y., Suna, A., McHugh, J., Hilinski, E.F., Lucas, P.A. and Johnson, R.D., *J.Chem.Phys.*, **1990**, 92, 6927.

17. Morgan, R.A., Park, S.-H., Koch, S.W. and Peyghambrain, N., *Semicond. Sci. Technol.*, **1990**, 5, 544.

18. Haase, M., Weller, H. and Henglein, A., *J.Phys.Chem.*, **1988**, 92, 4706.

19. (a) Roussignol, P., Kull, M., Ricard, D., Rougemont, F., Frey, R. and Flytzanis, C., *Appl.Phys.Lett.*, **1987**, 51, 1882.
(b) Rougemont, P., Frey, F., Roussignol, P., Ricard, D. and Flytzanis, C., *Appl.Phys.Lett.*, **1987**, 50, 1619.
(c) Roussignol, P., Ricard, D., Lukasik, J. and Flytzanis, C., *J. Opt. Soc. Am., B*, **1987**, 4, 5.

20. Horan, P. and Blau, W., *J.Opt.Soc.Am.,B*, **1990**, 7, 304.

21. Ekimov, A.I. and Efros, A.L., *phys.stat.sol.(b)*, **1988**, 150, 627.

22. Henglein, A., Kumar, A., Janata, E. and Weller, H., *Chem. Phys. Lett.*, **1986**, 132, 133.

23. Warnock, J. and Awschalom, D.D., *Phys.Rev.B*, **1985**, 32, 5529.

24. Kamat, P.V. and Dimitrijevic, N.M., *Sol.Energy*, **1990**, 44, 83; and references therein.

25. Henglein, A., *Top.Curr.Chem.*, **1988**, 143, 113.

26. a) Zimin, L.G., Gaponenko, S.V., Lebed, V. Yu., Malinovskii, I.E., Germanenko, I.N., Podorova, E.E. and Tsekhmonskii, V.A., *phys.stat.sol.(b)*, **1990**, 159, 267.
b) Zimin, L.G., Gaponenko, S.V., Lebed, V.Yu., Malinovskii, I.E. and Germanenko, I.N., *J.Lumin.*, **1990**, 46, 101.
c) Zimin, L.G., Gaponenko, S.V., Malinovskii, I.E., Lebed, V.Yu., Kuznetsov, P.I., Yakushcheva, G.G. and Kuznetsov, A.V., *phys. stat. sol.(b)*, **1990**, 159, 449.

27. Warnock, J. and Awschalom, D.D., *Appl.Phys.Letters*, **1986**, 48, 425.

28. Gaponenko, S.V., Grobkovskii, V.P., Zimin, L.G. and Nikeenko, N.K., *Zh. Prikl. Spektr.*, **1982,** *37,* 863; ibid., **1984,** 41, 844.

29. Jain, R.K. and Lind, R.C., *J.Opt.Soc.Am.*, **1983,** 73, 647.

30. Kull, M., Coutaz, J.L., Manneberg, G. and Grivickas, V., *Appl. Phys. Lett.*, **1989,** 54, 1830.

31. Olbright, G.R. and Peyghambarian, N., *Appl. Phys. Lett.*, **1986,** 48, 1184.

32. Acioli, L.H., Gomes, A.S.L. and Rios Leite, J.R., *Appl.Phys.Lett.*, **1988,** 53, 1788.

33. Ekimov, A.I., Efros, A.L. and Onushchenko, A.A., *Solid State Commun.*, **1985,** 56, 921.

34. Borelli, N.F., Hall, D.W., Holland, H.J. and Smith, S.D., *J.Appl.Phys.*, **1987,** 61, 5399.

35. Banyai, L. and Koch, S.W., *Phys.Rev.Lett.*, **1986,** 21, 2722.

36. Hanamura, E., *Phys.Rev.B,* **1988,** 37, 1273.

37. Brus, L.E., *IEEE J.Quant.Electron.*, **1986**, 22, 1909.

38. Brus, L.E., *J.Phys.Chem.*, **1986,** 90, 2555.

39. Bawendi, M., Steigerwald, M.L. and Brus, L.E., *Annual Revs. Phys.Chem.*, **1990,** 41, 1.

40. Kumar, A., Janata, E. and Henglein, A., *J.Phys.Chem.*, **1988,** 92, 2587.

41. Nenadovic, M.T., Comor, M.T., Vasic, V. and Micic, O.I., *J. Phys. Chem.*, **1990,** 94, 6390.

42. Nakabayashi, S. and Kira, A., *J.Phys.Chem.*, **1990,** 94, 7571.

43. Dannhauser, T., O'Neil, M., Whitten, D. and McLendon, G., *J. Phys. Chem.*, **1986,** 90, 6074.

44. Karton, A.R., Hull, R., Opila, R.L., Bawendi, M., Steigerwald, M.L., Carroll, D.J. and Brus, L.E., *J.Am.Chem.Soc.*, **1990,** 112, 1327.

45. Ramsden, J.J. and Gratzel, M., *J.Chem.Soc.Faraday Trans.I,* **1984**, 80, 919.

46. Spanhel, L., Haase, M.H., Weller, H. and Henglein, A., *J. Am. Chem. Soc.*, **1987**, 109, 5649.

47. Rajh, T., Vucemilovic, M.I., Dimitrijevic, N.M., Micic, O.I. and Nozik, A.J., *Chem.Phys.Lett.*, **1988**, 143, 305.

48. Since the acidic glasses were prepared with HCl, chloride substitution into the CdS lattice might lead to Cd^{2+} ion vacancies which are responsible (*Appl.Phys.Lett.*, **1967**, 10, 339) for the red luminescence, at least in part, reported earlier at 740 nm. Despite this assertion, other workers {Kulp, B.A. and Kelley, R.H. *J.Appl.Phys.*, **1960**, *31*, 1057; Vuylsteke, A.A. and Schvonen, Y.T. *Phys.Rev.*, **1959**, *113*, 40; and reference 45} have inferred that this red emission originates with sulfur vacancies, as also noted herein. CdS sols prepared in the presence of Cl^- ions show only the green (band-edge) luminescence (ref.45), and especially prepared chloride-doped CdS microcrystallites emit strong green emission, whose intensity increased with NaCl concentration (Uchida, I. *J.Phys.Soc.Japan*, **1966**, 21, 645). In the present study, broad emissions are observed from 600 nm to 750 nm for the CdS/HMP glasses. Although we have carried out no EDAX measurements to determine the colloid's composition, it is unlikely that Cl^- plays any significant role, if at all, in the observed photoluminescence in the acidic glasses for the following reasons: (i) preparations of CdS/HMP colloids with and without Cl^- ions present yield sols which show emission bands at 490 nm and at 540 nm only - no 740 nm band was seen; (ii) as noted in Table 9.1, $CdSO_4$ remains in excess after CdS formation has been arrested, thereby making it unlikely that there would be cadmium ion vacancy defects in the CdS lattice or on the surface; and (iii) the slow method used to prepare CdS microcrystallites in the silicate glasses makes it unlikely that chloride substituted for the S^{2-} ions in the CdS lattice. It may be concluded that chloride plays no role in the systems investigated here.

49. Ekimov, A.I., Kuoryactsev, L.A., Ivanov, M.G. and Efros, A.L., *J. Lumin.*, **1990**, 46, 83.

50. a) Wang, Y., Suna, A., McHugh, J., Hilinski, E.F., Lucas, P.A. and Johnson, R.D., *J.Chem.Phys.*, **1990**, 92, 6927.
b) Gratzel, M. in *"Heterogeneous Photochemical Electron Transfer"*, CRC Press, Boca Raton, Florida, 1989, p. 87.

51. Kuczynski, J.P., Milosavljevic, B.H. and Thomas, J.K., *J.Phys.Chem.*, **1984,** 88, 980.

52. Albery, W.J., Brown, G.T., Darwent, J.R., and Salevar-Iranizad, E.J., *J.Chem.Soc. Faraday Trans.I,* **1985,** 81, 1999.

53. Kamat, P.V., Dimitrijevic, N.M. and Fessenden, R.W., *J.Phys.Chem.*, **1987,** 91, 396.

54. Hayes, D., Micic, O.I., Nenadovic, M.T., Swayambunathan, V. and Meisel, D., *J.Phys.Chem.*, **1989,** 93, 4603.

55. Nenadovic, M.T., Comor, M.I., Vasic, V. and Micic, O.I., *J. Phys. Chem.*, **1990,** 94, 6390.

56. Soera, T,Ya. and Serdyuk, V.V., *Opt.Spectrosc.*, **1960,** 9, 210.

57. Baral, S., Fjotik, A., Weller, H. and Henglein, A., *J.Am.Chem.Soc.*, **1986,** 108, 375.

58. Kamat, P.V., Ebbesen, T.W., Dimitrijevic, N.M. and Nozik, A.J., *Chem.Phys.Lett.*, **1989,** 157, 384.

59. a) Gopidas, K.R., Bohorquez, M. and Kamat, P.V., *J.Phys.Chem.*, **1990,** 94, 6435.
b) Kamat, P.V. and Dimitrijevic, N.M., *J.Phys.Chem.*, **1989**, 93, 4259.
c) Kamat, P.V., Gopidas, K.R. and Dimitrijevic, N.M., *Molec.Cryst.Liq.Cryst.*, **1990,** 183, 439.

60. a) Serpone, N. in *"Photoelectrochemistry, Photocatalysis and Photoreactors"*, Schiavello, M., Ed., Reidel Publ.Co., Dordrecht, Holland, 1985, pp. 351-372.
b) Serpone, N.; Pelizzetti, E. in *"Homogeneous and Heterogeneous Photocatalysis"*, Pelizzetti, E. and Serpone, N., Eds., Reidel Publ.Co., Dordrecht, Holland, 1986, pp. 51-89.

61. Harzion, Z., Huppert, D., Gottesfeld, S. and Croitoru, N., *J.Electroanal.Chem.*, **1983,** 150, 571.

62. Serpone, N., Sharma, D.K., Jamieson, M.A., Gratzel, M. and Ramsden, J.J., *Chem.Phys.Lett.*, **1985**, 115, 473.

CHAPTER 10
FINAL CONCLUSIONS

10.1 CONCLUDING REMARKS

The photophysical and photocatalytic properties of crystalline (anatase)/ amorphous TiO_2 particulates, doped in the bulk with a number of transition metal ions, have been investigated using conventional spectroscopic techniques (UV/Vis absorption and fluorescence spectroscopy), pulse radiolysis, and transient absorption and emission spectroscopy. The dopants (as salts) added at various concentrations to the bulk of TiO_2 included: chromium(III), iron(III), vanadium(V) and vanadium(III), ruthenium(III), platinum(IV), rhodium(III), palladium(II), copper(II), manganese(II), nickel(II), tungsten(VI), molybdenum(VI), cerium(III), cobalt(II), neodynium(III), rhenium(III) and rhenium(VII), yttrium(III), and titanium(III). In addition, TiO_2 was doped with equal amounts of vanadium(III) and vanadium(V), ruthenium(III) and platinum(IV), chromium(III) and iron(III), and rhenium(III) and rhenium(VII). During the course of the work, the size, morphology, crystal structure and surface area of both the doped and undoped TiO_2 specimens were determined using, respectively, dynamic light scattering, electron microscopy, x-ray diffraction and surface area measurements. The effect of different anatase/rutile ratios, particle size and nature of the dopant on the photocatalytic activity was also examined. The relative photo-oxidative ability of the samples was

explored using the oxidation of oxalic acid as a model reaction, while the photoreductive ability was explored by monitoring the reduction of water (pH 3) to hydrogen gas. The effect of particle size on the photophysics of electron/hole separation/recombination events was examined in TiO_2 colloids of various size (23, 133 and 281 Å), in AgI colloids (25, 35 and 100 Å) and in CdS microcrystallites (33 Å), the latter in aqueous media and in a silicate matrix.

The pulse radiolysis technique was used to study the reaction of •OH radicals with 133-Å TiO_2 particles. Hydroxyl radicals reacted with these particles in a diffusion-controlled rate. The hydroxyl radical was trapped on the TiO_2 and exhibited a broad absorption band centred at about 350 nm. Oxygen had no effect on this reaction and its product characteristics. The product decayed via first-order kinetics which were assigned to the collapse of two species trapped on the same particle to yield peroxides. The oxidative abilities of this product were confirmed by oxidation of SCN^- to give the anion radical $(SCN)_2^{\bullet-}$. The identity of the product of the •OH reaction with the particles was identified as a trapped hole at the TiO_2 particle surface.

There were no differences between 23, 133 and 281 Å diameter TiO_2 particle in terms of the absorption properties; however, significant variations in the dynamics of charge carrier recombination were noted. Colloidal sols of 23, 133 and 281 Å diameter TiO_2 particles do not display typical quantum-size properties such as blue shifts in the UV-vis spectrum associated with decreasing particle size. The absorption depends on particle concentration and followed a Beer-Lambert behaviour in the 0 to 15 g/L concentration range examined. The band-edge luminescence was most intense in the 133

Å TiO_2 particles. Further, transient emission studies indicated that radiative electron/hole recombination is slowest in the 133 Å TiO_2 particles. The picosecond transient absorption spectra indicated that the localization of the electron as a Ti^{III} species was strongest in the 23 Å TiO_2 particles and decreased with increasing particle size. The fast component of the transient absorption decay was smallest in the 281 Å particles, contrary to the slow component which is somewhat longer in these particles.

A number of transition metal dopants added to the lattice of TiO_2 appear to extend the absorption characteristics of TiO_2 into the visible part of the spectrum. Some of the metal dopants do not seem to affect the band-edge absorbance of TiO_2 but rather seem to sensitize the material through a broad band observed in the visible region (however, see below). The concentration and the oxidation state of the dopant had a marked effect on the absorption properties. Increasing the metal dopant concentration increased the spectral features observed. The effect of the dopant concentration on the band-edge emission intensity of TiO_2 is non-linear. In many cases, low dopant concentrations caused increased quenching of the band edge emission as compared to the higher dopant concentrations. Variations in the extent of emission quenching on particle size cannot be ruled out as a possible explanation. Transient emission studies showed that the different dopants had small but finite effects on the band-edge emission decay times. Transient absorption studies have indicated that the different dopants may act as either electron or hole traps.

A number of conclusions may be reached regarding the photocatalytic activity of both naked and transition metal doped TiO_2. The high photocatalytic activity of P-25

Degussa TiO_2 is not simply related to the fact that the material is comprised of anatase and rutile fractions. Instead, it would appear that the method of preparation of the material and its surface properties are likely more important factors. The particle size (23 to 281 Å) of TiO_2 (hence, surface area) appears to have a slight effect on the photooxidative activity of TiO_2. Finally, addition of transition metal dopants to the bulk of TiO_2 does not enhance the photooxidative activity of TiO_2; however, in some cases it does improve the reductive properties of the materials. Increasing the dopant concentration, in general, leads to decreased photocatalytic activity. These studies have shown that contrary to the expectation based on the spectroscopic results, addition of the metal dopants does not extend the photo-action spectrum of TiO_2 into the visible region.

The reaction of reducing species from acetonitrile media with silver iodide particles ($\sim$ 25-Å diameter) was investigated using the pulse radiolysis technique. Injection of electrons into these ultrasmall particles led to transient bleaching of the absorption of AgI at wavelengths close to the onset of absorption ($\sim$ 400 nm) with the concomitant reduction of AgI to silver(0) deposits. The reduction of Ag^+ ions and formation of silver atoms and/or dimeric Ag_2 molecules on three different size AgI particles ($\sim$ 100, 35 and 25 Å) were also examined by picosecond laser spectroscopy. The rates of formation of these silver species and/or higher nuclearity clusters followed simple exponential growth kinetics (average particle diameter): $k \sim 20 \times 10^8\ s^{-1}$ (100 Å), $9 \times 10^8\ s^{-1}$ (35 Å), and $\sim 2 \times 10^8\ s^{-1}$ (25 Å). These rates correlated linearly with $(size)^{-1}$, yielding a limiting rate of $2.6 \times 10^9\ s^{-1}$ (limiting rise time $\sim$ 0.38 ns).

The optical properties of CdS quantum dots, capped with different surface-active

materials and suspended in transparent silicate glasses were examined by photoluminescence and picosecond laser spectroscopy. Glasses prepared with different surface-active materials {poly(vinyl)alcohol), PVA; hexametaphosphate, HMP} displayed different charge carrier dynamics, demonstrating the importance of the CdS particle/silicate glass interface. Excitation of the glasses at high laser power (2-3 mJ/pulse; ca 30-ps pulses) generated several excitons in the same particle to give multiexcitonic states. Upon relaxation, these excited states led to Auger recombination which ejected an electron that got trapped at the particle surface either as cadmium atom(s) or clusters of atoms, Cd_n^0, or on the silicate glass network (photodarkening), leaving excess positive charge on the CdS particle to give $S^{\bullet-}$ radicals. Transient absorption and emission spectra showed variation in the different time domains examined from -20 to 10 ns. From the congruence between transient absorption rise times and decay times with those from double-exponential fits of the emission decay, it was argued that charge carrier dynamics have photochemical origins. Charge carrier migration to the glass host occurred in several stages, initiated first by rapid carrier trapping into very shallow energy traps (ca. a few millivolts), followed by slower trap to trap diffusion until a deeper energy trap is encountered.

APPENDIX A

PARTICLE SIZE DISTRIBUTIONS OF TRANSITION METAL DOPED TiO_2 COLLOIDS OBTAINED USING DYNAMIC LIGHT SCATTERING

The particle size distributions of the transition metal doped TiO_2 samples presented in this Appendix were obtained during studies aimed at characterizing the particles as discussed in chapter 3. The histograms representing the particle size distribution were fitted to a normal Gaussian curve and the results of the fit gave identical results to those calculated using equations 2.4 to 2.6 as presented in chapter 2.

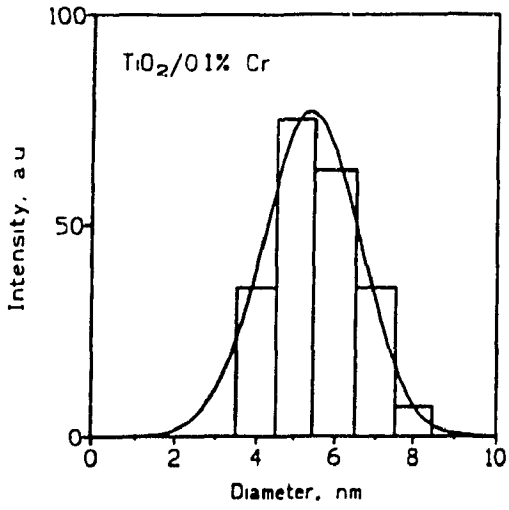
TiO2/0.1% Cr
Intensity, a u
Diameter, nm
0
50
100
0 2 4 6 8 10

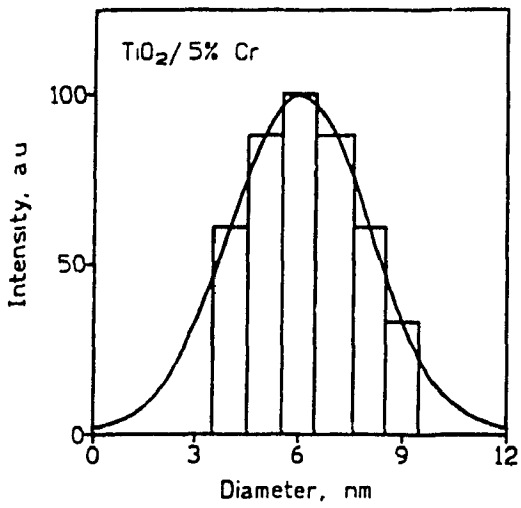
TiO2/ 5% Cr
Intensity, a u
Diameter, nm
0
50
100
0 3 6 9 12

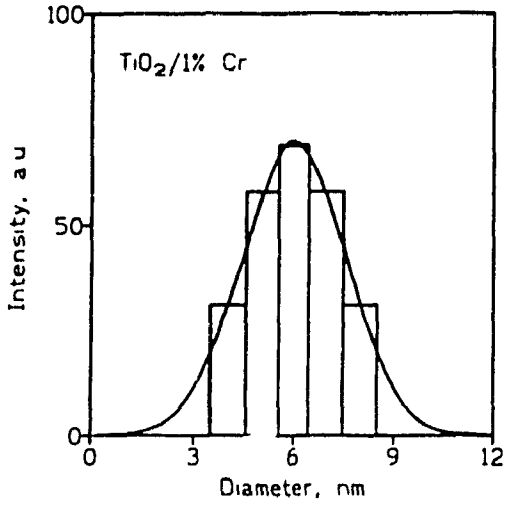
TiO2/1% Cr
Intensity, a u
Diameter, nm
0
50
100
0 3 6 9 12

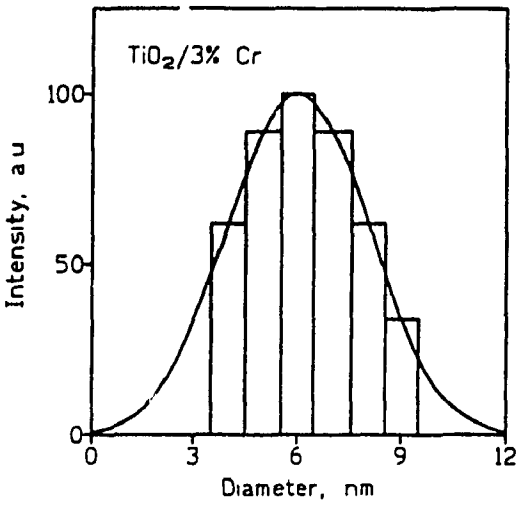
TiO2/3% Cr
Intensity, a u
Diameter, nm
0
50
100
0 3 6 9 12

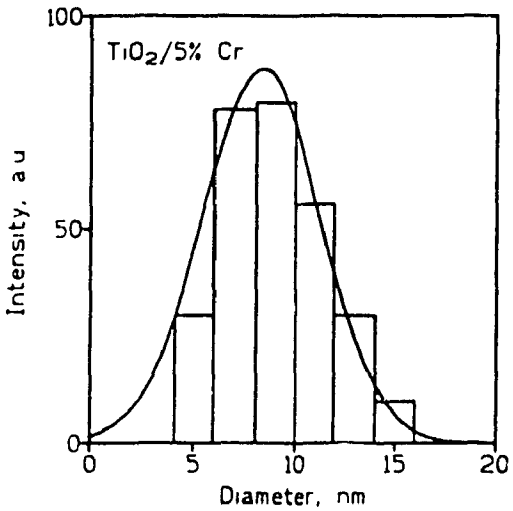
TiO2/5% Cr
Intensity, a u
Diameter, nm
0
50
100
0 5 10 15 20

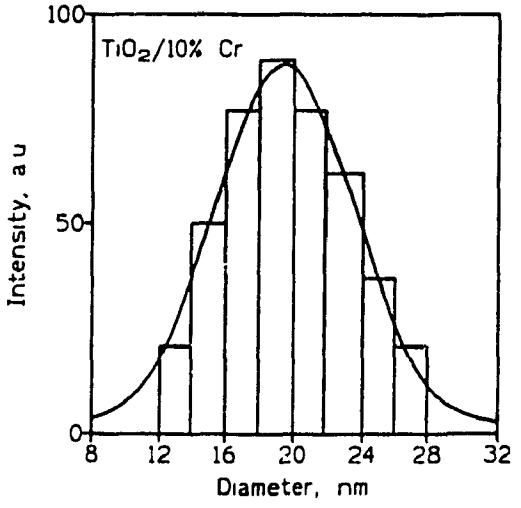
TiO2/10% Cr
Intensity, a u
Diameter, nm
0
50
100
8 12 16 20 24 28 32

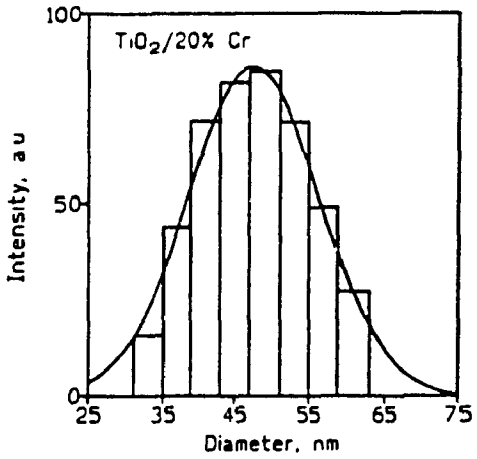
TiO2/20% Cr
Intensity, a u
Diameter, nm
100
50
0
25
35
45
55
65
75

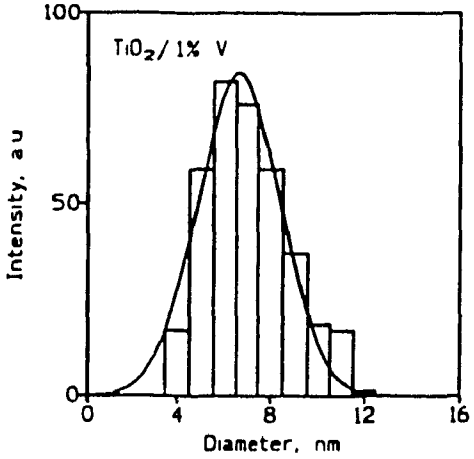
TiO2/ 1% V
Intensity, a u
Diameter, nm
100
50
0
0
4
8
12
16

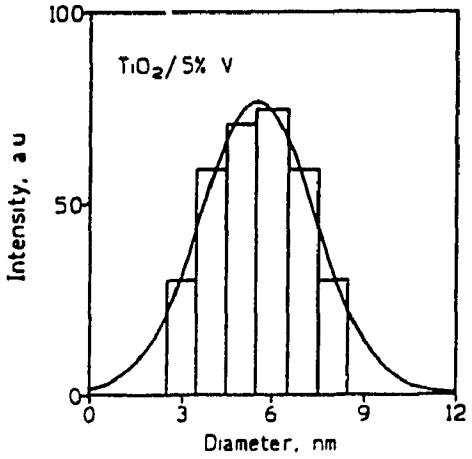
TiO2/ 5% V
Intensity, a u
Diameter, nm
100
50
0
0
3
6
9
12

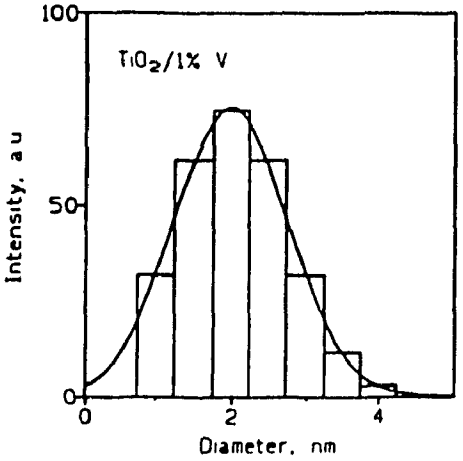
TiO2/1% V
Intensity, a u
Diameter, nm
100
50
0
0
2
4

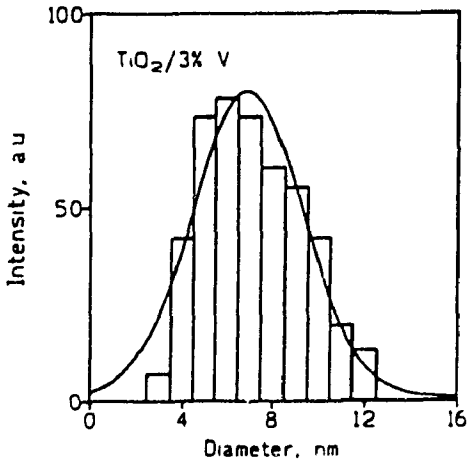
TiO2/3% V
Intensity, a u
Diameter, nm
100
50
0
0
4
8
12
16

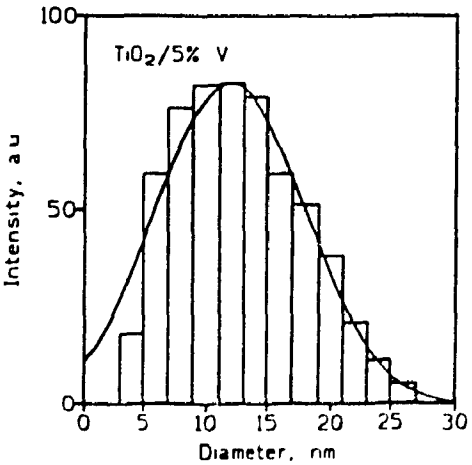
TiO2/5% V
Intensity, a u
Diameter, nm
100
50
0
0
5
10
15
20
25
30

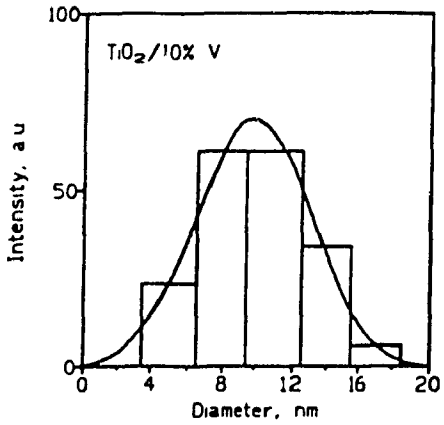
TiO2/10% V
Intensity, a u
Diameter, nm

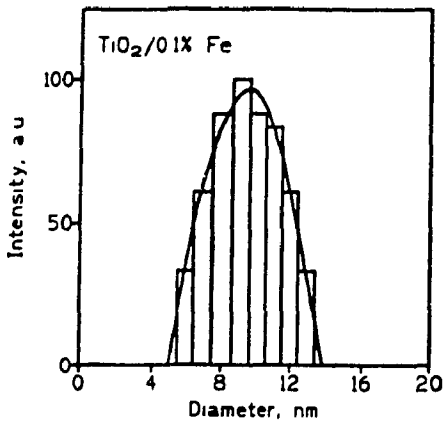
TiO2/0.1% Fe
Intensity, a u
Diameter, nm

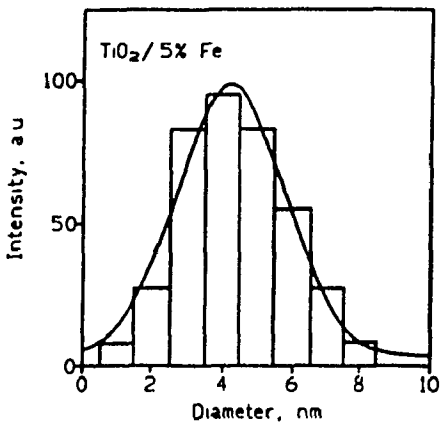
TiO2/ 5% Fe
Intensity, a u
Diameter, nm

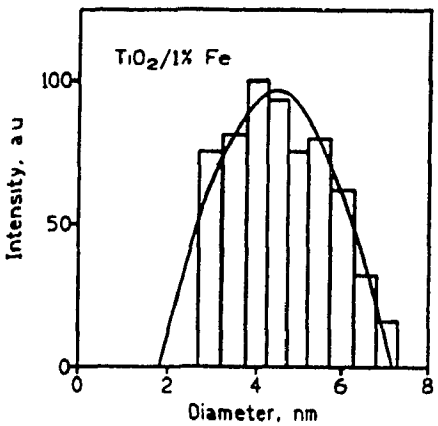
TiO2/1% Fe
Intensity, a u
Diameter, nm

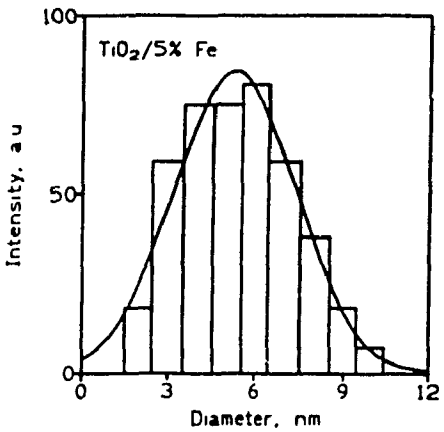
TiO2/5% Fe
Intensity, a u
Diameter, nm

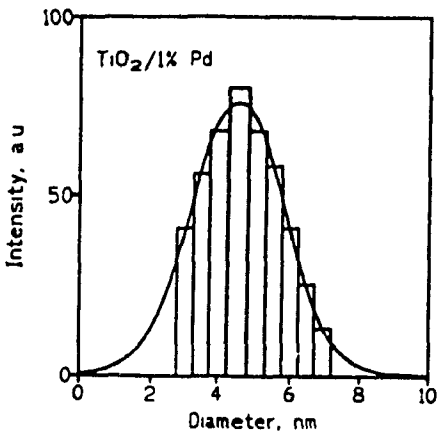
TiO2/1% Pd
Intensity, a u
Diameter, nm

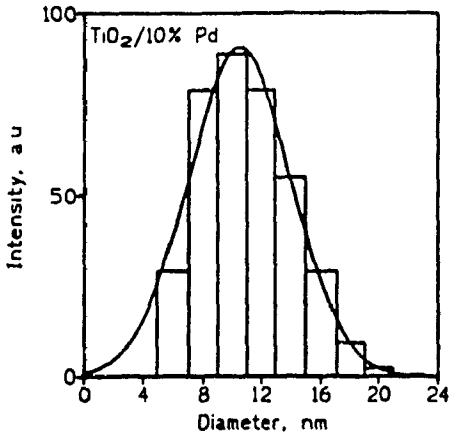
TiO2/10% Pd
Intensity, a u
Diameter, nm

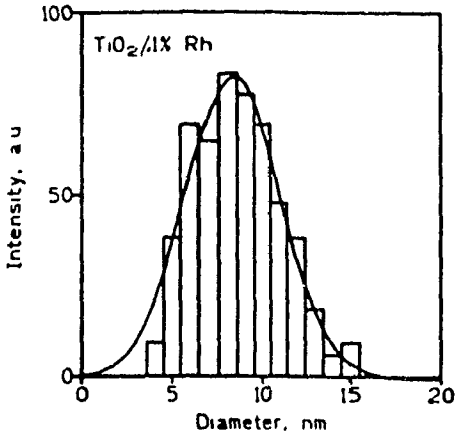
TiO2/1% Rh
Intensity, a u
Diameter, nm

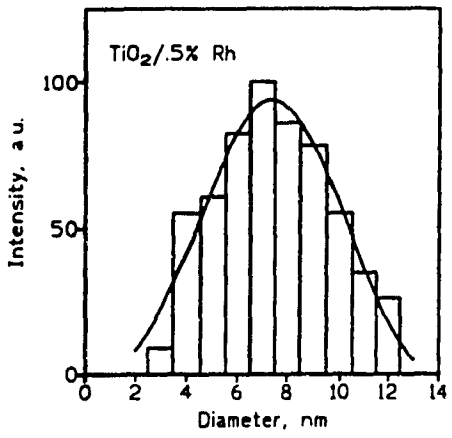
TiO2/.5% Rh
Intensity, a u.
Diameter, nm

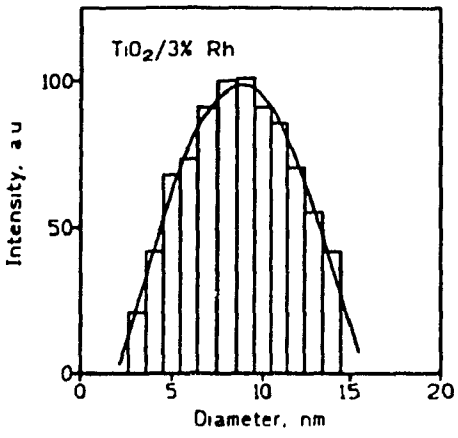
TiO2/3% Rh
Intensity, a u
Diameter, nm

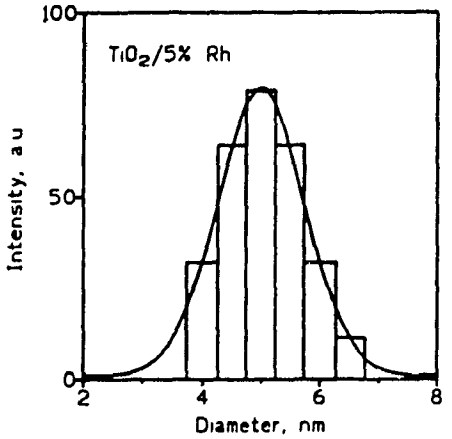
TiO2/5% Rh
Intensity, a u
Diameter, nm

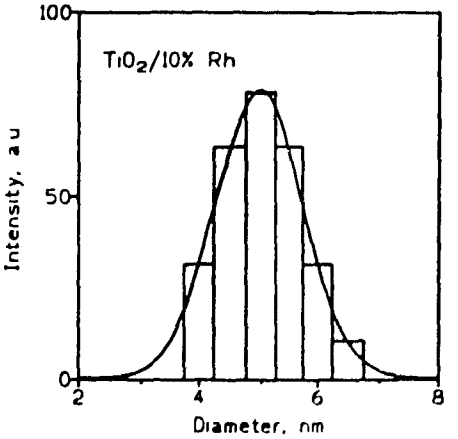
TiO2/10% Rh
Intensity, a u
Diameter, nm

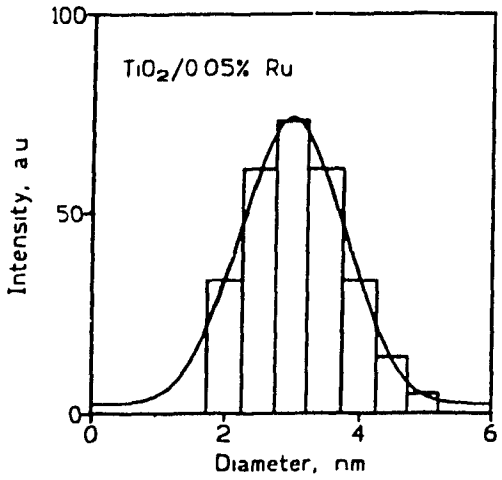
TiO2/0 05% Ru
Intensity, a u
Diameter, nm
0
50
100
0
2
4
6

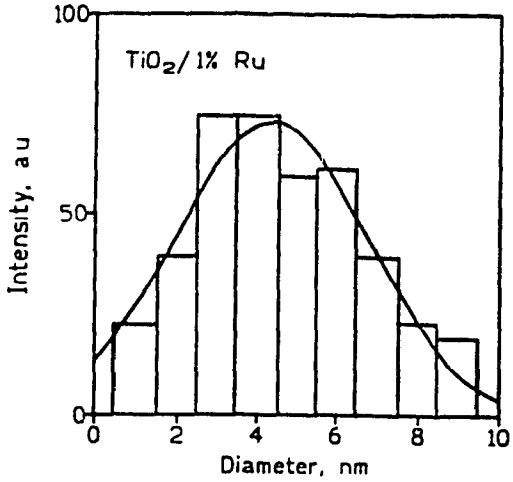
TiO2/1% Ru
Intensity, a u
Diameter, nm
0
50
100
0
2
4
6
8
10

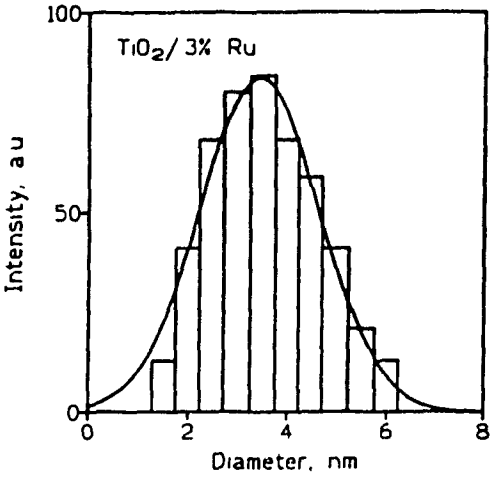
TiO2/3% Ru
Intensity, a u
Diameter, nm
0
50
100
0
2
4
6
8

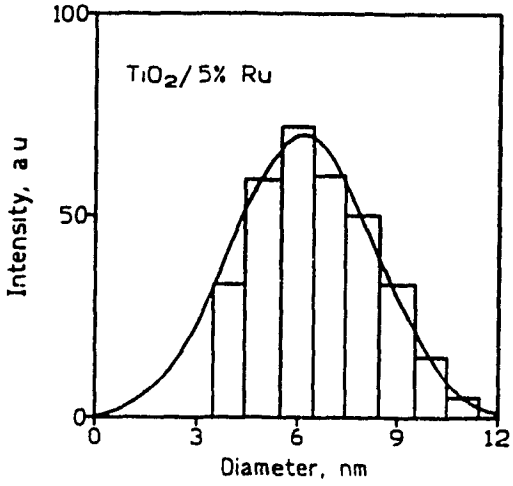
TiO2/5% Ru
Intensity, a u
Diameter, nm
0
50
100
0
3
6
9
12

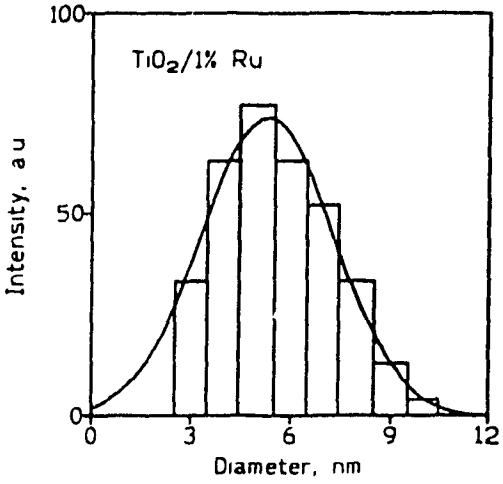
TiO2/1% Ru
Intensity, a u
Diameter, nm
0
50
100
0
3
6
9
12

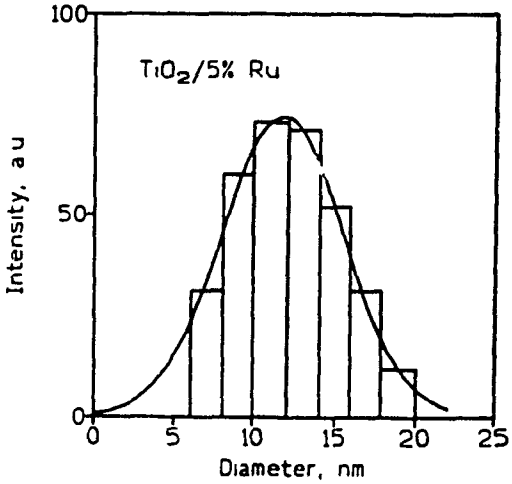
TiO2/5% Ru
Intensity, a u
Diameter, nm
0
50
100
0
5
10
15
20
25

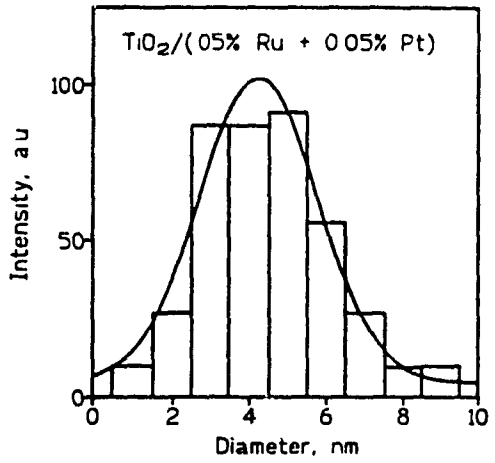
TiO2/(05% Ru + 0 05% Pt)
Intensity, a u
Diameter, nm

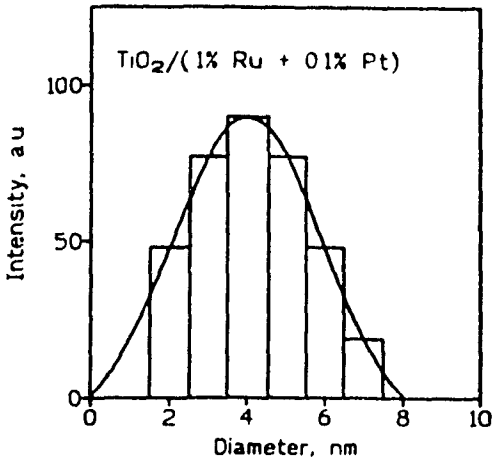
TiO2/(1% Ru + 0 1% Pt)
Intensity, a u
Diameter, nm

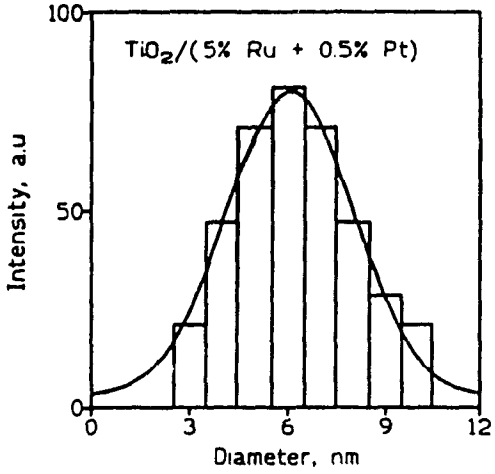
TiO2/(5% Ru + 0.5% Pt)
Intensity, a u
Diameter, nm

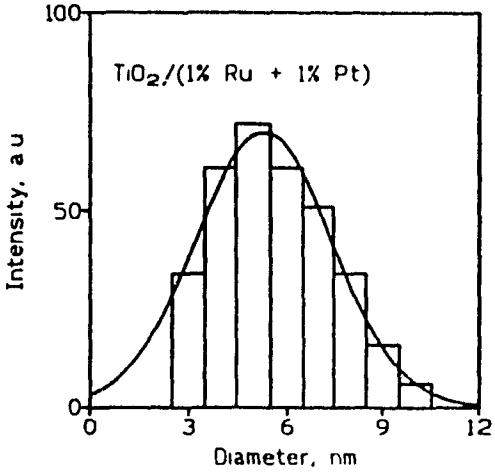
TiO2/(1% Ru + 1% Pt)
Intensity, a u
Diameter, nm

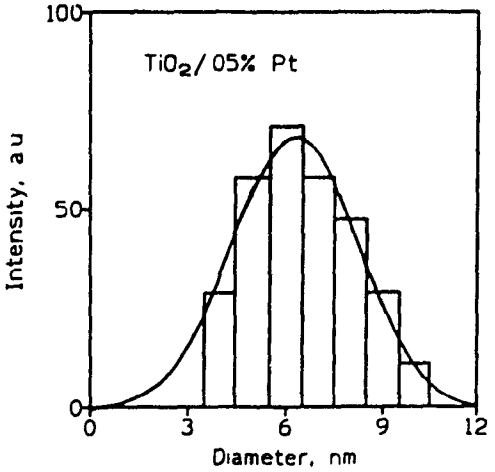
TiO2/ 05% Pt
Intensity, a u
Diameter, nm

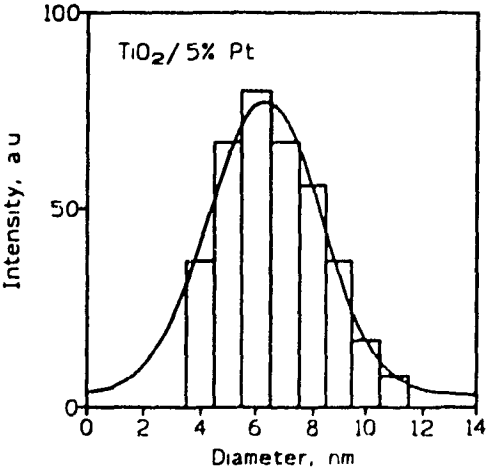
TiO2/ 5% Pt
Intensity, a u
Diameter, nm

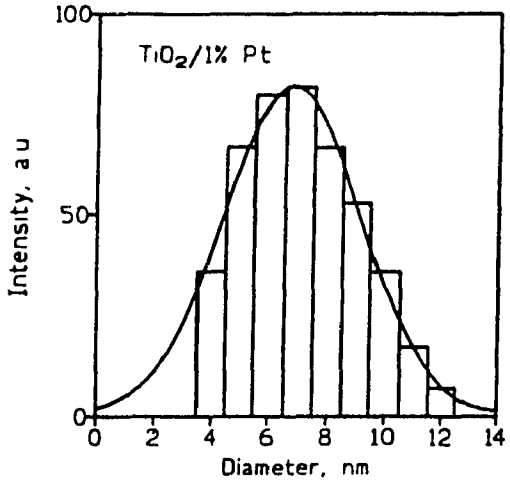
TiO2/1% Pt
Intensity, a u
Diameter, nm

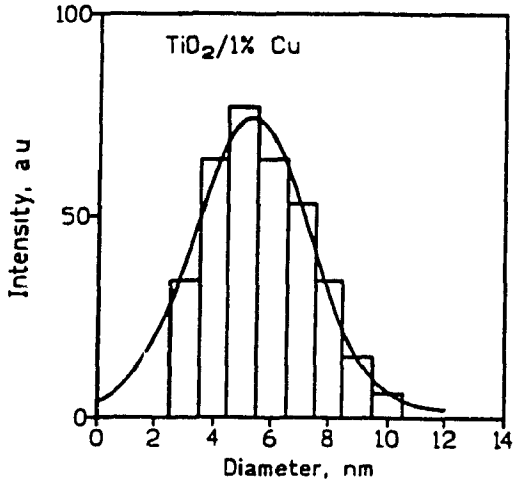
TiO2/1% Cu
Intensity, a u
Diameter, nm

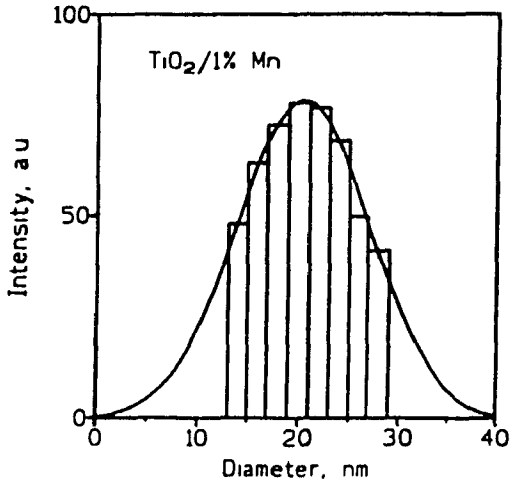
TiO2/1% Mn
Intensity, a u
Diameter, nm

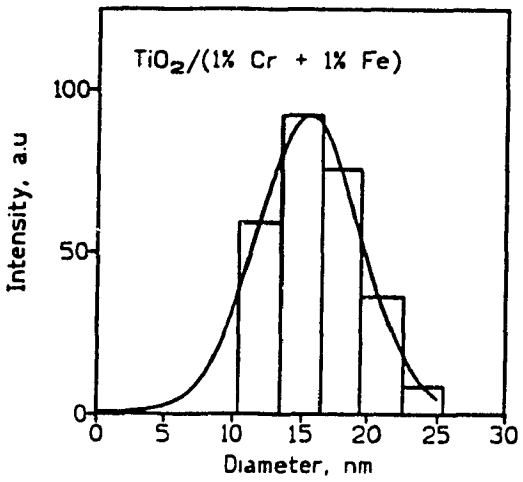
TiO2/(1% Cr + 1% Fe)
Intensity, a u
Diameter, nm

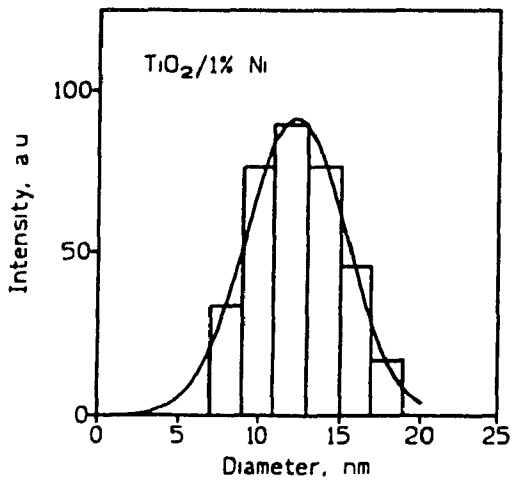
TiO2/1% Ni
Intensity, a u
Diameter, nm

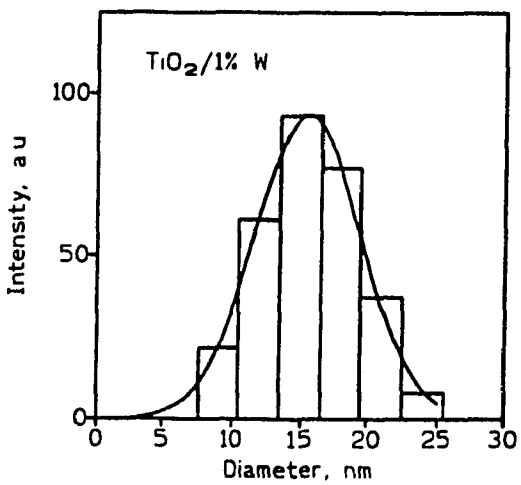
TiO2/1% W
Intensity, a u
Diameter, nm

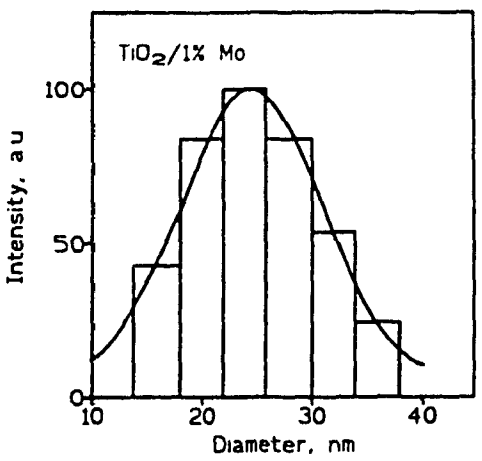
TiO2/1% Mo
Intensity, a u
100
50
0
10
20
30
40
Diameter, nm

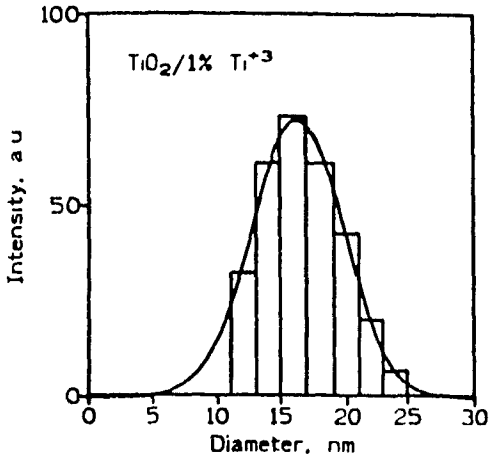
TiO2/1% Ti+3
Intensity, a u
100
50
0
0
5
10
15
20
25
30
Diameter, nm

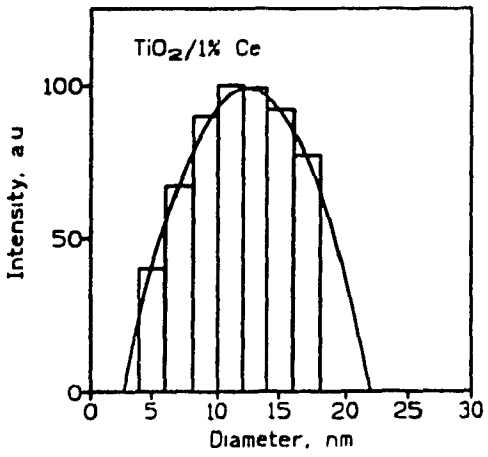
TiO2/1% Ce
Intensity, a u
100
50
0
0
5
10
15
20
25
30
Diameter, nm

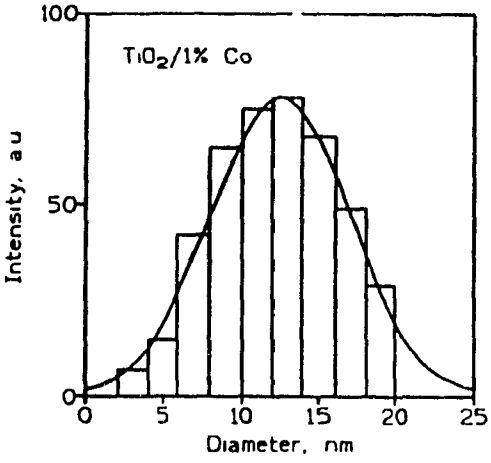
TiO2/1% Co
Intensity, a u
100
50
0
0
5
10
15
20
25
Diameter, nm

APPENDIX B

TRANSMISSION ELECTRON MICROSCOPE PHOTOGRAPHS OF TRANSITION METAL DOPED TiO_2

The transmission electron microscope (TEM) photographs presented in this Appendix were obtained during the course of physical characterization studies of the transition metal doped TiO_2 as presented in chapter 3.

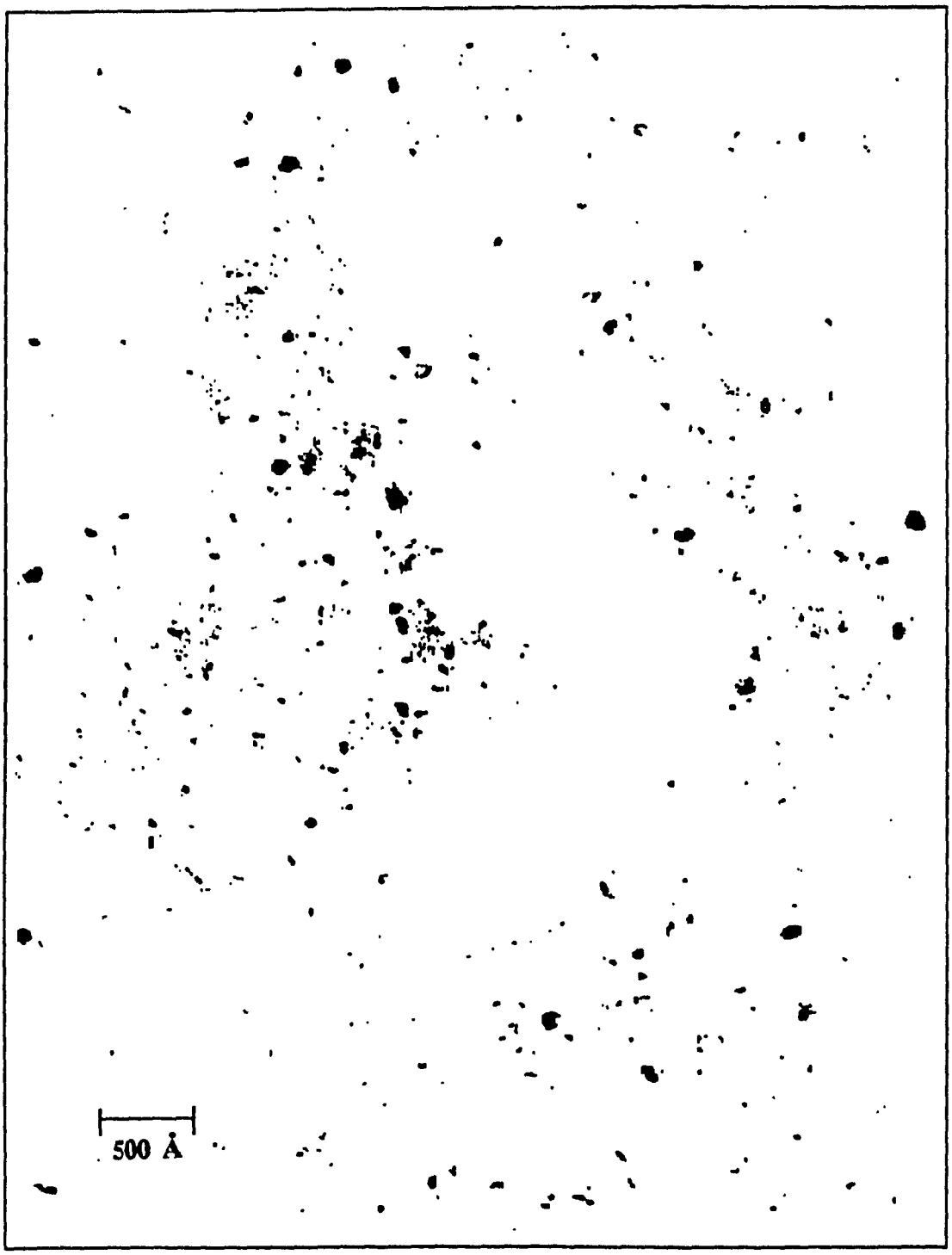

Figure B1 T.E.M. photograph of a representative sample of TiO_2/10 wt.% Cu determined using a Philips EM 420 at a magnification of 105 000.

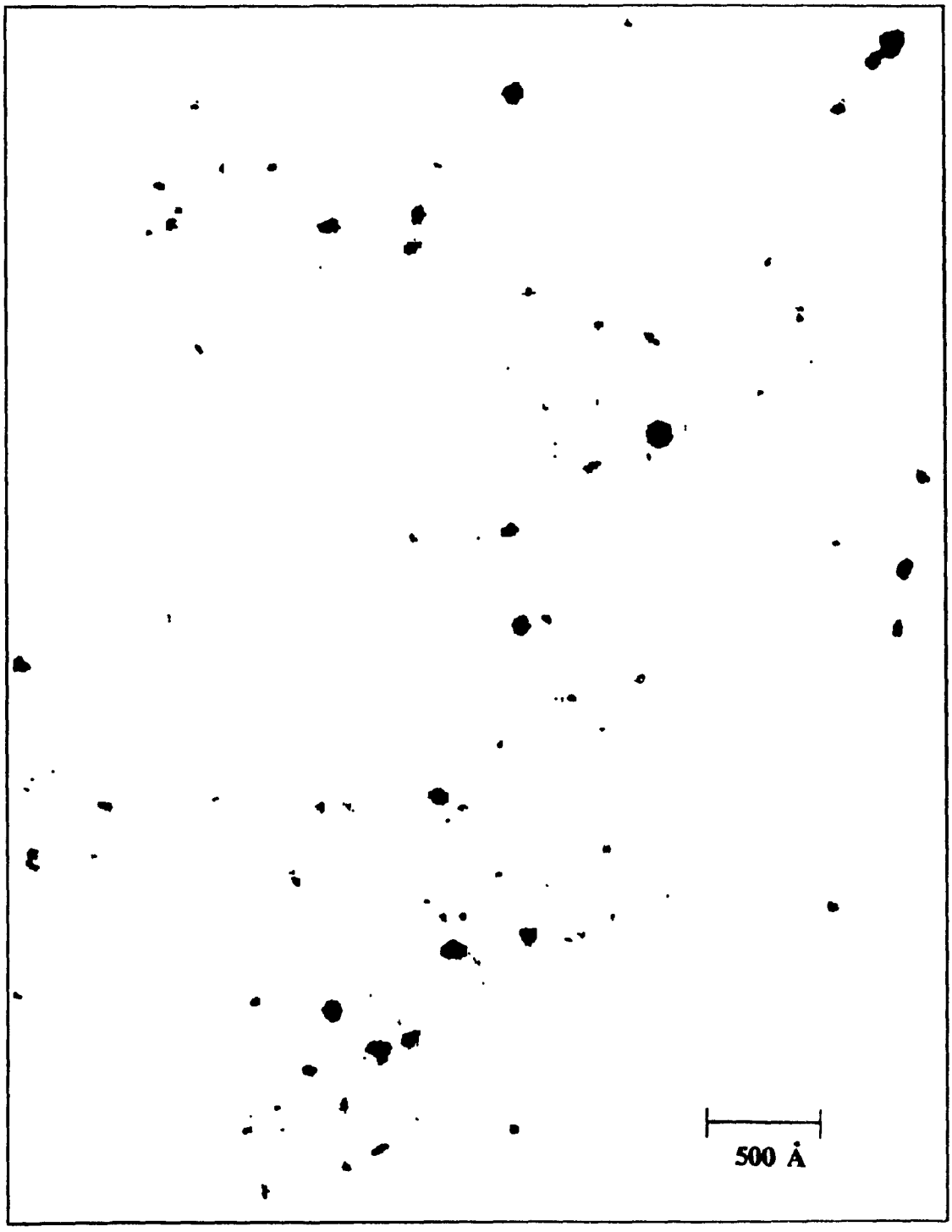

Figure B2 T.E.M. photograph of a representative sample of TiO_2/10 wt.% Ru determined using a Philips EM 420 at a magnification of 120 000.

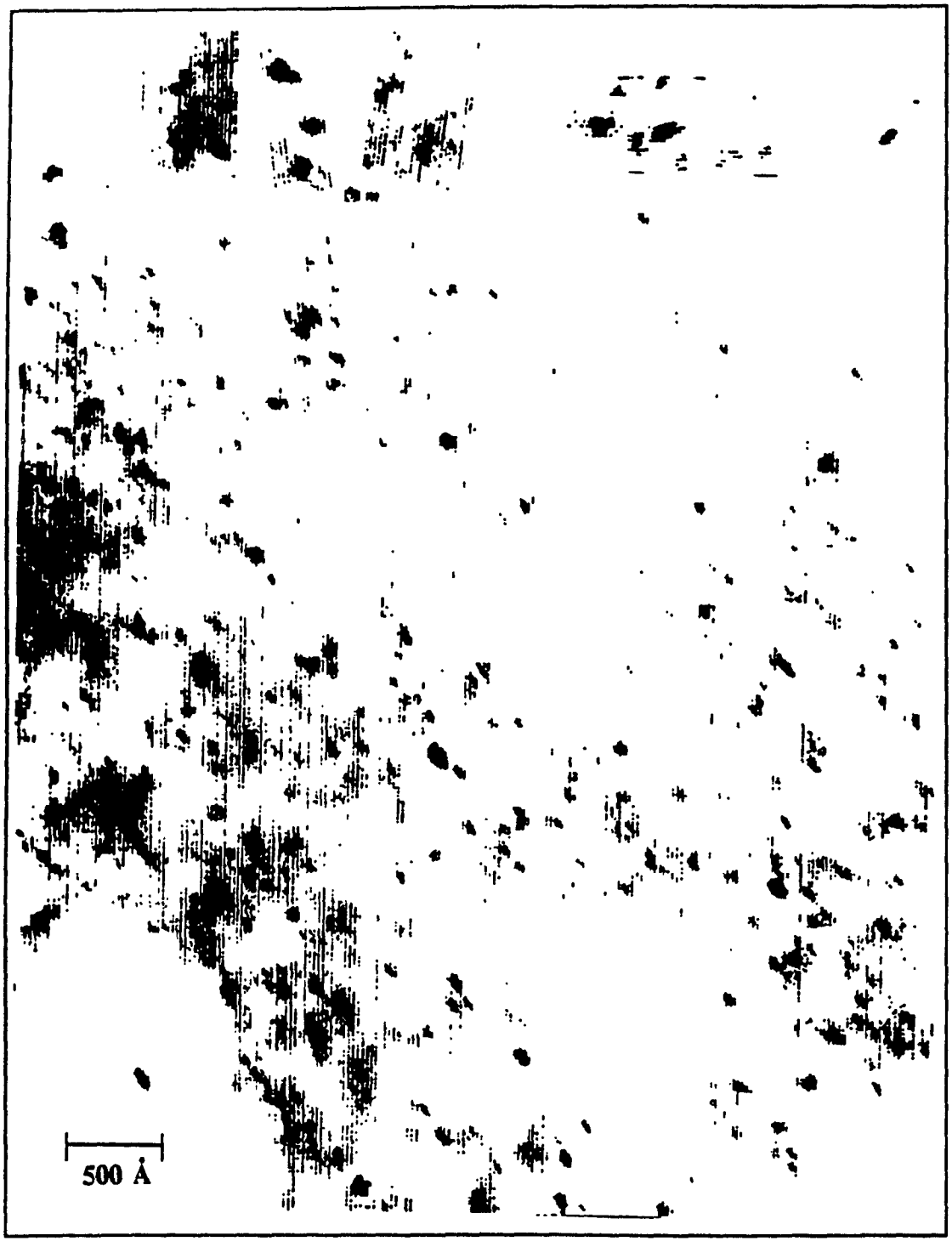

Figure B3 T.E.M. photograph of a representative sample of TiO_2/10 wt.% V determined using a Philips EM 420 at a magnification of 105 000.

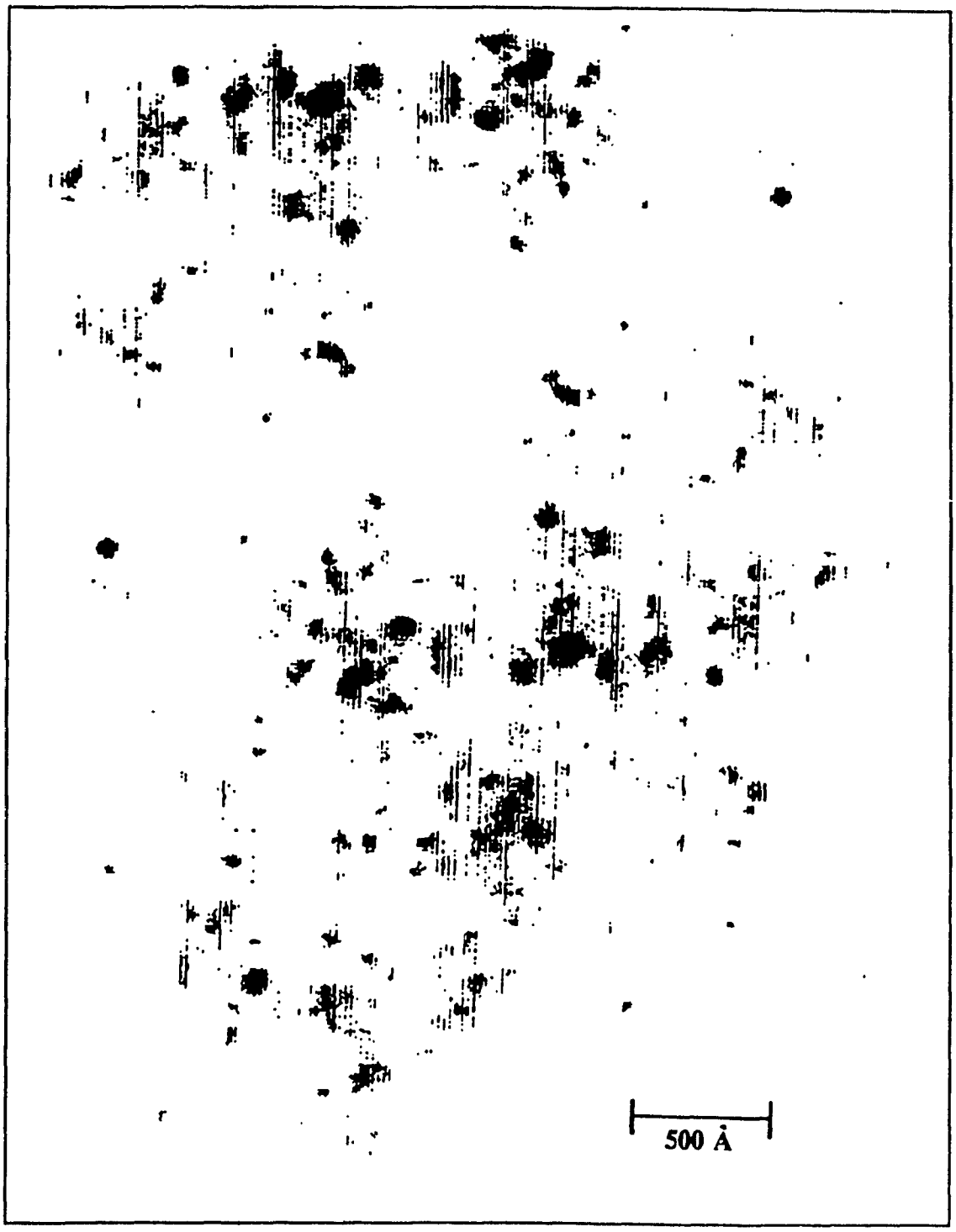

Figure B4 T.E.M. photograph of a representative sample of TiO_2/1 wt.% V determined using a Philips EM 420 at a magnification of 160 000.

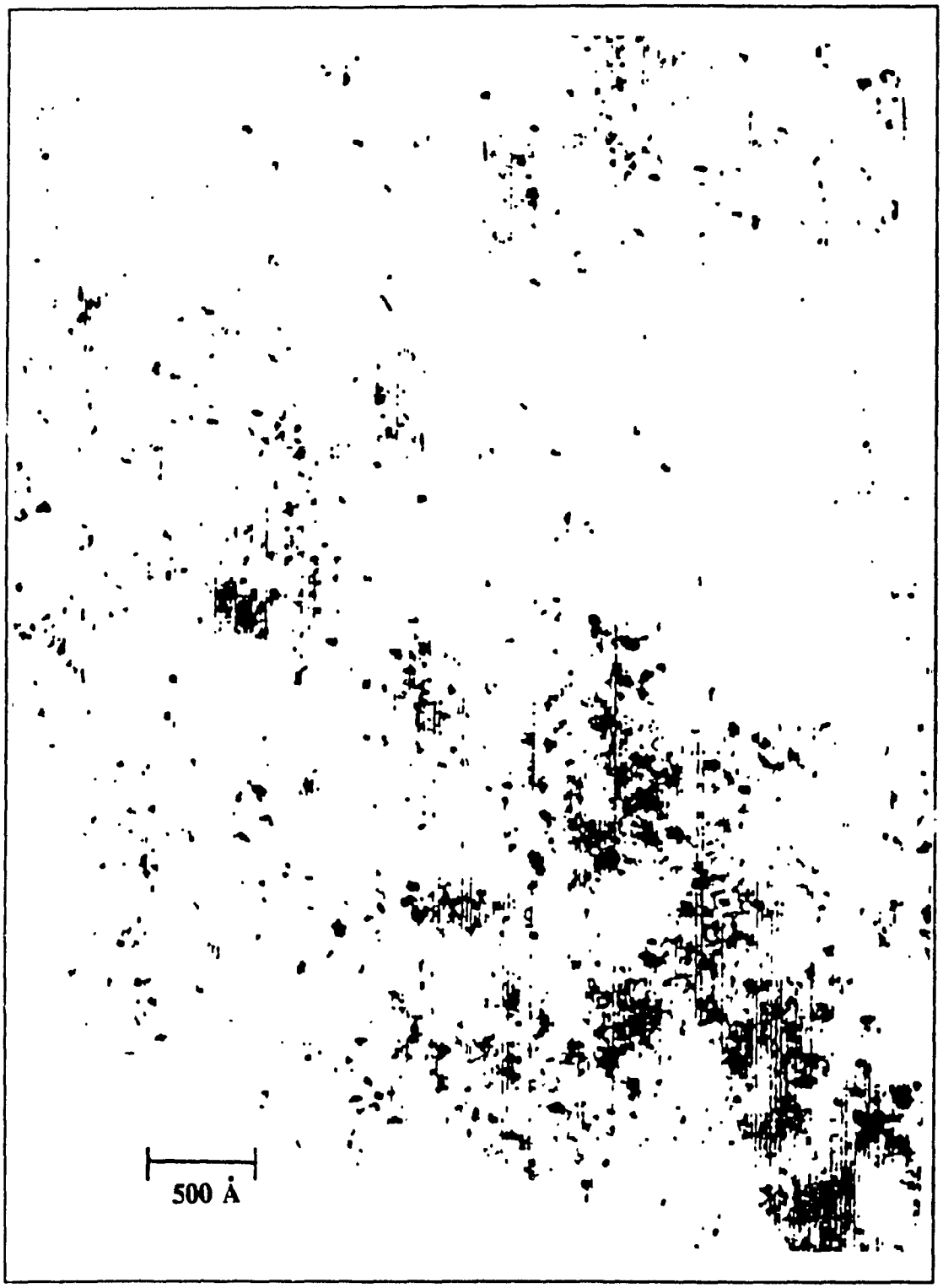

Figure B5 T.E.M. photograph of a representative sample of TiO_2/10 wt.% Rh determined using a Philips EM 420 at a magnification of 105 000.

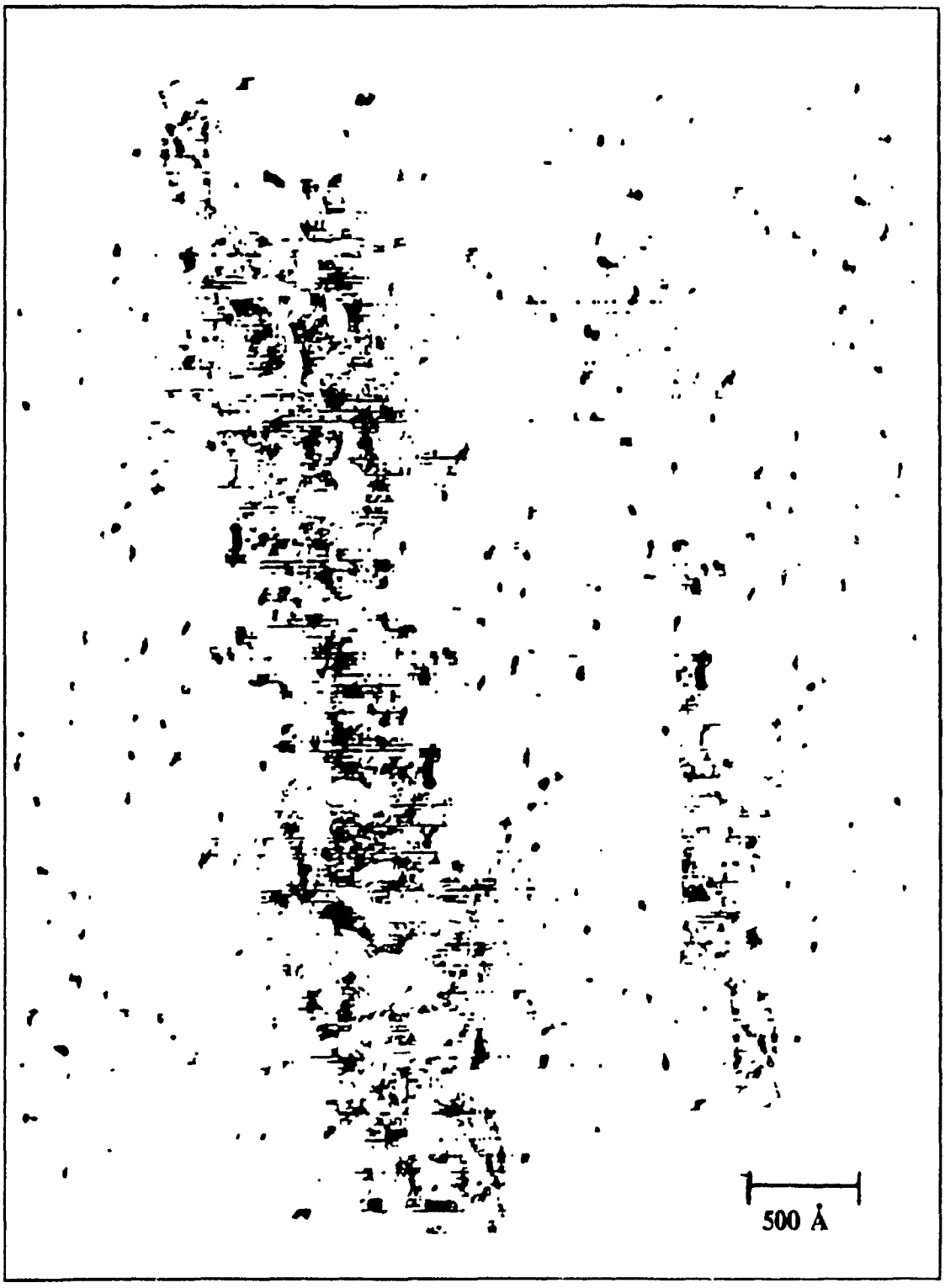

Figure B6 T.E.M. photograph of a representative sample of TiO_2/20 wt.% Cr determined using a Philips EM 420 at a magnification of 120 000.

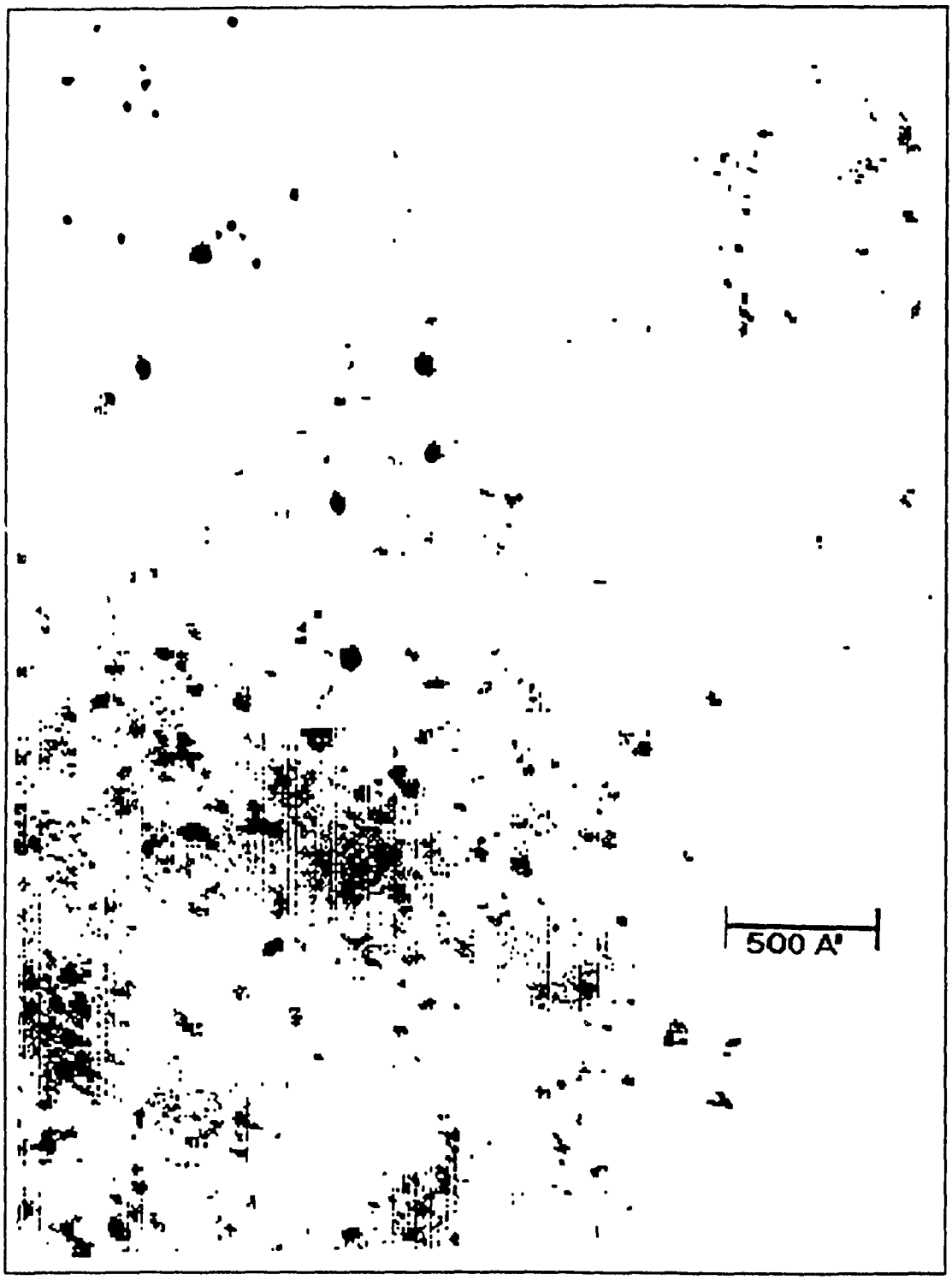

Figure B7 T.E.M. photograph of a representative sample of TiO_2/10 wt.% Pd determined using a Philips EM 420 at a magnification of 120 000.

APPENDIX C

X-RAY DIFFRACTION PATTERNS OF TRANSITION METAL DOPED TiO_2

The x-ray diffraction patterns of the transition metal doped TiO_2 samples presented in this Appendix were obtained during studies aimed at characterizing the particles as discussed in chapter 3. All diffraction patterns were obtained at the maximum sensitivity of the instrument and with 40 KV applied to the x-ray tube at a current of 20 mA.

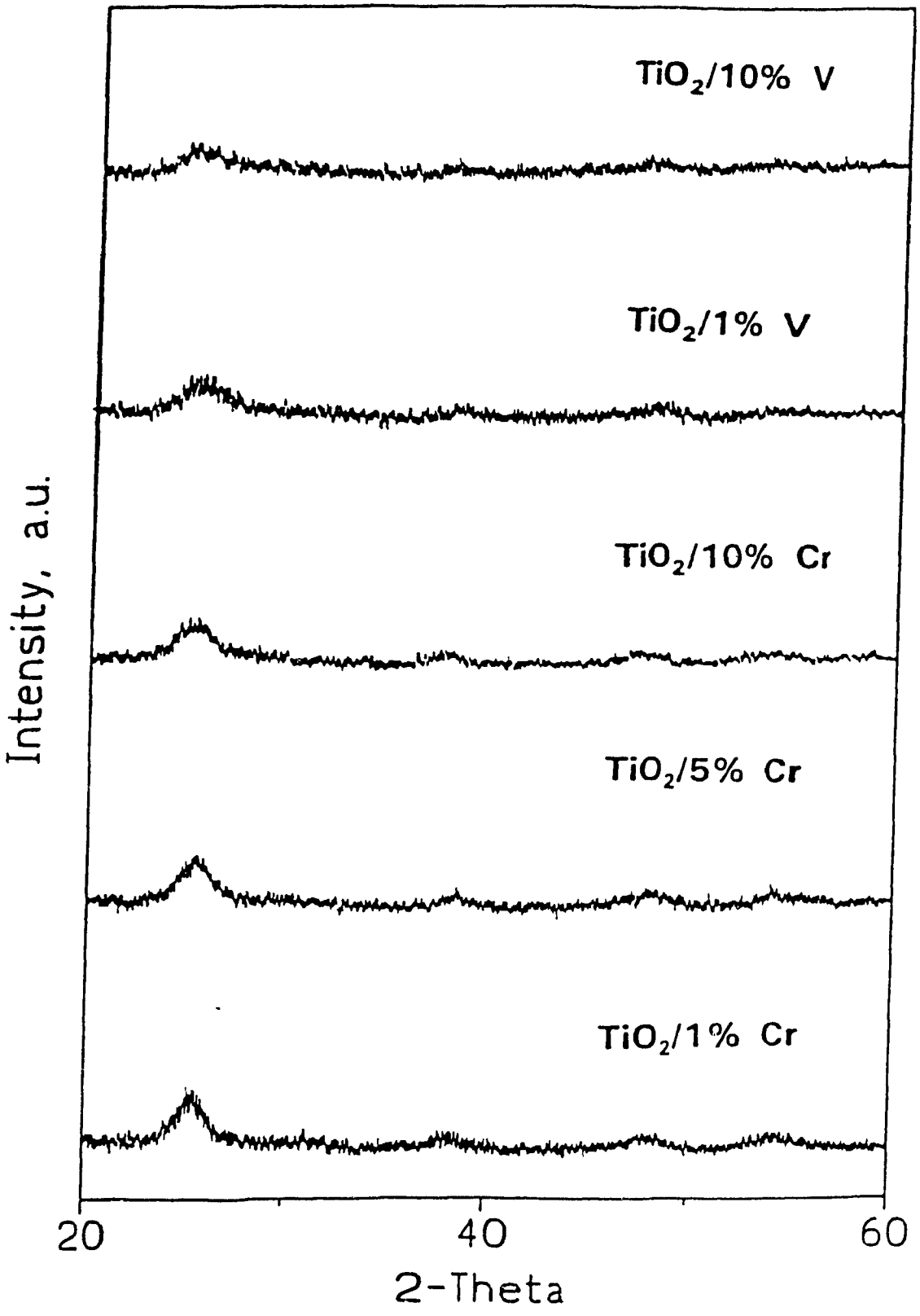
TiO2/10% V
TiO2/1% V
TiO2/10% Cr
TiO2/5% Cr
TiO2/1% Cr
Intensity, a.u.
20
40
60
2-Theta

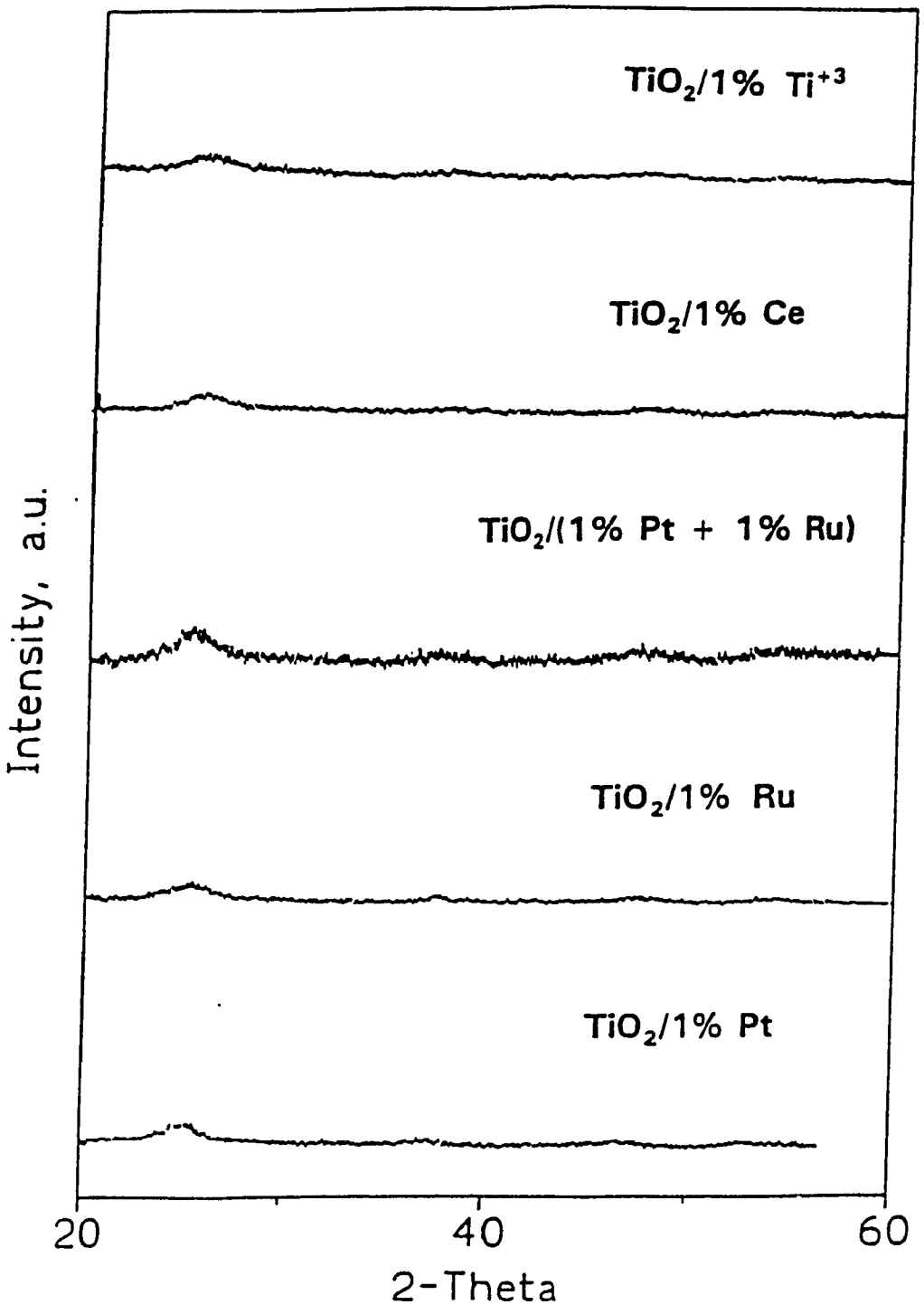
TiO2/1% Ti+3
TiO2/1% Ce
TiO2/(1% Pt + 1% Ru)
TiO2/1% Ru
TiO2/1% Pt
Intensity, a.u.
20
40
60
2-Theta

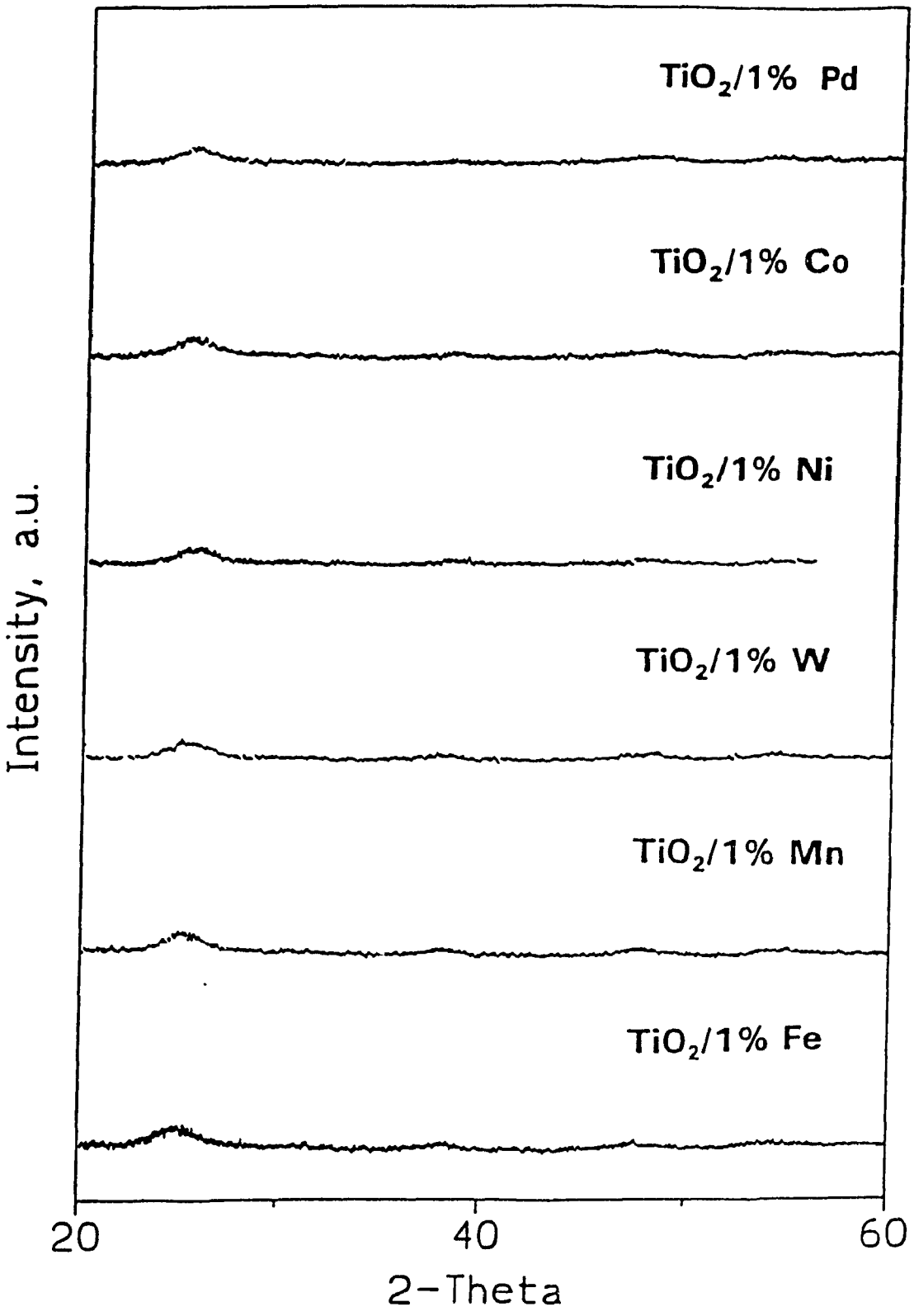
TiO2/1% Pd
TiO2/1% Co
TiO2/1% Ni
TiO2/1% W
TiO2/1% Mn
TiO2/1% Fe
Intensity, a.u.
20
40
60
2-Theta

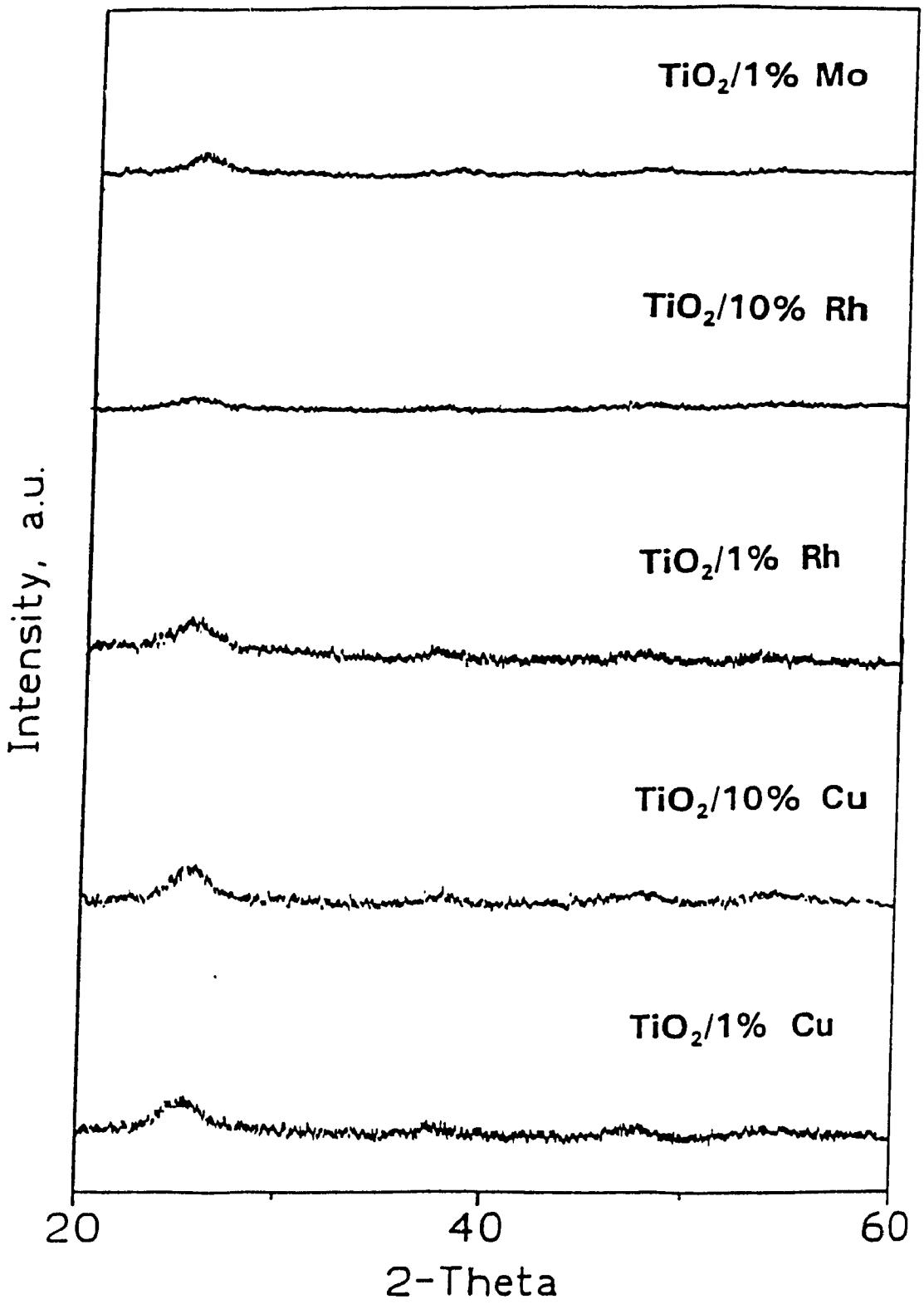
TiO2/1% Mo
TiO2/10% Rh
TiO2/1% Rh
TiO2/10% Cu
TiO2/1% Cu
Intensity, a.u.
20
40
60
2-Theta

APPENDIX D

PICOSECOND TRANSIENT ABSORPTION SPECTRA OF VARIOUS TRANSITION METAL DOPED TiO_2

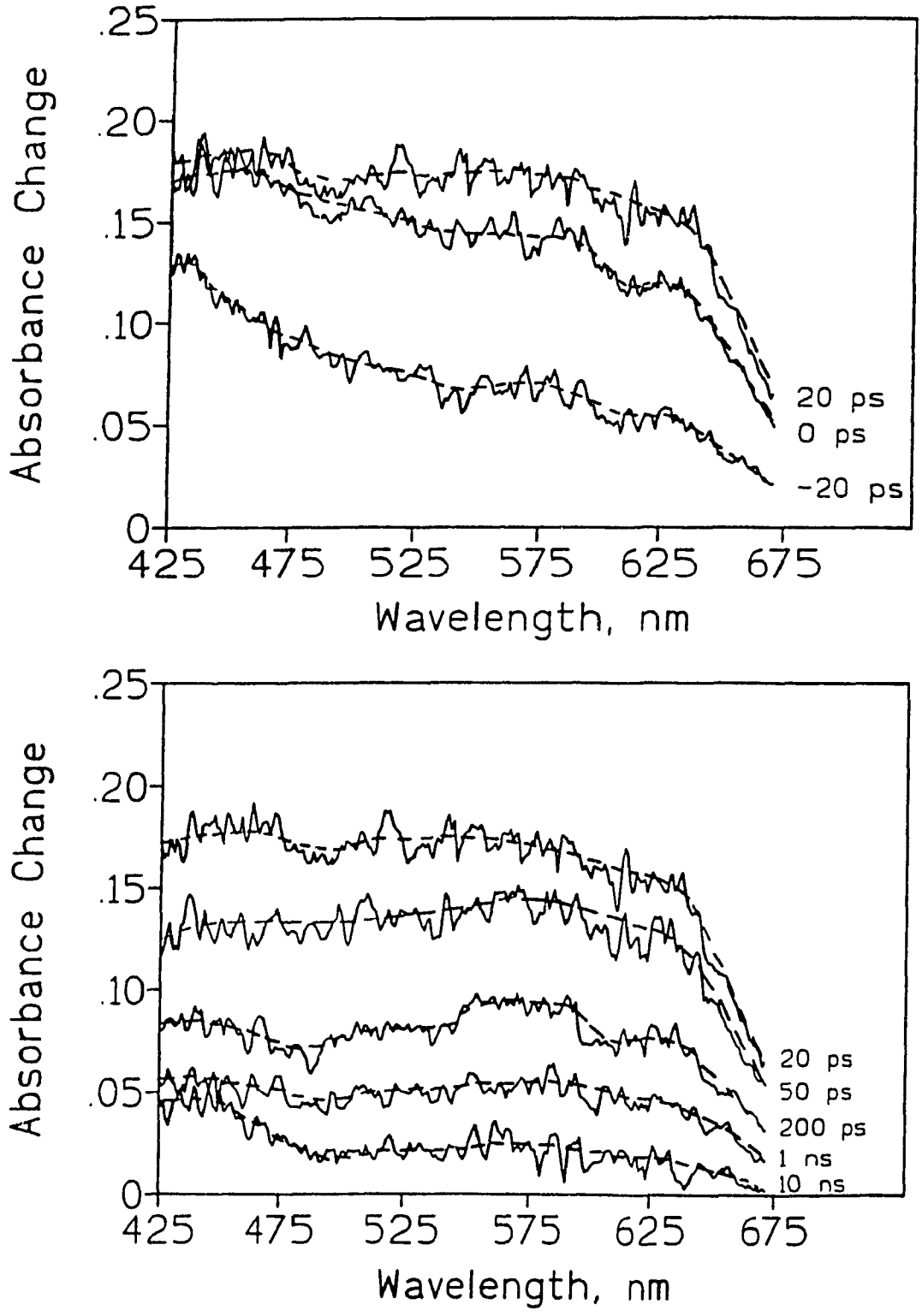

Figure D1 Transient spectra observed at various delay times after picosecond excitation (355 nm) of colloidal TiO_2 doped with 0.1 wt.% Rh^{+3}. [TiO_2/1 wt.% Rh^{+3}] = 15 g/L; pH 2.6; optical path length 0.2 cm.

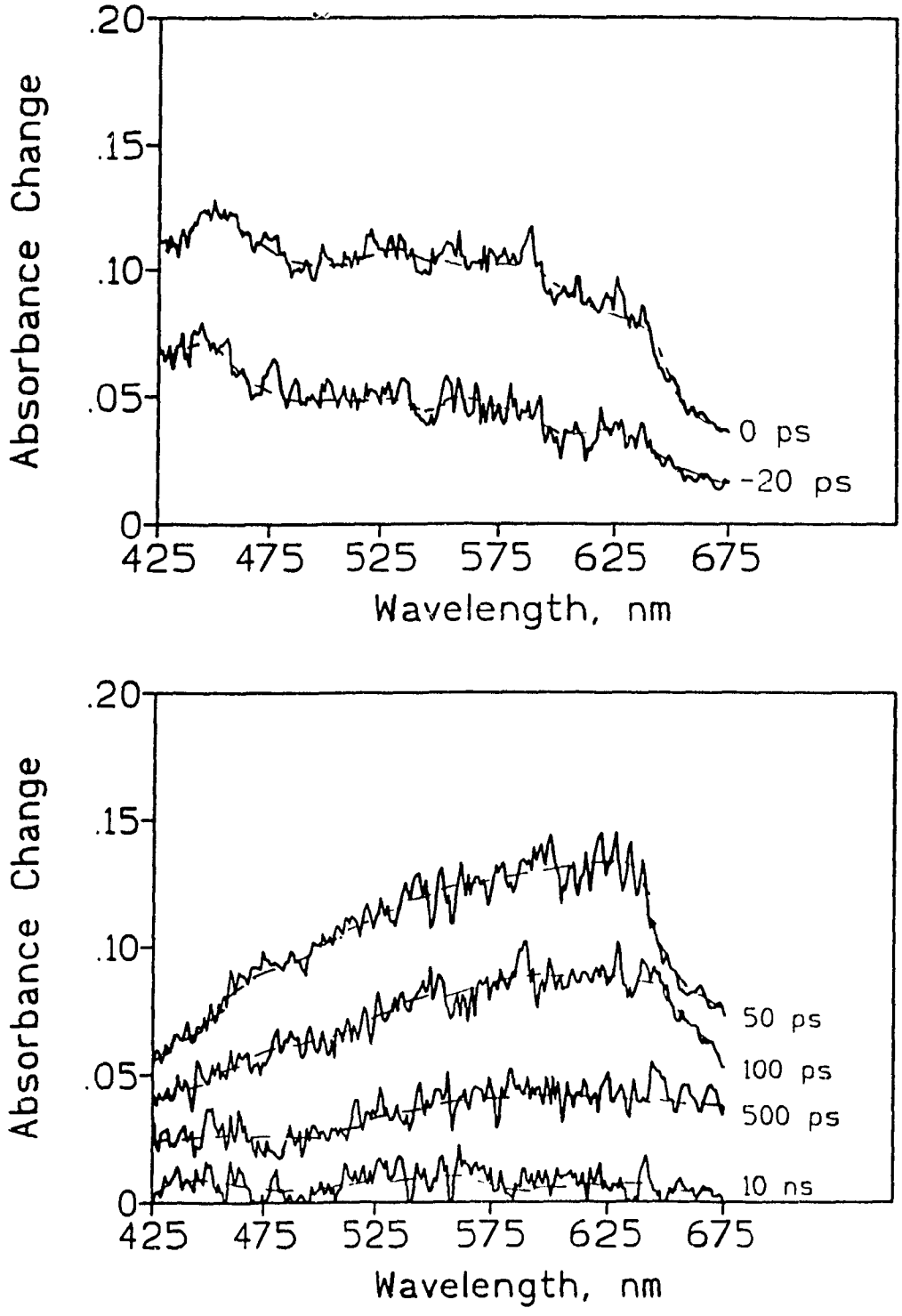

Figure D2 Transient spectra observed at various delay times after picosecond excitation (355 nm) of colloidal TiO_2 doped with 10 wt.% Cr^{+3}. [TiO_2/10 wt.% Cr^{+3}] = 15 g/L; pH 2.6; optical path length 0.2 cm.

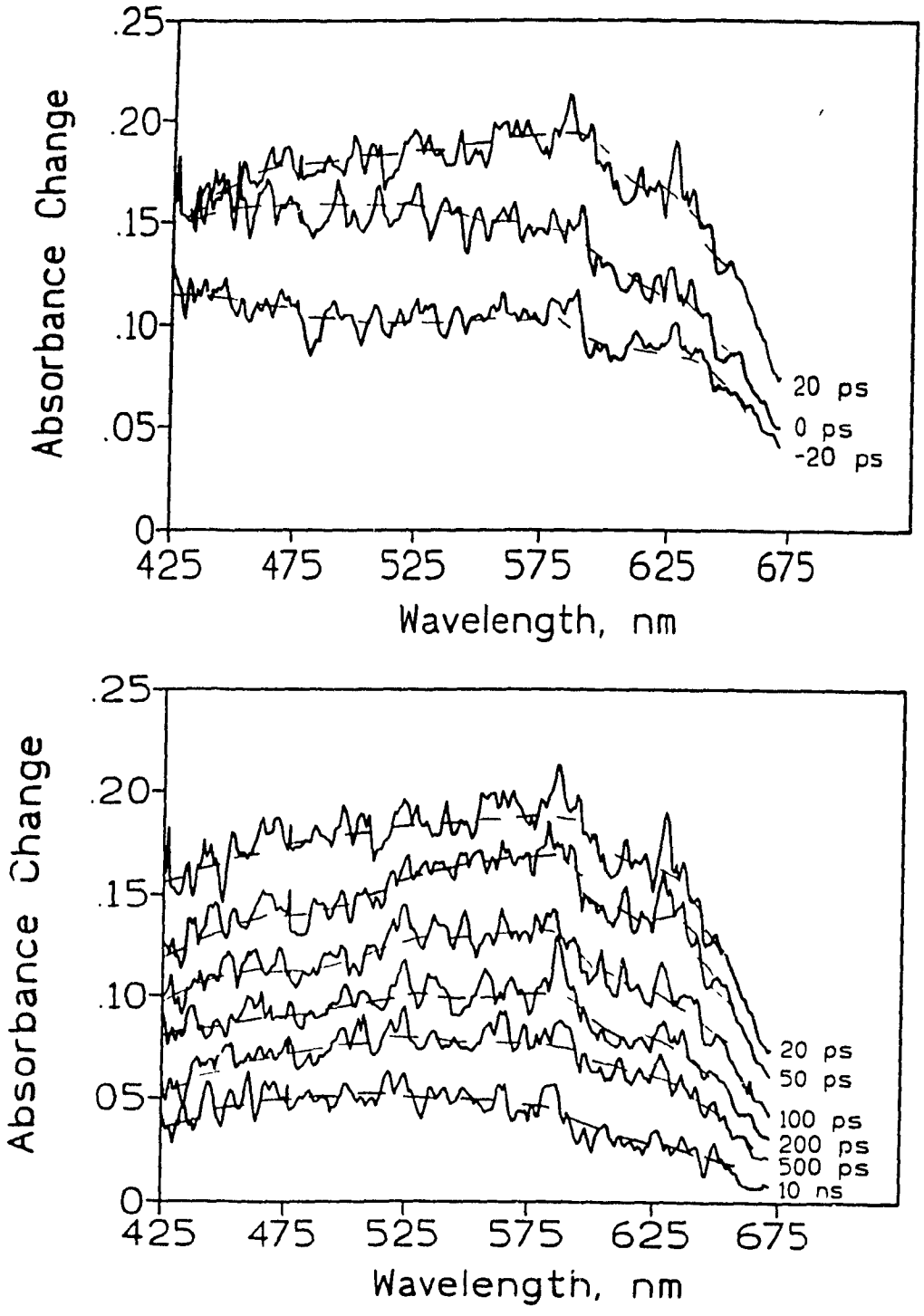

Figure D3 Transient spectra observed at various delay times after picosecond excitation (355 nm) of colloidal TiO_2 doped with 0.1 wt.% V^{+5}. [TiO_2/0.1 wt.% V^{+5}] = 15 g/L; pH 2.6; optical path length 0.2 cm.

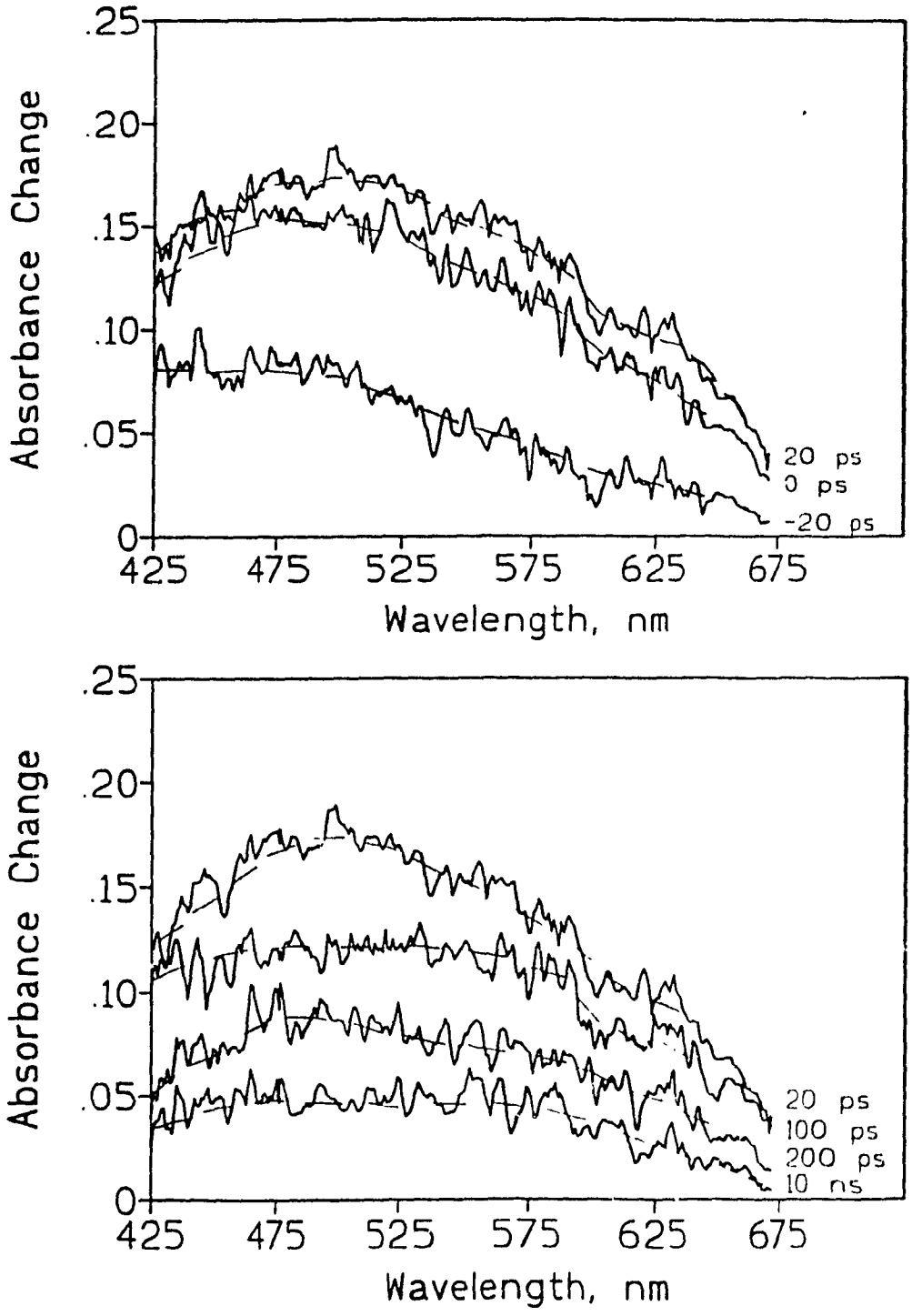

Figure D4 Transient spectra observed at various delay times after picosecond excitation (355 nm) of colloidal TiO_2 doped with 1 wt.% V^{+5}. [TiO_2/1 wt.% V^{+5}] = 15 g/L; pH 2.6; optical path length 0.2 cm.

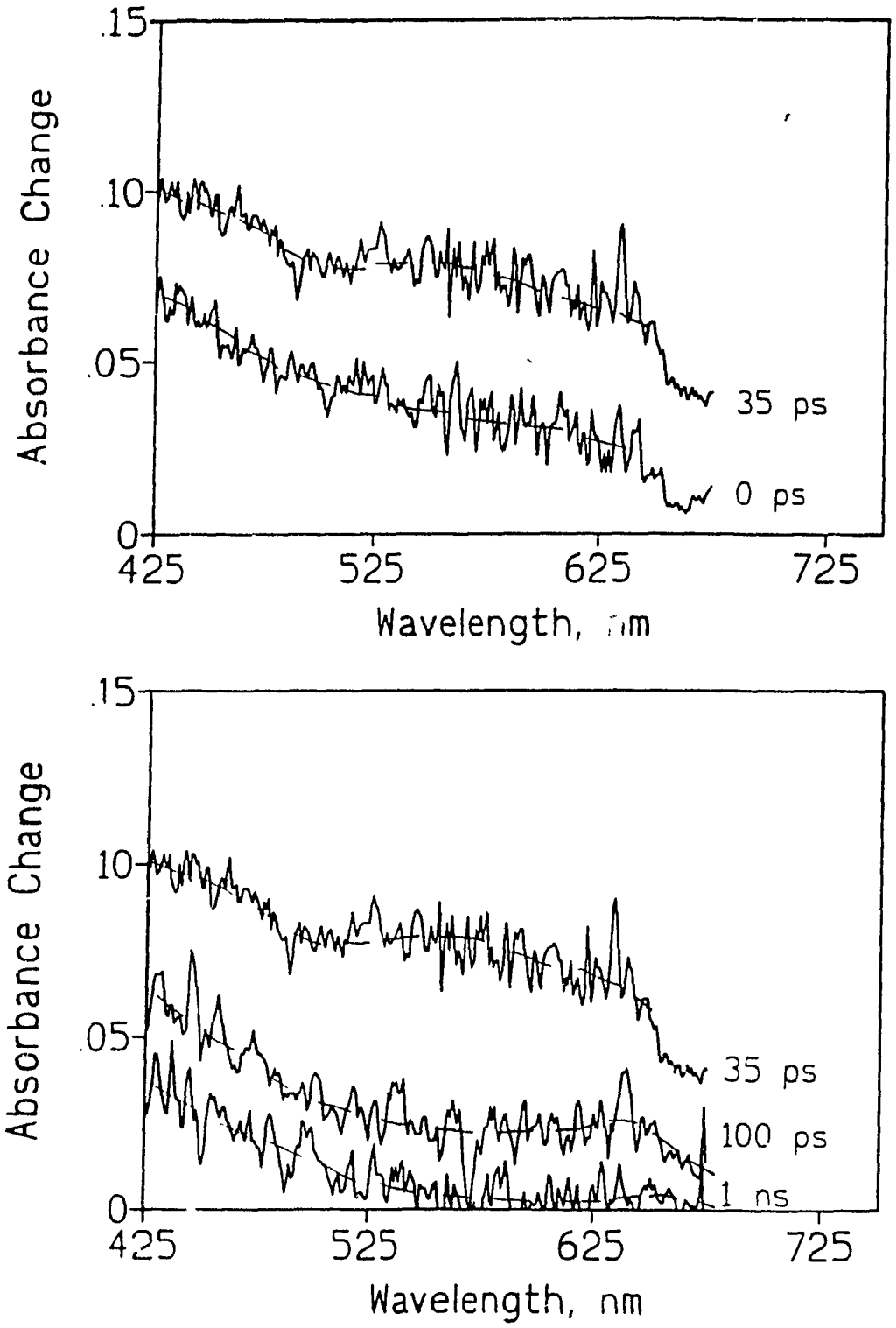

Figure D5 Transient spectra observed at various delay times after picosecond excitation (355 nm) of colloidal TiO_2 doped with 10 wt.% Fe^{+3}. [TiO_2/10 wt.% Fe^{+3}] = 15 g/L; pH 2.6; optical path length 0.2 cm.

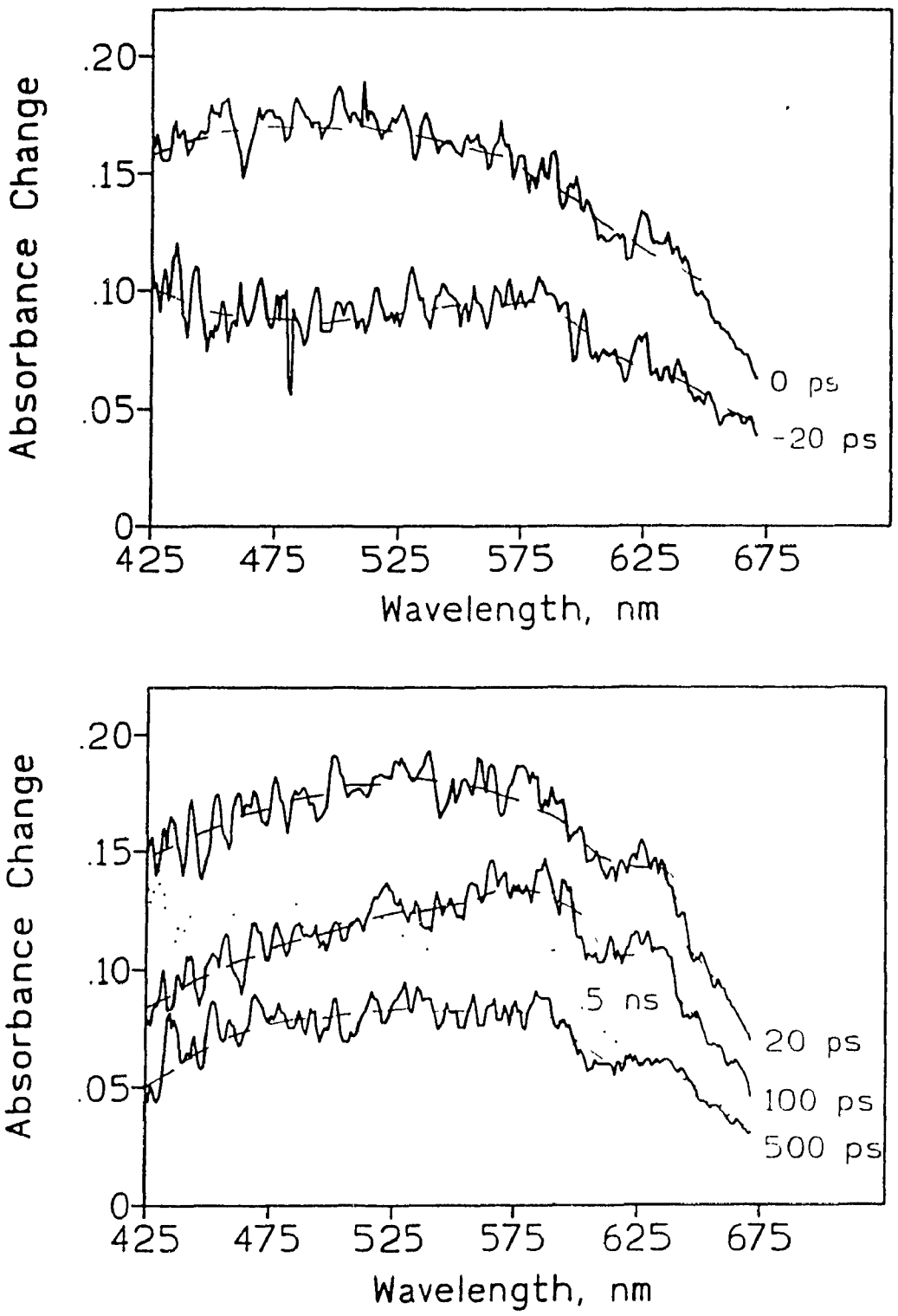

Figure D6 Transient spectra observed at various delay times after picosecond excitation (355 nm) of colloidal TiO_2 doped with 0.1 wt.% Ru^{+3}. [TiO_2/0.1 wt.% Ru^{+3}] = 15 g/L; pH 2.6; optical path length 0.2 cm.

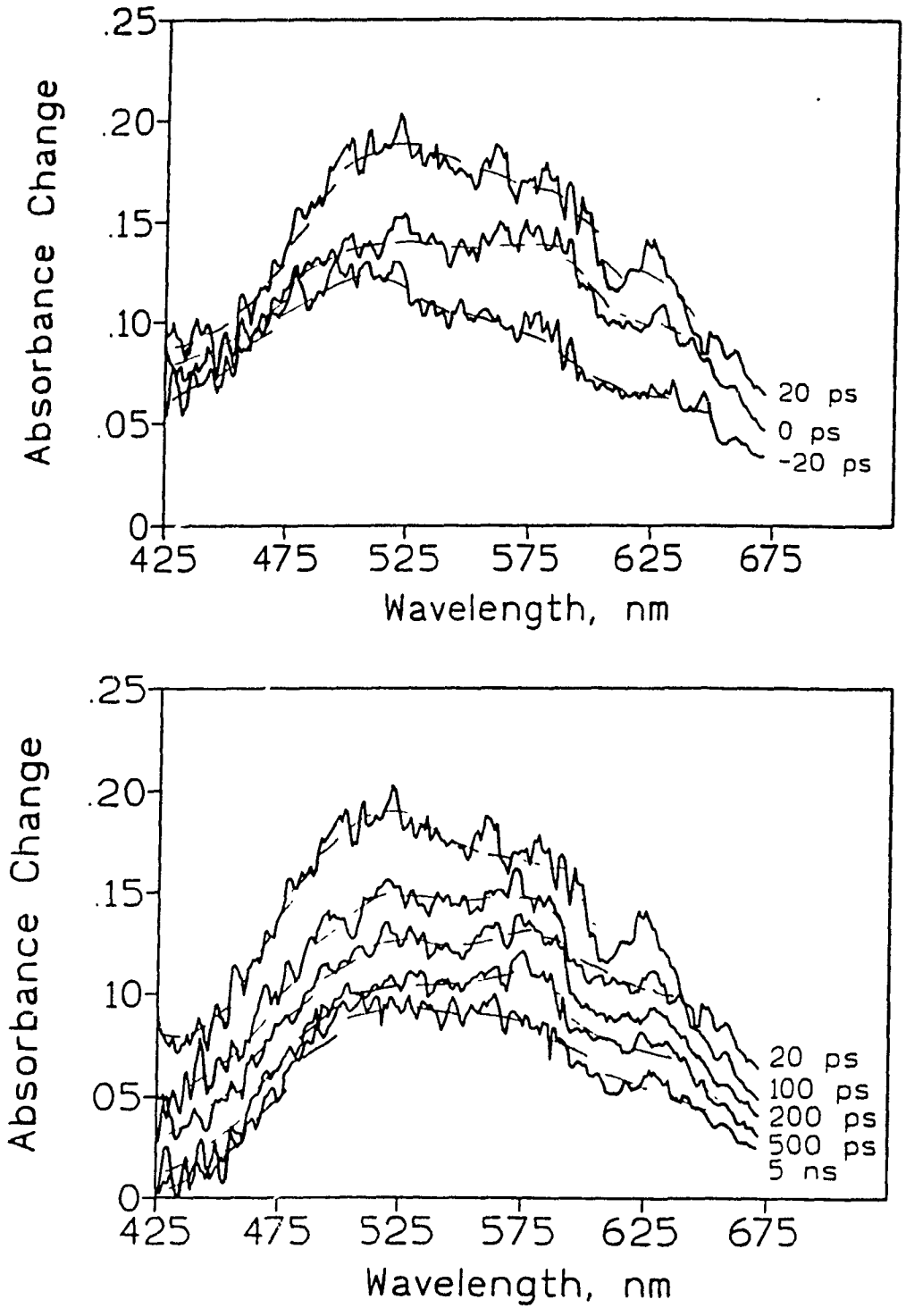

Figure D7 Transient spectra observed at various delay times after picosecond excitation (355 nm) of colloidal TiO_2 doped with 1 wt.% Ru^{+3}. [TiO_2/1 wt.% Ru^{+3}] = 15 g/L; pH 2.6; optical path length 0.2 cm.

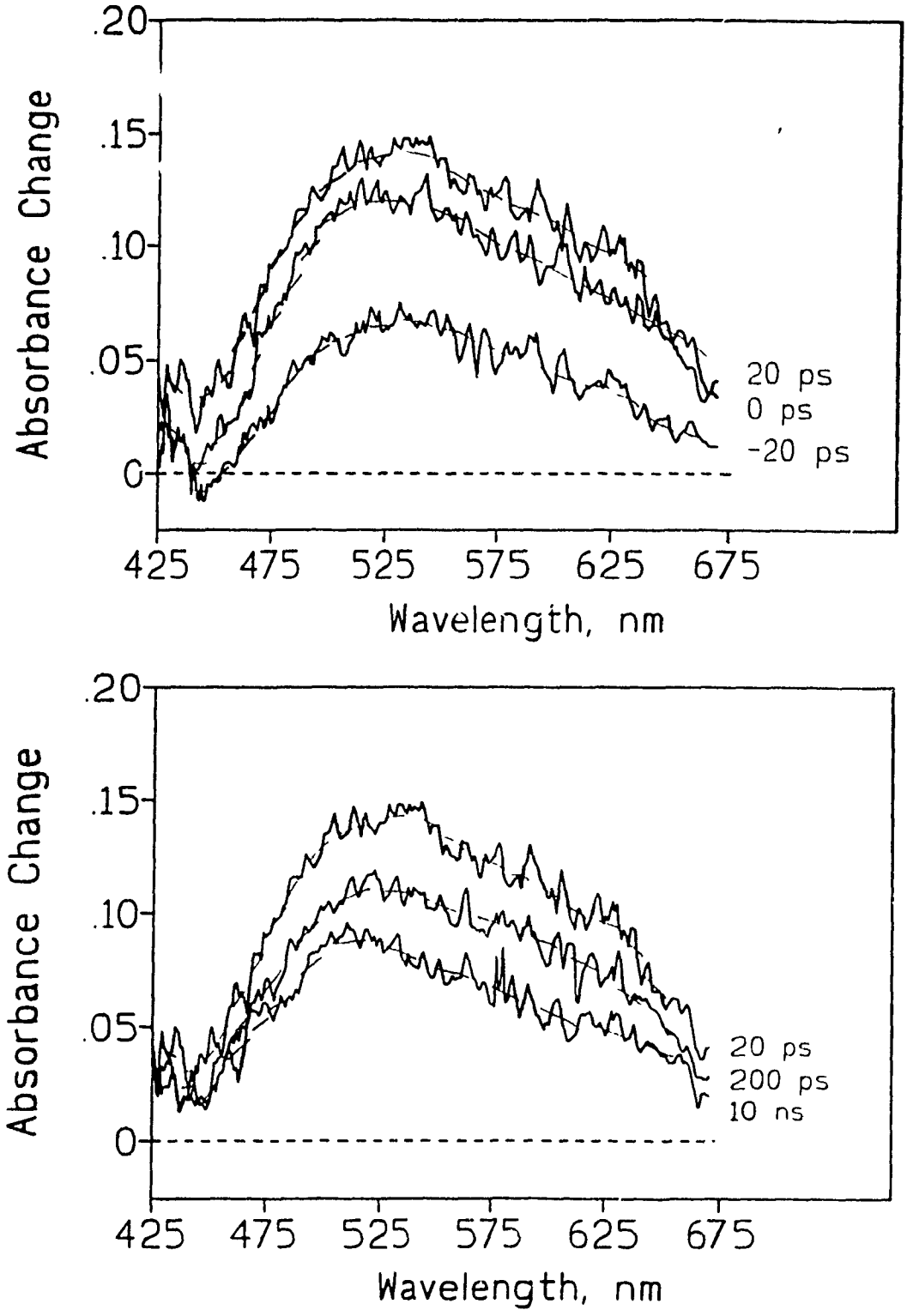

Figure D8 Transient spectra observed at various delay times after picosecond excitation (355 nm) of colloidal TiO_2 doped with 1 wt.% Ru^{+3} and 1 wt.% Pt^{+4} [TiO_2/(1 wt.% Ru^{+3}, 1 wt.% Pt^{+4})] = 15 g/L; pH 2.6; optical path length 0.2 cm.